

Optical Microscopy of Magnetic Phenomena Beyond the Diffraction Limit

Dissertation

zur Erlangung des Doktorgrades der Naturwissenschaften
(Dr. rer. nat.)

der Naturwissenschaftlichen Fakultät II
Chemie, Physik und Mathematik

der Martin-Luther-Universität
Halle-Wittenberg

vorgelegt von
Chris Marcel Körner

Date of submission: 16.10.2025

Date of defense: 12.02.2026

Supervisor: Prof. Dr. Georg Woltersdorf
(Martin-Luther-University Halle-Wittenberg)

Co-Supervisor: Prof. Dr. Stuart Parkin
(Max Planck Institute of Microstructure Physics,
Martin-Luther-University Halle-Wittenberg)

First referee: Prof. Dr. Georg Woltersdorf

Second referee: Prof. Dr. Stuart Parkin

External referee: Prof. Dr. Mathias Weiler
(Rheinland-Pfälzische Technische Universität
Kaiserslautern-Landau)

Abstract

This thesis focuses on optical methods for investigating magnetization dynamics, with a particular emphasis on techniques that circumvent the optical diffraction limit. Using optical methods, a discovery was made that is presented in the first part of this thesis. It describes the generation of a six-octave spanning magnonic frequency comb that forms in a $\text{Ni}_{80}\text{Fe}_{20}$ thin film under excitation with MHz radio waves. To study this process, various methods were employed to characterize the magnetic material and to detect the magnetization dynamics. Confocal nitrogen-vacancy (NV) center magnetometry is employed to detect the high harmonic spin waves directly via their stray fields. Furthermore, super-Nyquist-sampling MOKE (SNS-MOKE) microscopy provides spatially-resolved imaging of the spin wave modes. Micromagnetic simulations were used to elucidate the origin of the observed spin waves and to develop a model for the generation of the high harmonic spin waves. This model is based on synchronized switching processes within different regions of the film. The distribution of these regions is determined by a distinctive magnetization pattern that soft magnetic films exhibit under low bias fields, referred to as concertina pattern. This pattern provides the local symmetry breaking which ultimately allows for this process. To achieve a higher spatial resolution in the imaging of the high harmonic spin waves generated, scanning NV center magnetometry is employed. This technique is especially useful for the investigation of small microstructured devices.

The second part of this thesis describes the construction of a novel optical setup to detect magnetization dynamics with a spatial resolution that exceeds the optical diffraction limit. This method combines Brillouin light scattering (BLS) with scanning near field optical microscopy (SNOM). In comparison to scanning NV center microscopy, the use of inelastic light scattering for the detection of magnetization dynamics is much less restricted in terms of detectable frequencies. At the same time, the near field microscope provides sub-100 nm spatial resolution. To realize this instrument, a multi-purpose near field system was set up, in combination with a narrow-band light source which is stabilized to an absolute frequency standard. In addition, a high-throughput, high-resolution spectrometer was designed, constructed, and integrated with the instrument. Test measurements using various polymer samples demonstrate the functionality of the spectrometer and the successful integration with the near field microscope. This method will be instrumental in future experiments, facilitating the imaging of magnetization dynamics occurring at the nano-scale and the imaging of spin waves with large wave vectors.

Kurzzusammenfassung

Diese Arbeit befasst sich mit optischen Methoden zur Untersuchung von Magnetisierungsdynamik. Ein besonderer Schwerpunkt liegt dabei auf Techniken, welche die optische Auflösungsgrenze umgehen. Unter Verwendung optischer Methoden wurde ein Effekt entdeckt, der im ersten Teil dieser Arbeit vorgestellt wird: die Erzeugung eines magnonischen Frequenzkamms mit einer Spannweite von über sechs Oktaven, der sich in einer $\text{Ni}_{80}\text{Fe}_{20}$ -Dünnschicht unter Anregung mit MHz-Radiowellen ausbildet. Um diesen Prozess zu untersuchen, wurden verschiedene Methoden zur Charakterisierung des magnetischen Materials und der Magnetisierungsdynamik eingesetzt. Konfokale NV-Center-Magnetometrie wird benutzt, um die höheren harmonischen Spinwellen direkt über ihre Streufelder zu detektieren. Darüber hinaus liefert SNS-MOKE-Mikroskopie räumlich aufgelöste Bilder der angeregten Spinwellenmoden. Mikromagnetische Simulationen wurden verwendet, um den Ursprung der beobachteten Spinwellen aufzuklären und ein Modell für deren Erzeugung zu entwickeln. Dieses Modell basiert auf synchronisierten Schaltprozessen innerhalb verschiedener Bereiche des Films. Die Verteilung dieser Bereiche wird durch ein charakteristisches Magnetisierungsmuster bestimmt, das weichmagnetische Filme unter Einfluss nur geringer äußerer Magnetfelder aufweisen. Dieses wird als Concertina-Muster bezeichnet. Es sorgt für eine lokale Symmetriebrechung, die diesen Prozess letztendlich ermöglicht. Um eine höhere räumliche Auflösung bei der Abbildung der erzeugten hochharmonischen Spinwellen zu erreichen, wird Scanning NV-Center Magnetometrie eingesetzt. Diese Technik ist besonders nützlich für die Untersuchung von Mikrostrukturen.

Der zweite Teil dieser Arbeit beschreibt den Aufbau einer neuartigen optischen Anordnung zur Detektion von Magnetisierungsdynamik mit einer räumlichen Auflösung, die über das optische Auflösungslimit hinausgeht. Diese Methode kombiniert Brillouin-Lichtstreuung mit optischer Nahfeldmikroskopie. Verglichen mit NV-Zentren-Mikroskopie ist die Verwendung von inelastischer Lichtstreuung zur Detektion von Magnetisierungsdynamik weniger limitiert hinsichtlich der detektierbaren Frequenzen. Das Nahfeldmikroskop bietet gleichzeitig eine räumliche Auflösung von unter 100 nm. Zur Realisierung des Aufbaus wurde ein multifunktionales Nahfeldmikroskop installiert, zusammen mit einer schmalbandigen Lichtquelle, welche auf einen absoluten Frequenzstandard stabilisiert ist. Zusätzlich wurde ein hochauflösendes Spektrometer mit kurzen Messzeiten entwickelt, konstruiert und in den Aufbau integriert. Testmessungen mit verschiedenen Polymeren belegen die Funktionsfähigkeit des Spektrometers und die Integration in das Nahfeldmikroskop. Diese Methode kann in zukünftigen Experimenten eine wichtige Rolle spielen und die Untersuchung von Magnetisierungsdynamik im Nanobereich, sowie die Abbildung von Spinwellen mit hohen Wellenvektoren ermöglichen.

Contents

Abstract	iii
Kurzzusammenfassung	v
List of Figures	xi
List of Abbreviations	xv
List of Optical Components	xix
1. Introduction	1
2. Theoretical Background	7
2.1. Theory of Magnetism	7
2.1.1. Origin of Magnetism	7
2.1.2. Static Properties of Magnetic Materials	10
2.1.3. Magnetization Dynamics in Magnetic Materials	18
2.1.4. Magneto-Optical Effects	28
2.1.5. Transport Effects	30
2.1.6. Magnetic Order Beyond Ferromagnetism	32
2.2. Optics, Spatial Resolution and Near Field Interaction	34
2.2.1. Far Field Diffraction Limit and Optical Resolution	35
2.2.2. Optical Near Field and Electric Dipole Interaction	37
2.3. Inelastic Scattering of Light	40
2.3.1. Scattering Process and Energy Conservation	41
2.3.2. Stokes and Anti-Stokes Spectrum	41
2.3.3. Conservation of Momentum	42
2.4. Optical Fluorescence of Defect Centers in Diamond	43
2.4.1. Electronic Properties of the NV Center	43
2.4.2. Optical Transitions and Mechanism of Fluorescence Contrast	45
3. Experimental Probing Methods	49
3.1. Non-Local Methods	50
3.1.1. Inductive FMR	50
3.1.2. Transport Measurements	52
3.2. Diffraction-Limited Optical Methods	53
3.2.1. Wide-Field Kerr Microscopy	53
3.2.2. Static Kerr Microscopy	54

3.2.3.	Time-Resolved MOKE Microscopy	54
3.2.4.	Super-Nyquist-Sampling MOKE Microscopy	55
3.2.5.	Inelastic Light Scattering	59
3.3.	Probing Beyond the Diffraction Limit	60
3.3.1.	NV Center Magnetometry	60
3.3.2.	Confocal NV Center Magnetometry	61
3.3.3.	Atomic Force Microscopy	63
3.3.4.	Scanning NV Center Magnetometry	65
3.3.5.	Scanning Near Field Optical Microscopy	67
4.	Sample Preparation	75
4.1.	Electron Beam Lithography	75
4.2.	Thermal Evaporation	76
4.3.	Magnetron Sputtering	76
4.4.	Atomic Layer Deposition	77
5.	Micromagnetic Simulations	79
6.	All-Magnonic Frequency Comb Generation	81
6.1.	Previous Works on Frequency Multiplication	82
6.2.	Sample Preparation and Layout	84
6.3.	Confocal NV Center Magnetometry Measurements	85
6.4.	Analyzing the Response at the Excitation Frequency	89
6.5.	SNS-MOKE Maps at Low Bias Fields	90
6.6.	Simulation of an Ideal NiFe Film	95
6.6.1.	Simulation Geometry and Sequence	95
6.6.2.	Simulation Results	96
6.7.	Kerr Microscopy Measurements	98
6.8.	Simulation of a Stripe with Inhomogeneous Magnetization	99
6.8.1.	Simulation Geometry	99
6.8.2.	Static Behavior	100
6.8.3.	Dynamic Response	101
6.9.	Simulation of an Individual Boundary Between Two Magnetic Regions	104
6.9.1.	Simulation Geometry	104
6.9.2.	Static Behavior and Switching Model	104
6.9.3.	Dynamic Response	105
6.10.	Miniaturizing Active Structures	109
6.10.1.	Sample Layout	109
6.10.2.	SNS-MOKE Measurements on NiFe Devices	110
6.10.3.	Scanning NV Center Magnetometry on NiFe Devices	111
6.11.	Assessment of the Different Optical Methods	117

7. Construction of a Multi-Purpose Near Field Setup	119
7.1. General s-SNOM Setup	121
7.1.1. Light Sources	122
7.1.2. Detection of Scattered Light	124
7.1.3. Measurement Geometries	124
7.1.4. Interferometric Detection of Near Fields	126
7.1.5. Interferometric Detection in Transmission Geometry	126
7.2. Inelastic Light Scattering Beyond the Diffraction Limit: Nano-Focused BLS	128
7.2.1. Previous Technical Developments	128
7.2.2. Overview of the Nano-Focused BLS Setup	129
7.2.3. Frequency-Stabilized Single Mode Laser Source	129
7.2.4. High Throughput VIPA Spectrometer	134
7.2.5. Spectral Filtering of Rayleigh Scattering	138
7.2.6. Evaluation of the Setup and Test Measurements	139
7.2.7. Future Application of the Technique in Experiments	140
7.2.8. Outlook to Further Improvements of the Setup	141
8. Conclusion	143
A. Heat-Assisted Detection of Magnetization	145
A.1. Imaging of Ferromagnetic Domains in In-Plane Magnetized CoFeB	146
A.2. Imaging of Ferromagnetic Domains in Out-of-Plane Magnetized Co-Ni Multilayer Stack	148
A.3. Imaging of the Magnetization State of the Non-Collinear Antiferromag- net Mn_3Sn	149
B. Nano FTIR Spectroscopy	151
B.1. Working Principle of FTIR Spectroscopy	151
B.2. Nano FTIR Spectroscopy Setup	151
B.2.1. Broad Band MIR Light Source	152
C. Confocal NV Center magnetometry	155
C.1. Comparison of Modulation Techniques	155
C.2. Comparison of NV Measurements on the Signal Line and in the Gap of the CPW	156
C.3. Nonlinear Spin Waves at Half Integer Multiples of the Driving Frequency	157
C.4. Standing Spin Wave Modes at the Edge of the CPW	158
C.5. Measurement on YIG	159
C.6. NV-Center Ground State Hamiltonian	160
D. SNS-MOKE: Phase Maps at Different Excitation Frequencies	161

E. SNS-MOKE: High Harmonic Spin Waves in Microstructures	165
F. Comparison of SNS-MOKE with Inductive FMR	171
G. Sample Fabrication Recipes	173
G.1. Electron Beam Lithography	173
G.2. Atomic Layer Deposition of Al ₂ O ₃	173
H. Micromagnetic Simulations	175
H.1. Material Parameters	175
Bibliography	I
List of Publications	XIX
Curriculum Vitae	XXI
Eidesstattliche Erklärung	XXV
Acknowledgments	XXVII

List of Figures

2.1. Sketch of DOS for itinerant ferromagnet	10
2.2. Macrospin and magnetic hysteresis	15
2.3. Magnetization pattern in small structures	16
2.4. Precession of the magnetization vector	20
2.5. Uniform spin wave	21
2.6. Non-uniform spin wave	22
2.7. Dispersion in ferromagnetic thin film	25
2.8. MOKE geometries	29
2.9. Types of magnetic order	32
2.10. Diffraction-limited focusing of light	36
2.11. Mirror dipole model of near field interaction.	38
2.12. Stokes- and anti-Stokes scattering	42
2.13. Diamond lattice with NV center	43
2.14. NV center energy levels	45
2.15. NV center ESR spectrum	47
3.1. Alias frequency generation in SNS-MOKE	56
3.2. Optical path of the SNS-MOKE setup	57
3.3. Wiring schematics of the SNS-MOKE setup	58
3.4. Optical path of the confocal NV center magnetometry setup	62
3.5. Wiring schematics of the confocal NV center magnetometry setup	63
3.6. Working principle of AFM	64
3.7. Working principle of scanning NV center magnetometry	66
3.8. Working principle of s-SNOM	68
3.9. Fourier spectrum of the detected light in s-SNOM	73
4.1. Cartoon of the electron beam lithography (EBL) procedure	75
6.1. Sample layout of Ni ₈₀ Fe ₂₀ film on CPW	85
6.2. NV center magnetometry measurement up to ESR frequency	86
6.3. NV center magnetometry measurement of harmonics	88
6.4. SNS-MOKE measurements of the uniform mode	89
6.5. SNS-MOKE measurement of 1 st , 10 th and 20 th harmonic	90
6.6. SNS-MOKE measurement of harmonics at different driving frequencies	91
6.7. SNS-MOKE measurement of harmonics evaluated at the same detection frequency	92
6.8. SNS-MOKE phase measurement of series of harmonics	93

6.9. Wave vector analysis of harmonics and dispersion	94
6.10. Simulation of a perfect thin film, time trace and FFT	97
6.11. Kerr microscopy image and hysteresis trace	99
6.12. Simulation of a semi-infinite stripe with magnetic disorder, ground state	100
6.13. Simulation of a semi-infinite stripe with magnetic disorder, snapshots of the magnetization when excited	101
6.14. Simulation of a semi-infinite stripe with magnetic disorder, time trace and FFT of the magnetization	102
6.15. Simulation of a semi-infinite stripe with magnetic disorder, maps of 1 st , 10 th and 20 th harmonic	103
6.16. Simulation of a semi-infinite stripe with a single step, model and ground state	105
6.17. Simulation of a semi-infinite stripe with a single step, snapshots of the magnetization when excited	106
6.18. Time trace and FFT of the magnetization in the stripe with a step . . .	107
6.19. Sample layout of Ni ₈₀ Fe ₂₀ microstructures	109
6.20. SNS-MOKE measurement of spin waves in 10 μm × 5 μm-sized rectangu- lar microstructure	110
6.21. SNS-MOKE measurement of spin waves in 10 μm × 5 μm-sized elliptical microstructure	111
6.22. Geometry of the scanning NV center magnetometry measurements . . .	112
6.23. Scanning NV center microscopy maps of rectangular structures, thick- ness 10 nm	112
6.24. Exemplary PL spectra at different positions from which the stray field is extracted	113
6.25. Scanning NV center microscopy maps of rectangle and ellipse, compari- son of thickness of 20 nm and 5 nm	114
6.26. PL quenching maps of rectangular element, excited at 2.87 GHz	115
6.27. PL quenching maps of rectangular element, excited at 1.43 GHz, detected at 2 nd harmonic	116
6.28. PL quenching maps of rectangular element, excited at 0.91 GHz, detected at 3 rd harmonic	117
7.1. Overview of the near field microscopy setup	120
7.2. Core parts of the s-SNOM setup	123
7.3. Interferometric s-SNOM measurement geometries	125
7.4. Interferometric s-SNOM measurement on Au disk	127
7.5. Overview over nano-focused BLS setup	130
7.6. Laser line filter for BLS light source	133
7.7. Schematic of a VIPA	135
7.8. Schematic of the two-stage VIPA spectrometer	137

7.9. Camera images of the laser spot in the VIPA spectrometer.	138
7.10. BLS measurements of polymers taken with VIPA spectrometer	139
7.11. Schematic of a sample holder design for nano-focused BLS	141
A.1. Measurement geometry and ANE measurements of CoFeB device	146
A.2. ANE measurement of Landau pattern to determine spatial resolution	147
A.3. Sketch of heat gradient in the sample and domain pattern deduced from ANE measurement	148
A.4. Scanning ANE measurements of Mn ₃ Sn wire	149
B.1. Optical path of the nano FTIR spectroscopy setup	152
C.1. Comparison of modulation techniques used in NV magnetometry	155
C.2. Comparison of NV magnetometry measurements in the gap and on top of the CPW	156
C.3. NV magnetometry measurements of nonlinear spin waves and power de- pendence	157
C.4. NV magnetometry measurements of MSSW modes	158
C.5. NV magnetometry measurement on 200 nm-thick YIG thin film	159
D.1. SNS-MOKE phase map of high harmonics, $f_{\text{rf}} = 79.1$ MHz	161
D.2. SNS-MOKE phase map of high harmonics, $f_{\text{rf}} = 159$ MHz	162
D.3. SNS-MOKE phase map of high harmonics, $f_{\text{rf}} = 319$ MHz	162
D.4. SNS-MOKE phase map of high harmonics, $f_{\text{rf}} = 399$ MHz	163
E.1. SNS-MOKE measurement of spin waves in the center of a $30 \mu\text{m} \times 15 \mu\text{m}$ - sized elliptical microstructure	165
E.2. SNS-MOKE measurement of spin waves in $20 \mu\text{m} \times 10 \mu\text{m}$ -sized elliptical microstructure	166
E.3. SNS-MOKE measurement of spin waves in $5 \mu\text{m} \times 2.5 \mu\text{m}$ -sized elliptical microstructure	167
E.4. SNS-MOKE measurement of spin waves in the center of a $30 \mu\text{m} \times 15 \mu\text{m}$ - sized rectangular microstructure	168
E.5. SNS-MOKE measurement of spin waves in $20 \mu\text{m} \times 10 \mu\text{m}$ -sized rectan- gular microstructure	169
E.6. SNS-MOKE measurement of spin waves in $5 \mu\text{m} \times 2.5 \mu\text{m}$ -sized rectan- gular microstructure	170
F.1. Inductive FMR measurement of a NiFe sample with different micrometer- sized devices	171
F.2. SNS-MOKE measurements on two elliptical devices showing different FMR conditions	172

List of Abbreviations

AC	alternating current
AHE	anomalous Hall effect
AFM	atomic force microscopy
ALD	atomic layer deposition
AM	amplitude modulation
AMR	anisotropic magneto-resistance
ANE	anomalous Nernst effect
APD	avalanche photodiode
ASE	amplified spontaneous emission
BLS	Brillouin light scattering
BPD	balanced photodetector
BS	beamsplitter
BVSW	backward volume spin waves
CCD	charge coupled device
CMOS	complementary metal-oxide semiconductor
CPW	co-planar waveguide
CW	continuous wave
DBS	dichroic beamsplitter
DC	direct current
DE	Damon-Eshbach
DFB	distributed feedback
DFG	difference frequency generation
DOS	density of states
DMI	Dzyaloshinskii–Moriya interaction
EBL	electron beam lithography
EPR	electron paramagnetic resonance
ESR	electron spin resonance
fcc	face centred cubic

FFT	fast Fourier transform
FI	Faraday isolator
FM	frequency modulation
FMR	ferromagnetic resonance
FPI	Fabry-Pérot interferometer
FSR	free spectral range
FTIR	Fourier transform infrared
FVSW	forward volume spin waves
FWHM	full width at half maximum
GGG	gadolinium gallium garnet
GPU	graphics processing unit
GT	Glan-Thompson polarizer
HM	field modulation
HWHM	half width at half maximum
HWP	half wave plate
IPA	isopropyl alcohol
IR	infrared
ISC	inter system crossing
LED	light emitting diode
LIA	lock-in amplifier
LLG	Landau-Lifshitz-Gilbert equation
MCD	magnetic circular dichroism
MCT	mercury cadmium telluride
MFM	magnetic force microscopy
MIBK	methyl isobutyl ketone
MIR	mid infrared
MOKE	magneto-optical Kerr effect
MR	magneto resistance
MSSW	magneto-static surface waves
NA	numerical aperture
NIR	near infrared
NN	nearest neighbor

NV	nitrogen-vacancy
PBS	polarizing beam splitter
PID	proportional-integral-differential
PL	photo-luminescence
PLL	phase-locked loop
PMMA	polymethyl methacrylate
PC	polycarbonate
PS	polystyrol
PH	pseudo-heterodyne
PSSW	perpendicular standing spin waves
QWP	quater wave plate
RF	radio frequency
RKKY	Ruderman–Kittel–Kasuya–Yosida interaction
SAS	saturated absorption spectroscopy
SEM	scanning electron microscope
SHE	spin Hall effect
SHG	second harmonic generation
SNOM	scanning near field optical microscopy
SNR	signal-to-noise ratio
SNS-MOKE	super-Nyquist-sampling MOKE
SOC	spin orbit coupling
SOT	spin orbit torque
s-SNOM	scattering scanning optical near field microscopy
STT	spin transfer torque
STXM	scanning transmission X-ray microscopy
TEM	transmission electron microscopy
TERS	tip enhanced Raman spectroscopy
TMA	trimethylaluminium
TR-MOKE	time-resolved MOKE
UHV	ultra high vacuum
UV	ultra violet
VHG	volume holographic grating

VIS	visible light
VIPA	virtually imaged phased array
WP	Wollaston prism
XMCD	X-ray magnetic circular dichroism
YIG	yttrium iron garnet
ZPL	zero phonon line

List of Optical Components

This list contains abbreviations for optical parts, which are used in the figures throughout this thesis.

Focusing Elements

Generic Convex Lens	L
Spherical Lens	SL
Aspheric Lens	AL
Concave Lens	CL
Cylindrical Lens	CYL
Lens Pair	LP

Polarization Optics

Polarizer	P
Glan-Thompson Prism	GT
Wollaston Prism	WP
Half Waveplate	HWP
Quarter Waveplate	QWP
Faraday Isolator	FI

Spatial Filter

Pinhole	PH
Iris	IR
Horizontal Slit	HS
Vertical Slit	VS

Wavelength Filter

Generic Optical Filter	F
Color Filter	CF
Long Pass Filter	LPF
Rubidium Gas Cell	RB

Mirrors and Beamsplitters

Plane Mirror	M
Parabolic Mirror	PM
Beamsplitter	BS
Polarizing Beamsplitter	PBS
Dichroic Beamsplitter	DBS

Interferometric Elements

Volume Holographic Grating	VHG
Fabry P�erot Interferometer	FPI
Virtually Imaged Phased Array	VIPA

Light Sources

Laser Diode	LD
Light Emitting Diode	LED

Detectors

Photodetector	PD
Balanced Photodetector	BPD
HgCdTe Detector	MCT
CMOS Camera	CAM

Introduction

Magnetism plays a central role in numerous technical applications. These range from large scale applications in engineering, such as the use of ferromagnets in electric motors, generators and energy conversion devices, to modern magnetic imaging machines in medicine, and all the way down to the micro- and nanometer-sized magnetic devices for data storage and processing.

Especially the field of information technologies is rapidly developing, following ever increasing demands for computational power and data storage [1]. Currently, logic circuitry is almost exclusively based on complementary metal-oxide semiconductor (CMOS) transistors. This technology is projected to reach its limits in terms of scalability, speed and energy consumption within the next decade [2]. Novel approaches for information processing, which utilize new materials and concepts that go beyond the von Neumann architecture [3], promise better energy efficiency and scalability [4]. In addition, upcoming new techniques, such as machine learning and quantum computing require the development of new physical platforms for their realization. Magnetic materials can, and most certainly will, play a role in the design of functional devices which operate under such new principles.

Conventional electronics is based on the electric charge of electrons. Electric currents are run through circuits and electric voltages signal bits of information. In addition to its charge, the electron possesses another property, the spin. This fundamentally quantum-mechanical property is a form of intrinsic angular momentum. It is tied to a magnetic moment, which may be used as a carrier of information, alternatively to the electric charge. An electron bound to an atom possesses, in addition, orbital angular momentum, which couples to the spin. Furthermore, all the moments of all the electrons in an atomic shell interact in a complicated way and form a total magnetic moment of the atom. In magnetic materials, the individual magnetic moments of the atoms, again, interact and form a macroscopic magnetization. The magnetization can be understood as a vector field, which determines a magnitude and direction at every position in space. It may be persistent and stable over time, it may be influenced, for example by magnetic fields, and it can be dynamically excited by radio frequency (RF) fields. In this way, information can be stored, manipulated, and transported using collective magnetic excitations, known as *spin waves*. Replacing electric charge with magnetic moment promises less dissipation of energy and, thus, strongly reduced Joule heating [4]. The quanta of spin wave excitations are called *magnons*, and the area of research especially concerned with the dynamics taking place in magnetic materials is hence called *magnonics*.

The field of magnonics currently undergoes rapid development [5], as more and more functionalities are translated into the wave-based logic of magnonic devices. The long list of functionalities, that have already been realized, includes magnonic signal manipulation, such as phase inversion [6], amplification [7, 8], and filtering [9, 10]. These are the building blocks for devices, like magnonic diodes [11], directional couplers [12, 13], frequency demultiplexers [14], magnonic transistors [15] and even logic gates [16–18]. In addition, new unconventional schemes for information processing are developed, which utilize the specific properties of magnons, for example in-memory computing [19], neuromorphic computing [20, 21] or reservoir computing [22].

For the realization of all of these spin wave-based devices, it is crucial to understand the generation, propagation, and interaction of spin waves. Devices, which exploit the wave character of magnons, may be operated at high-GHz frequencies, competing with or even superseding current CMOS technology. A central aspect in terms of implementing magnonic devices is the conversion of spin waves, which precess at one frequency, into other frequencies within the magnonic system, as this allows to couple different spin wave modes to create a large variety of functionalities. Crucial building blocks, such as sources of high-frequency spin waves and frequency multipliers, still need improvement in both, their efficiency and lateral footprint, to compete with conventional nanometer-scale electronics.

At this point, magnonics has a fundamental advantage over other fields: The equation of motion governing the dynamics of spin waves is inherently nonlinear. This has the consequence that, in contrast to other wave-based phenomena in physics, spin-wave excitations allow to access the nonlinear regime at small excitation amplitudes. Studies of magnon nonlinearities already started in the 1960s [23, 24]. They built a solid theoretical and experimental basis for the description of nonlinear processes in the framework of three- or four-magnon scattering events [25–27]. Nonlinear scattering typically generates spin waves at frequencies which differ from the excitation frequency. For example, second harmonic frequencies can be generated through the propagation of spin waves in nonlinear waveguides [28], or due to the nonlinear motion of domain walls [29]. So far, all of these findings only lead to the generation of a few harmonics and are insufficient to fulfill the aim, which is the generation of high-frequency spin waves using much lower frequencies for excitation.

This leads to the first topic of this thesis: To explore the effect of frequency multiplication, which was found in the well studied ferromagnet $\text{Ni}_{80}\text{Fe}_{20}$ [30]. When excited with MHz RF fields coherent spin waves are generated inside the ferromagnet, which precess at up to the 60th harmonic of the excitation frequency, forming a six-octave-spanning frequency comb which reaches all the way into the GHz range. The discovered effect could provide functionality for future magnonic devices, as a fully magnonic frequency multiplier and a source of coherent spin waves. The aim is to find answers to the following questions:

- What is the nature of the high harmonic spin waves?

- What is the mechanism for their generation?
- What are relevant parameters that influence the generation of the harmonics?

To address these questions, suitable samples were fabricated and investigated using a combination of different optical methods, in order to learn about the magnetic properties of the material and to image and analyze the generated high harmonic spin waves. The experiments are combined with micromagnetic simulations to develop a model for the comb generation process.

For the investigation of magnetization dynamics, optical methods uniquely combine certain advantages: They offer high spatial resolution, potentially high time resolution and allow to investigate systems that may otherwise be inaccessible. Static optical methods can be used to investigate the magnetization state of a sample, i.e. its domain pattern or magnetic hysteresis. Time- and frequency-resolved methods allow to examine the dynamic response of the magnetic system to different excitations. Examples for well established methods are Brillouin light scattering (BLS) microscopy [31] and Kerr microscopy [32, 33], which both rely on the interaction of light with magnetic matter, i.e. inelastic scattering and polarization rotation, respectively, both mediated by the magneto-optical Kerr effect (MOKE).

A main concern for all measurement techniques is spatial resolution, as ever smaller devices and features of interest demand for an ever increasing resolution. For optical techniques, such as MOKE microscopy, the achievable resolution usually is limited by the optical diffraction limit to approximately half of the wavelength of the light. There are approaches circumventing that limit, for example by periodic patterning of a metallic grating on top of a sample [34], but their use remains largely impractical.

New techniques based on nitrogen-vacancy (NV) defect centers in diamond have already expanded the toolbox. A magnetic stray field emitted by the sample modulates the fluorescence of the NV centers, which can be detected optically. NV centers can either be used in confocal geometry or as a scanning probe [35, 36] and allow for static imaging of domain patterns. NV center magnetometry already is an example for a method that circumvents the optical diffraction limit. It can improve the achievable resolution significantly to below 100 nm. NV center magnetometry is a very sensitive tool, but it relies on stray fields emerging from a sample. Especially dynamic measurements are challenging, since the NV center is only sensitive in a narrow frequency range, limited to frequencies around 2.87 GHz. This limits the applicability of NV-based methods.

A well established optical scanning probe technique is scanning near field optical microscopy (SNOM). It allows to measure optical properties of samples with nano-scale resolution, well beyond the optical diffraction limit. Based on SNOM, many different measurement schemes exist, such as optical absorption and reflection measurements of the scattered light, including spectroscopy techniques. In addition to these techniques which rely on elastic scattering, tip enhanced Raman spectroscopy (TERS) has been realized [37]. TERS is a combination of Raman scattering with SNOM that can be

used to detect vibrational modes even in individual molecules. So far, none of these methods is tailored toward the investigation of magnetic materials and excitations.

As mentioned before, BLS is a commonly used and well established technique to investigate magnetization dynamics [38]. It provides a means to investigate spin waves in magnetic materials via the inelastic scattering of light off these excitations. The scattered light is analyzed using a high-resolution spectrometer. The shifts in photon energy directly encode the frequency of the magnetic excitations. The working principles of BLS and Raman scattering are very similar, but aiming at different energy ranges.

This motivates the second aim of this work: To develop an optical method that combines the spatial resolution of scattering scanning optical near field microscopy (s-SNOM) with the energy resolution of BLS. Such a technique will enable the investigation of magnetization dynamics via inelastic light scattering with a spatial resolution beyond the optical diffraction limit. To accomplish this, the second part of the thesis has the following goals:

- Constructing a multi-purpose near field system.
- Setting up a laser source suitable for BLS measurements and align it into the near field setup.
- Designing and building a fast, high-resolution spectrometer to detect GHz shifts in photon frequency.
- Conducting test measurements to evaluate the function of the spectrometer.

The thesis is structured as follows: Chapter 2 covers the fundamentals of the physical processes which are involved. As this thesis is about the investigation of magnetic materials, a major emphasis lies on explaining the origins of magnetic behavior. Furthermore, some groundwork is laid out, which is relevant to understand the different measurement techniques used throughout this thesis. This also covers the basics of optics and spatial resolution, near field effects, inelastic scattering of light, and the fluorescence in NV defect centers in diamond.

Chapter 3 introduces different techniques which can be used to investigate magnetization and its dynamics. The order in which these techniques are introduced roughly follows the spatial resolution that is achievable. It starts with non-local methods, mainly inductive ferromagnetic resonance (FMR) and transport experiments. This is followed by diffraction-limited optical methods, most importantly the different forms of static Kerr microscopy and dynamic MOKE microscopy, as well as inelastic light scattering. The last section introduces methods that go beyond the optical diffraction limit. These are confocal and scanning NV center microscopy, as well as SNOM.

In Chapter 4, methods and processes are described, which were used to prepare suitable (thin-film) samples.

Chapter 5 briefly introduces the concept of micromagnetic simulations, which are used to simulate the dynamics of magnetic samples.

In Chapter 6 the investigations of the frequency multiplication process found in the $\text{Ni}_{80}\text{Fe}_{20}$ thin film are presented. Here, different optical methods are combined. This involves confocal NV center magnetometry measurements to detect the high harmonics and SNS-MOKE measurements to image the spatially varying spin wave pattern. The results are compared and reproduced by micromagnetic simulations which are conducted at different levels of complexity and realism to pinpoint the origin of the effect. Finally, micrometer-sized devices are structured to learn about the influence of shape and size of the devices on the efficiency of the generation of higher harmonic spin waves and move from an extended film closer toward actual devices. In this context, scanning NV center magnetometry is employed to image the domain pattern inside the devices with high spatial resolution. In this context, a new dynamic detection scheme is explored which allows for a phase-resolved detection of spin waves using this method.

Chapter 7 concerns the setup of a multi-purpose s-SNOM system and the development of a nano-focused BLS setup. First, the working principles of the s-SNOM system are laid out. This is followed by a detailed explanation of the parts necessary for the function as a BLS system, which are a stable narrow band light source and a high-throughput spectrometer, which allows to analyze the scattered light with respect to its inelastic frequency shifts. Finally, initial test measurements on different polymer samples are presented, which proof the functionality of the BLS spectrometer. The chapter closes by discussing future steps that have to be taken on the path to a fully operational nano-focused BLS system, which allows for BLS measurements of magnetic excitations with the nano-scale resolution provided by SNOM.

The final chapter concludes the results. The appendix includes supplementary measurements and two additional measurement techniques that have been set up in connection with the SNOM system, one of which is especially tailored to measuring nano-scale magnetic domain patterns.

Theoretical Background

2.1. Theory of Magnetism

This chapter starts by exploring the origin of ferromagnetism and the magnetic behavior of materials. It briefly describes the quantum mechanical nature of magnetism. An interplay of magnetic fields and magnetic anisotropies results in static properties, hysteretic behavior and inhomogeneous magnetization patterns. Subsequently, the view is extended to the dynamic behavior of the magnetic moments in magnetic samples. The dynamics is described by the equation of motion, the Landau-Lifshitz-Gilbert Equation, which gives rise to a resonance behavior. The collective response of the magnetic moments to external stimuli can be uniform or inhomogeneous across a sample, exhibiting a wave-like character. These magnetic excitations are hence called *spin waves*. Spin waves can also be understood in terms of their quanta, called *magnons*. In this section, the most important types of magnons are examined, with a special focus on magnetic thin films. When the magnetic moments are strongly excited to large precessional angles, nonlinear effects occur, which, in combination with the unique dispersion properties of spin waves in confined materials, are the origin of frequency conversion phenomena. These phenomena are of core interests in this thesis and will be introduced in this section. This is followed by an overview about magneto-optical and transport effects, which arise from static and dynamic magnetic behavior. Many of them either are subjects of study on their own or can be utilized to detect the underlying magnetic properties of a sample. The chapter concludes with a brief overview about materials which exhibit a magnetic order beyond ferromagnetism.

2.1.1. Origin of Magnetism

To understand the origin of magnetism, a quantum-mechanical consideration is necessary, as magnetic order cannot exist in purely classical approach. This is proven by the Bohr-van Leeuwen theorem, which states that, in thermal equilibrium, the magnetization of any solid material must be zero [39, 40]. The reason is that classically, the magnetic field does not change the free energy of the system as it cannot perform any work on the particles which comprise the system. Hence, in thermal equilibrium the distribution of motions of the particles does not depend on the magnetic field and therefore the average magnetic moment is zero.

In quantum-mechanics, however, this theorem does not apply. To understand the emergence of magnetic order, one first has to consider the individual atoms that make up a material. These atoms may or may not possess a magnetic dipole moment. This

dipole moment is almost exclusively determined by the spin- and orbital angular momentum of the electrons filling the atoms' shell. The occupation of the orbitals is governed by Hund's rules, ultimately originating from the Pauli exclusion principle. Spin- and orbital angular momentum of the electrons couple and result in a quantized total angular momentum, often denoted as \mathbf{J} . This gives rise to an atomic magnetic dipole moment of

$$\boldsymbol{\mu}_{\text{Atom}} = g_J \mu_B \mathbf{J} \quad (2.1)$$

with the gyromagnetic ratio g_J and the Bohr magneton μ_B .

When exposed to an external magnetic field, atoms with a non-vanishing magnetic dipole moment experience Pauli paramagnetism, i.e. their moments align with the field and a magnetic order is created. This magnetic order, however, is volatile and vanishes if the external magnetic field is removed.

In solids comprised of atoms with persistent magnetic moments, those moments interact and couple to each other via dipolar and exchange coupling. In the simplest model of two magnetic moments, this dipolar interaction can be understood as one moment exposed to the magnetic field which originates from the other. The magnetic field \mathbf{H} exerts a torque on the moment. The resulting energy potential can be expressed as a dipolar Hamiltonian:

$$\hat{H}_D = -\mu_0 \boldsymbol{\mu} \cdot \mathbf{H}. \quad (2.2)$$

Here, μ_0 denotes the vacuum permeability. The energy scale of dipolar coupling is on the order of 0.1 meV [41]). It is easily overcome by random thermal fluctuations which inevitably occur at temperatures above absolute zero; i.e. the thermal energy at room temperature is $k_B T \approx 25$ meV. Hence, dipolar coupling alone is not sufficient to sustain any magnetic order beyond paramagnetism, which vanishes if no external magnetic field is present. However, as elaborated later in this chapter, dipolar interactions are essential to understand many static and dynamic phenomena in ferromagnetic materials and thin films, like magnetic domains and certain kinds of spin waves.

The dominant interaction to stabilize local magnetic order in the first place is *exchange interaction*. It arises from the Fermionic nature of the electrons, which demands the electrons' wave functions to be antisymmetric upon exchange of particles (Pauli principle). In the simple model of two electrons A and B with spin operators \mathbf{S}_A and \mathbf{S}_B , the exchange energy can be expressed as

$$E_{\text{ex}} = C - \frac{1}{2} J_{\text{ex}} - 2J_{\text{ex}} \langle \mathbf{S}_A \cdot \mathbf{S}_B \rangle. \quad (2.3)$$

The angled brackets represent the expectation value of the spin operators. J_{ex} is the exchange constant (or exchange integral) [42, p. 318]. The sign of the exchange constant can be positive or negative. If J_{ex} is positive, the Coulomb energy C between two interacting electrons is reduced if their spins align parallel. A negative sign of J_{ex} favors antiparallel alignment. The exchange energy is on the order of 10 meV to 100 meV [41]

and, thus, dominant over dipolar coupling and can compete with thermal fluctuations at room temperature. It is, thus, capable of enforcing persistent magnetic order.

Moving from the simple two-spin system to an extended solid material leads to the *Heisenberg model* [43]. It assumes, that the electrons which contribute to magnetism are well localized. In this case, one can transition from the two individual spins to an extended atomic lattice by summing up the exchange energy over all nearest neighbors (NNs) with a coupling constant J_{Heis} . This interaction is described by the Heisenberg Hamiltonian:

$$\hat{H}_{\text{Heis}} = -J_{\text{Heis}} \sum_{\substack{\text{NN} \\ i \neq j}} \langle \mathbf{S}_i \cdot \mathbf{S}_j \rangle. \quad (2.4)$$

Materials which exhibit this kind of magnetic order are called Heisenberg ferromagnets. Direct exchange coupling favors, depending on the distance between the adjacent magnetic moments and the orbitals involved, either parallel or anti-parallel alignment of the magnetic moments. This distance-dependence is due to interactions of electrons localized in different shells with conduction electrons. It is described by the Ruderman–Kittel–Kasuya–Yosida interaction (RKKY) [44].

In conducting materials, magnetism can be understood in terms of the electronic bands which form as a consequence of a periodic crystal lattice. For many ferromagnetic transition metals, the wave functions of the electrons which contribute to the magnetic properties are de-localized. While being spin-degenerate in most (paramagnetic) materials, in ferromagnets the electronic bands are spin split, i.e. the band energy for the different spin species is shifted with respect to each other. This splitting is caused by exchange interaction. Occupying the bands up to the Fermi energy E_F yields a different number of spin-up and spin-down electrons. This gives rise to *itinerant ferromagnetism*, also called *band ferromagnetism*. This model was introduced by Stoner, who derived a criterion for a material to undergo a spontaneous phase transition to be ferromagnetic. This criterion is now known as the *Stoner criterion* [45]:

$$\text{DOS}(E_F) \cdot I > 1. \quad (2.5)$$

It states, that the density of states (DOS) at the Fermi energy E_F multiplied by the Stoner parameter I must be greater than one. The Stoner parameter describes the strength of electron-electron correlations in the material. Stoner derived this criterion from energy considerations and the interplay of exchange and the kinetic energy of the electrons. A sketch of the DOS in such a spin-split system is shown in Figure 2.1. Due to a spin splitting of the bands, the DOS at the Fermi level is different for spin-up and -down spin species.

The most prominent examples for ferromagnetic materials at room temperature are iron, cobalt, and nickel. These transition metals possess partially filled 3d-orbitals, which provide the atoms with a large magnetic moment and let them, as well as their compounds, form ferromagnetic solids. Some rare earth elements like gadolinium also

possess a large magnetic moment, which in this case is caused by partially filled 4f-orbitals.

Note that, in a simple atom, the orbital and spin moment of the electrons couple and form a total magnetic moment. In solids, the angular momentum is often quenched due to the interaction of the electrons with adjacent atoms. Therefore, the magnetic moment of a single atom might significantly differ from the moment per atom in a solid, which usually is dominated by the electron spin.

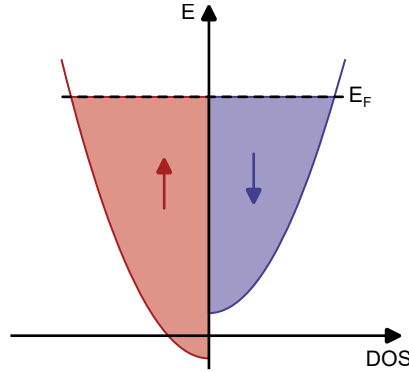


Figure 2.1. | Model of itinerant ferromagnetism showing the DOS versus energy. The electronic bands for spin-up and -down electrons, which are usually degenerate, split and shift in energy due to exchange interaction. Populating the bands with spin-up (red) and -down (blue) electrons up to the Fermi level E_F results in an imbalance in the numbers of both species, which causes a net magnetization.

2.1.2. Static Properties of Magnetic Materials

Magnetic Susceptibility

In the following, a homogeneous ferromagnet is considered, for which the magnetic properties can be macroscopically described by a small set of quantities. The magnetic susceptibility tensor $\underline{\chi}$ describes the influence of an external magnetic field \mathbf{H}_{ext} on the macroscopic magnetization \mathbf{M} of the material, which is defined as integral over all microscopic magnetic moments per volume V . The magnetic susceptibility is a 2nd rank tensor, which accommodates the fact that \mathbf{M} and \mathbf{H}_{ext} do not necessarily need to be directly proportional.

$$\underline{\chi}_{ij} = \frac{\partial M_i}{\partial H_{\text{ext},j}} \quad (2.6)$$

In a simplified, linearized, isotropic picture, χ is just a scalar representing the proportionality between the magnetization and the external field:

$$\mathbf{M} = \chi \mathbf{H}_{\text{ext}} \quad (2.7)$$

It is related to the relative magnetic permeability μ_r by

$$\chi = \mu_r - 1. \quad (2.8)$$

The magnetic susceptibility allows for a fundamental classification of materials. In the case that $\chi < 0$ the material is diamagnetic, i.e. it is repelled from an inhomogeneous magnetic field. If $\chi > 0$ the material is paramagnetic. Ferromagnets possess a much larger susceptibility $\chi \gg 0$, which is not constant but changes due to remanence, i.e. the magnetic moments align with the external magnetic field \mathbf{H}_{ext} and remain aligned, even if the field is removed.

The most relevant contributions to the total energy E_{tot} of the magnetic system are the Zeeman energy E_Z , magnetic anisotropy energies E_A , and the demagnetizing energy E_D . The origin of all terms is briefly discussed in the following.

$$E_{\text{tot}} = E_Z + E_A + E_D \quad (2.9)$$

Zeeman Energy

In presence of an external magnetic field, the energy which contributes to the total energy of the magnetic system is the Zeeman energy E_Z . It favors a parallel alignment of the individual magnetic dipoles, and hence of the magnetization, with the external field.

$$E_Z = -\mu_0 \int_V \mathbf{M} \cdot \mathbf{H}_{\text{ext}} dV'. \quad (2.10)$$

Magneto-crystalline Anisotropy

Additional energy contributions may oppose the parallel alignment of the magnetization with the external field and render the behavior more intricate. These contributions are called anisotropies. An example is magneto-crystalline anisotropy, which is often present in ferromagnetic crystals. It arises from spin orbit coupling (SOC), which ties the electrons spin to the orbital motion of the electrons. At the same time, the overlap of the orbitals with the orbitals of the nearest neighbor atoms determines the arrangement of the atoms in the crystal lattice. Thus, the magnetic moments experience an anisotropic energy landscape that is related to the symmetries of the crystallographic lattice. Two common examples are uniaxial anisotropy present in many hexagonal materials, such as cobalt, and cubic anisotropy in cubic iron. The energy arising from magneto-crystalline anisotropies in those cases can be described as

$$E_A = K_1 V \sin^2(\theta) + K_2 V \sin^4(\theta), \quad (2.11)$$

where K_1 and K_2 are the uniaxial and cubic anisotropy constants, respectively. θ denotes the angle of the magnetization with respect to a certain crystal axis, called *easy axis*. In this direction, the contribution of the anisotropy to the total energy is minimal. Materials with cubic anisotropy possess two easy axes. The directions along which the anisotropy energy is maximal are called *hard axes*. In the ground state the magnetization tends to align with an easy axis.

Magneto-Elastic Anisotropy

Related effects are the magneto-elastic anisotropy and the corresponding effect of magnetostriction. It occurs when the magnetic lattice is strained such, that the distance of the atoms is stretched or compressed in one direction, creating an additional uniaxial anisotropy. This effect is relevant for crystalline magnetic thin films, as they are usually grown on a substrate which might have a slight mismatch in lattice constant distorting the adjacent atomic layers of the thin film. In addition, built in strain from thermal expansions resulting from deposition temperatures might be present and give rise to magneto-elastic anisotropy. Magnetostriction essentially is the inverse effect, i.e. a change in magnetization has an influence on the lattice spacing of the atoms and can even cause a macroscopic contraction or expansion of a material, see for example [46].

Demagnetizing Field and Shape Anisotropy

In magnetostatics and without any currents, any finite magnetic material itself generates a magnetic stray field. This is a consequence of Ampère's law

$$\nabla \times \mathbf{H} = 0, \quad (2.12)$$

and Gauss's law for magnetism

$$\nabla \cdot \mathbf{B} = 0. \quad (2.13)$$

The magnetic flux \mathbf{B} inside an isotropic material can be written as

$$\mathbf{B} = \mu_0 (\mathbf{H} + \mathbf{M}) = \mu_0 \mu_r \mathbf{H}. \quad (2.14)$$

The two fields must fulfill continuity requirements at the surface of the object: The component \mathbf{H}_{\parallel} , parallel to the surface of the object, as well as \mathbf{B}_{\perp} , perpendicular to the surface, are conserved. The exact field distributions must satisfy Poisson's equation. As a result, an object with finite magnetization must generate a non-zero magnetic field \mathbf{H}_D surrounding it. This *stray field* approximately points along the direction of the magnetic flux \mathbf{B} .

Inside the material, there must be a field, as well, with equal magnitude, but opposite direction. This so-called *demagnetizing field* tends to reduce the magnetization. The demagnetizing field comes along with a cost in energy to create it. This energy can be calculated by integrating the scalar product of magnetization and magnetic field across the volume of the magnet.

$$E_D = \frac{\mu_0}{2} \int_V \mathbf{M} \cdot \mathbf{H}_D dV' \quad (2.15)$$

If an otherwise isotropic magnetic material is considered, the energy solely depends on the shape of the magnet and, in general, is anisotropic. It causes a favored direction for the magnetization in the ground state, i.e. where E_D is minimal. This effect is called *shape anisotropy*.

Shape anisotropy is captured by the demagnetizing tensor $\underline{\mathcal{N}}$, which allows to express the demagnetizing field as

$$\mathbf{H}_D = \underline{\mathcal{N}}\mathbf{M}. \quad (2.16)$$

For simple shapes, the demagnetizing tensor only contains the diagonal elements \mathcal{N}_{xx} , \mathcal{N}_{yy} and \mathcal{N}_{zz} , which are called shape factors or demagnetizing factors. In the case of a perfect sphere, the demagnetizing factors are all equal to $1/3$ and no shape anisotropy is present. A thin and long rod has the factors $(1/2, 1/2, 0)$, while in a magnetic thin film, they amount to $(0, 0, 1)$ [47]. The given numbers are only strictly valid for extreme aspect ratios. In a magnetic rod the magnetization is forced to follow the direction of the rod, while in a thin film an easy-plane anisotropy is induced. This leads to the magnetization laying within the plane of the film. This example is particularly important, since all samples which are investigated in this thesis are thin films. They are fabricated with thicknesses of a few to tens of nanometers. In this thickness range and for the materials which were used, i.e. $\text{Ni}_{80}\text{Fe}_{20}$ alloy, the assumptions made above are well fulfilled and in the ground state the magnetization vector stays in the plane of the film. For ultra-thin films with thicknesses of only a few monolayers, the anisotropy can begin to point in out-of-plane direction, an effect called *spin reorientation transition*.

Magnetic Hysteresis

This section will examine how the presence of an external magnetic field influences the magnet macroscopically. The following considerations are made in the framework of the model introduced by Stoner and Wohlfahrt in 1948 [48]. For simplicity, it is assumed that the magnetization in the ferromagnet is homogeneous, i.e. all moments are aligned and can be expressed as a single macroscopic magnetic moment (*macrospin model*). This assumption is, in fact, valid for small magnetic particles, while for larger magnetic structures the behavior becomes more complicated, as will be discussed in Section 2.1.2. Furthermore, a uniaxial magnetic anisotropy is assumed in the model and the effects of a finite temperature are neglected.

As stated before, the external magnetic field couples to the magnetic system via Zeeman coupling. Changing the Zeeman energy contribution will distort the landscape of the total energy potential, which may lead to a rotation of the magnetization vector. The energy expressed as a function of angle takes the form

$$E = K_1 \sin^2 \theta - \mu_0 M_S H_{\text{ext}} \cos(\alpha - \theta). \quad (2.17)$$

Here, θ denotes the angle between the magnetization and the easy anisotropy axis c and α is the angle between external field and the easy axis. M_S denotes the magnitude of the magnetization, i.e. the length of the magnetization vector, also called *saturation magnetization*. A sketch is shown in Figure 2.2 A. In the equilibrium state, the energy is minimal, hence 1st the 2nd derivative of the energy with respect to θ must be zero

and greater than zero, respectively.

$$\frac{\partial E}{\partial \theta} = 0 \qquad \frac{\partial^2 E}{\partial \theta^2} > 0 \qquad (2.18)$$

From these constraints, the resulting angle of the magnetization can be calculated. When there is no externally applied magnetic field, the magnetization will orient along an easy axis determined by the anisotropy. In the limit of a sufficiently strong external magnetic field the magnetization will fully align with the direction of the field, as determined by the magnetization state which minimizes the total energy. In between these two extremes, the behavior is governed by an interplay of the two energy contributions determined by the angle between the anisotropy axis and the external field α . In this situation a hysteretic behavior of the magnetization with respect to field changes arises.

If the external field is aligned with an easy anisotropy axis of the magnetic material ($\alpha = 0$), the magnetization will also fully align with this direction. When the external magnetic field is cycled between positive and negative values along this easy axis, the magnetization exhibits a square-shaped hysteresis, called *easy-axis loop* (red curve in Figure 2.2 B). The magnetization always points along the field axis and switches direction when the applied field overcomes the anisotropy field. The switching field, where the magnetization curve crosses zero, is called *coercive field* H_C . It is related to the saturation magnetization and the anisotropy by:

$$H_C = \pm \frac{2K_1}{\mu_0 M_S}. \qquad (2.19)$$

When the external magnetic field points along a hard axis a of the anisotropy energy landscape ($\alpha = 90^\circ$), with increasing external field, the magnetization gradually tilts toward the field direction until a saturation sets in when both are fully aligned. Sweeping the external field in this configuration yields a so-called *hard-axis loop*, which displays a characteristic linear slope around zero field (blue curve in Figure 2.2 B). It can be observed, for example, in magnetic thin films, which often show in-plane shape anisotropy, when exposed to an out-of-plane magnetic field. In general, an arbitrary angle α between external field and anisotropy axis yields a mixture of both, resulting in a rounded shape of the hysteresis loop (grey curve in Figure 2.2 B).

The projected value of the magnetization that is reached when it fully aligns with the external magnetic field corresponds to the saturation magnetization M_S , as all magnetic moments point in the same direction as the applied field. Decreasing the external field to zero yields, depending on the direction observed, a *remanent magnetization* M_R , as the magnetization aligns back with the easy anisotropy axis. The hysteretic relation between M and H has the consequence, that the magnetic state of the system depends on its history. To deal with this dependence in experiments, it is crucial to prepare a reproducible initial state, e.g. by saturating the magnetization in one direction before conducting an experiment. By measuring hysteresis loops under different angles, one

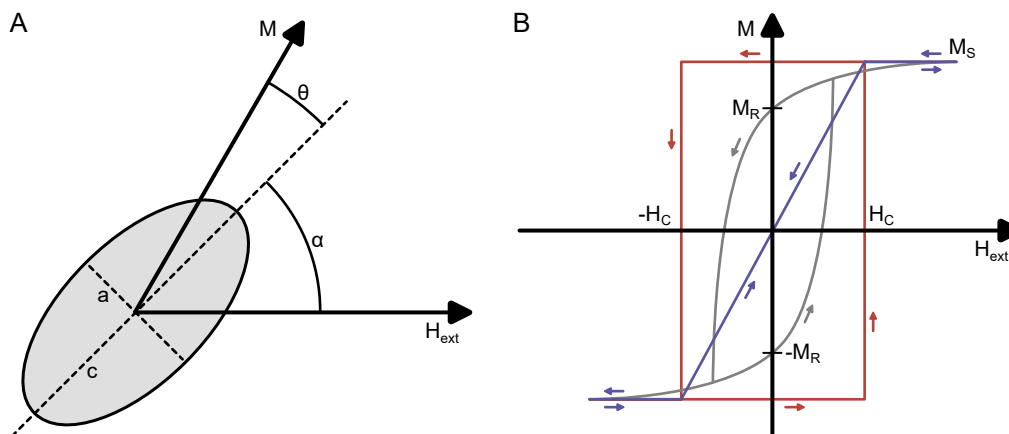


Figure 2.2. | **A:** Sketch illustrating a magnetic macrospin \mathbf{M} in an external magnetic field \mathbf{H}_{ext} . The macrospin possesses an easy anisotropy axis c and a hard anisotropy axis a . **B:** Example of idealized magnetic hysteresis curves which show the magnetization of a sample with respect to an applied external field. A field along the easy axis yields a square-loop behavior (red). Applying the field along the hard axis results in a linear increase up to saturation M_S (blue). A field direction in between yields a mixture of both (grey). The remaining magnetization at zero external field is called remanent magnetization M_R ; the field necessary to reach zero magnetization is the coercitive field H_C .

can determine the shape of the anisotropy potential and magnetic properties like M_S .

An important limitation of the Stoner-Wohlfart model is that it assumes a homogeneous magnetization across the sample in order to treat it as a single macroscopic magnetic moment. In real samples larger than a few micrometers, this limit is almost never satisfied, especially in the vicinity of H_C . In the following section, it will be discussed how inhomogeneous magnetization changes the picture.

Inhomogeneous Magnetization and Magnetic Domains

As previously explained, the origin of ferromagnetism lies in the dominance of the exchange interaction of neighboring magnetic moments. For ferromagnets, this leads to a parallel alignment of all moments across the magnet. However, anisotropy and demagnetizing fields contribute to the potential energy, as well. The competition between exchange, dipolar and anisotropy energies can lead to inhomogeneous arrangements of the magnetic moments. For example, in small magnetic elements the magnetization can curl around, in order to avoid energetically costly stray fields at the expense of a small tilting of neighboring magnetic moments. Depending on the shape of the elements, a “buckling” of the magnetization can arise, meaning in large parts of the elements the magnetization aligns with the easy anisotropy axis but it curls in the vicinity of the edges. In any case, the driving force behind these inhomogeneities is the interplay of the different energy contributions, resulting in a new, inhomogeneous ground state of the magnetic system.

An even more extreme case of this interplay are magnetic domains. Magnetic domains are regions of largely uniform magnetization. For neighboring regions, however, the magnetization points in very different directions. The formation of magnetic domains is governed by the same forces, and thus favoring configurations that yield closed loops of magnetic flux within the magnet to minimize stray field energy. As an example, in micrometer sized discs or ellipses of the soft magnetic material $\text{Ni}_{80}\text{Fe}_{20}$, *vortex configurations* are possible (see Figure 2.3 A) where the magnetization vector circulates around a central vortex core which points in the out-of-plane direction. Rectangularly shaped structures often display a *Landau pattern* (see Figure 2.3 B) and in elongated stripes *concertina patterns* are present at low fields (see Figure 2.3 C). Other materials may show a wide variety of different magnetic domain patterns.

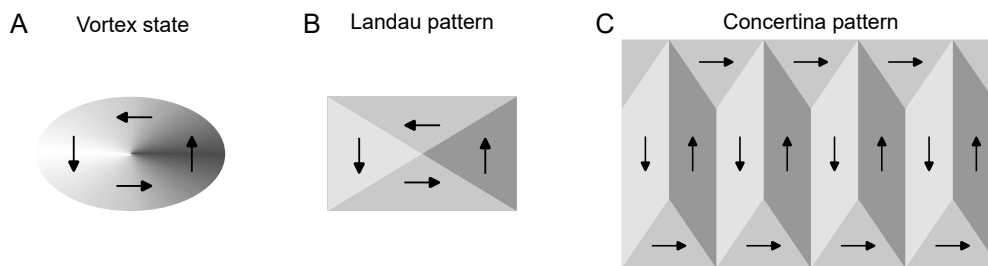


Figure 2.3. | Inhomogeneous magnetization patterns in small magnetic structures. **A:** Vortex state with a vortex core in the center of the structure, usually present in discs or ellipses. **B:** Landau pattern, present in small rectangular elements. **C:** Concertina-like domain pattern in stripes. The arrows indicate the direction of magnetization.

Adjacent magnetic domains are separated by a domain wall, where the magnetic moments gradually tilt across the wall to align with the neighboring domain. The creation of domain walls costs comparably large amounts of energy to tilt the moments out of the parallel alignment favored by exchange coupling. There are two major types of domain walls, *Bloch walls*, where the magnetic moments rotate about the normal direction of the domain wall, and *Néel walls*. Here, the magnetic moments rotate about a direction orthogonal to the wall's normal. Which of the two domain wall types is present in a magnet depends on its internal fields, its shape, and thickness. For in-plane magnetized thin films, Néel walls are the common domain wall type [49]. A domain wall has a certain width, which is the result of the interplay between exchange and dipolar fields. Domain walls themselves generate stray fields and are thus susceptible to external magnetic fields. In the presence of an external field, they move as one of the adjacent domain grows in size, while the other one shrinks until a new equilibrium is reached. Such an equilibrium state might be influenced by magnetic defects, which are inevitably present in real samples. These defects can act as pinning sites keeping the domain wall fixed at a certain position, even in the presence of an external field. Once the external field strength overcomes the pinning field associated with the defect, the domain wall rapidly snaps to a new equilibrium position. Both, defects and magnetic domains influence the hysteretic behavior of a sample, as different regions have different coercive

fields. Averaging over those regions usually leads to a washed-out, rounded hysteresis curve with small jumps in the magnetization when the external field overcomes the local pinning and a certain domain switches.

In current technology, magnetic domains play an important role to store information in the form of the magnetization state. Modern hard disk drives typically use ferromagnetic materials with out-of-plane magnetic anisotropy. They represent the bits of information as up- or down-domains in this magnetic layer. Furthermore, magnetic domains are of interest for future technologies to process and store information. An example for this is the Racetrack memory proposed by Parkin *et al.* [50]. The first iteration of Racetrack memory uses magnetic domain walls inside a ferromagnetic stripe as carrier of information (up-down or down-up domain walls). Inside a single wire, there can be many domain walls (many bits of information) at once. The domain walls can be moved by short current pulses and detected using magnetic tunnel junctions.

Thermal Disorder and Demagnetization

The saturation magnetization M_S is the maximal macroscopic magnetization in a ferromagnetic material, when all magnetic moments are perfectly aligned. This can be achieved by applying a sufficiently strong external field. Without magnetic field, the average magnetization of a sample may be reduced when the parallel alignment of the moments is disturbed. It drops to zero if the alignment of the moments is fully random. A major cause for magnetic disorder is temperature. Elevated temperatures cause incoherent fluctuations of the magnetic moments, reducing the macroscopic magnetization. Temperature effects on the magnetization were subject of an early study by Holstein and Primakoff, who theoretically derived the expected behavior and compared it to experiments [51]. The magnetic behavior of a ferromagnetic material drastically changes at a critical temperature, the *Curie temperature* T_C . As the temperature approaches T_C the magnetization is reduced

$$\mathbf{M}(T) \propto (T_C - T)^\beta. \quad (2.20)$$

The critical exponent β is a material constant, examples for its value are $\beta = 0.34$ for iron and 0.51 for nickel [52]. Above the Curie temperature, all ferromagnetic order vanishes and the material becomes paramagnetic. The temperature-dependence of the magnetic susceptibility is then described by the Curie-Weiss law:

$$\chi = \frac{C}{T - T_C}. \quad (2.21)$$

When attempting to detect the magnetization of a sample, inevitably only the average of the magnetization across the probed volume can be obtained. Non-uniformity of the magnetization within that volume reduces the measured value. The larger the probed volume, the more important this effect becomes. Especially magnetic domains

inside the volume lead to such a reduction. Besides the impact of temperature and the formation of magnetic domains, a third mechanism reducing the effective magnetization of a sample are dynamic excitations of the magnetization, which are covered in the following section.

2.1.3. Magnetization Dynamics in Magnetic Materials

This section covers the dynamic properties of magnetic materials and their response to external stimuli; most importantly, to external magnetic fields \mathbf{H}_{ext} . The fundamentals of the dynamic response are, again, discussed in the frame of the macrospin model in a classical approach. A magnetic moment \mathbf{m} experiences a torque \mathbf{T} due to an external magnetic field:

$$\mathbf{T} = \mu_0 \mathbf{m} \times \mathbf{H}_{\text{ext}}. \quad (2.22)$$

In addition to the external field, internal energy contributions, such as anisotropies, can be present in the system. They are usually treated together with the external field in the form of an *effective field* $\mathbf{H}_{\text{eff}} = \mathbf{H}_{\text{ext}} + \mathbf{H}_{\text{int}}$ acting on the magnetic moment. The magnetic moment is tied to an angular momentum \mathbf{L} via the relation $\mathbf{m} = \gamma \mathbf{L}$, where the proportionality constant γ is the gyromagnetic ratio. The torque, which represents the change in angular momentum, therefore is also related to a change of the magnetic moment and leads to the dynamics described by the equation of motion

$$\mathbf{T} = \frac{d}{dt} \mathbf{L} = \frac{1}{\gamma} \frac{d}{dt} \mathbf{m} = \mu_0 \mathbf{m} \times \mathbf{H}_{\text{eff}}. \quad (2.23)$$

The solution to this equation describes a precessional motion of the magnetic moment about the field direction, the *Larmor precession*. It occurs at an angular frequency of

$$\omega_L = \gamma \mu_0 H_{\text{eff}}. \quad (2.24)$$

It should be noted, that this consideration is simplified. Most importantly, it does not include damping, i.e. the inevitable loss of energy from the precessing magnetic moment. Furthermore, a more accurate treatment of the precession would need to include relativistic effects, which lead to additional corrections [53].

Ferromagnetic Resonance

It is intuitively clear that, in reality, a magnetic moment cannot precess without the inevitable dissipation of energy, as this would violate the laws of thermodynamics. A first experimental evidence of dissipation effects in a magnetic system was brought up by Griffiths, who observed a sudden peak in resistance due to additional dissipation of energy when a high-frequency current was sent through a ferromagnetic metal [54]. For any oscillator, dissipation leads to a broadening of its resonance linewidth.

Moving forward, instead of considering only an individual magnetic moment, the

discussion is extended to the vector field of magnetization \mathbf{M} , which is defined as

$$\mathbf{M} = \frac{d}{dV} \mathbf{m}. \quad (2.25)$$

Landau and Lifshitz investigated the effects of time-dependent magnetic fields on the magnetic permeability [55]. They came up with a phenomenological description of the dynamics of the magnetization, the *Landau-Lifshitz equation*:

$$\frac{d}{dt} \mathbf{M} = \mu_0 (\gamma \mathbf{M} \times \mathbf{H}_{\text{eff}} - \lambda \mathbf{M} \times (\mathbf{M} \times \mathbf{H}_{\text{eff}})). \quad (2.26)$$

The primary term of this equation, analog to the undamped case discussed in the previous section, describes the precessional motion of the magnetization around the effective field. Landau and Lifshitz expanded the equation of motion with a second term, which captures the dissipation of energy in the form of a torque that acts on the magnetization perpendicularly to the trajectory of motion, towards the equilibrium direction where $\mathbf{M} \parallel \mathbf{H}_{\text{eff}}$. The dissipation of energy leads to damping of the precessional motion of the magnetization, which is responsible for this relaxation. Hence, the second term in the equation is often referred to as *damping term*. The phenomenological constant λ in the Landau-Lifshitz equation is related to the material-dependent damping parameter α via

$$\lambda = \alpha \frac{\gamma}{M_S}. \quad (2.27)$$

The Landau-Lifshitz equation falls short when the damping parameter exceeds the limit of being a small perturbation. To solve this issue, Gilbert came up with a new equation by starting from the Lagrangian of the undamped system and adding a velocity-dependent dissipative force term. The resulting equation of motion is called Landau-Lifshitz-Gilbert equation (LLG) [56, 57]:

$$\frac{d}{dt} \mathbf{M} = \mu_0 \gamma \mathbf{M} \times \mathbf{H}_{\text{eff}} - \frac{\alpha}{M_S} \mathbf{M} \times \frac{d}{dt} \mathbf{M} \quad (2.28)$$

It can be shown, that the LLG can be obtained from the Landau-Lifshitz equation. This is done by reformulating Equation 2.26 as

$$\mathbf{M} \times \mathbf{H}_{\text{eff}} = \frac{1}{\gamma \mu_0} \frac{d}{dt} \mathbf{M} + \frac{\lambda}{\gamma} \mathbf{M} \times (\mathbf{M} \times \mathbf{H}_{\text{eff}}) \quad (2.29)$$

and self-consistently substituting it back into its own damping term, which changes the Landau-Lifshitz equation to

$$\frac{d}{dt} \mathbf{M} = \mu_0 \gamma \mathbf{M} \times \mathbf{H}_{\text{eff}} - \mu_0 \lambda \mathbf{M} \times \left(\frac{1}{\gamma \mu_0} \frac{d}{dt} \mathbf{M} + \frac{\lambda}{\gamma} \mathbf{M} \times (\mathbf{M} \times \mathbf{H}_{\text{eff}}) \right). \quad (2.30)$$

The terms of the equation can be rearranged and the triple cross product can be

evaluated using $\mathbf{M} = M_S \hat{\mathbf{e}}_M$, which yields

$$\frac{d}{dt} \mathbf{M} = \mu_0 \gamma \mathbf{M} \times \mathbf{H}_{\text{eff}} - \frac{\lambda}{\gamma} \mathbf{M} \times \frac{d}{dt} \mathbf{M} + \frac{\mu_0 \lambda^2 M_S^2}{\gamma} \mathbf{M} \times \mathbf{H}_{\text{eff}}. \quad (2.31)$$

Furthermore, λ is substituted using Equation 2.27, leading to

$$\begin{aligned} \frac{d}{dt} \mathbf{M} &= \mu_0 \gamma \mathbf{M} \times \mathbf{H}_{\text{eff}} - \frac{\alpha}{M_S} \mathbf{M} \times \frac{d}{dt} \mathbf{M} + \mu_0 \alpha^2 \gamma \mathbf{M} \times \mathbf{H}_{\text{eff}} \\ &= \mu_0 \gamma (1 + \alpha^2) \mathbf{M} \times \mathbf{H}_{\text{eff}} - \frac{\alpha}{M_S} \mathbf{M} \times \frac{d}{dt} \mathbf{M}, \end{aligned} \quad (2.32)$$

which in the limit of small damping ($\alpha^2 \ll 1$) reduces into the Landau-Lifshitz-Gilbert equation. Both equations describe how an effective field exerts a torque on the magnetization, which points perpendicular to the cross product of both. The resulting precessional motion of the magnetization vector around an effective magnetic field is illustrated in Figure 2.4.

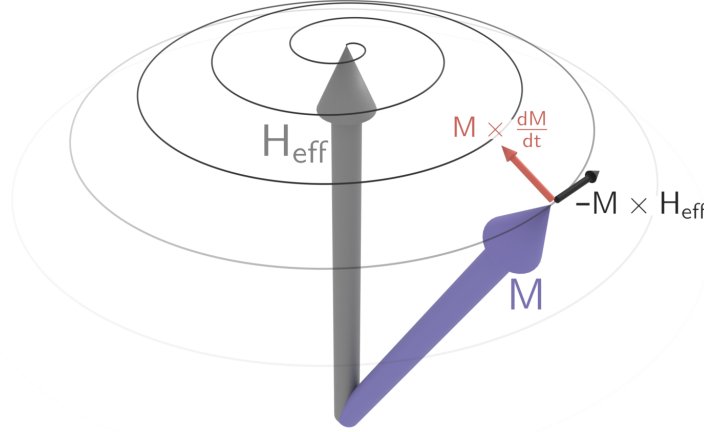


Figure 2.4. | Magnetization vector (blue) precessing around a static external field (grey) on the Bloch sphere. The external field exerts a torque (black) on the magnetization tangential to the circumference of the precession curve, while damping generates a torque in radial direction, towards the equilibrium position. As a result the magnetization follows a spiral-shaped trajectory.

The LLG can be expanded to also include spin torques, such as spin transfer torques [58] and spin orbit torques, which in some cases can be of significant magnitude and even lead to switching of the magnetization [59].

If, in addition to a static external field H_0 , the magnetic system is exposed to an oscillating magnetic field \mathbf{H}_{osc} with the angular frequency of the oscillation ω , a resonance behavior can be observed. The effective field takes the form

$$\mathbf{H}_{\text{ext}}(t) = H_0 \hat{\mathbf{e}}_z + \mathbf{H}_{\text{osc}} e^{i\omega t}. \quad (2.33)$$

It is assumed that the static field points along the z -direction and is much stronger than the oscillating field. The magnetization is subjected to an oscillating torque. It

can be separated in a constant term M_0 and an oscillating term \mathbf{M}_{osc} :

$$\mathbf{M}(t) = M_0 \hat{\mathbf{e}}_z + \mathbf{M}_{\text{osc}} e^{i\omega t} \quad (2.34)$$

Using this *ansatz* together with Equation 2.26, a resonance condition was derived by Herring and Kittel [60]. It yields an excitation mode of the magnetic system, where all magnetic moments precess with the same phase with respect to the excitation field. This mode is called *ferromagnetic resonance (FMR) mode*, or *uniform mode*. This uniform precession can be interpreted as a wave with infinite wavelength, or a wave vector of $k = 0$. Such an excitation mode is depicted in Figure 2.5 for a one-dimensional chain of coupled magnetic moments.

In general, the effective field contains the demagnetizing field and, thus, depends on the different components of the demagnetizing tensor. Under the simplification of neglected damping and assuming small excursion angles (i.e. the magnetization vector almost entirely points along the x -direction: $M_x \approx M_S$), the LLG equation can be linearized and solved analytically. This was first done by Kittel who derived an equation for the FMR condition [61].

$$\omega = \gamma\mu_0 \sqrt{(H_{\text{eff}} + (\mathcal{N}_{xx} - \mathcal{N}_{yy}) M_S) \cdot (H_{\text{eff}} + (\mathcal{N}_{zz} - \mathcal{N}_{yy}) M_S)} \quad (2.35)$$

Often, and most relevant in this work, in-plane magnetized thin film samples without magneto-crystalline anisotropy are considered. In this case the resonance condition takes a simple form, known as the *Kittel equation*

$$\omega = \gamma\mu_0 \sqrt{H_{\text{eff}} (H_{\text{eff}} + M_S)}. \quad (2.36)$$

It describes the angular frequency at which the system is in resonance, which, in the limit of $H_{\text{eff}} \ll M_S$, follows a square-root behavior with respect to the effective field.

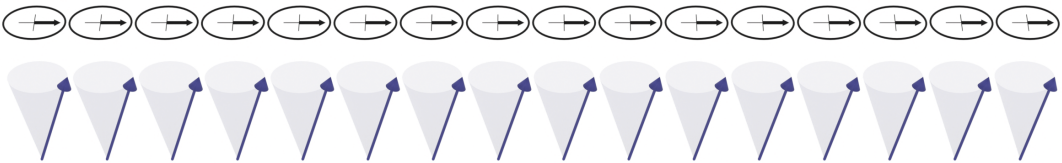


Figure 2.5. | Uniform spin wave mode with a wave vector of $k = 0$. All magnetic moments precess in phase around the effective field.

Since the damping torque is friction-like, i.e. proportional to ω , the resonance line shape is described by a Lorentzian with a linewidth determined by the damping factor of the material. This shape is identical to that of a damped mechanical harmonic oscillator. Damping can have different causes. A first channel is due to eddy currents, which are induced by the precessing magnetization. This is especially relevant in samples with high conductivity, i.e. magnetic metals, and large thickness. Second, damping can be intrinsic due to magnon-phonon scattering, most relevant in materials with large mag-

netostriction. A third mechanism which adds to the damping is spin-orbit mediated electron-magnon scattering, which is dominant in thin metal films. Last, extrinsic scattering processes can increase the effective damping, for example two-magnon scattering. It strongly depends on the material and sample dimensions which of these processes is dominant.

In practice, it is challenging to measure the damping of a material, as the FMR line shape can also be broadened due to inhomogeneous magnetic properties throughout the sample. These inhomogeneous properties lead a spatial variation of the resonance frequency. Integrating over a finite area of the sample during a measurement yields an average response, which appears as a smeared resonance line shape. In this case, the intrinsic damping might be much smaller than suggested by the measured linewidth. This effect is known as *inhomogeneous linewidth broadening*. It can be mitigated by using spatially resolved measurement techniques, which integrate over much smaller regions of a sample.

Inhomogeneous Excitations

The previous section covered the equation of motion and the resonance condition of a magnetic system that can be viewed as a single macroscopic moment, i.e. the *macrospin model*. A real magnetic system is comprised of many individual, coupled magnetic moments. If one allows for the moments to not simply precess all with the same phase, but with a phase difference between neighboring moments, wave-like excitations appear. These inhomogeneous excitations, sketched in Figure 2.6, are known as *spin waves*.

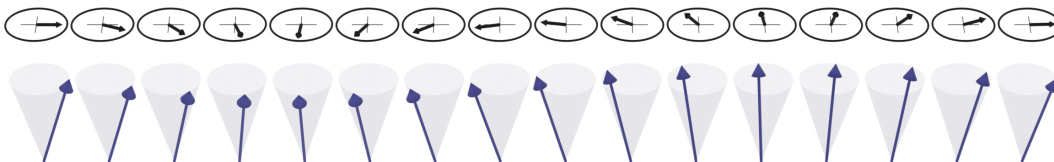


Figure 2.6. | Non-uniform spin wave mode with a finite wave vector of $k \neq 0$. Unlike for the uniform mode there is a non-zero phase difference between neighboring moments.

Due to the inherently quantum mechanic nature of the magnetization, spin waves are quantized. The quantum of magnetic excitations is called *magnon*. A magnon possesses an angular momentum equivalent to flipping a single magnetic moment. In reality, it is much more energetically favorable to not have two adjacent moments pointing in opposite directions, but to spread-out the quasi-particle over many moments, all of which with just slight deviations from their equilibrium orientations [62]. Magnons are Bosons following Bose-Einstein statistics, which means that multiple magnons can coexist in the same state.

For a one-dimensional chain of magnetic moments with only nearest neighbor interaction, a simple dispersion relation can be derived [63]. It takes a form which is very

similar to the dispersion relation of phonons:

$$\hbar\omega = 4J_{\text{ex}}S(1 - \cos(ka)), \quad (2.37)$$

where J_{ex} is the exchange energy, k the wave vector and a the distance between the moments. A proper mathematical description of spin waves in a magnetic thin film needs to take into account exchange and dipolar fields. Herring and Kittel incorporated the exchange contribution of inhomogeneous excitations and arrived at a new resonance condition [60]:

$$\omega_k = \gamma \sqrt{\left(\mu_0 H_{\text{eff}} + \frac{2A_{\text{ex}}}{M_S} k^2\right) \cdot \left(\mu_0 H_{\text{eff}} + \frac{2A_{\text{ex}}}{M_S} k^2 + \mu_0 M_S \sin^2 \theta_k\right)}. \quad (2.38)$$

The angle between the magnetization and the film normal is described by θ_k , which equals 90° for in-plane magnetized films. A_{ex} is the exchange stiffness, which is proportional to J_{ex} and the spin expectation value. It furthermore depends on the crystal structure and the lattice parameter. Equation 2.38 accurately describes spin waves with large wave vectors, as for those the magnetization dynamics is determined by exchange interaction. Hence, those spin waves are called *exchange spin waves*. The meaning of “large”, in this context, depends on the energy scales of the exchange energy and dipolar contributions (which are neglected here). For thin films from common magnetic materials, a rough estimate is $>100 \mu\text{m}^{-1}$. Direct exchange interaction favors parallel alignment of the spins. The energy penalty for tilts of neighboring moments strongly increases with tilt angle. For exchange spin waves, Equation 2.38 reproduces a quadratic dispersion relation, i.e. the energy (and the angular frequency of the spin wave) scales quadratically with the wave vector [60]:

$$\omega_{\text{ex}} \propto k^2. \quad (2.39)$$

For smaller wave vectors, in general, dipolar contributions cannot be neglected and the magnetization dynamics is governed by the interplay of dipolar and exchange fields. It is quite challenging to incorporate these dipolar contributions, since the stray fields generated by an inhomogeneous magnetization act back on the magnetization itself. A thorough derivation of the spin wave spectrum has been conducted by Kalinikos and Slavin in 1986 [64]. Their model is restricted to small excursion angles of the magnetization, i.e. the linear response to a driving field, and describes the situation as it appears in thin films (thickness of a few 100 nm at maximum) that are in-plane magnetized. Kalinikos and Slavin derived the following relation for *dipolar spin waves*:

$$\omega_n = \gamma \sqrt{\left(\mu_0 H_{\text{eff}} + \frac{2A_{\text{ex}}}{M_S} k^2\right) \cdot \left(\mu_0 H_{\text{eff}} + \frac{2A_{\text{ex}}}{M_S} k^2 + \mu_0 M_S F_n(\theta, k_{\text{IP}} d)\right)} \quad (2.40)$$

with the coefficients

$$F_n = 1 + P_n(1 - P_n) \cdot \left(\frac{M_S}{H_{\text{eff}} + 2A_{\text{ex}}k^2/\mu_0 M_S} \right) \cdot \sin^2 \theta - P_n \cos^2 \theta \quad (2.41)$$

$$P_n = 1 + \frac{1 - (-1)^n e^{-k_{\text{IP}} d}}{k_{\text{IP}} d} \quad (2.42)$$

$$k^2 = k_{\text{IP}}^2 + k_{\text{OOP}}^2 = k_{\text{IP}}^2 + \left(\frac{n\pi}{d} \right)^2. \quad (2.43)$$

Here, the thickness of the film is denoted with d and k_{IP} and k_{OOP} are the wave vectors in the plane of the film and perpendicular to it (out-of-plane), respectively. n represents a quantization index for standing spin waves along the film thickness. Because of the small phase velocities $v_{\text{ph}} = \omega/k$ of the spin waves, which are much smaller than the velocity of the electromagnetic waves which excite them, they can be approximated as quasi-static in relation to photons (magnetostatic approximation). Therefore, they are often called *magnetostatic spin waves*. The angle between the magnetization \mathbf{M} and the wave vector of the spin wave k is crucial for determining the exact dispersion.

Damon and Eshbach investigated the spin wave spectrum in a thin in-plane magnetized slab by solving Maxwell's equations with a purely dipolar approach [65]. They were the first to describe *magneto-static surface waves (MSSW)*, also known as *Damon-Eshbach (DE)* modes, which are the lowest-order approximate solutions to the problem. These modes are localized at the top or bottom surface of the film with thickness d . They display an in-plane wave vector of $\mathbf{k}_{\text{IP}} \perp \mathbf{M}$ and follow the dispersion

$$\omega_{\text{MSSW}} = \gamma\mu_0 \sqrt{H_{\text{eff}}(H_{\text{eff}} + M_S) + \left(\frac{M_S}{2} \right)^2 \cdot (1 - e^{-2k_{\text{IP}} d})}. \quad (2.44)$$

The situation changes considerably when in-plane wave vectors parallel to the magnetization are considered. These spin wave modes with $\mathbf{k}_{\text{IP}} \parallel \mathbf{M}$ are called *backward volume spin waves (BVSW)*. Remarkably, in the dipolar-dominated regime, BVSWs exhibit a negative group velocity (despite their positive phase velocity) due to the negative slope of their dispersion. Unlike MSSW modes, BVSWs are localized in the bulk of the film, hence the name. They follow the dispersion relation

$$\omega_{\text{BVSW}} = \gamma\mu_0 \sqrt{H_{\text{eff}} \left(H_{\text{eff}} + M_S \frac{1 - e^{-k_{\text{IP}} d}}{k_{\text{IP}} d} \right)}. \quad (2.45)$$

As the behavior of BVSW fundamentally differs from MSSW, the frequency of in-plane spin waves is highly anisotropic with respect to the magnetization direction, as can be seen from the calculated exemplary dispersion curves shown in Figure 2.7.

In addition to the in-plane directions, the magnetization can show a non-uniform precession across the film thickness (z -direction). When the film thickness is small, rather than propagating through the bulk of the material, standing waves form, with a quantization along the film normal [66]. They are hence called *perpendicular standing*

spin waves (PSSW). The PSSW dispersion is given by

$$\omega_{\text{PSSW}} = \gamma\mu_0 \sqrt{\left(H_{\text{eff}} + \frac{2A_{\text{ex}}}{\mu_0 M_S} k^2\right) \cdot \left(H_{\text{eff}} + \frac{2A_{\text{ex}}}{\mu_0 M_S} k^2 + M_S\right)}. \quad (2.46)$$

The total wave vector $k = \sqrt{k_{\text{IP}}^2 + k_{\text{OOP}}^2}$ is composed of the in-plane wave vector k_{IP} , as well as the quantized out-of-plane wave vector $k_{\text{OOP}} = n\pi/d$, where $n = 0, 1, \dots$. The out-of-plane wave vector, and hence the frequencies at which PSSWs can be observed, is strongly dependent on the film thickness.

The three geometries in which spin waves can occur in in-plane magnetized samples and the dispersion of the associated spin wave modes is shown in Figure 2.7. The spin wave energy is a result of the interplay between the exchange energy and dipolar contributions, which in turn strongly depend on the film thickness. The dipolar contribution, depicted as dashed lines in the figure, becomes dominant at small wave vectors, while at large wave vectors the quadratic exchange contribution takes over.

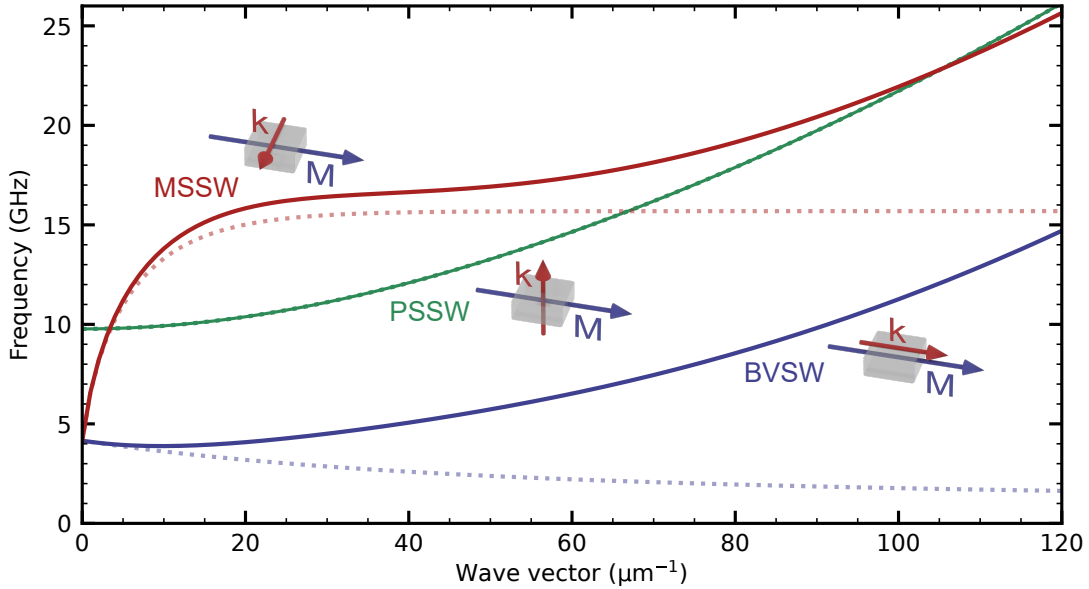


Figure 2.7. | Dispersion of MSSW (red), BVSW (blue) and 1st PSSW (green) spin wave modes calculated for a 60 nm-thick Ni₈₀Fe₂₀ film at 20 mT external field. The dispersion branches follow Equation 2.44, Equation 2.45, and Equation 2.46, respectively. Dotted lines show only the dipolar contribution, which dominates the behavior at small wave vectors. Solid lines include the exchange contribution, which leads to $\omega \propto k^2$ behavior for large wave vectors. The wave vector of $k = 0$ marks the uniform mode.

Last, in out-of-plane magnetized thin films another type of spin wave modes can be observed, so-called *forward volume spin waves (FVSW)* [64, 67]. The nature of this mode is analog to BVSW modes in in-plane magnetized films. They follow the

dispersion relation

$$\omega_{\text{FVSW}} = \gamma\mu_0 \sqrt{H_{\text{eff}} \left(H_{\text{eff}} + M_{\text{S}} \left(1 - \frac{1 - e^{-k_{\text{IP}}d}}{k_{\text{IP}}d} \right) \right)}. \quad (2.47)$$

For all of the different spin wave modes, the externally applied field plays an important role to determine the energy and therefore the frequency of the mode. If applied along an easy anisotropy axis, the external field leads to an increase in magnetic stiffness, analogous to an increase of the spring constant of a mechanical oscillator. Consequently, it leads to an increase of the mode energy and thus the spin wave frequencies. If applied along a hard axis the external field can counter internal energy contributions. Hence its effect can be opposite, lowering the resonance field.

Nonlinear Dynamic Effects

The previous section introduced the dynamics that arises when the magnetization is weakly excited. In this case the system resembles a harmonic oscillator. Analogous to the harmonic oscillator, when the excitation amplitude is increased, anharmonicities arise. These anharmonicities are the origin of nonlinear dynamic effects. A variety of effects has been observed, which, in many cases, lead to the generation of frequency components different from the excitation frequency. Such frequency conversion typically occurs in parametric processes. A process is called parametric if an internal parameter of an oscillator is modulated during the course of the oscillation. In a magnetic system, this could, for example, be the magnetic stiffness of the magnetization. Here, an excited spin wave mode becomes unstable after exceeding a certain threshold in excitation amplitude.

The theoretical treatment of nonlinear processes was first conducted by Suhl in 1957 [68] in a semi-classical way, by moving from the LLG equation to rate equations for the spin wave modes. In this framework, a positive rate means an increase of spin wave amplitude over time and marks the onset of the nonlinearity. A rigorous description of this regime was introduced by L'vov [69], Zakharov [70] and later extended by Krivosik and Patton [71]. They established a particle-like picture to describe these instabilities as magnon-magnon scattering processes and use their model to describe the so-called Suhl instabilities of 1st and 2nd order, which occur beyond the excitation threshold.

The 1st order Suhl instability is a three-magnon process, where a magnon excited with frequency ω_{ex} and wave vector k_{ex} scatters into two new magnons (ω_1, ω_2 and k_1, k_2) under the conservation of energy and momentum. These two magnons are observed as an additional resonance peak in FMR experiments [23]. This example is well studied and these spin waves can efficiently be excited when the excitation field is applied along the direction of the magnetization [7, 72, 73], in *parallel-pumping* geometry. In this geometry, the torque on the magnetization, at first glance, should be zero according to the Equation 2.28. However, a slight initial misalignment between magnetization and

the excitation field leads to a finite torque, followed by a precession of the magnetization around the equilibrium direction. Such a misalignment might simply be caused by an imperfect setup, random thermal fluctuations of the magnetization, or by intentionally engineering anisotropies. Further excitation increases the precessional amplitude more and more and thus leads to a coherent amplification of certain spin wave modes. This process, of course, is counteracted by damping of the motion until a stationary state is reached. In the particle picture, energy and momentum are conserved.

$$\hbar\omega_{\text{ex}} = \hbar\omega_1 + \hbar\omega_2 \quad (2.48)$$

$$k_{\text{ex}} = k_1 + k_2 \quad (2.49)$$

In the simplest case of uniform excitation ($k_{\text{ex}} = 0$) and a symmetric dispersion, these conservation requirements yield

$$k_1 = -k_2 \quad (2.50)$$

$$\omega_1 = \omega_2 = \frac{\omega_{\text{ex}}}{2} \quad (2.51)$$

In other words, the excited spin waves will precess at a frequency half of the excitation frequency and, following the dispersion, possess finite but opposing wave vectors.

Suhl instabilities of 1st order can only occur when suitable states exist for the generated magnons to scatter into, such that the requirements of conservation of energy and momentum are fulfilled. They are prohibited, for example, at low bias fields, where there are simply no states at lower frequencies present. 1st order Suhl instabilities might also be prohibited when the dispersion is asymmetrical and thus does not allow for this type of magnon scattering without violating energy or momentum conservation. In this case, the 2nd-order Suhl instability might be observed. This is a four-magnon process, where two primary magnons scatter into two new magnons, with equal frequencies, but finite wave vectors. Due to the greater number of magnons involved, this process, in general, is less likely than the 1st-order process. Suhl instabilities are predicted to appear at very high excitation amplitudes [24].

The aforementioned mechanisms for spin wave generation are described by S-theory under the assumption of energy conservation for each individual scattering process. This restriction, however, is lifted in case of a periodic excitation, where energy is transferred continuously to the magnetic system [74]. Bauer *et al.* introduced a model which describes the behavior of the magnetization in thin films at low magnetic bias fields [75]. When the excitation field is of the same order of magnitude as the external bias field, amplitude-phase oscillations occur. Due to the highly elliptical precession of the magnetization with large excursion angles, which occurs in soft magnetic thin films subjected to small magnetic bias fields, the underlying anisotropic spin wave dispersion changes during one precessional period. This leads to the coherent generation of nonlinear spin waves at odd half-integer harmonics of the driving frequency. Moreover, the excitation threshold is greatly reduced compared to the threshold expected from

Suhl instabilities. The existence of this spin wave generation process was predicted theoretically [75] and experimentally verified in $\text{Ni}_{80}\text{Fe}_{20}$ thin films by means of X-ray magnetic circular dichroism (XMCD) and SNS-MOKE microscopy [76, 77].

2.1.4. Magneto-Optical Effects

When light interacts with any material, it can, depending on the material properties, be transmitted, reflected, or absorbed by the material. This section will provide an overview of the phenomena which occur specifically when the material is exposed to magnetic fields or itself is ferromagnetic.

Mathematically, the interaction of light with a solid is described by the permittivity $\underline{\varepsilon}$, which is a measure of how easy the material can be polarized by an incident electric field. In general, $\underline{\varepsilon}$ is a 2nd rank tensor with complex coefficients. In that case, the imaginary part describes the absorption of light. For a simple isotropic medium, the permittivity can be treated as a scalar. However, the situation becomes more complex if a magnetic material (or a magnetic field) is present, as off-diagonal elements show up (shown below for a field along z -direction). The off-diagonal components lead to an anisotropic permittivity and are the origin of the magneto-optical effects which will be discussed in the following.

$$\underline{\varepsilon} = \begin{pmatrix} \varepsilon_{xx} & \varepsilon_{xy} & 0 \\ -\varepsilon_{xy} & \varepsilon_{yy} & 0 \\ 0 & 0 & \varepsilon_{zz} \end{pmatrix} \quad (2.52)$$

Light transmitted through a material experiences the *Faraday effect*, named after Michael Faraday, who discovered it in 1845 [78]. The effect describes the rotation of the polarization direction of linearly polarized light when it passes through a medium that is subjected to a magnetic field oriented parallel to the propagation direction. It can be best understood by decomposing the linear polarization in two left- and right-hand circularly polarized components. In a semi-classical picture, the electric fields of the two components cause charge carriers inside the material to move. The moving charges, in turn, generate own magnetic fields which are either parallel or antiparallel to the external field, depending on the direction of the polarization. This influences the dynamics of the interaction depending on the light polarization. Specifically, it causes a different phase shift of the transmitted electrical field for both components, depending on the handedness of the polarization. This effect can be understood as a consequence of Lorentz force. Superimposing the two components back up after passing through the medium again yields linear polarization of the light, but with a net rotation of the polarization with respect to the incident direction. The underlying microscopic reason for the phase difference of left- and right-hand circularly polarized light is SOC. It couples the electrons' spin to its direction of motion and ultimately leads to different phase velocities of both light components.

This effect also occurs upon reflection of light from a magnetic sample. This was discovered by John Kerr in 1877 when he studied the polarization change of linearly polarized light reflected from a polished Iron surface [79]. It is, hence, called *magneto-optical Kerr effect (MOKE)*. The Kerr effect can be quantified in terms of a rotation θ of the polarization state of the reflected light. Additionally, an ellipticity ϵ might be induced upon reflection of the light, due to a different reflectivity for both circularly polarized components. Equivalently to the Faraday effect, MOKE can be understood in terms of the same mechanism, i.e. a different permittivity for left- and right-hand circular components of which the incident light is composed.

There are three different MOKE geometries, depending on the relative orientation of the magnetization vector with respect to the plane of incidence of the light. These geometries are depicted in Figure 2.8. In the polar geometry the magnetization vector points out of the plane of the sample. In longitudinal MOKE it points in the plane of the sample and the plane of incidence of the light, while in transverse MOKE the magnetization points perpendicular to the plane of incidence. Depending on the magnetization component of interest the according MOKE geometry provides a convenient means to optically detect static and dynamic magnetic properties of thin film samples.

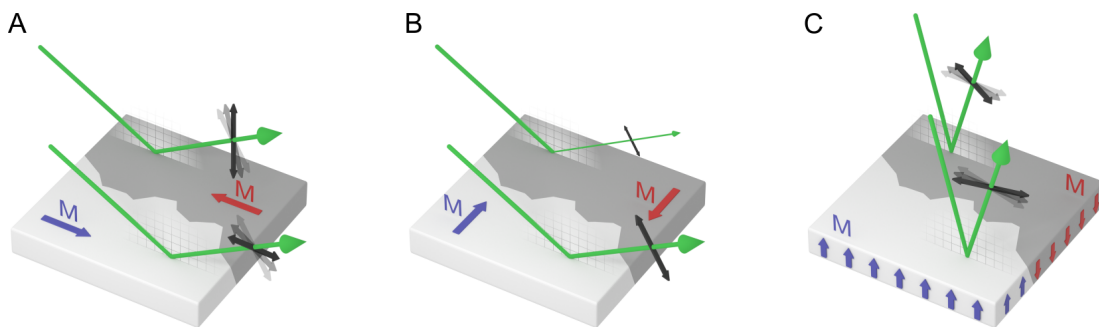


Figure 2.8. | Sketch of the different MOKE geometries. The red and blue arrows indicate the direction of the magnetization. Green arrows depict the beams of light reflecting off the sample. Black arrows represent the polarization direction of the light. **A:** Longitudinal geometry. The magnetization vector lies in the plane of the sample and parallel to the plane of incidence of the light. Upon reflection, the polarization of the light is rotated. **B:** Transverse geometry. The magnetization vector lies within the plane of the sample, but perpendicular to the plane of incidence of the light. The absorption of the light depends on the direction of magnetization, leading to a change in reflected intensity. **C:** Polar MOKE geometry. The magnetization vector points out of the plane of the sample. The light is reflected under near-normal incidence. This is in contrast to the shallow incidence angles used in the longitudinal and transverse MOKE geometries. Like in the longitudinal geometry, the polarization of the reflected light is rotated depending on the direction of the magnetization.

A final magneto-optical effect to be mentioned is *magnetic circular dichroism (MCD)*. It describes a difference in absorption of left- and right-hand circularly polarized light incident on a sample. MCD is often used with X-rays (XMCD), where the photon energy is tuned to match a specific transition between an elements' core levels (e.g. L-edge). In this way, it provides an element-specific method to probe magnetization [80].

However, working with X-rays involves complications and challenges, i.e. a tunable and brilliant light source is required, which usually means that such experiments can only be carried out at large-scale synchrotron facilities.

2.1.5. Transport Effects

Electronic transport is a versatile tool to probe various properties of materials. Fundamentally, electrons in solids travel as wave packets in electronic states, *Bloch states*. These are influenced by external stimuli, such as an imbalance in chemical potential, electrical potential, temperature gradient or magnetic fields. These stimuli directly influence the electronic motion and lead to a number of effects visible in transport measurements.

Boltzmann transport considers the diffusion and scattering of charge carriers in a material. In a stationary and linearized *ansatz* it yields the electrical conductivity $\underline{\sigma}$ (or its inverse, the resistivity $\underline{\rho}$). This describes the ability of a material to conduct electrical current j in a presence of an electrical field \mathbf{E} . In the simple case of parabolic bands the conductivity is a scalar, while in general it takes the form of a 3×3 tensor.

$$\mathbf{j} = \underline{\sigma}\mathbf{E}. \quad (2.53)$$

In different materials various effects modify the conductivity or lead a detectable voltage. Some examples are described in the following.

Transport Effects in Non-Magnetic Materials

The ordinary *Hall effect* is a direct consequence of a magnetic field acting on charges q , which move with the velocity v , i.e. the Lorentz force \mathbf{F}_L [81]

$$\mathbf{F}_L = q\mathbf{v} \times \mathbf{B}. \quad (2.54)$$

Due to this force, the charge carriers are deflected towards a direction perpendicular to their direction of motion and the magnetic field. If there is an unequal number of positive and negative charge carriers, or if their mobilities differ, this leads to the build-up of a charge imbalance in a finite sample. The result is an electric potential in this transverse direction. The electric field due to the charge imbalance causes an electric force which counteracts \mathbf{F}_L . The charge build-up ends when an equilibrium between the two forces is reached. It can be measured as a Hall voltage. Simultaneously, a change in resistance (Hall resistance) of the sample can be detected.

When a metal is subjected to a temperature gradient, a charge gradient arises along with the temperature gradient. This effect is called *Seebeck Effect* [82]. Electrons from the high-temperature side of the metal possess a higher kinetic energy than the electrons at the low-temperature side. Hence, they diffuse along the temperature gradient faster than in the opposite direction, leading to a charge imbalance, i.e. a Seebeck voltage.

The inverse effect is the *Peltier effect*.

If both, a temperature gradient and a transverse magnetic field are present, the *Nernst effect* can be observed. As the charge carriers move along the temperature gradient (see Seebeck effect), they are deflected by the Lorentz force in a direction perpendicular to the magnetic field and the temperature gradient (similar to the Hall effect). This leads to a charge build up perpendicular to both and a Nernst voltage can be observed.

Transport Effects in Magnetic Materials

In ferromagnetic materials the situation becomes more intricate as now the non-zero magnetization comes into play. This is reflected by the spin-split bandstructure of the materials, i.e. at a certain momentum a spin-up electron possesses a different energy than a spin-down electron. This, of course directly leads to different transport coefficients for the different spin species and is the reason for a whole zoo of new effects.

For example, an effect related to the Hall effect, the *anomalous Hall effect (AHE)*, can be observed. Even if no external magnetic field is applied (hence the prefix 'anomalous'), a Hall-like voltage is generated transverse to the direction of an applied current and the magnetization of the material. The magnetization itself can be seen as the source of an internal magnetic field, which in turn causes a Lorentz force to act on the charge carriers. Similar to the Hall resistivity, there is a *magneto resistance (MR)* linked to the effect. Also, a negative MR possible, which can be caused by scattering between s- and d- states. Lastly, *anisotropic magneto-resistance (AMR)* can be observed, which is caused by an anisotropic charge distribution due to SOC. AHE and MR/AMR are useful effects for the investigation of magnetic order.

Analogously to the AHE in magnetic materials the *anomalous Nernst effect (ANE)* can be observed. A temperature gradient perpendicular to the magnetization of the material generates an ANE voltage perpendicular to both [83]. As this voltage is directly linked to the magnetization, it provides an additional handle to measure the magnetization of a material [84]. In this thesis, ANE measurements will play a role and it will be shown how it can be used to overcome the optical diffraction-limit.

Spin Transport Effects

In addition to the aforementioned effects, a whole variety of additional effects appear when the transport of angular momentum is considered. This, most prominently, includes the *spin Hall effect (SHE)* [85], which describes the generation of a spin current from a charge current. It has been observed in heavy metals [86], as well as in semiconductors [87, 88].

Considering magnetic materials, in general, electronic transport through the material causes a spin polarization of a current. This originates from the band-splitting for spin-up and -down electrons, which results in a different number of spin-up and -down

carriers at the Fermi level. Therefore, the transport is dominated by one species. Due to the conservation of angular momentum, a torque (spin orbit torque (SOT)) acts on the magnetization in return.

Other examples for magnetization-related effects are the *spin Seebeck effect* [89] and the *spin Nernst effect* [90, 91]. In both, as a full analogon to the classical Seebeck and Nernst effects, instead of voltages, a spin polarization is generated due to temperature gradients across a magnetic material. The enumerated effects lay the ground of the field of spintronics [92] and can be used for the investigation of magnetization.

2.1.6. Magnetic Order Beyond Ferromagnetism

The well known ferromagnetic order, which is stabilized by exchange interaction, is not the only possibility of magnetic order. In fact, it is not even the most abundant one in nature. A variety of types of magnetic order can be observed with more and more complex forms of coupling of the individual magnetic moments. Figure 2.9 shows a sketch of the important material types. This section briefly introduces these types of magnetic order, since some of them are investigated in this thesis.

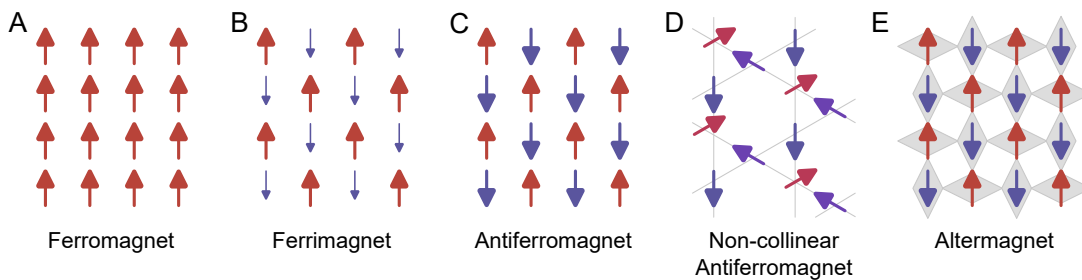


Figure 2.9. | Different types of magnetic order. These include the previously described ferromagnetic order, where all magnetic moments point along the same direction. More complex forms are ferri- and antiferromagnetic order, where the magnetic moments of two sub-lattices point in alternating directions, as well as non-collinear antiferromagnets, where the lattice positions of the magnetic moments provokes magnetic frustration and makes them point in different directions within certain crystal planes. Lastly, altermagnetism is the most recently discovered type of magnetic order, where the magnetic symmetry acts together with the symmetry of the atomic lattice and yields all sorts of magnetic effects which would be forbidden otherwise.

Ferrimagnets

In ferrimagnets, the lattice on which the magnetic moments are located is composed of two sub-lattices. Due to effects like magnetic super-exchange, the two sub-lattices couple antiferromagnetically, i.e. the magnetic moments are oriented in opposite directions. When different species of atoms possessing different magnetic moments are located on the two lattice sites, these moments cancel only partially. This leaves a net magnetization of the material. In many ways, ferrimagnets behave very similarly to conventional ferromagnets. They, for example, can host spin waves at similar frequencies (GHz range) and hence show FMR behavior. However, the two sub-lattices

allow for different high-energy modes, where they precess in-phase or out-of-phase with each other. Like ferromagnets, ferrimagnetic materials display effects, such as AMR or MOKE, which are useful tools for their investigation.

A material of this class is yttrium iron garnet (YIG). YIG is a magnetic insulator with an exceptionally low Gilbert damping ($\alpha \sim 10^{-4}$ range) [93]. This makes very narrow resonance linewidths possible. The low damping can be partially explained by the fact that it is an insulating material, which is not affected by certain damping mechanisms, i.e. magnon-electron scattering and eddy currents. YIG can be fabricated with exceptional quality, i.e. a very small amount of defects and high homogeneity, resulting in a reduced damping due to scattering processes and the suppression of inhomogeneous broadening of the resonance linewidth. Because of its properties YIG is widely used in microwave devices, such as couplers, filters and isolators.

YIG can be fabricated in thin films, which are most useful for magnonic devices. They, as well, display low damping and narrow resonance linewidths [94] and allow for the propagation of spin waves over millimeter-long distances. Because of this, YIG it is a common material to investigate spin wave phenomena, like their propagation, interference, filtering [95] and amplification [8] and to realize more complex magnonic devices [18].

Antiferromagnets

Coming from ferrimagnets, the next logical extension are antiferromagnets. Here, the two sub-lattices are populated with the same species of atoms. Hence, the magnetic moments on both lattice sites are equal and perfectly compensate each other. Because of this, antiferromagnets do not possess any macroscopic net magnetic moment under ambient conditions and they are not affected by external magnetic fields.

In the bandstructure, contrary to ferromagnets, the bands for spin-up and -down electrons have exactly the same energy. This, to a large extent, prevents antiferromagnets from exhibiting transport effects like AHE and MOKE, rendering their investigation and manipulation quite challenging. However, antiferromagnets are affected by THz fields, as well as SOT and spin transfer torque (STT). Their fast dynamics together with absent stray fields render them promising materials for future spintronic devices [96].

Most prominent examples for this class of materials are oxides, like NiO. The antiferromagnetic coupling of the nickel-moments is induced by super-exchange mediated by the oxygen atoms.

Non-collinear Antiferromagnets

Non-collinear antiferromagnets in many ways behave like antiferromagnets. Here, the magnetic moments of two neighboring lattice sites do not necessarily compensate each other directly. However, globally the moments are arranged in a way such that the net

moment is (almost) zero. An example for this class of materials is Mn_3Sn [97]. The magnetic moments, stemming from the Mn atoms, are arranged in a so-called Kagome lattice. They orient in a way such that they almost perfectly compensate. However, the presence of anisotropic exchange, known as Dzyaloshinskii–Moriya interaction (DMI) [98, 99], leads to a slight canting of the moments out of the Kagome plane and therefore results in a small, but finite out-of-plane magnetic moment. This allows to polarize the material in one of six states using sufficiently strong magnetic fields. This is useful in applications, like antiferromagnetic tunnel junctions [100]. The non-collinear, chiral orientation of the magnetic moments leads to a non-zero Berry curvature. This gives rise to magneto-transport effects, like the AHE. This material and related materials are an active area of research and new effects as well as their classification are under continuous discussion.

Altermagnets

Altermagnets conclude the list of magnetic orders other than the ferromagnet order. This recently discovered class of materials is related to antiferromagnets, however, it introduces the complication that the atomic surrounding at two neighboring sites of the same sub-lattice is not identical, but rather alternately rotated [101, 102]. An example is a two-fold spin-symmetry (\mathcal{C}_2) in combination with a four-fold lattice symmetry (\mathcal{C}_4). This unique fact lifts the degeneracy of the spin-up and -down bands depending on the k -vector and allows for direction-dependent magneto-transport effects. Altermagnets are a very active area of research. Many previously as antiferromagnets classified materials, on closer look, turn out to actually obey the symmetry relations which classify them as altermagnets. An example for this class of materials is RuO_2 [103].

2.2. Optics, Spatial Resolution and Near Field Interaction

As this thesis is about optical microscopy beyond the diffraction limit, a few words need to be said about optical principles and what is actually meant by this. The first section covers the principles of optical resolution, which is crucial for any optical microscopy technique. The second section is about the optical near field. The optical near field is the region where the usual far field approximations do not apply, as there are no plane wave fronts and the local properties of the elements and materials have crucial influence on the exact shape and form of the interacting electrical fields. Special emphasis is placed on the interaction of a surface with the near field of an electrical dipole in close vicinity. This describes the fundamental working principle of the s-SNOM technique, which will be used in the second part of this thesis.

2.2.1. Far Field Diffraction Limit and Optical Resolution

An important measure for all optical methods is the spatial resolution, because it describes on which scales a local signal can be observed. In general, it is determined by the size of the volume the probing light can be focused to, as every signal measured will be the convolution of the point spread function of the focal spot with the actual sample properties.

When light propagates through a round aperture and is focused onto a screen at a certain distance, one finds a characteristic pattern of a bright central spot surrounded by concentric rings. This phenomenon is known at least since the 19th century and for example was described by the British astronomer Herschel in 1828 [104]. A thorough treatment of the physics behind the phenomenon later was done by Airy [105] and is roughly described in the following.

The aperture blocks parts of the incident light and diffracts others. Behind it, different orders of diffraction interfere and add up to a resulting electric field distribution, which in the focal plane of the focusing element mathematically is described by a Bessel function of 1st kind J_1 .

$$E(r) = E_0 \frac{2J_1(\pi r)}{\pi r} \quad (2.55)$$

Here, r denotes the distance to the focal point in radial direction and E_0 the incident electric field strength. From the electric field, the light intensity can be calculated by taking the absolute of the time-average of the square of the electric field.

$$I = \sqrt{\frac{\varepsilon_0}{\mu_0}} \left| \langle E(t)^2 \rangle_t \right| = \frac{1}{2} \sqrt{\frac{\varepsilon_0}{\mu_0}} E^2 \quad (2.56)$$

The bright central region of the intensity pattern that stretches until the first minimum is called *Airy disc*. The Airy disc defines the smallest region to which light of a certain wavelength can be focused. Its size, or more correctly the angle θ under which the first minimum occurs, are determined by the diameter d of the aperture and the wavelength of the light λ .

$$\sin(\theta) \approx 1.22 \frac{\lambda}{d} \quad (2.57)$$

The resolution of an optical instrument is fundamentally linked to the size of the Airy disc. When an object is observed through such an instrument, i.e. a telescope or a microscope, an image is formed in a certain image plane in the instrument, at which a screen or detector can be placed to view the image of the object. The image of a point source turns out to be exactly such an Airy disc, since ultimately the light is passing through a series of apertures which effect it as described above. To connect the appearing size of the Airy disc to the optical resolution of the instrument, one has to consider the minimal distance in which two Airy discs produced by two point sources can appear, such that they still can be observed as separate. This condition is described by the Rayleigh criterion [106]. It defines the minimal observable separation

as the distance, where the center of the first Airy disc coincides with the first minimum of the second Airy disc. Figure 2.10 A depicts the overlapping intensity profiles of the two point Airy discs stemming from two point sources, separated by a distance that matches their full width at half maximum (FWHM). In this case the criterion mentioned above is fulfilled. It should be noted, that slightly different definitions exist which may also take into account the sensitivity of the detector.

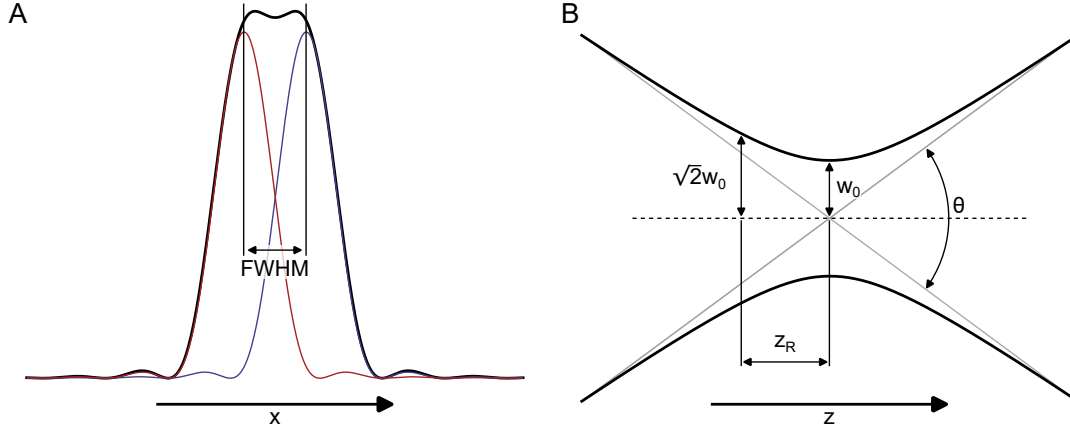


Figure 2.10. | **A:** Cross sections of the intensity of two overlapping airy discs (red and blue) shifted by one FWHM. At approximately this shift, a local minimum in the combined intensity (black line) occurs and makes the two discs distinguishable. **B:** Beam waist $w(z)$ around the focal spot. The Rayleigh length is defined as the distance to the focal spot where the beam waist has increased by the factor $\sqrt{2}$.

For an optical microscope, taking into account the focusing optics (usually the objective lens and aperture are the most critical parts), this translates into a minimal resolvable distance between two point sources.

$$d_{\min} = 1.22 \frac{\lambda}{2NA} = 0.61 \frac{\lambda}{n \cdot \sin \alpha} \quad (2.58)$$

Here, NA is the numerical aperture of the objective, n the index of refraction of the surrounding (i.e. air or an immersion medium like water or immersion oil) and α is the opening angle of the objective. The factor of 1.22 originates from the FWHM of the Airy disc. This relation was derived by Abbe in 1873, as he observed optical gratings under a microscope which were illuminated from below [107]. He found that the microscope can only resolve line spacings down to a certain limit. In his description, the grating diffracts the light in different diffraction orders into increasing diffraction angles. To be able to resolve the grid structure, additionally to the not-diffracted light (0^{th} diffraction order), also the 1^{st} diffraction order has to enter the objective and contribute to the image. In this case, the resulting law for the optical resolution matches the Rayleigh criterion.

Finally, note that the spatial resolution is not only limited in the in-plane directions, but also in the direction along the light path. In general, the waist w of a focused

Gaussian-shaped beam of light changes along its propagation direction z as

$$w(z) = w_0 \sqrt{1 + \left(\frac{z}{z_R}\right)^2}. \quad (2.59)$$

w_0 is the beam waist in the focal point, i.e. the radius of the Airy disc. z_R is the Rayleigh length, which is defined as the distance from the focal point where the beam waist has expanded to $\sqrt{2}w_0$. The changing beam waist along the z -direction is visualized in Figure 2.10 B. It mainly depends on the divergence of the beam given by the numerical aperture (NA). The Rayleigh length can be understood as the perpendicular equivalent to the lateral spot size of the focused beam. Both quantities together determine the probed volume.

2.2.2. Optical Near Field and Electric Dipole Interaction

The optical near field describes the electromagnetic field in close vicinity to the surface of an object. Solving Maxwell's equations for the interaction of local dipole moments constituting the object in combination with an external electromagnetic field yields a field that can be separated in two terms. These are the electromagnetic (radiating) *far field* term and the *near field*. The near field decreases rapidly with increasing distance from the surface of the object, i.e. exponentially in the case of evanescent fields. Due to the small distances involved, in contrast to the electromagnetic far field, the retardation of the electromagnetic waves due to the finite speed of light can be neglected in the description of optical near fields.

An experimental method used in this thesis is scattering scanning optical near field microscopy (s-SNOM). It relies on the electromagnetic interaction of an illuminated, metallic tip and the near field it generates with the sample. To understand the scattering mechanism, a simplified model is presented following the considerations that were made by Keilmann and Hillenbrand [108]. The model approximates the tip by a conducting sphere with a radius a , which corresponds to the radius of the tip at its apex. This sphere is exposed to an electric field \mathbf{E}_{in} due to the laser illumination. The dielectric functions of the sphere and the environment are ε and ε_{env} , respectively. The sphere together with the surrounding medium has a polarizability of α . As the surrounding medium is air ($\varepsilon_{\text{env}} = 1$), the polarizability simplifies to

$$\alpha = 4\pi\varepsilon_0 a^3 \frac{\varepsilon - \varepsilon_{\text{env}}}{\varepsilon + 2\varepsilon_{\text{env}}} \approx 4\pi\varepsilon_0 a^3 \frac{\varepsilon - 1}{\varepsilon + 2}. \quad (2.60)$$

The incident electric field induces a dipole moment \mathbf{p}_0 inside the sphere of

$$\mathbf{p}_0 = \alpha \mathbf{E}_{\text{in}} = 4\pi\varepsilon_0 a^3 \frac{\varepsilon - 1}{\varepsilon + 2} \mathbf{E}_{\text{in}}. \quad (2.61)$$

The polarized sphere itself is the source of an additional dipole field. It can be approx-

imated by the field of a point dipole located in the center of the sphere:

$$\mathbf{E}_0 = \frac{|\mathbf{p}_0|}{4\pi\epsilon_0 r^3} (2 \cos(\theta)\hat{\mathbf{e}}_r + \sin(\theta)\hat{\mathbf{e}}_\theta), \quad (2.62)$$

where r is the distance from the dipole and θ is the angle with respect to the dipole axis. $\hat{\mathbf{e}}_r$ and $\hat{\mathbf{e}}_\theta$ are the unit vectors in radial and azimuthal direction.

The situation gets more complicated when the sphere is brought close to the surface of a medium which represents the sample. The model of a conducting sphere next to a planar surface was described by Aravind and Metiu in 1983 [109]. They solved the Laplace equation and demonstrated, that in the electrostatic limit the field distribution between tip and sample appears as if there was a mirror dipole induced inside the medium. This situation is depicted in Figure 2.11. For simplicity, from now on only an electrical polarization in z -direction is considered, i.e. perpendicular to the surface ($\theta = 0$). Furthermore, it is assumed that the medium cannot be polarized directly by the incident external electric field \mathbf{E}_{in} , but only indirectly by the sphere's dipolar field. This assumption is justified since the strength of the dipolar near field in close vicinity to the sphere exceeds the strength of the incident field.

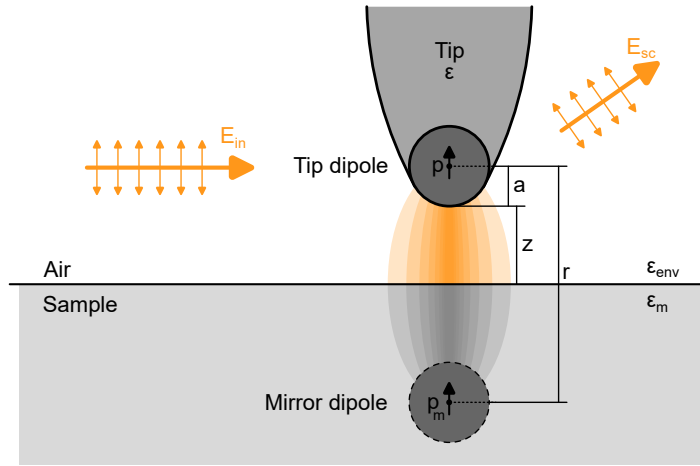


Figure 2.11. | Mirror dipole model of near field interaction. A metallic tip, located above the surface of a at a distance z , is polarized by an electric field \mathbf{E}_{in} . The tip is approximated by a sphere with radius a . The induced dipole in the tip generates a field, which in turn induces a mirror dipole in the sample. The field of the mirror dipole acts back on the tip dipole and vice versa. The scattered light is proportional to the total effective dipole of the tip-sample system. Figure based on [108].

The induced mirror dipole is located inside the medium at the same distance $r/2$ from the interface as the sphere. Its dipole moment $\mathbf{p}_{\text{m},0}$ equals the dipole moment of the sphere, but scaled by a factor of β due to the dielectric function of the medium $\epsilon_m \neq 1$. It can be expressed as

$$\mathbf{p}_{\text{m},0} = \beta \mathbf{p}_0 = \beta \alpha \mathbf{E}_{\text{in}} \quad (2.63)$$

with the scaling factor

$$\beta = \frac{\varepsilon_m - 1}{\varepsilon_m + 1}. \quad (2.64)$$

The mirror dipole generates a mirror electric field of

$$\mathbf{E}_{m,0} = \frac{1}{2\pi\varepsilon_0 r^3} \mathbf{p}_{m,0}. \quad (2.65)$$

This field acts back on the sphere and induces an additional dipole moment, which can be understood as a first order correction term to the spheres dipole moment:

$$\begin{aligned} \mathbf{p}_1 &= \alpha \mathbf{E}_{m,0} \\ &= \frac{1}{2\pi\varepsilon_0 r^3} \alpha \mathbf{p}_{m,0} \\ &= \frac{1}{2\pi\varepsilon_0 r^3} \alpha^2 \beta \mathbf{E}_{in}. \end{aligned} \quad (2.66)$$

This, in turn, adds a correction to the mirror dipole and so on. The mutual back-interaction can be written as a sum of correction terms for the spheres dipole moment:

$$\mathbf{p} = \sum_{i=0}^{\infty} \mathbf{p}_i = \alpha \left[1 + \frac{\alpha\beta}{2\pi\varepsilon_0 r^3} + \left(\frac{\alpha\beta}{2\pi\varepsilon_0 r^3} \right)^2 + \dots \right] \mathbf{E}_{in}, \quad (2.67)$$

and likewise for the mirror dipole:

$$\mathbf{p}_m = \alpha\beta \left[1 + \frac{\alpha\beta}{2\pi\varepsilon_0 r^3} + \left(\frac{\alpha\beta}{2\pi\varepsilon_0 r^3} \right)^2 + \dots \right] \mathbf{E}_{in}. \quad (2.68)$$

The scattering from the whole system, which consists of tip and sample, is observed in the far field, i.e. at a distance which is much greater than the distance between the two dipoles r . Hence, the individual dipoles can be interpreted as a single, effective dipole \mathbf{p}_{eff} with an effective polarizability $\alpha_{\text{eff}}^{\perp}$.

$$\mathbf{p}_{\text{eff}} = \mathbf{p} + \mathbf{p}_m \quad (2.69)$$

$$= \alpha(1 + \beta) \sum_{n=0}^{\infty} \left(\frac{\alpha\beta}{2\pi\varepsilon_0 r^3} \right)^n \mathbf{E}_{in} \quad (2.70)$$

$$= \alpha_{\text{eff}}^{\perp} \mathbf{E}_{in} \quad (2.71)$$

The effective out-of-plane polarizability can be rewritten by using the geometric series and the substitution of $r = 2(z + a)$ into

$$\begin{aligned} \alpha_{\text{eff}}^{\perp}(z) &= \alpha(1 + \beta) \left(1 - \frac{\alpha\beta}{2\pi\varepsilon_0 r^3} \right)^{-1} \\ &= \alpha(1 + \beta) \left(1 - \frac{\alpha\beta}{16\pi\varepsilon_0 (z + a)^3} \right)^{-1}. \end{aligned} \quad (2.72)$$

The effective dipole generates the scattered field \mathbf{E}_{sc} which it is directly proportional to the effective polarizability:

$$\mathbf{E}_{\text{sc}} \propto \mathbf{p}_{\text{eff}} = \alpha_{\text{eff}}^{\perp} \mathbf{E}_{\text{in}}. \quad (2.73)$$

The effective polarizability strongly depends on the tip-sample distance z and the apex radius of the tip a . The near field is localized in a small area under the tip. This area, in general, has a size in the order of the tip radius, which can be as small as 10 nm. As a result, the light can be localized to a region much smaller than its wavelength [110]. Due to the localization, the field intensity in close vicinity to the tip is strongly enhanced compared to free space. Because the scattering is facilitated by the near field interaction, the scattered light mostly originates from that region.

In the same way, the above considerations can be made for in-plane polarized light, which leads to an in-plane polarization of the tip and the mirror dipole [111]. This yields a similar in-plane effective polarizability of

$$\alpha_{\text{eff}}^{\parallel}(z) = \alpha(1 - \beta) \left(1 - \frac{\alpha\beta}{32\pi\epsilon_0(z+a)^3} \right)^{-1}. \quad (2.74)$$

In general, ϵ_m , α_m and β are complex quantities, so α_{eff} is complex, too. It can be written in the form $\alpha_{\text{eff}} = se^{i\phi}$, where s is the scattering amplitude and the angle ϕ describes the phase shift of the scattered field with respect to the incident field. The above consideration makes it clear that the scattered electric field contains information about the dielectric function ϵ_m of the sample. This renders it useful as a measurement probe and is the principle behind s-SNOM.

2.3. Inelastic Scattering of Light

When light interacts with matter it can be transmitted, reflected, or absorbed, which changes its intensity and polarization state. Usually, these effects are described in the particle picture in the framework of elastic scattering of photons. In addition, inelastic scattering alters the photon energy, or the frequency of the light, due to the exchange of energy between the photon and the material. This energy can be transferred to or from the atomic lattice, but also to the magnetic moments in the system and generate or annihilate phonons or magnons, respectively. Inelastic light scattering turns out to be very helpful to study these excitations. When the excitation energy is in the range of many THz, which is the case for most phonon modes, the process is called *Raman Scattering*. Inelastic scattering off lower energy excitations, in the MHz-to-GHz range, is called *Brillouin light scattering (BLS)*. This is the energy range of interest for the detection of magnons in ferromagnetic materials.

2.3.1. Scattering Process and Energy Conservation

Inelastic light scattering off phonons can be described by the indirect coupling of the electric field of the incident light wave with the crystal lattice, which is mediated via the electrons. A theoretical treatment of the Raman scattering process was developed by Loudon [112]. He came up with a Hamiltonian consisting of two separate parts. The first part describes the interaction of the radiation with the electrons, which accounts for the absorption and the emission of photons, and the second part captures electron-lattice interaction, describing phonons. He calculates the transition probabilities in a process involving three virtual electronic interactions: (i) a photon with frequency ω_1 is absorbed, (ii) a phonon is created or annihilated and (iii) a second photon is emitted with a frequency $\omega_2 \neq \omega_1$. The phonon energy is equal to the difference of the two photon energies. This makes it possible to deduce this energy from the shift in photon energy in the Raman spectrum.

The Raman spectrum can be used to fingerprint materials by their phonon modes and to deduce the molecular or crystal structure. However, it should be noted that not all possible phonon modes can be observed. The decisive criterion for Raman active modes is that the electrical polarizability of the molecule or material changes during a period of oscillation of the phonon. A niche application of Raman scattering is the detection of THz magnons. The theory of Raman scattering off phonons can be adapted to magnons, as was done by Elliott and Loudon in 1963 [113]. In ferromagnets, magnons usually have frequencies in the GHz range. Therefore, the energy shifts which are induced upon magnon-photon interaction are too small to be detectable with Raman spectroscopy, but are instead covered by BLS spectroscopy. In antiferromagnets, however, certain magnon modes easily reach up into the THz range which brings them just in the reach of Raman spectroscopy. The theoretical description of Raman scattering later was extended by Fleury and Loudon to include antiferromagnetic magnons, as well [114]. The general rules of energy conservation apply, in the same way as for phonons, to photon-magnon scattering, which is why this technique can be also used to probe the magnon spectrum.

2.3.2. Stokes and Anti-Stokes Spectrum

A typical Raman or BLS spectrum consists of three main features. A sketch of the spectrum of the scattered light is depicted in Figure 2.12. The figure also includes a representation of the optical transitions involved in the different scattering processes. The system has an electronic ground and an excited state, denoted by G and E , respectively. These states are separated in energy by ΔE , which is the energy of the phonon or magnon excitation. In addition, there is a virtual energy level V . Elastically scattered light appears at zero frequency shift (in the center of the figure) as the so-called *Rayleigh peak*. Here, no phonons or magnons have been excited or annihilated. Positive energy shifts, by convention, denote the loss of energy compared to the incident light

due to the an excitation in the material. This is called *Stokes scattering* (right side of the figure). Negative energy shifts denote the gain of photon energy due to *anti-Stokes scattering*, which originates from the annihilation of a previously existent excitation in the sample (left side of the figure).

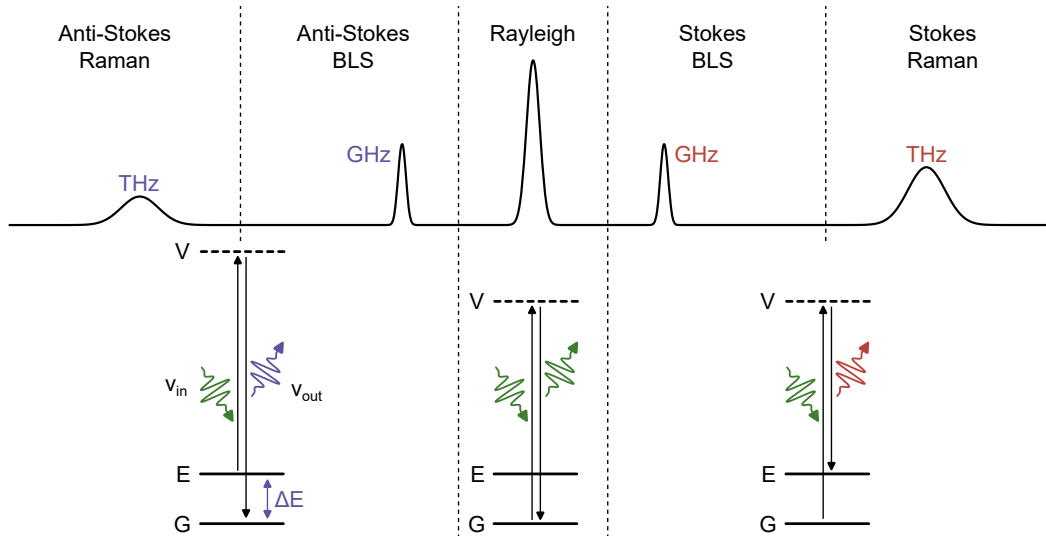


Figure 2.12. | Sketch of the spectrum of scattered light and optical transitions involved in the scattering process. Positive energy shifts of the scattered vs. the incident photon energy (blue-shifts) are captured in the anti-Stokes spectrum, while negative (red-) shifts comprise the Stokes spectrum. Small (GHz) differences in energy are measured with BLS and large shifts (THz) by means of Raman spectroscopy. In anti-Stokes scattering, the system already starts in an excited state and transitions via the virtual level V to the ground state. The difference in energy ΔE due to the annihilation of an excitation in the sample is transferred to the scattered photon. Stokes scattering describes the opposite process, where the photon loses energy and an excitation is created in the sample. Rayleigh scattering describes the elastic scattering process, where the initial and the final state are identical and the photon energy does not change.

The Stokes and anti-Stokes spectrum are usually identical in peak positions as they are predefined by the phonon or magnon dispersion of the sample. Only the magnitude can differ due to a different occupation of bands, which governs the transition probabilities. The larger the energy shift the more anti-Stokes peaks are suppressed with respect to Stokes peaks.

2.3.3. Conservation of Momentum

In a periodic crystal lattice the in-plane linear momentum is conserved (i.e. $k \parallel$ to sample surface). This has implications for both, Raman and BLS spectroscopy. When a photon is incident onto a surface from a certain angle, in general, it has a finite projection of its angular momentum onto the surface. The same is valid for a photon scattered from the surface leaving under a different angle. Conservation of linear momentum requires that the momentum of the excited phonon or magnon must equal the change in photon momentum parallel to the surface. Hence, the spectrum of excitations

is not only restricted by the photon energy, but also by the linear momentum that is provided by the incident photon, or that can be carried away by the scattered photon.

2.4. Optical Fluorescence of Defect Centers in Diamond

When it comes to circumventing the diffraction limit of optical microscopy, it is helpful to utilize a probe that already has the size in the order of just an atom. An example for this is a special type of defect in a diamond crystal, called *nitrogen-vacancy (NV) center*. Understanding the physical properties of NV centers used to be an exotic niche, which grew and, until now, was exhaustively investigated theoretically [115, 116], as well as experimentally [117–119].

2.4.1. Electronic Properties of the NV Center

An ideal diamond crystal consists only of carbon atoms, which are arranged in a face centred cubic (fcc) crystal lattice with a two-atomic basis, $(0, 0, 0)$ and $(1/4, 1/4, 1/4)$, which yields the familiar diamond structure. This is due to the fact that each carbon atom has four valence electrons and can, thus, form four bonds to neighboring atoms. In a real diamond crystal, there inevitably are defects, in the simplest case point defects. For example, a carbon atom can be substituted by a different species or be missing (vacancy). The NV center is a two-atomic defect, where one carbon atom is substituted by nitrogen, which is slightly larger and possesses five valence electrons instead of four. Additionally, a neighboring lattice site is vacant, i.e. the carbon atom is missing. This type of defect is depicted in Figure 2.13.

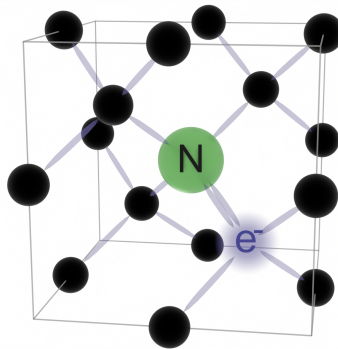


Figure 2.13. | Unit cell of a diamond which contains an NV center. It consists of carbon atoms (black) in a diamond lattice. One carbon atom is replaced by a nitrogen atom (green), which introduces an additional valence electron. A neighboring carbon atom is missing, forming a vacancy, which has captured an additional electron from the lattice (blue), creating a negatively charged NV^- center.

The NV center in total has five electrons associated with it, three from the valence electrons of the carbon atoms neighboring the vacancy and two unpaired valence electrons from the nitrogen atom. Furthermore, the NV center can catch an additional electron from the lattice which makes it a negatively charged, six-electron defect. In

a real diamond, uncharged NV^0 centers coexist with charged NV^- centers. The negatively charged NV^- center is the defect of interest here, since it possesses quite useful electronic properties. In the following those properties are examined. From now on, the term “NV center” always refers to the negatively charged nitrogen vacancy center and the “ $-$ ” sign is omitted.

It has been shown that, electronically, the NV center can be treated as if it possesses only two electrons [115]. Hence, there exist two possible configurations, a singlet configuration and a triplet configuration. When spins of the two electron are paired to yield a total angular momentum of $S = 0$, the NV is in the singlet configuration, where it can either be in the ground (1E) or in an excited singlet state (1A). Both states are split by 1.19 eV (infrared (IR) transition at 1046 nm) [120]. If both electron spins are correlated such that $S = 1$, the system is in triplet configuration, again either in a ground (3E) or an excited triplet state (3A). The transition energy between these triplet states is in the optical range (1.945 eV or 637 nm) [118]. This energy is the *zero phonon line (ZPL)*, i.e. a pure electronic transition without the involvement of lattice vibrations. There are, however, additional vibrational bands at higher energies. The levels involved in fluorescence lie well within the band gap of the diamond crystal, indicated by the sharp ZPL.

Unlike the singlet configuration, the triplet states possess a fine structure, which is described by the following ground state Hamiltonian:

$$\hat{H} = D\hat{S}_z^2 + E(\hat{S}_x^2 - \hat{S}_y^2) + \gamma\mathbf{B} \cdot \hat{\mathbf{S}}, \quad (2.75)$$

where $\hat{S}_{x,y,z}$ are the $S = 1$ spin operators and $\hat{\mathbf{S}}$ is a vector consisting of those, while \mathbf{B} is the external magnetic field. $D = 2870$ MHz [121], $E = 5$ MHz and $\gamma = g\mu_B/\hbar = 28$ GHz/T [122] are empirically determined scaling factors. The energy eigenvalues of this Hamiltonian yield the energy levels, which are shown in Figure 2.14. Most importantly, there is the so-called zero field splitting between the $|0\rangle$ state and the $|\pm 1\rangle$ states, which is caused by electron-electron interactions that are captured in the first term of the Hamiltonian. The second term leads to a small splitting between the $|\pm 1\rangle$ states. This contribution is caused by strain in the crystal lattice, which depends on the quality of the diamond. The third term captures Zeeman splitting due to the interaction of the electron spins with an external magnetic field \mathbf{B} , which shifts the $|\pm 1\rangle$ levels. The exact energy of the eigenstates depends on the angle of the external magnetic field, i.e. its projection onto the NV center’s axis. For the excited states, a very similar consideration can be made. The main difference is that the zero field splitting constant takes a smaller value of $D = 1.41$ GHz [117].

The lowest energy level of the NV center is the triplet ground state 3E , while the singlet ground state 1E is slightly elevated in energy. Due to the smaller gap, the excited singlet state is below the excited triplet state in energy. These energies have dramatic consequences and lead to the intriguing optical properties of the NV center.

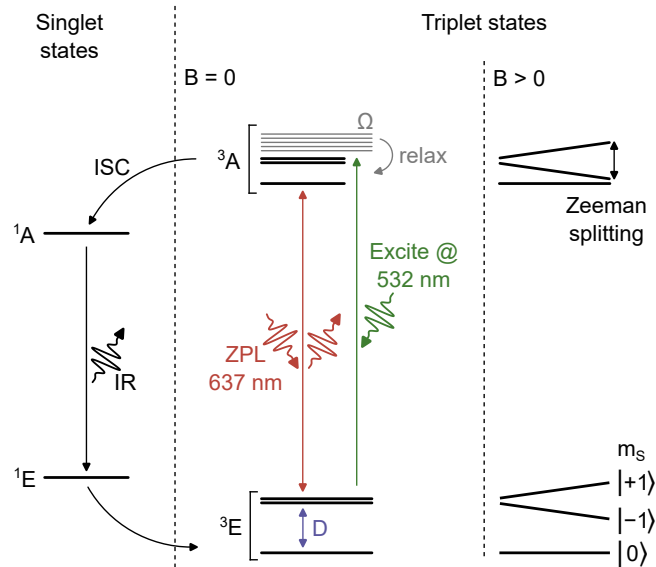


Figure 2.14. | Energy level scheme of the negatively charged NV center. **Left:** Singlet states with an IR transition between ground and excited state. **Center:** Triplet states at zero external magnetic field. Between the $|\pm 1\rangle$ states and the $|0\rangle$ state there is a splitting of energy D . The absorption of an RF photon with a matching frequency of 2.87 GHz leads to a transition between those states (electron spin resonance (ESR)). The absorption of an optical photon leads to an optical transition from the ground to the excited states. Vibrational excited states are depicted in grey (Ω). These can be reached by an optical transition at a higher energy than the ZPL. Once excited, the NV center relaxes due to the emission of phonons into the normal excited states (black). From here, an optical relaxation back into the ground states leads to the emission of fluorescence light. Alternatively, an inter system crossing (ISC) into the singlet scheme is possible, where after the IR decay another ISC leads to the $|0\rangle$ triplet ground state. **Right:** For finite magnetic fields, the triplet $|\pm 1\rangle$ states shift due to Zeeman splitting, changing the ESR frequency.

2.4.2. Optical Transitions and Mechanism of Fluorescence Contrast

The complexity of the energy levels of the NV center gives rise to a very useful property: the ability to optically polarize the NV center into a specific spin state. Essential for this is the fact that there exist two excitation and decay pathways, the IR transition in the singlet configuration and the optical fluorescence transition in the triplet configuration.

In optical transitions, certain selection rules apply. Especially, the total angular momentum is only allowed to change by $\Delta L = \pm 1$. Hence, only transitions between the ground and excited states with the same m_s quantum number are allowed in the triplet spectrum. Due to the different zero field splitting, they appear at slightly different energies, but this difference can be neglected because it is vanishingly small compared to the splitting between ground and excited state ($2.87 \text{ GHz} \cong 12 \mu\text{eV}$ as compared to 1.945 eV). The NV center can be excited with an optical laser from the ground state into the excited state and will emit red-shifted fluorescence light upon relaxation. The presence of vibrational bands at higher energies than the excited state turns out to be helpful to technically realize an NV fluorescence experiment. They

allow to optically excite the NV center at larger photon energies than the ZPL (e.g. green light at $532\text{ nm} \hat{=} 2.33\text{ eV}$). This wavelength is then easily separable from the emitted fluorescence light using a dichroic mirror. The excitation of additional phonons generally shifts the absorption spectrum to higher energies compared to the emission (fluorescence) spectrum.

In addition to optical transitions from the ground into the excited state, transitions within the fine structure of these states are possible, as well. These transitions can be excited by radio frequency (RF) photons. In the ground state, the orbital angular momentum $L = 0$. Hence, the spin quantum number m_S has to change by ± 1 to accommodate the angular momentum of the absorbed photon. In this way, switching between the $|0\rangle$ and the $|\pm 1\rangle$ states can be realized. This effect is called *electron spin resonance (ESR)* (or *electron paramagnetic resonance (EPR)*). At zero field, the ESR frequency is given by the zero field splitting $D = 2.87\text{ GHz}$ in the ground state. Due to the Zeeman interaction, the resonance frequency shifts at higher magnetic fields.

Because a two-electron system is considered, additional to the triplet states there are a singlet ground state and a corresponding singlet excited state. Those play an important role in the mechanism that is responsible for the NV center's fluorescence contrast. The excited singlet state is located lower in energy than the excited triplet states. Electron scattering processes enable the transition from the excited triplet states into the singlet system. This is called *inter system crossing (ISC)*. During this transition, the spin is not conserved. The transition probabilities depend on the spin quantum number in the triplet system and are higher for the $|\pm 1\rangle$ than for the $|0\rangle$ states. The energy gap between singlet ground and excited state is smaller than the gap in the triplet system, and lies in the IR wavelength range. The transition from the excited singlet into the ground state, thus, is IR active and, due to the absence of optical photons, sometimes called "dark transition". Furthermore, the singlet ground state is located energetically above the triplet ground state, which can be reached through another scattering event (2nd ISC). In this way, the singlet states provide an additional decay channel, alternatively to the direct fluorescent transition between the triplet states.

Due to the position in energy and the transition probabilities, the dark decay channel is most likely taken when the excited $|\pm 1\rangle$ triplet states are populated. At the end of this transition, the electrons predominantly populate the $|0\rangle$ triplet ground state. Continuous optical excitation of the NV center, thus, leads to a polarization of the NV center in exactly this $|0\rangle$ state. When the singlet relaxation path is taken, no optical fluorescence light is emitted (just an IR photon is emitted, which is not detected). Therefore this relaxation path leads to a reduction of the detected optical fluorescence. Once the NV center is fully polarized in the $|0\rangle$ state the singlet channel is less likely than the direct decay and the fluorescence intensity is maximal.

Starting from a fully populated $|0\rangle$ triplet ground state, microwave excitation with a frequency that matches the energy difference to the $|\pm 1\rangle$ states causes a transition

and therefore reduces the polarization. Upon optical excitation, this translates into the excited states, where now the IR active singlet channel again is more likely taken when the system relaxes. The result is that ESR quenches the fluorescence of the NV center. This provides the possibility to probe optically. It furthermore makes the NV center a useful sensor to probe the presence of RF fields of a certain frequency. The exact frequency to which it is sensitive depends on the relative orientation and strength of an external magnetic field, rendering the NV center a very precise and sensitive probe for magnetic fields. A spectrum of possible ESR transitions is shown in Figure 2.15. The figure displays the calculated field- and frequency range, where the NV center can be directly used as a probe. The projection of the field onto the NV center's axis is a decisive parameter, as the resonance field depends on the relative orientation of both. Furthermore, the NV center's spin can couple to the nuclear moments of the surrounding atoms which introduces an additional hyperfine splitting. This, however, is beyond what is necessary to be discussed for NV center magnetometry.

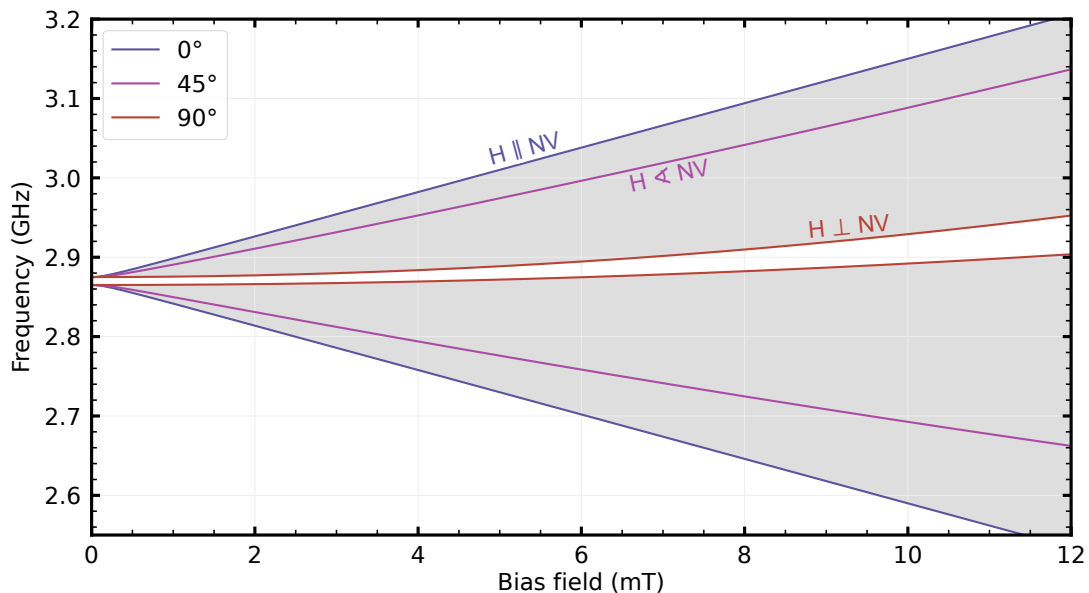


Figure 2.15. | Calculated frequencies of ESR transitions in dependence of an external magnetic bias field. The transition frequency depends on the projection of the magnetic field on the NV center's axis. The shaded region marks all possible angles between 0° and 90° .

The above described scheme just covers continuous wave (CW) excitations with RF frequencies. NV fluorescence experiments are not limited to that, as also pulsed schemes like Rabi, Ramsey, and spin-echo experiments can be performed [123–125]. Here, a first 90° RF pulse rotates the NV magnetic moments from their equilibrium direction (z) into the equatorial plane of the Bloch sphere, followed by a dephasing of the spins. A second, delayed 180° RF pulse flips all moments and lets them rephase until they align again and form a spin echo. In this way, the coherence time can be determined. It is influenced by the surrounding of the NV center and decreases if any disturbances, like magnetic noise, are present, resulting in a reduction of fluorescence intensity.

Due to their quantum mechanical nature, NV centers are a promising candidate for qubits for quantum computing [126]. They possess long coherence times, even at room temperature (in the order of milliseconds [124, 127]) and are optically addressable. The challenge in that field is to couple the qubits to each other, which is a fundamental requirement to realize quantum logic gates. A recent approach is to utilize spin waves in YIG, that couple to the NV spin via their magnetic fields to enable this inter-qubit communication to transfer entanglement [128].

Experimental Probing Methods

A wide range of experimental methods can be used to probe magnetization dynamics down to the nanoscale. These methods can be classified into non-local and local methods. Examples for non-local methods to detect magnetization dynamics are inductive ferromagnetic resonance experiments, and certain transport measurements. These methods typically average over a large probed volume, and thus provide insights into macroscopic properties of a sample. On the other hand, local methods allow for spatially resolved detection. There is a wide variety of methods which can be used to detect magnetic properties, ranging from electron microscopy (e.g. Lorentz transmission electron microscopy (TEM)) or electron emission experiments (e.g. photo-emission electron microscopy), to X-ray methods, such as X-ray magnetic circular dichroism (XMCD) or scanning transmission X-ray microscopy (STXM).

In this thesis, the focus is on optical methods. As discussed in the previous chapter, the interaction of light with a magnetic material is described by magneto-optical effects, which can be utilized for a variety of optical probing methods. Most prominently, the magneto-optical Kerr effect (MOKE) is exploited in static and dynamic Kerr-Microscopy. Another experimentally accessible channel is inelastic scattering of light. As incoming photons interact with phonons or magnons, they gain or lose energy upon scattering, which can be detected using a spectrometer. This is done in Raman scattering experiments for large energy gains or losses (10 THz to 100 THz), which usually occur due to photon-phonon interactions or high-energy magnons present in antiferromagnetic materials (0.5 THz to 10 THz). In ferromagnets, magnons possess even smaller excitation energies. This regime is accessible via Brillouin light scattering (BLS), which can resolve shifts in photon energy on the order of 100 MHz up to a few GHz.

Any local probing method has a certain limit of spatial resolution. This is due to the nature of the particles which are used as a probe, i.e. the wavelength of the corresponding wave, and the geometric constraints due to the numerical aperture (NA) of the focusing elements in the setup. For optical photons, the wavelength is on the order of 500 nm. The NA of an optical microscope can easily reach 0.9 and even beyond, if immersion lenses are used. In most practical cases, this leads to a spatial resolution on the order of 250 nm. While for X-rays, the wavelength can be as low as 1 nm, X-ray methods often suffer from a low NA due to the lack of materials with sufficiently high refractive index, which can be used to fabricate high-NA lenses and mirrors. This leads to a practical resolution limit on the order of 10 nm. Other methods which use electrons or even neutrons have an equivalent de Broglie wavelength, which, depending

on the acceleration energy, can be as small as 0.1 \AA . This is a direct consequence of the quantum-mechanical particle-wave duality [129]. As discussed in a previous section, the Rayleigh criterion links the wavelength of the probing particles to the smallest features that can be resolved. In this regard, one may conclude that methods which involve optical wavelengths are fundamentally inferior to X-ray or electron methods. However, optical methods are often preferable, since they allow for easy implementation in a tabletop setup without the need for expensive electron microscopes or even a synchrotron light source for the generation of brilliant X-ray radiation.

The aim of this thesis is to shine a spotlight on optical methods which circumvent the resolution limit, and allow for a spatial resolution potentially orders of magnitude beyond the optical diffraction limit. The last section of this chapter will introduce mainly two methods able to achieve this, with a specific focus on probing magnetization. The first method is NV center magnetometry, which utilizes point defects in diamond crystals as quantum sensors, which are extremely sensitive to local magnetic stray fields. The quantum state of these probes can be detected optically with high sensitivity. Secondly, scattering scanning optical near field microscopy (s-SNOM) is a method which uses a microscopic metal tip acting as an antenna to focus light down to a spot with a size of up to two orders of magnitude below the actual diffraction limit. To probe magnetic properties of a sample, this method can be combined with the detection of inelastically scattered light by means of BLS. An alternative approach is to combine s-SNOM with an indirect electrical detection using transport measurements, i.e. via the anomalous Nernst effect (ANE).

3.1. Non-Local Methods

3.1.1. Inductive FMR

In inductive FMR experiments, a (ferro-) magnetic sample is subjected to an RF magnetic field aligned perpendicular to the magnetization of the sample. The field exerts a torque on the magnetization and continuously excites the precessional motion. When the resonance condition is met, the precession of the magnetization is excited most effectively and energy of the microwave field is most efficiently transferred to the magnetic system. This leads to an increased RF absorption. Usually, the absorption signal is monitored as a function of external magnetic bias field at a fixed excitation frequency. In order to sweep the magnetic field, an electromagnet is used. The magnetic field tunes the magnetic stiffness of the material and thus shifts the FMR frequency. It also determines the magnetization direction, which for thin films can be set either in the plane of the film along certain crystal directions, or out-of-plane. By measuring in different geometries and at different orientations of the external field, the anisotropy energy landscape can be determined. Examining the line shape of the ferromagnetic resonance curves as a function of excitation frequency provides access to the Gilbert

damping parameter of the material, as it corresponds to the dissipated energy during the precessional motion.

There are two common methods to apply RF fields to a sample. Microwave cavities can be used to provide a uniform excitation field at certain fixed frequencies. The usually high Q-factors of cavities render them suitable for narrow-band FMR experiments. For broad band FMR, the sample can either be placed on top of a printed circuit board with a broad band waveguide, or a co-planar waveguide (CPW) can be directly structured onto the sample. Such waveguides allow to vary the excitation frequency in a much broader range compared to a cavity, which is designed for a specific frequency. The microwave losses can be measured either by monitoring the reflected power from the cavity or the transmitted power through the waveguide. As detector, a Schottky diode can be used to convert the RF power into a rectified voltage.

The magnetic system may be modeled as a damped harmonic oscillator. Its equation of motion can be solved, leading a Lorentzian behavior for the absorbed power with respect to the magnetic stiffness of the system, i.e. the external magnetic field H . The situation is more complicated when the RF system itself has resonances, which introduce phase shifts and lead to mixing of the real and imaginary parts of the signal. This mixing can be represented as a mixing angle ϵ . A typical function for the absorption A , dependent on the external field H , has the form of

$$A(H) \sim \cos \epsilon \chi'' + \sin \epsilon \chi' \sim \frac{\Delta H \cos \epsilon + (H - H_{\text{FMR}}) \sin \epsilon}{\Delta H^2 + (H - H_{\text{FMR}})^2}. \quad (3.1)$$

It contains both, the real and the imaginary part of the magnetic susceptibility $\chi = \chi' + i\chi''$. ΔH is the half width at half maximum (HWHM) of the resonance line, H_{FMR} is the resonance field.

To improve the signal to noise ratio, a small modulation, e.g. of the magnetic field, can be applied, which enables lock-in amplification of the signals. In case of a lock-in measurement with field modulation, the measured line shape takes the form of the derivative of A with respect to the field H . Fitting this function to the measured absorption spectra for different measurement geometries allows to determine the resonance line width and position.

$$\frac{d}{dH} A \sim \frac{\Delta H^2 - (H - H_{\text{FMR}})^2}{(\Delta H^2 + (H - H_{\text{FMR}})^2)^2} \sin \epsilon - \frac{2(H - H_{\text{FMR}})\Delta H}{(\Delta H^2 + (H - H_{\text{FMR}})^2)^2} \cos \epsilon \quad (3.2)$$

Inductive FMR experiments have the advantage of achieving a high sensitivity with a rather simple setup. However, the obtained parameters are always an average over a large volume or even the whole sample. This non-local method therefore is less suitable for small structures or inhomogeneous materials. Inhomogeneous properties, for example, lead to a broadening of the observed absorption lines, simply due to different FMR conditions across the sample. If the different inhomogeneous contributions also depend on the excitation frequency, they can easily be misinterpreted as a large Gilbert

damping. That said, it is still possible to engineer microscopic waveguides in order to restrict the RF excitation to a small volume. Local, spatially resolved methods can help to avoid the need for nano-scale structuring of waveguides on a sample and to probe the influence of inhomogeneities.

3.1.2. Transport Measurements

A second class of typically non-local methods, which can be used to investigate magnetic properties of a sample, are transport-based methods. Different effects can be exploited, for example the different varieties of Hall effects, magneto-resistive effects, Seebeck effects or Nernst effects.

A commonly used geometry in transport devices is the so-called Hall-bar. It consists of a structured main wire, which is contacted at different positions along its length, allowing to apply currents or to measure voltages at different positions and angles. Using contact pads, it can be electrically contacted, either by tips or by wire bonding. The Hall-bar provides a defined area for the measurement. Usually, more than two connections are made. Even if only a voltage drop is to be measured, a 4-contact measurement allows to correct for the resistance of the contacts and wires themselves and to retrieve the actual signal from the sample. A simpler, alternative approach is to contact an unstructured thin film sample at different positions using electric tips. In this way, a voltage can be applied or picked up between the tips to analyze the response of the sample to different external stimuli, such as magnetic fields or temperature gradients.

The conceptual simplicity is an advantage of transport techniques. Nevertheless, there are certain drawbacks, too. For once, the device under test needs to allow for transport measurements, i.e. it needs to be conducting. A second and the most crucial limitation is the actual spatial resolution. In many cases, devices can be fabricated with nanoscale dimensions, which makes it possible to localize features on small length scales. For example, magnetic domain walls in nanoscopic magnetic racetrack wires have been measured with a resolution of better than 40 nm by using electrical read out via the AHE [130]. None of these studies, despite the small probed volumes, represent real, spatially resolved measurements. No matter how the connections to the sample are made, the entire region in between contributes to the received signal. True spatially resolved imaging of extended devices is hardly possible with such techniques.

Inductive FMR and transport measurements are just two examples for non-local measurement techniques. They, for sure, are very useful and widely applied, but lack the ability to really map extended areas of a sample and to investigate spatially inhomogeneous properties. Nevertheless the ANE is used in this thesis in combination with optical near field microscopy to circumvent this limitation and make it possible to reach a spatial resolution of below 100 nm. This is further evaluated in Appendix A.

3.2. Diffraction-Limited Optical Methods

This section will cover optical methods which allow for spatially resolved measurements, but are limited in spatial resolution by the optical diffraction limit. The emphasis, again, is on investigating magnetic properties of materials and devices.

3.2.1. Wide-Field Kerr Microscopy

The basis for Kerr microscopy is the magneto-optical Kerr effect, which was introduced in Section 2.1.4. Kerr microscopy is a special type of polarization microscopy, where a sample is illuminated with polarized light and the polarization state of the collected light is analyzed. The general setup is as follows. Incoherent light, usually from an light emitting diode (LED), is linearly polarized using a polarizer and coupled into a wide-field microscope. In the microscope the light is focused using an objective lens on the sample. The reflected light is collected again using the same lens and imaged on a camera. In front of the camera, a quarter wave plate and a second polarizer (called analyzer) are mounted. Due to the MOKE, the polarization of the light changes upon reflection. This can be in the form of a rotation of the polarization direction or an induced ellipticity. The quarter wave plate can be used optimize the contrast for either polarization rotation or ellipticity. The polarizer is set to an angle where contrast between different magnetization directions is optimal. In this way, Kerr microscopy enables to image the domain state of a sample.

To manipulate the domain state and obtain measurements such as hysteresis loops, usually an electromagnet is used to provide adjustable in-plane or out-of-plane magnetic fields. In Section 2.1.4, different MOKE geometries were introduced. The geometry determines in which direction a magnetic field has to be applied in order to achieve contrast with regard to a certain magnetization direction. In addition, the angle under which the light illuminates the sample needs to be set accordingly in order to provide a preferential range of wave vectors to achieve MOKE contrast. Therefore, the objective lens is not illuminated evenly, but only partially, i.e. one half of it. This comes at the expense of spatial resolution.

By combining measurements with all three geometries, all components of the magnetization vector can be obtained. Yet, there is the issue that, due to the finite incidence and reflection angles of the light, always a mix of the different magnetization components contributes to the Kerr signal, which complicates the interpretation. A solution for this is to alternate the illumination direction, i.e. take one image by illuminating one half of the objective and a second image illuminating the other half. In this way, the sign of the contribution of some components to the signal changes, while for others it stays the same. Taking the difference of both images allows to recover the pure magnetization components.

Wide-field Kerr microscopy enables to image a whole area of the sample at a time. Its limits are the slightly decreased spatial resolution due to the illumination geometry,

as well as the rather slow camera (milliseconds integration time), which restricts the method to imaging of the (quasi-) static magnetization patterns.

3.2.2. Static Kerr Microscopy

Instead of employing a camera in wide-field microscopy, also a scanning approach is possible. The illumination of the sample is usually done by a laser, while for detection the camera is replaced by a point detector. In this way, only a single point of the sample is imaged on the detector and probed at a time. This is especially useful for measuring hysteresis loops of a homogeneous sample with high sensitivity and when spatial mapping is not required. To obtain an image, the sample has to be scanned under the microscope, which is much slower compared to wide-field Kerr microscopy. On the other hand, the scanning approach has the advantage that it allows for certain modulation/demodulation techniques, which can improve signal-to-noise ratio (SNR).

3.2.3. Time-Resolved MOKE Microscopy

For dynamic measurements, the detection scheme can be improved by using a balanced photodetector consisting of two photodiodes tied back-to-back, instead of a single one. The analyzer is replaced with a Wollaston prism (WP), that splits the light into two perpendicular polarized components, which are detected by either one of the photodiodes. The measured signal, hence, is the difference voltage between the two diodes. The undisturbed polarization is oriented in a 45° angle to the prism, resulting in equal amounts of light reaching both detectors and a difference signal of zero. Rotation of the polarization due to MOKE results in a proportional imbalance. This scheme greatly improves the sensitivity of the setup and can help to reduce artifacts in the signal.

To investigate magnetization dynamics, time-resolved MOKE (TR-MOKE) can be employed [131]. TR-MOKE usually involves pulsed light sources in a pump-probe scheme. In such an experiment, two pulses with variable time delay are directed on a sample. The first pulse, the pump pulse, manipulates the magnetization state of the sample. The second pulse, the probe pulse, is influenced by the interaction with the sample, directed on a detector and analyzed in terms of its polarization state. By changing the time delay between both pulses, the time evolution of the magnetic system after the excitation can be recovered over a typical time scale of a few picoseconds to nanoseconds. The time resolution achievable with this method depends on the pulse width of the laser sources, which can be as low as a few femtoseconds. Because of that, TR-MOKE can be used to investigate ultrafast dynamics of magnetic systems [132], ultrafast demagnetization [133] or ultrafast magnetization reversal [134, 135].

Alternatively to pumping the system with a pump laser, the magnetization can be excited by means of (CW-) microwave radiation, for example via a waveguide or antenna structures on the sample. The RF excitation needs to be synchronized with the laser pulses that probe the magnetization. The phase difference between the excitation and

the probe pulses can then be varied to obtain the time-dependent dynamics. Unlike inductive FMR, TR-MOKE can do so in a spatially resolved manner. This is especially useful to map spatially inhomogeneous samples [131]. In this way, different magnetic excitation modes, like the uniform (FMR-) mode, or other non-uniform propagating spin wave modes can be investigated [136]. Even element specificity is possible by tuning the laser wavelength to achieve maximal contrast in the MOKE signal of the different elements involved [137, 138].

To increase SNR, lock-in techniques are utilized, where either the microwaves are modulated (e.g. amplitude- or frequency-modulation) or the external bias field is varied. To obtain FMR-like traces, either the external field or the microwave frequency are swept, while the other one is kept constant.

3.2.4. Super-Nyquist-Sampling MOKE Microscopy

The technique of super-Nyquist-sampling MOKE (SNS-MOKE) microscopy, which was developed by Dreyer *et al.* [76, 139], is very related to TR-MOKE. During the measurement, the magnetization in the sample is continuously excited with an RF field and sampled with ultrafast laser pulses. As for TR-MOKE, the rotation of the laser polarization due to MOKE is measured. In contrast to TR-MOKE, SNS-MOKE does not use individual laser pulses for sampling, but a series of pulses that sample the dynamics. The repetition rate of the laser pulses is much slower than the sampled frequencies of the magnetization dynamics, meaning that SNS-MOKE operates in a regime of strong undersampling. Therefore the laser pulses sample the magnetization at different times/phases throughout the precession cycle. Crucially for this technique, the sampling is synchronized with the excitation field to generate repeating signals.

In ferromagnets the dynamics typically takes place at frequencies in the GHz range (in antiferromagnets even THz). To directly sample this dynamics, any detector would need to have a sufficient bandwidth. This is a technical challenge, since typical photodetectors have bandwidths only in the MHz range. Some advanced models reach into the low-GHz range but have the significant drawback of high detection noise, which scales proportional to the bandwidth. SNS-MOKE utilizes frequency mixing to circumvent this technical limitation.

Instead of sampling the dynamics in the time domain, SNS-MOKE works in the frequency domain. In Fourier space, the probing laser resembles a frequency comb. The comb lines are spaced apart by the frequency corresponding to the repetition rate of the laser ω_r , as depicted in Figure 3.1, green lines. The magnetization is excited with a frequency ω_{ex} and, in the simplest case, precesses with a single frequency ω_{sw} . The light reflected from the sample is modulated by both, the intensity modulation of the incoming laser pulses ($n \cdot \omega_r$), as well as the modulation of the light polarization due to the Kerr effect in the sample (ω_{sw}). When passing the analyzer, the modulated polarization is converted into an intensity modulation, as well. The light reaching the

detector is intensity-modulated with both frequencies, which mix. This mixing product contains not only the two base frequencies, but also mixing components (*alias frequencies*). One of which oscillates with the sum and the other one with the difference of both modulation frequencies. In the SNS-MOKE scheme, the difference frequency ω_a is the important figure. When both input frequencies are close, the difference approaches zero. It now comes into play that one of the two modulation frequencies is not a single frequency, but a frequency comb, which has a comb line in the vicinity of the actual precession frequency of the magnetization. The difference between the precession frequency and the frequency of the closest comb line ends up between zero and, at maximum, half of the repetition frequency of the laser, which in the setup used amounts to 40 MHz (grey area in Figure 3.1). This range is called *first Nyquist zone*. Technically, SNS-MOKE represents a case of strong under-sampling. It can be understood analogous to a low-frame rate movie of a driving car, where the wheels seem to turn much slower than they actually do, stand still, or even rotate backwards, dependent on the difference between the sampling rate of the camera and the angular velocity of the wheels.

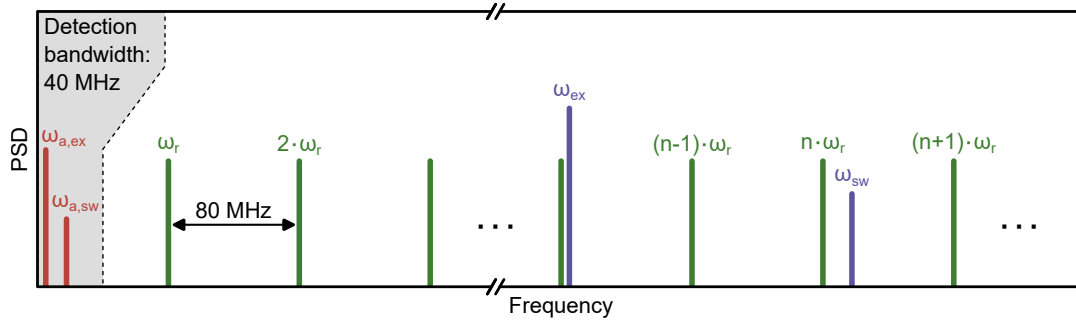


Figure 3.1. | Alias frequency generation in SNS-MOKE. The fs-laser generates a frequency comb, whose lines are spaced by the laser repetition frequency $\omega_r = 80$ MHz (green lines). On the sample, spin waves with GHz frequencies are excited (ω_{ex} and ω_{sw} , blue lines) and mix with the comb lines. The optical MOKE signal contains different mixing components, including the difference frequency between the closest comb line and the spin wave frequency (red lines). This mixing signal lies in a frequency range of half of the comb line spacing (40 MHz) and therefore inside the detection bandwidth (grey shaded area). Figure adapted from [76].

The mixing technique strongly reduces the detection bandwidth necessary to detect the GHz frequencies down to the frequency corresponding to half of the laser repetition rate (e.g. 80 MHz). To recover the actual signal, a lock-in demodulation at the mixing frequency is performed. As long as the mixing frequency is precisely calculated, it is possible to sample and demodulate any spin wave frequency of choice, independently of the excitation frequency (compare $\omega_{a,ex}$ and $\omega_{a,sw}$). Modern digital lock-in amplifiers even allow to demodulate at different harmonics simultaneously, so a number of different spin wave modes can be investigated at the same time.

SNS-MOKE fundamentally requires a high frequency stability of the components of the setup. It is crucial that laser repetition rate, the RF generator, and the lock-in am-

plifier are synchronized to the same frequency standard to prevent the resulting mixing frequency from drifting and fluctuating uncontrollably. Furthermore, SNS-MOKE relies on the repeatability of the process under investigation. SNS-MOKE can only detect repeating and therefore coherent precession of the magnetization.

The SNS-MOKE technique has proven to be a valuable tool to investigate a variety of materials and effects, for example the propagation of spin waves in YIG thin films [139], or to explore the generation of nonlinear spin waves in NiFe microstructures [77]. The technique can also be used to investigate magnonic device structures, for example a Fabry Pérot-based spin wave filter [95]. Most relevant for this thesis, SNS-MOKE allows to investigate the generation of a magnonic frequency comb in NiFe thin films [30].

In the following section, a description of the SNS-MOKE setup that was used in this thesis is provided. A sketch of the optical setup is shown in Figure 3.2. The setup consists of a custom wide-field microscope into which the probing laser is coupled. In general, the geometry of the microscope corresponds to the polar MOKE geometry, meaning that the setup measures the dynamic out-of-plane component of the magnetization. The laser is a pulsed solid state laser (*Onefive Origami*) with a wavelength of

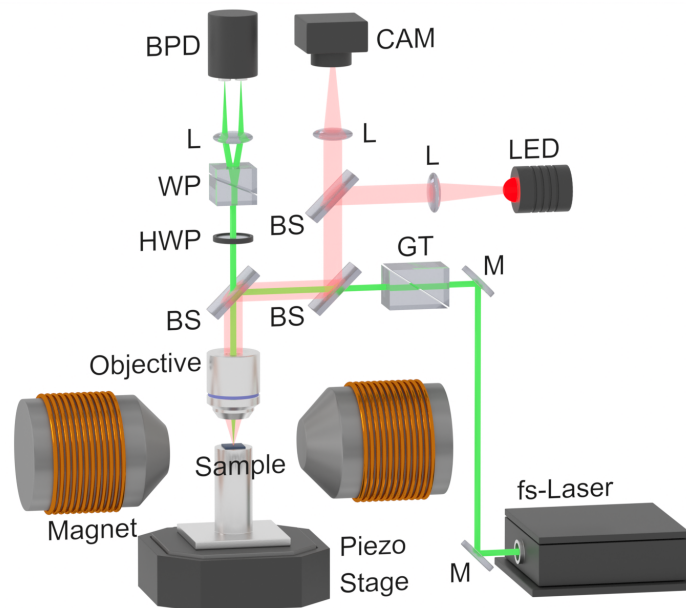


Figure 3.2. | Sketch of the optical path of the SNS-MOKE setup. The light from a femtosecond-laser is polarized by a Glan-Thompson polarizer (GT), reflected from a beamsplitter (BS) and focused on a sample through an objective lens. The lens collects the reflected light and collimates it. The collimated light transmits through the beamsplitter, followed by a half wave plate (HWP) and is split into two cross-polarized beams by means of a Wollaston prism (WP). The two beams are focused on two photodiodes of the balanced photodetector (BPD). The HWP is used to match the intensity of both beams, such that the detector can operate most efficiently. A secondary beam path with a red LED and a camera is used to observe the sample during measurements. The sample is mounted on an RF-capable sample holder and can be scanned under the objective lens by a piezo stage. An electromagnet can be used to generate static magnetic bias fields during the measurements.

515 nm, a pulse width of <200 fs and a repetition rate of 80 MHz. The repetition rate of this laser is stabilized and locked to an external time base. To position the sample, the setup has a built-in wide-field microscope using a red LED and a camera. The sample is placed under the objective lens ($NA = 0.7$) of the microscope on a piezo stage, which can be scanned to perform spatially resolved measurements with diffraction-limited resolution. The reflected probe light is detected by splitting it into two orthogonally polarized components using a Wollaston prism (WP). The two components are detected by a custom balanced photodetector with a bandwidth of 40 MHz. A half wave plate positioned prior to the WP is used to rotate the polarization such that the difference signal of the detector is close to zero, to ensure maximum dynamic range. The signal is demodulated by a digital lock-in amplifier (*Zurich Instruments HF2LI*) capable of demodulating up to six channels simultaneously at arbitrary frequencies, which allows to measure signals at different frequencies and phases at the same time.

On the RF side, a signal generator (*Agilent MXG N5183A*) generates frequencies of up to 10 GHz, again, synchronized with the external time base. The generated RF signal is amplified and applied to the sample, which typically consists of a patterned, impedance-matched RF CPW, that provides the RF driving field for the excitation of the magnetization. In addition to the RF excitation field, a static magnetic bias field of up to 250 mT can be applied in-plane via a rotatable electromagnet. Lock-In amplifier, microwave generator and the pulsed laser use the same time base, which is provided by a Rubidium clock, that generates a 10 MHz reference signal. The peripherals lock their internal oscillators to this time base with a phase-locked loop (PLL). A schematic of the wiring of the setup is provided in Figure 3.3.

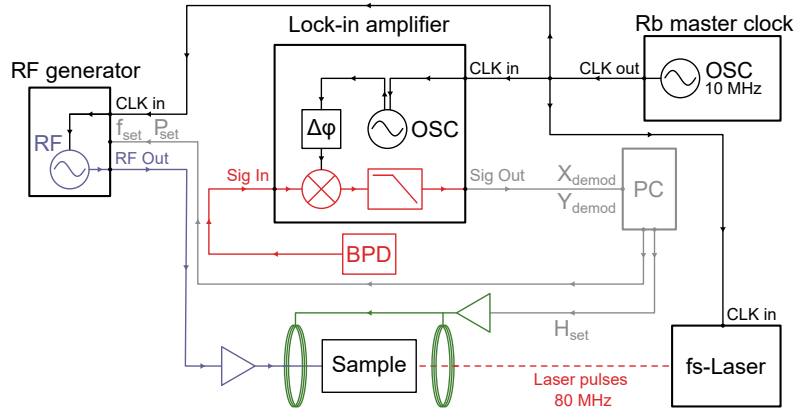


Figure 3.3. | Wiring schematics of the SNS-MOKE setup. Blue lines indicate RF connections, green lines are voltages related to magnetic field generation, black lines are for clock signals, red indicates the detected signal and grey lines represent communication connections with the control PC. The dashed line symbolizes the laser pulses. A central master clock synchronizes RF generator, lock-in amplifier (LIA), and the repetition rate of the laser. The LIA calculates the alias frequency and demodulates the MOKE-signal from the BPD.

3.2.5. Inelastic Light Scattering

Two common methods which are based on inelastic light scattering are Raman and BLS spectroscopy. In both techniques, the sample is illuminated with narrow-band light of a certain frequency. The scattered light is collected and analyzed in a spectrometer to obtain a spectrum of energy shifts that occur due to inelastic scattering. Contrary to elastic light scattering, inelastic scattering relies on the photons to interact with excitation modes in a sample and can thus be used to probe these excitations. Conceptually, Raman scattering and BLS originate from the same physical process, which is described in Section 2.3.

Raman scattering usually deals with shifts in photon energy which correspond to frequencies of 10 THz to 100 THz. Hence, it is a common mean to probe the presence of phononic excitations in a sample. BLS covers smaller shifts between a few MHz up to THz. There is an overlap between both methods in the low-THz range. BLS has proven to be useful, not only for investigating phonons, but also for studying magnetic excitations in the frequency range below 1 THz. BLS spectroscopy can be used to probe coherent linear [38] or nonlinear magnons [140–142], and even (incoherent) thermal magnons [143, 144]. Furthermore, modified BLS techniques can achieve time- or phase-resolution [31]. Sensitivity to incoherent magnons is an advantage of BLS over the SNS-MOKE technique.

A major technical challenge in both, Raman and BLS spectroscopy is the suppression of elastically scattered light (Rayleigh peak), which usually is stronger than the inelastically scattered light by many orders of magnitude. This poses technical challenges for the detection. In addition to that, BLS requires a high-resolution spectrometer to detect the scattered light. To achieve MHz energy resolution at the same time as a high Rayleigh suppression, many BLS spectroscopy setups use a tandem Fabry-Pérot design for the spectrometer, which was developed by Sandercock *et al.* [145–147].

The conservation of in-plane linear momentum during the scattering process leads to two approaches that can be taken for experiments. The first approach is *micro-focused BLS*, where laser light is focused on the sample using a high-NA objective lens. As a consequence, a range of photon incidence angles is provided and collected, at the same time. The different incidence and scattering angles of the photons translate into a range of in-plane projections of the momentum of the photons, restricting the possible excitations. In this way, all changes in Δk from 0 to $\Delta k_{\parallel, max}$ are allowed and the corresponding magnons and phonons can be excited and detected. A photon with the wavelength λ has a momentum of

$$p = \hbar k = \frac{h}{\lambda}. \quad (3.3)$$

The maximal allowed in-plane projection due to the available photon momentum and

the NA of the objective lens amounts to

$$\Delta k_{\parallel, max} = \frac{2NA}{n} k = \frac{2NA}{n} \frac{2\pi}{\lambda}. \quad (3.4)$$

As an example, for light with a commonly used wavelength of 532 nm and an objective lens with NA = 0.9 surrounded by air, this yields a maximal transferable linear momentum of $\approx 21.3 \mu\text{m}^{-1}$. This limits the spatial resolution of the technique and corresponds to a smallest detectable wavelength for spin waves of 295 nm. A second, alternative approach is to shine collimated light under a fixed angle and detect light scattered into a fixed angle. In this way, the wave vector of the excitations can be studied at the expense of losing spatial resolution. This technique is called *k-resolved BLS*. It allows to map the dispersion of an excitation mode.

When investigating magnons, the conservation of angular momentum has the result that the incident and scattered photon have opposite helicities. Technically, this allows to separate incoming and scattered light with high efficiency by using a polarizing beamsplitter. This also suppresses the elastically scattered light, since its polarization remains unchanged. Even more importantly, it provides a way to separate magnonic from most phononic contributions to the spectrum, which in most cases do not carry angular momentum and therefore do not change the helicity of the light.

3.3. Probing Beyond the Diffraction Limit

The diffraction limit is a fundamental obstacle for conventional optical microscopy as it dictates the minimal detectable feature size (or maximal detectable wave vectors). It is highly desirable to overcome this limit to enable the detection of smaller-sized features, i.e. spin waves with larger wave vectors. The following sections cover different approaches which have in common that they use nanometer-sized probes. The first two of the presented methods rely on the fluorescence of the NV centers in diamond which can be used in a confocal microscope as well as in a scanning probe scheme. The third method utilizes the optical near field. Here, the sample is illuminated with a laser beam which is confined to a nanometer-sized volume by means of a metallic atomic force microscopy (AFM) tip. This nano-focusing strongly enhances light-matter interaction and enables for different effects to be exploited, such as elastic light scattering, near field heating and inelastic light scattering. These different approaches will be discussed later in this section and in Chapter 7.

3.3.1. NV Center Magnetometry

In general, any probe is sensitive to variations of the detected quantity, e.g. the magnetization or the magnetic field, which occur at least on the length scale of its own size. An NV center is an atomically small defect, and therefore sensitive to wave vectors much smaller than the optical diffraction-limit. In that sense, all measurement

schemes which utilize NV centers can be classified as going beyond the diffraction limit. However, this does not necessarily mean that they also allow to detect those variations in a spatially-resolved manner with a great spatial resolution.

To utilize NV centers in a measurement apparatus, different schemes have been developed, which allow for a wide variety of experiments [148]. A simple way is to fabricate a sample on a diamond substrate which contains NV centers [149] or to disperse nanodiamonds containing NV centers on a sample [150, 151]. More advanced is the use of a micromanipulator to place a single-crystal diamond slab with NV centers on the sample. The most sophisticated way is to fabricate an AFM tip from diamond and implant a single NV center close to the tip apex [36]. Scanning this tip across the sample promises AFM-like nanometer spatial resolution, while the other techniques only allow for measurements at the positions where the NV centers happen to be.

Scanning an NV center across a sample can be used to map ferromagnetic domains [152, 153], inhomogeneous magnetic textures, like skyrmions [154], and even antiferromagnetic textures due to minute stray fields [155] or magnetic noise originating from antiferromagnetic domain walls [156, 157]. Scanning NV magnetometry in many regards surpasses magnetic force microscopy (MFM) because of its higher sensitivity, resolution and nearly no influence on the magnetic state of the sample, due to the negligibly small stray field from the NV center compared to the MFM tip. It is also well compatible with cryogenic temperatures [158].

NV center magnetometry has developed into a versatile method to probe magnetization [159] with high sensitivity [160–162] and nanometer resolution [163]. It is even possible to reconstruct the three-dimensional magnetization vector [164] from NV center magnetometry measurements. The strong response of NV centers to dynamical fields makes them a useful probe to study FMR [150, 151, 165, 166], as well as linear [167] and nonlinear spin waves in thin films [168, 169], magnetic wires [170], or small magnetic discs [149]. Recently, it has been demonstrated that using spin wave mixing, it is possible to probe the whole frequency band from direct current (DC) up to several GHz [171]. The unique properties of NV centers, i.e. high sensitivity, stability under ambient conditions and destruction free optical read out, have lead to applications not just in physics and materials science, but also in biology [35, 172]. Besides measuring magnetic fields, NV centers can be used to sense electric fields [173] or as high precision nano-thermometers [174–176].

3.3.2. Confocal NV Center Magnetometry

The confocal NV center magnetometry setup used in this thesis is based on a home-built confocal microscope. A green 532 nm CW diode laser is coupled into the microscope via a dichroic beamsplitter and focused on the sample with an objective lens ($NA = 0.7$). The red fluorescence light (600 nm to 800 nm), which is emitted by the NV centers, is collected by the same objective. It passes the dichroic beamsplitter and subsequent

optical filters, which remove remaining components of reflected green light, before it is focused on a photodetector. Additionally, the light from a blue LED is coupled into the microscope, focused on the sample and detected with a camera, to obtain a wide-field image of the sample and to allow to position it under the microscope. The sample is mounted on a piezo stage to be able to scan it under the microscope objective and to perform spatially resolved measurements. A sketch of the optical path of the setup is provided in Figure 3.4.

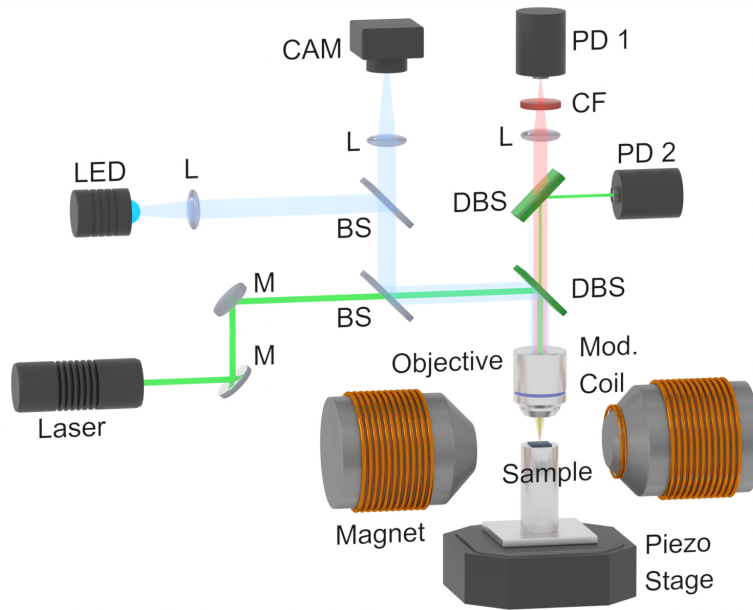


Figure 3.4. | Optical path of the confocal NV center magnetometry setup. A green laser is focused on the sample through an objective lens to excite the NV centers. The red fluorescence light emitted by the NV centers is collected and split from the reflected green light by a dichroic beamsplitter (DBS). A second DBS reflects most of the remaining green light on a second photodiode (PD 2), which is used to measure the topography of the sample in a scanning scheme. The fluorescence light is focused on a sensitive photodiode (PD 1) using a lens, for detecting the fluorescence intensity. An absorptive red color filter (CF) prevents the still remaining green light from reaching the detector. The setup includes a wide-field microscope with a blue LED and a camera to obtain an image of the sample. The sample is mounted on a custom-made sample holder which is located on a piezo stage in between the pole pieces of an electromagnet.

A typical sample, similar to the samples used in SNS-MOKE measurements, consists of a CPW to generate the RF driving field that excites the magnetization in the magnetic structures. These structures can be fabricated either on top of the waveguide or next to it. The CPW is connected to a signal generator (*Agilent MXG N5183A* or *Rhode & Schwarz SMB 100A*), which generates the RF current with frequencies of up to 12.5 GHz. The RF signal can be amplified to up to 30 dBm.

In frequency-swept measurements one encounters the issue that the RF power at the sample varies with frequency. Even if the RF generator had a calibrated output power and the amplifier a flat frequency characteristics, there will be back reflections from the connections to the sample (bonding wires) due to an inevitable slight impedance

mismatch. This leads to the formation of standing waves inside the RF cable. In addition, frequency-dependent losses in the substrate or resonances inside the CPW may influence the actual power at the magnetic structure. To compensate for this, the RF power transmitted through the sample is measured and the generator output level corrected accordingly. This ensures a flat frequency characteristics of the excitation throughout the whole frequency range. The wiring schematics of the setup are displayed in Figure 3.5.

The microscope is equipped with an electromagnet capable of generating an in-plane magnetic field of up to 150 mT. An additional small modulation coil allows to apply field modulation (HM), which enables the demodulation of the signal using a lock-in amplifier (*Zurich Instruments HF2LI*). Alternatively to the modulation of the bias field, amplitude modulation (AM) or frequency modulation (FM) of the microwaves can be used.

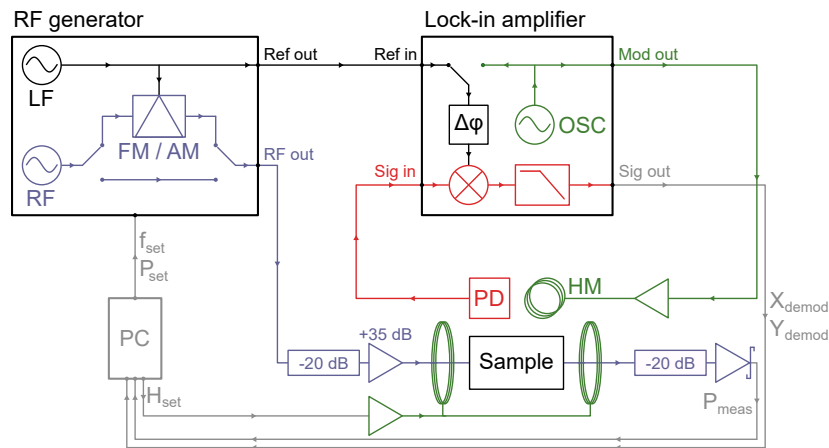


Figure 3.5. | Wiring schematics of the confocal NV center magnetometry setup. Blue lines indicate RF connections, green lines are voltages related to magnetic field generation, black lines are for reference signals, red indicates the detected signal and grey lines represent communication connections with the control PC. The RF generator has a built-in option for FM or AM of the microwaves. Alternatively, the LIA can generate a reference voltage using its internal oscillator, which is amplified and send to a small additional coil for HM.

3.3.3. Atomic Force Microscopy

A method which needs to be discussed at this point is atomic force microscopy (AFM) as it is the basis for the two optical scanning probe techniques which are described in the following two sections, scanning NV center microscopy and s-SNOM. Both rely on different kinds of cantilevers as probes and use an AFM to control the cantilever position and distance to the sample.

AFM relies on the mechanical interaction of a cantilever with the sample, as shown schematically in Figure 3.6 A. The cantilever is usually etched from silicon and has a nano-scale tip, which is brought close to the surface of a sample. When the distance is

in the range of a few 100 nm, an attractive force between the tip and the sample can be observed, which is due to van der Waals interaction. At distances below the 10 nm, repulsion between tip and sample sets in and becomes dominant below 0.1 nm. The interplay of these forces gives rise to different distance-dependent regimes of attraction or repulsion, see Figure 3.6 B. The aim of the technique is to keep the force acting on the cantilever constant and, by doing so, to detect and follow the topography of the sample while scanning it under the cantilever. Lateral scanning and height correction is done via a 3-axis piezo stage.

To detect the force that acts on the cantilever, its bend can be measured. This is done with the help of a laser beam, which reflects off the back of the cantilever and is detected on a segmented photodiode (BPD). The laser beam is aligned such that, in the default case without any additional forces acting on the cantilever, both segments of the BPD are illuminated equally. A bend of the cantilever causes the laser spot on the detector to shift, resulting in a non-zero difference signal of both segments.

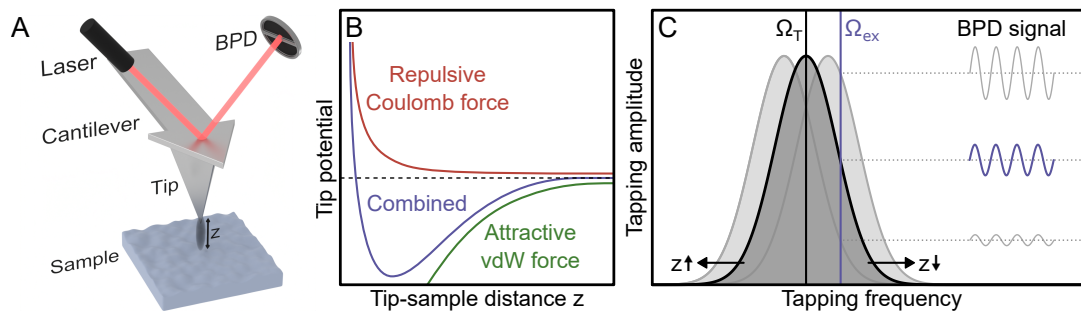


Figure 3.6. | **A:** Schematic of an AFM. A tip is brought close to the surface of a sample. The tip experiences a force, symbolized by the grey-shaded region. To detect the force-induced deflection of the tip, a laser is reflected from its back side onto a segmented photodiode (BPD). **B:** Mechanical potential of the tip, which depends on the distance to the sample surface z . Two forces act on the sample, an attractive van der Waals force (green) and a repulsive Coulomb force (red). Due to their different dependence on z , the tip potential follows a distinct shape (blue). Different modes of AFM operate in different regimes of the potential. Contact mode uses the repulsive regime while tapping mode works in both, the repulsive and the attractive regime. **C:** Resonance curve of the tip-sample system (grey). The resonance frequency Ω_T depends on the force acting between tip and sample and hence on distance between both. Exciting the tip with a frequency Ω_{ex} , which is slightly offset from Ω_T , leads to a sinusoidally oscillating BPD signal with a certain amplitude (blue). A change in the tip-sample distance shifts the resonance frequency and therefore increases or decreases the amplitude. Thus, the amplitude is a measure for the tip-sample distance and the basis for AFM measurements.

There are mainly two measurement schemes. In contact mode, the tip is brought in the repulsive regime of the potential. The topography of the sample directly translates into a bend of the tip, leading to a proportional DC photodiode signal. A proportional-integral-differential (PID) regulation in combination with a piezo stage is used to keep the distance to the sample such, that the tip deflection stays constant. In this case, the error signal directly represents the sample topography. Contact mode has the drawback that it is more prone to vibrational disturbances of the measurements and

noise. Additionally, the wear-down of the tip is quite severe, which results in a quick degradation of spatial resolution.

The second, and more important operational mode is tapping mode. In this mode, the AFM cantilever is mechanically excited with a frequency close to its resonance frequency by a piezo actuator. A typical resonance frequency is in the order ~ 250 kHz, depending on the stiffness of the cantilever. This mechanical excitation leads to an oscillation of the tip with a typical amplitude in the range of 30 nm to 100 nm, and consequently to a sinusoidally varying difference signal from the photodetector, see Figure 3.6 C. A change in tip-sample distance, and hence a change in force acting on the cantilever, changes the eigenfrequency of the cantilever. Throughout the measurement, frequency and amplitude of the piezo excitation of the tip Ω_{ex} are kept constant. This results in a change in oscillation amplitude of the cantilever, as well as a change in the phase of its oscillation with respect to the driving. The excitation frequency is slightly detuned from the eigenfrequency of the tip. As a result, attractive and repulsive forces lead to changes in the oscillation amplitude of the tip with opposite sign. The oscillation amplitude is either increased by bringing the eigenfrequency closer to the driving frequency, or decreased by shifting it further away. This change is then used in a PID regulation to keep the average tip-sample distance constant while scanning the sample under the tip. The error signal is recorded, as it represents the sample topography. Since in tapping mode the tip continuously oscillates, this mode is much more gentle to the tip, resulting in less degradation over time.

3.3.4. Scanning NV Center Magnetometry

The most advanced version of NV center magnetometry involves scanning a single NV center across the sample. A first description of this approach was done by Degen *et al.* in 2008 [36]. The idea of sensing small magnetic fields by scanning a fluorescent probe across a sample and optically detecting its magnetic resonance dates back to Chernobrod and Berman in 2005 [177]. Current scanning NV center microscopes are usually based on an AFM, where a cantilever is scanned across a sample. In scanning NV center magnetometry, the cantilever usually is made of a single-crystal diamond with a single NV center implanted close to the apex of the tip. The distance between the sample and the tip, and hence the sample and the NV center, is kept constant by the AFM. During the measurement, the NV center is illuminated with a laser (532 nm). A close-by antenna emits RF radiation which excites the ESR of the NV center. The fluorescence light emitted from the NV center is detected during the scan. A sketch of the above described setup is shown in Figure 3.7.

Even though a single NV center can be considered as a point defect with a negligible size, when sensing magnetic fields which originate from a certain distance, the detectable wave vector is limited by that distance. Fields with smaller wave vectors will average out due to the positive and negative field components, i.e. due to destructive

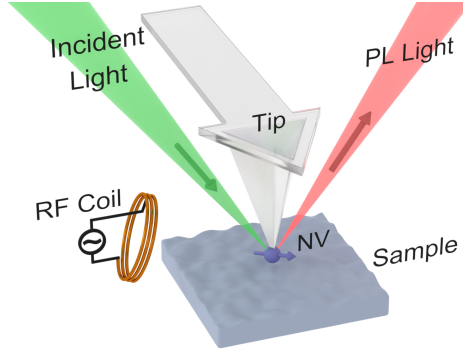


Figure 3.7. | Schematic of scanning NV center magnetometry. A tip, usually etched from a singly-crystal diamond is scanned across a sample. The tip contains a single NV center (blue) close to its apex, which is illuminated by a green laser. A microwave antenna in the vicinity of the tip is used to excite ESR of the NV center. The NV center emits red fluorescence light which is detected.

interference. Thus, a spatial filter function needs to be applied to obtain an accurate estimate of the expected detection limit for small wave vectors. The detectable wave vector of the magnetic field scales inversely with the distance d .

$$k \propto 1/d \quad (3.5)$$

Therefore, the spatial resolution of this method is, to a large extent, determined by the distance between the NV center and the sample, which is on the order of some 10 nm to 100 nm.

Measurement Schemes

Scanning NV center magnetometry offers different measurement schemes. First, there is the so-called *constant B* scheme. During the scan, a constant RF frequency is applied together with CW laser excitation. Whenever the projection of the local magnetic field matches the ESR, a decrease in the photo-luminescence (PL) signal is detected. This method yields a signal corresponding to the contour line of the local magnetic field at a field strength predetermined by the excitation frequency.

An alternative mode is to continuously scan the excitation frequency and determine the Zeeman splitting of the $|\pm 1\rangle$ states for each position on the sample. During the scan, CW laser excitation is applied and the PL intensity is recorded. This method yields the exact magnitude of the magnetic field component parallel to the NV axis, which can be calculated from resonance splitting:

$$\Delta f_{\pm} = 2\mu_B B_{\parallel} \quad (3.6)$$

A third mechanism of magnetic contrast from the NV fluorescence is to not evaluate the frequency position of the ESR dips in the fluorescence-intensity, but to record the integral integrated change in intensity. This is a measure for the coherence time of

the spin polarization of the NV center. As explained in Section 2.4.2, the fluorescence intensity is maximal in the fully spin polarized state. This can be lifted either by ESR, or just by the presence of magnetic noise. It thus reduces the fluorescence intensity, which in turn can be used to detect the presence of magnetic fluctuations in the sample.

Additionally to the CW modes the aforementioned more complicated alternating current (AC) measurement modes are also possible in combination with the scanning approach. They involve a pulsed laser- and RF excitation, and allow, for example, for the observation of Rabi oscillations. From the Rabi frequency the magnetic field can be determined even more precisely.

Compared to MFM, while having a similar spatial resolution, NV center magnetometry is superior in terms sensitivity. Furthermore, a major advantage is that, unlike MFM tips, the NV center itself is not surrounded by large magnetic stray fields, which can influence the sample and distort the measurement.

3.3.5. Scanning Near Field Optical Microscopy

Scanning near field optical microscopy (SNOM) is an optical scanning probe technique that builds upon AFM. There are two major versions of the technique: aperture SNOM and scattering scanning optical near field microscopy (s-SNOM). In aperture SNOM a nanoscopic hole is etched through the tip, which can be used either for near field illumination through the confinement of the sample or for near field detection. Aperture SNOM was developed first, but has proven to be difficult to use. The tips require focused ion beam fabrication, are very expensive, and break easily. In addition, the measured signals are hard to interpret.

A more recently developed alternative is s-SNOM. It utilizes the near field enhancement of light around a metal-coated AFM cantilever. A general sketch of the working principle is shown in Figure 3.8. This section especially refers to the *neaScope* system of the company *Attocube/Neaspec*, who pioneered this method. In s-SNOM, the metal-coated tip is illuminated by a laser, usually in the mid infrared (MIR) range. The laser is focused by means of a parabolic mirror to a spot size of a few micrometers. The oscillating electric field in the focal spot of the laser excites a dipole moment in the tip which, due to its geometry, enhances the field strength underneath the tip by several orders of magnitude. The physics behind the field enhancement is described in Section 2.2.2. The local field enhancement allows for the illumination of a sample with a spot localized to way below the usual diffraction limit, as the area of field enhancement is roughly on the order of the tip radius (10 nm to 30 nm). The light interacts with the sample, and the near field is partially scattered, again by the tip, back into the far field. The scattered light is collimated by a parabolic mirror and sent to a detector.

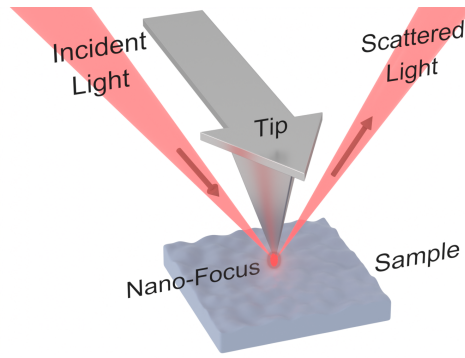


Figure 3.8. | Schematics of s-SNOM. A laser beam is focused on a metallic tip and induces a dipole moment. This leads to a strongly enhanced near field under the tip. The focal spot which is generated in this way has diameter of a few tens of nanometers. The tip is scanned across the sample and the scattered light is detected.

Light Detection and Background Suppression

For light in the visible range, silicon photodiodes can be used. A common detector to detect near-to-mid infrared wavelengths is a mercury cadmium telluride (MCT) detector. The active element is a photo-conductor made from a compound of CdTe and HgTe. The material has a band gap between 0 eV and 1.5 eV, depending on the composition, which is matched to the wavelength that should be detected. Due to the absorption of a photon in the active element, a carrier is excited across the band gap and leads to a spike in conductivity, which, when a voltage is applied, can be measured as a current. For laser light with wavelengths in the MIR range, the photon energies are only slightly above thermal noise at room temperature (photon energy of ~ 100 meV compared to 25 meV of thermal energy). Therefore, MCT detectors require a small enough band gap, which makes them especially susceptible to noise due to thermal excitations of charge carriers in the semiconductor. In order to reduce these, MCT detectors require cooling by liquid nitrogen to lower the temperature.

A major challenge for s-SNOM is to distinguish the light scattered from the near field, which contains information about the sample, from unwanted background light. In s-SNOM measurements, the AFM operates in tapping mode, i.e. the tip-sample distance is modulated with a frequency Ω_T . The scattered field can be expressed as a series of Fourier components at multiples of the tapping frequency. The first two frequency components are dominated by the background signal, which has two main origins. First, direct far field reflections, which are unaffected by the tapping motion of the tip and occur at DC in the frequency spectrum of the detected light. The corresponding electric field is denoted by E_0 in Equation 3.7. Second, a fraction of the field directly scatters from the tip shaft (E_1). This component is modulated with the tapping frequency. The modulation strongly influences the near field scattering process as, according to Equation 2.72, the modulated tip-sample distance translates into a modulation of the near field interaction and hence the intensity of the light scattered

from the near field. Because the interaction is nonlinear with respect to the distance, a sinusoidal modulation of the distance leads to higher harmonic frequency components in the near field. The combined scattered field can be expressed as

$$E_{\text{sc}} = E_0 + E_1 \cos(\Omega_{\text{T}}t') + E_2 \cos(2\Omega_{\text{T}}t') + \dots + E_n \cos(n\Omega_{\text{T}}t'), \quad (3.7)$$

with the time t' .

Considering the scattered intensity I_{sc} , the situation becomes more complicated due to mixing terms originating from interference of the different field components.

$$I_{\text{sc}} = \varepsilon_0 c |E_{\text{sc}}|^2 \quad (3.8)$$

This leads to

$$\begin{aligned} I_{\text{sc}} \propto & E_0^2 + E_1^2 \cos^2(\Omega_{\text{T}}t') + E_2^2 \cos^2(2\Omega_{\text{T}}t') \\ & + 2E_0E_1 \cos(\Omega_{\text{T}}t') + 2E_0E_2 \cos(2\Omega_{\text{T}}t') \\ & + 2E_1E_2 \cos(\Omega_{\text{T}}t') \cos(2\Omega_{\text{T}}t') \\ & + \dots, \end{aligned} \quad (3.9)$$

which can be rewritten using trigonometric identities into

$$\begin{aligned} I_{\text{sc}} \propto & E_0^2 + \frac{E_1^2}{2} + \frac{E_2^2}{2} \\ & + [2E_0E_1 + E_1E_2] \cos(\Omega_{\text{T}}t') \\ & + \left[2E_0E_2 + \frac{1}{2}E_1^2 \right] \cos(2\Omega_{\text{T}}t') \\ & + \text{higher harmonics of } \Omega_{\text{T}}. \end{aligned} \quad (3.10)$$

This shows, that all frequency components contain contributions from both, the near field and the background. The strongest component, by far, is E_0 . The higher order components E_1 and E_2 can be considered as only minor corrections and terms quadratic in E_1 and E_2 , as well as products of both, can be neglected [111]. Since E_0 is considered constant, indeed, the intensity spectrum of the scattered light contains the higher orders which are proportional to the near field components.

$$I_{\text{sc}} \propto \text{const.} + E_0E_1 \cos(\Omega_{\text{T}}t') + E_0E_2 \cos(2\Omega_{\text{T}}t') + \dots \quad (3.11)$$

This makes it possible to separate the near field signal from the background in the frequency domain by demodulating the signal at a higher harmonic of the tapping frequency ($2\Omega_{\text{T}}$ and higher). In fact, even the higher harmonics still contain a background contribution, which decreases with the harmonic number.

The interference between the near field and the static background signal turns out to be an advantage. The intensity of the higher harmonics is proportional to the product $(E_0 E_n)$, which means, that the (weak) near field contribution is amplified by the much stronger E_0 field, a process called *homodyne amplification*. When discussing interference, the actual phase of the electric fields has to be taken into account. For all components E_n the electric field oscillates with the frequency of the light ω , a certain amplitude E_n^0 and phase φ_n .

$$E_n = E_n^0 \sin(\omega t + \varphi_n) \quad (3.12)$$

For the harmonics of the scattered intensity, this has the consequence that the mixing term of two components, and hence the amplification, does depend on phase difference between them. As an example, the 2nd harmonic term is considered in the following. The scattered intensity in the 2nd harmonic of the tapping frequency is

$$I_{sc,2}(t) \propto E_0 E_2 \cos(2\Omega_T t') = E_0^0 \sin(\omega t + \varphi_0) E_2^0 \sin(\omega t + \varphi_2) \cos(2\Omega_T t'). \quad (3.13)$$

The frequency of the light is much higher than the bandwidth of any detection electronics. Therefore, only the time averaged intensity can be detected. Because the time scale of the oscillation of the electric field is much smaller than the time scale of the modulation due to the tapping motion of the tip ($t \ll t'$), the time average only affects the oscillation of the field and the intensity can be written as

$$\begin{aligned} I_{sc,2}^{\text{det}} &= \langle I_{sc,2}(t) \rangle_t \\ &\propto E_0^0 E_2^0 \cos(2\Omega_T t') \langle \sin(\omega t + \varphi_0) \sin(\omega t + \varphi_2) \rangle_t \\ &= E_0^0 E_2^0 \cos(2\Omega_T t') \cos(\varphi_0 - \varphi_2) \end{aligned} \quad (3.14)$$

This makes it clear that the signal intensity of a certain harmonic depends on the phase difference of the individual components. The interference can be constructive (if $\Delta\varphi = 0^\circ$ or 180°) or destructive (if $\Delta\varphi = 90^\circ$ or 270°), depending on the exact alignment of the instrument. This makes it hard to estimate the actual magnitude of the signal components.

Interferometric Detection of Near Fields

The s-SNOM measurement scheme can be extended to enable the detection of actual scattering-induced phase shifts of the detected light. The phase shift is a measure for resonances occurring in the dielectric function of the material. The complex and frequency-dependent dielectric function $\varepsilon(\omega) = \varepsilon'(\omega) - i\varepsilon''(\omega)$ describes how a material is influenced by an external electrical field. When the light, with an electric field of \mathbf{E}_{in} , interacts with matter it induces an electrical polarization of

$$\mathbf{P}_{\text{ind}}(\omega) = (\varepsilon(\omega) - \varepsilon_0) \mathbf{E}_{\text{in}}(\omega). \quad (3.15)$$

ε_0 denotes the dielectric constant. The induced polarization oscillates with the frequency of the incident light and, in turn, emits an electric field E_{sc} which the s-SNOM detects as scattered light.

$$\mathbf{E}_{\text{sc}}(\omega) \propto \mathbf{P}_{\text{ind}}(\omega). \quad (3.16)$$

This description is equivalent to the considerations in Section 2.2.2. The polarization is defined as the the dipole moment per volume (compare with Equation 2.73).

$$\mathbf{P} = \frac{d}{dV} \mathbf{p} \quad (3.17)$$

Resonances in the dielectric function can occur over wide range of frequencies due to ionic migrations (kHz to MHz), molecular (MHz to GHz/RF radiation) or lattice vibrations (THz/IR) or electronic excitations, such as plasma oscillation (few 1000 THz/visible light (VIS) and ultra violet (UV) light). In the vicinity of a resonance, the imaginary part of the dielectric function ε'' peaks with a Lorentzian line shape. It describes absorption losses in the material, which are maximal at resonance. The real part ε' follows a dispersive, bipolar behavior. This can be interpreted as a phase difference between the excitation field and the electrical polarization induced in the material. This phase difference also occurs in the scattered light and contains information about the permittivity. As direct measurement of the phase of the scattered light is impossible due to the limited detection bandwidth, a special detection scheme is employed to circumvent this limitation.

For simplicity, the following considerations are done for linearly polarized incident light (only x -component) in vacuum. It is assumed that an incident electromagnetic wave with an electric field

$$E_{\text{in}} = E_{\text{in}}^0 \sin(kx - \omega t) \quad (3.18)$$

interacts with matter as previously described. Due to the interaction, its electric field amplitude might change to E_{sc}^0 and it might pick up a certain phase shift $\Delta\phi$. The scattered wave reads as

$$E_{\text{sc}} = E_{\text{sc}}^0 \sin(kx - \omega t + \Delta\phi). \quad (3.19)$$

The detector senses the intensity of the scattered light.

$$I(t) = \varepsilon_0 c |E_{\text{sc}}|^2 = \varepsilon_0 c |E_{\text{sc}}^0 \sin(kx - \omega t + \Delta\phi)|^2, \quad (3.20)$$

where c denotes the the speed of light. Due to the limited bandwidth, it is only able to detect the time average of the intensity.

$$I_{\text{det}} = \langle I(t) \rangle_t = \frac{\varepsilon_0 c}{2} |E_{\text{sc}}^0|^2. \quad (3.21)$$

Hence, the phase information is lost. Moreover, the intensity is influenced by the sample, but it might still depend on external parameters, which makes it ambiguous

and hard to interpret. To circumvent this limitation an interferometric method, called *pseudo-heterodyne (PH) detection*, is employed [178, 179]. In PH detection, the light reaching the detector is superimposed with an additional reference wave

$$E_{\text{ref}} = E_{\text{ref}}^0 \sin(kx - \omega t). \quad (3.22)$$

On the detector, the reference wave and the scattered wave interfere. As a result, the detector senses an intensity $I_{\text{det}}^{\text{int}}$, which depends on the relative phase $\Delta\phi$ between the sample beam and the reference beam:

$$\begin{aligned} I_{\text{det}}^{\text{int}} &= \frac{\varepsilon_0 c}{2} |E_{\text{ref}} + E_{\text{sc}}|^2 \\ &= \frac{\varepsilon_0 c}{2} \left(|E_{\text{ref}}^0|^2 + |E_{\text{sc}}^0|^2 + 2|E_{\text{ref}}^0||E_{\text{sc}}^0| \cos(\Delta\phi) \right). \end{aligned} \quad (3.23)$$

Due to the interference, the phase information is retained even in the time-averaged intensity. However, a change in phase is indistinguishable from a change in amplitude of the electrical field. To recover this information, an additional modulation of the reference beam is employed in the form of a phase modulation at a low frequency Ω_M (in the 100 Hz range) and modulation amplitude a . This changes the electric field to

$$E_{\text{ref}}^{\text{mod}} = E_{\text{ref}}^0 \sin(kx - \omega t + a \cos(\Omega_M t)) \quad (3.24)$$

and the intensity to

$$I_{\text{det}}^{\text{mod}} = \frac{\varepsilon_0 c}{2} \underbrace{|E_{\text{ref}}^0|^2 + |E_{\text{sc}}^0|^2}_{\text{const.}} + \underbrace{\varepsilon_0 c |E_{\text{ref}}^0 E_{\text{sc}}^0| \cos(a \cos(\Omega_M t) - \Delta\phi)}_{I_{\text{det}}^{\text{ac}}}. \quad (3.25)$$

The intensity is comprised of a constant and a time-dependent part $I_{\text{det}}^{\text{ac}}$. The time-dependent term can be expanded into a Fourier series and separated into three parts, a constant part and two time-dependent terms which scale with the sine and the cosine of the phase shift, respectively.

$$\begin{aligned} I_{\text{det}}^{\text{ac}} &= \varepsilon_0 c |E_{\text{ref}}^0 E_{\text{sc}}^0| \cos(\Delta\phi) J_0(a) \\ &\quad + 2\varepsilon_0 c |E_{\text{ref}}^0 E_{\text{sc}}^0| \sin(\Delta\phi) \sum_{n \in \mathbb{N}} (-1)^{n-1} J_{2n-1}(a) \cos((2n-1)\Omega_M t) \\ &\quad + 2\varepsilon_0 c |E_{\text{ref}}^0 E_{\text{sc}}^0| \cos(\Delta\phi) \sum_{n \in \mathbb{N}} (-1)^n J_{2n}(a) \cos(2n\Omega_M t) \end{aligned} \quad (3.26)$$

The series represents even and odd sidebands, which appear around the carrier frequency and are spaced apart by the modulation frequency Ω_M , as depicted in Figure 3.9. J_n are Bessel coefficients. To recall, the SNOM tip is operated in tapping mode which generates frequency components in the optical signal at harmonics of the tapping frequency ($n \cdot \Omega_T$), around which now the additional sidebands occur. Performing a lock-in demodulation and comparing the relative amplitudes of even and

odd sidebands allows to separate the amplitude from the phase contributions to the intensity, due to the respective cosine and sine dependence of even and odd sidebands. This allows to recover the true amplitude and phase of the electrical near field at the surface of the sample and enables the detection of plasmonic resonances or resonances in the dielectric function.

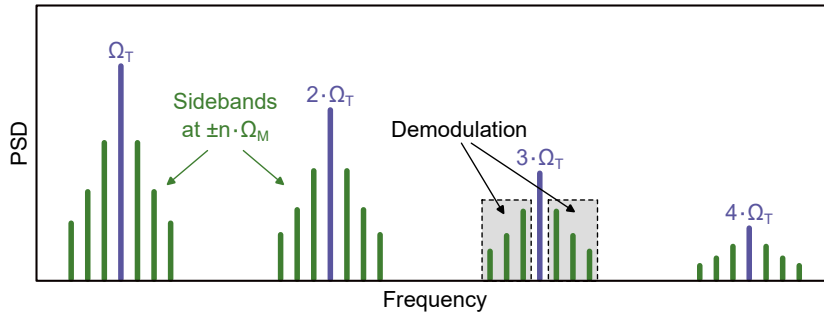


Figure 3.9. | Fourier spectrum of the detected light. Due to the tapping mode, the light is modulated with the tapping frequency Ω_T . Because of the nonlinearity of the near field interaction, higher harmonics of this frequency occur, which can be used to discriminate the actual near field from stray field components. The mixing of the scattered light with a low-frequency modulated reference beam introduces sidebands, which are spaced from the main harmonics by integer multiples of the modulation frequency Ω_M . A phase-sensitive signal can be obtained by demodulating the detected intensity on all of these sidebands.

Sample Preparation

The samples which were used in this thesis were fabricated with different techniques available within the group. All samples involve at least one lithography step for which electron beam lithography (EBL) was utilized. A cartoon of a typical fabrication process is shown in Figure 4.1. The cartoon describes a single layer positive EBL process, where the irradiated resist gets washed away. There are also negative processes, as well as more complicated two-layer resist systems.

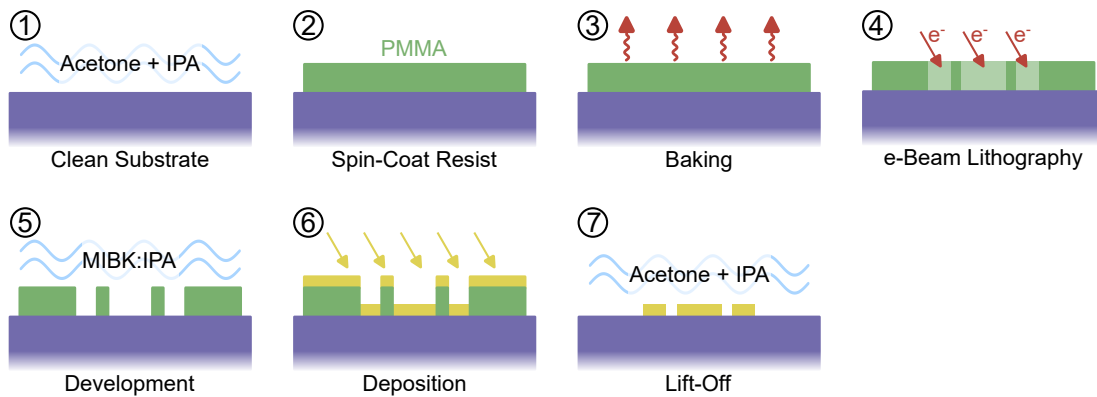


Figure 4.1. | EBL procedure, which consists of seven basic steps: Cleaning the substrate, spin-coating resist on the substrate, baking the sample, EBL, development, deposition of material, and lift-off.

4.1. Electron Beam Lithography

To fabricate a sample using EBL, first, a substrate is cleaned and spin-coated with a polymethyl methacrylate (PMMA)-based positive resist, that is sensitive to irradiation with high-energy electrons. As substrates, either undoped Si(100) or GaAs(100) were used. The substrate with the resist is baked to evaporate the solvent. The so-prepared samples are loaded into the lithography system (*Zeiss Supra VP40* scanning electron microscope (SEM) with *Nanonics* EBL system), where the structures are written with the electron beam according to a previously defined layout. The electron irradiation splits the PMMA chains and makes the positive resist more solvable in the exposed areas. After writing of the structures, the samples are chemically developed, using a mixture of methyl isobutyl ketone (MIBK) and isopropyl alcohol (IPA). This removes the resist in the irradiated areas, leaving a template of the layout on the substrate. This step is followed by the deposition of material. Different deposition techniques were used for different samples. The last step following deposition is lift-off. The samples are submerged in acetone, which removes the remaining resist and with it

the material which was deposited on top. Only in the previously exposed regions, the deposited material remains and forms the structure.

The lithography can be repeated multiple times to create different structures on top of each other. The only difference is an additional alignment step during the EBL, to align the new layout to the existing structures on the substrate. The details of the recipes can be found in Appendix Section G.1.

4.2. Thermal Evaporation

For thermal evaporation, the material to be deposited is located inside a crucible. The crucible is heated by a heating filament, through which a large current (on the order of 50 A) is sent. The energy supplied leads to melting of the material inside the crucible and its evaporation. The evaporated material is deposited on the sample, which is positioned above the crucible. The whole process takes place in an ultra high vacuum (UHV) chamber, as air molecules would contaminate the deposited material (oxidation).

Thermal evaporation is suitable for materials with a manageable melting point below the temperature where the materials from which crucible and heater are made would start to get damaged or even melt themselves. Suitable materials are, for example, gold, aluminum, nickel and iron. The deposition rates are usually low compared to sputter deposition (below 1 \AA s^{-1}), which makes the process more prone to contamination due to insufficient vacuum, as there is more time for remaining gas molecules to react with the deposited material.

4.3. Magnetron Sputtering

Magnetron sputtering, compared to thermal evaporation, is a rather rapid process with high deposition rates even above 10 \AA s^{-1} . The jet of material, which is deposited on the sample, is generated in an entirely different way. In sputter deposition, a plasma is generated inside the UHV chamber by inserting a small amount of argon gas and igniting it by applying a high voltage. Inside the sputter source, the fast-moving Ar^+ ions are deflected by magnetic fields towards a sputter target. The magnetic fields are generated by strong permanent magnets which are positioned close to the targets to provide the necessary field geometry. The ions impacting on the target kinetically eject atoms from it. The ejected atoms move towards the sample and are deposited as a layer. Equally to thermal evaporation, sputtering takes place in UHV to avoid contamination and to provide a sufficiently large mean free path for the atoms to reach the sample. The sputter sources are water-cooled to avoid thermal damage and melting.

Many materials are suitable for sputtering. Problems arise when the materials have a high saturation magnetization, like iron. In this case, the magnetic field that might be generated by the target itself competes with the magnet-generated field which steers the

plasma. Likewise, insulating materials are more challenging than conducting materials, since their charge-up prevents the argon ions from reaching the target. This is avoided by using AC sputtering.

In sputter deposition as well as in thermal evaporation, a quartz gauge is used to track the thickness of the deposited film. This works by measuring the resonance frequency of the quartz while material is deposited on it at the same time as it is deposited on the sample. The deposited material leads to a change of the mass of the quartz and consequently a reduction of its resonance frequency. From this frequency drop, the deposited thickness can be deduced with the help of previous calibration.

4.4. Atomic Layer Deposition

Atomic layer deposition (ALD) is a fabrication method to deposit extremely thin layers, potentially atomic monolayers, of a material on a sample. The process works by sequential exposure of the sample to pulses of gas-phase reactants, as is described in the following. After evacuating the sample chamber the sample is exposed to a specially designed precursor gas. The gas molecules are adsorbed at the surface of the sample and form a continuous monolayer. This process is self-limiting and stops after the monolayer is complete. The excess gas is pumped away and the reaction chamber is filled with a second gas, which reacts with the adsorbed monolayer and cracks the molecules. The chemistry of both reactants is designed such that this reaction yields a solid product, which is the desired material that stays on the sample, and gaseous components that can be easily removed. After pumping away the remains, one cycle of deposition is finished. The process is repeated until the desired layer thickness is reached.

Due to the self-limiting nature of the processes involved, the layer thickness deposited in one cycle is predetermined. Since each cycle only generates a single layer of material, the process is fairly slow, as even a single nanometer needs 10s to 100s of cycles. As the deposition of material in ALD originates from a gas phase, it is fully isotropic, i.e. it takes place on all surfaces of the sample. Because of this, ALD is capable of fully encapsulating a sample with a continuous layer of material, even if corners and edges are present. This unique feature sets it apart from sputter deposition or thermal evaporation which are both highly directional.

In this thesis, ALD (*Savannah 100* from *Cambridge Nano Tech*) was used to deposit layers of Al_2O_3 as capping layers to prevent oxidation of the sample material. The standard process to deposit Al_2O_3 uses trimethylaluminium (TMA) as precursor gas, which reacts with H_2O . The result of the reaction is Al_2O_3 deposited on the sample surface and methane gas which is removed. The details of the process are listed in Section G.2.

Micromagnetic Simulations

Throughout this thesis, micromagnetic simulations are employed to simulate the behavior of magnetic samples. The software package used for this is *mumax³* [180]. It uses a finite-difference method to solve the local equation of motion for the magnetization of the sample. Mumax utilizes the *NVIDIA CUDA* programming framework, which allows parallelization of matrix calculations with the help of graphics processing unit (GPU) hardware to accelerate the simulation.

The simulation volume is parametrically defined according to the shape and geometry of the of the sample. The geometry can, for example, be square-shaped, elliptical, or a more complex, 3D shape. This volume is divided into a grid of cells with previously defined lattice spacing in each direction. To simulate infinite (bulk) or semi-infinite (thin film or stripe) samples, the boundary conditions of the simulation need to be chosen accordingly. Periodic boundary conditions mimic a sample which is infinite in that direction.

In the simulation, each cell represents a single magnetic moment with defined magnetic parameters, such as saturation magnetization M_S , direction and strength of uniaxial and cubic anisotropies K_U and K_C , Gilbert damping parameter α , and exchange coupling energy A_{ex} . In addition to the intrinsic parameters, external stimuli, such as static or time-dependent (RF) magnetic fields can be defined. The package also allows to simulate SOT or STT [181]. All contributions are included in an effective field \mathbf{H}_{eff} acting on each cell. To mimic the effects of finite temperatures, a stochastic disorder can be applied to the magnetization at each simulation step.

The sample can be divided into up to 255 regions with different magnetic properties corresponding to the material. The regions can be defined manually, or distributed according to a randomized Voronoi pattern. This is useful to simulate polycrystalline materials or materials with magnetic disorder, which becomes crucial in Section 6.8.

The simulation starts by defining an initial magnetization in each cell. This can either be random or set already close to the expected ground state of the system. The first step is to find the true ground state of the system, i.e. to minimize the total energy. In this state, the torque acting on the magnetic moments is zero. The torque equation used by *mumax³* is the LLG equation, but cross-multiplied by $\mathbf{m} \times$ from the left.

$$\boldsymbol{\tau} = \mathbf{m} \times \frac{\partial}{\partial t} \mathbf{m} = -\gamma_0 \mathbf{m} \times (\mathbf{m} \times \mathbf{H}_{\text{eff}}) - \alpha \mathbf{m} \times \frac{\partial}{\partial t} \mathbf{m} \quad (5.1)$$

The LLG is numerically integrated in discrete time steps until the torque reaches the numerical noise floor. After the relaxation procedure, depending on what should be simulated, external stimuli can be applied and the time evolution of the full LLG

is simulated further. In this work, this is mostly a combination of a static bias field and a dynamic RF field representing microwave excitation. The time evolution of the magnetization is simulated in discrete time steps by propagating the LLG and the magnetization vector is recorded for each cell. This yields a 3-dimensional data cube of magnetization traces in the time domain. A subsequent fast Fourier transform (FFT) yields the frequency spectrum of the motion of the magnetization.

Besides this, *mumax³* can be used to simulate magnetic hysteresis curves or domain wall motion (by employing a moving frame of reference). It can also simulate magnetic stray fields originating from the sample.

All-Magnonic Frequency Comb Generation

In this chapter, the first of the two main results of this thesis is presented. It focuses on a study about the dynamic response of a ferromagnetic $\text{Ni}_{80}\text{Fe}_{20}$ thin film under RF excitation. To investigate the material, several diffraction-limited optical methods are utilized, including Kerr microscopy and SNS-MOKE microscopy, as well as confocal NV center microscopy. Micromagnetic simulations were performed to understand the origin of the observations. Furthermore, microstructures, fabricated from the same material, were investigated to learn about the influence of their shape, size and thickness on the spin wave generation. For this, SNS-MOKE was used in combination with scanning NV center microscopy. In addition to static imaging of the magnetization patterns with scanning NV microscopy, a dynamic measurement scheme was used to enable the observation of magnetization dynamics and spin waves excited inside the structures.

The ferromagnetic alloy $\text{Ni}_{80}\text{Fe}_{20}$, known as Permalloy, is one of the most prototypical ferromagnets in scientific research and often used as a reference standard to test and gauge experimental setups. It was first investigated and produced by Arnold and Elmen of Bell laboratories in the beginning of the 20th century to be used as a shielding for submarine telegraph cables [182]. It consists of the ferromagnetic metals iron and nickel in a stoichiometric ratio such, that the magnetoelastic contributions of its constituents perfectly cancel. Therefore, it has very little to no magnetostrictive effects. Other features are a comparably high saturation magnetization, on the order of $\mu_0 M_S \approx 1 \text{ T}$, and a very low coercivity (below 0.5 mT), which makes it a soft magnetic material that can be easily switched using small magnetic fields. The FMR frequency at low fields (few mT) lies in the range of 0.5 GHz to 2 GHz. The fabrication of thin films or microstructures of Permalloy is rather straightforward, as the material is suitable for thermal evaporation as well as sputtering. All of these properties lead to a wide usage of the material. In the following, the term NiFe refers to the alloy with a composition of 80 % iron and 20 % nickel; the stoichiometric indices are omitted.

The initial aim of this study was to evaluate if confocal NV magnetometry is a viable tool to investigate the magnetization dynamics in ferromagnets. Since the method utilizes NV centers as extremely sensitive, atomically-sized probes for magnetic fields, NV center magnetometry has an advantage compared to traditional, diffraction-limited methods in terms of the range of detectable wave vectors. To use the method, it first will be demonstrated that the technique is indeed viable to detect the tiny stray fields which originate from spin waves. Even more, a previously unknown response of this well

studied material to dynamic RF fields is revealed. In the study, a NiFe layer is excited by RF fields at MHz and GHz frequencies generated by a co-planar waveguide (CPW). As is shown later in this chapter, confocal NV center magnetometry measurements indicate fingerprints of a new mechanism to generate spin waves which precess in the GHz range, but are excited with low-frequency (MHz) fields.

The chapter is structured as follows. First, a summary is given about previous works on the topic of magnonic frequency multiplication. The section that follows discusses the design and preparation procedure for the samples which were investigated in this chapter. Subsequently, measurement results obtained with different measurement techniques, i.e. NV center magnetometry, SNS-MOKE and Kerr microscopy are presented. The next section covers micromagnetic simulations, which were performed in order to understand the mechanism that is responsible for the observed dynamic response of the samples. From these simulation results, a model of the actual physical mechanism is deduced. The section is followed by an outlook towards the investigation of frequency multiplication in micrometer-sized devices. This includes first static and dynamic scanning NV center magnetometry measurements. A final section concludes the results.

6.1. Previous Works on Frequency Multiplication

Spin waves which precess at higher harmonics of the excitation frequency can be generated by different mechanisms. In the following, a couple of previous works on this topic are briefly discussed. While the generation of magnonic frequency combs has been demonstrated before, only a few higher harmonics have been obtained in experiments. The examples which are discussed in the following go beyond the well-known generation of second harmonic spin waves by parallel-pumping, which as been mentioned in Section 2.1.3. The studies can be roughly divided into works concerning structures which generate a nonlinearity in the system, and studies about nonlinear interactions in magnetic waveguides.

An example for a structure which generates a nonlinearity is a magnetic domain wall. Such a system was studied theoretically by Hermsdorfer *et al.*. The authors simulated domain walls pinned in a 5 nm-thick NiFe waveguide. The domain walls are excited using an external magnetic field with their eigenfrequencies, in this case 5 GHz, and oscillate with that frequency. The oscillating domain walls emit spin waves, which propagate away from the domain wall along the waveguide. The waveguide is engineered such that the propagation of directly excited spin waves, which precess at the excitation frequency of 5 GHz, is prohibited. Nevertheless, Hermsdorfer *et al.* still found propagating spin waves in their simulations, spin waves that oscillate at twice the excitation frequency (10 GHz) [29]. These spin waves are generated because the domain wall oscillation is not entirely harmonic.

Roudrigues *et al.* simulated the generation of higher harmonics in topological magnetic

textures, like a magnetic vortex or Skyrmion [183]. A vortex possesses a number of eigemodes, such as a breathing mode, a gyrotropic mode and elliptical modes, all of which represent certain eigenfrequencies. Exciting the vortex with a frequency will excite a mixture of those modes. Roudriges *et al.* simulated excitation frequencies in the few-GHz range and observed a non-vanishing amplitude whenever the excitation frequency matched a fraction of the eigenfrequency of one of those modes. This means, that the excitation frequency is actually up-converted. This effect is attributed to the nonlinear potential due to the presence of the spin texture.

Demidov *et al.* demonstrated frequency multiplication experimentally in elliptically-shaped NiFe elements with dimensions of $0.5 \mu\text{m} \times 1 \mu\text{m}$ and a thickness of 160 nm. The elements were microstructured on top of a micro-stripline [184], which was used to excite the magnetization in the element via the magnetic field when an RF current is applied. Using micro-focused BLS, Demidov *et al.* were able to measure spin waves inside the element, which precess at the 2nd and 3rd harmonic of the excitation frequency in the range of a few GHz. These higher harmonic spin waves precess at 7 GHz to 11 GHz. The authors find a strong resonant enhancement of spin wave magnitude when the harmonic of the frequency matches one of the eigenmodes of the structure, which in this case are at 9.3 GHz and 10.2 GHz. Demidov *et al.* attribute the generation of the higher order spin waves to the intrinsic nonlinearity of the LLG. A similar study was conducted by Ulrichs *et al.* [185].

In a second study by Demidov *et al.*, the generation of second harmonic spin waves in a nonlinear magnonic waveguide was demonstrated [28]. The waveguide consisted of NiFe, had a width of $2 \mu\text{m}$ and a thickness of 36 nm. The spin waves were excited using a microstrip antenna and propagate along the stripe, which is magnetized in perpendicular direction by a 30 mT bias field. The authors excited the stripe with frequencies of 4 GHz to 7 GHz and detect spin waves at twice the frequency by means of micro-focused BLS. They attribute the generation of the second harmonic to an effect which they call three-wave confluence. The process is non-resonant and without a power threshold.

In a similar study, Hula *et al.* excited a $3 \mu\text{m}$ -wide and 30 nm-thick $\text{Co}_{25}\text{Fe}_{75}$ waveguide simultaneously with two frequencies using two antennas [186]. Using BLS, they showed that the spin waves which are generated at those frequencies inside the stripe interact and mix. For example, they excited the stripe with frequencies of 8 GHz and 8.5 GHz and found that a frequency comb is forming around those frequencies. Harmonics are generated towards lower and higher frequencies with a line spacing of 0.5 GHz. The comb generation is attributed to nonlinear interaction of the spin waves in the form of four-magnon scattering. Hula *et al.* furthermore studied the time evolution of the spin waves, when both microwave excitation frequencies are not applied at the same time as CW excitation, but instead as pulses. They found, that the onset of the comb generation is delayed with respect to the excitation pulse. The authors explain this with additional states that need to be populated first after switching on the excitation,

before they can scatter into the comb spin waves.

A final example is a work by Groß *et al.*, who patterned periodic holes in a 50 nm-thick NiFe layer. Exciting this using a microstrip antenna also yields higher harmonics. They imaged the spin waves generated by means of STXM and found that exciting the system with a frequency of about 1 GHz yields up to the 7th higher harmonic of the excitation frequency [187]. This represents, so far, one of the best results toward the generation high harmonics.

All of the works mentioned above discuss the generation of spin waves precessing at integer harmonics of the excitation frequency. Nonlinear processes also allow, for example, for the generation of spin waves which precess at half-integer multiples. An example for this is a work by Dreyer *et al.*. The authors investigated NiFe structures on top of a CPW by means of SNS-MOKE. They found that, given high enough excitation amplitudes, nonlinear spin waves are generated due to a parametric process. The process has previously been described by Bauer *et al.* [75]. The half-integer spin waves are a result of increased lifetimes due to large precessional angles of the magnetization at low bias fields, which lead to a parametric modulation of the spin wave band during the precession cycle. These nonlinear spin waves appear at lower power thresholds than conventional nonlinear processes, i.e. Suhl instabilities. Half integer spin waves possess an ambiguous phase relation with respect to the excitation. For the spin wave mode at 3/2 of the excitation frequency, two phase states are possible. This leads to fluctuations of the spin wave phase, as the system stochastically switches between the two states. Seeding a system with a second, weak signal at the frequency of the nonlinear spin waves, Dreyer *et al.* were able to control and manipulate this phase state.

All studies discussed in this section have in common, that they work for excitation frequencies in the GHz range and generate spin waves with frequencies which are also in that range or, at maximum, one order of magnitude higher. These results are quite different from the effect observed here, which is a frequency comb that is excited with MHz-range frequencies and spans far into the GHz range. Such wide-spanning frequency combs are very unusual in the field of magnonics. In the following section the layout for the samples, which exhibit this effect, is presented.

6.2. Sample Preparation and Layout

The sample investigated in this part of the thesis was prepared using the methods which have been described in Chapter 4. The layout features a large area of the soft ferromagnetic material NiFe on top of the signal line of a CPW. A schematic of the sample layout is shown in Figure 6.1.

Initially, a resist mask of a CPW was fabricated with electron beam lithography (EBL) on undoped GaAs(001) substrate. Subsequently, using thermal evaporation a few nanometer-thick chromium adhesion layer followed by 100 nm of gold and 20 nm of

NiFe were deposited. To prevent oxidation of the NiFe, an Al_2O_3 layer was deposited using ALD to encapsulate the sample. Afterwards the sample was mounted in a sample holder and electrically connected using wire bonding. In the final step, a solution which contains nano-diamonds was drop-cast on the sample and dried.

The dimensions of the CPW are chosen such, that the impedance of the CPW matches $50\ \Omega$, which is required to minimize reflection losses in the RF circuit of the measurement apparatus. At the same time, they ensure sufficiently large Oersted fields which originate from RF currents sourced by a connected RF generator. These fields are used to excite the magnetization dynamics in the ferromagnet. The signal line is $50\ \mu\text{m}$ wide, the gap size is $30\ \mu\text{m}$ and the ground lines have a width of $25\ \mu\text{m}$. Toward the ends of the CPW, the signal and ground lines widen into large pads to provide space for wire bonding and minimize the DC resistance.

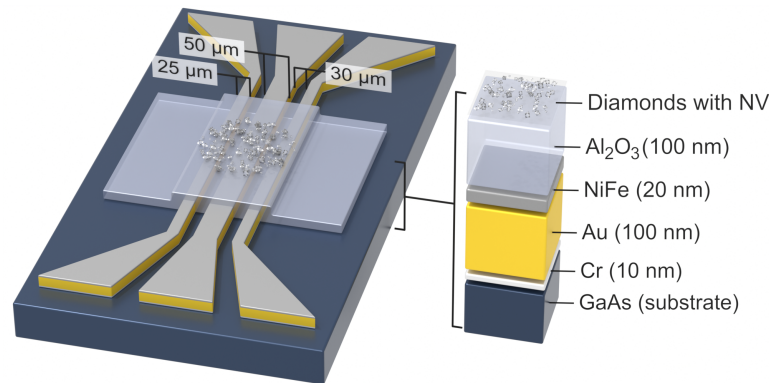


Figure 6.1. | Sample layout, consisting of a 100 nm-thick CPW made from Au on undoped Si substrate. The CPW is fully covered by a 20 nm-thick NiFe layer. The structure is capped with Al_2O_3 to prevent oxidation. Nano-diamonds are deposited via drop-casting.

6.3. Confocal NV Center Magnetometry Measurements

The setup used to conduct the measurements has been introduced in Section 3.3.2, together with a detailed description of the measurement technique. During the measurement, an externally applied magnetic field points along the CPW. The RF excitation field is oriented perpendicular to the CPW. On the signal line it points in the plane of the film and in the gap it points out-of-plane. To obtain an overview of the response, excitation frequency and static bias field are scanned, and the NV center photo-luminescence (PL) signal is recorded.

The RF excitation through the CPW not only excites the uniform mode in the ferromagnetic layer, but also a number of inhomogeneous spin wave modes. As NiFe is a very soft ferromagnetic material with almost no internal anisotropies, it is very susceptible to small external magnetic fields. This makes it easy to manipulate the magnetization by means of static bias fields. More importantly, dynamic RF fields can easily excite the magnetization to precess with large excursion angles ($>10^\circ$). This

makes the material a good candidate to study nonlinear effects, which occur at large excitation power. All of these excitations in the NiFe leave an imprint in the PL signal of the NV centers via the dynamic magnetic stray fields that are generated by the inhomogeneous magnetization.

Figure 6.2 shows a measurement obtained in the center of the CPW. The bias field was varied from 0 mT to 12 mT and the excitation frequency was changed from a few MHz up to 3.2 GHz. To enable lock-in amplification, the magnetic field was modulated during the measurement (HM). Hence, the demodulated signal actually represents the derivative of the PL intensity with respect to the magnetic field. It thus can be bipolar and only deviates from zero if the PL intensity changes within the range of the modulated field, which in the following measurements is on the order of $700 \mu\text{T}$. If, for example, a signal is present over a certain field range, as a result of the field modulation, only the rising or falling edges appear in the detected signal with opposite polarity. See Appendix Section C.1 for a side by side comparison of different modulation methods.

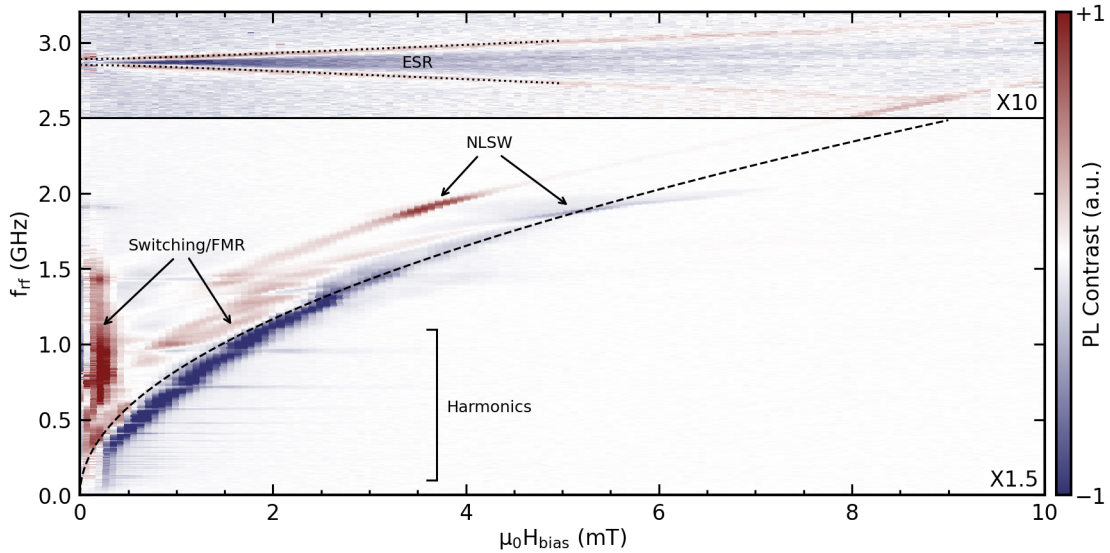


Figure 6.2. | NV center magnetometry measurement on the extended NiFe layer. During the measurement HM was used. This is why the signal is bipolar and resembles the derivative of the PL with respect to the bias field. A series of features can be observed apart from the direct excitation of the NV centers' ESR, these are nonlinear spin waves at 1.91 GHz, a spin wave continuum below 1.5 GHz and a series of sharp resonances below 1 GHz. For better visibility, the signal was amplified by a factor of X1.5 below and X10 above the frequency of 2.5 GHz, respectively. The dotted lines indicate the calculated ESR of the NV centers. The dashed line indicates the FMR of the NiFe layer. Figure adapted from [30].

The measurement reveals a number of features. The signal at an excitation frequency of 2.87 GHz is expected, as it originates from the direct excitation of the ESR of the NV center, i.e. the electronic transition between the $|0\rangle$ and the $|\pm 1\rangle$ triplet states. As the energy of the $|\pm 1\rangle$ states shifts with increasing bias field due to Zeeman interaction, the signal splits in an almost linear way. For a theoretical treatment of this behavior, see Section 2.4.2. The slope of the upper and lower boundaries of the signal is determined

by the gyromagnetic ratio of the NV center. It can be deduced from the measurement and amounts to ≈ 28 GHz/T, i.e. at a bias field of 10 mT, the $|\pm 1\rangle$ states shift in energy by ± 280 MHz, leading to a splitting at this field of 560 MHz.

Note, that the ESR of a single NV center only leads to signals at exactly the mentioned ESR frequencies. However, in the measurements, an ensemble of many nano-diamonds is probed at the same time. The NV centers inside these nano-diamonds are randomly oriented with respect to the external field and experience only the projection of the magnetic field with respect to their orientation axis. This leads to a reduction of the effective field in case of a deviating NV axis, resulting in PL signals at frequencies also in between the two boundary frequencies.

All additional features at frequencies below the ESR frequency only occur in the presence of the magnetic material. This is demonstrated by a control measurement on the same sample, but in the gap of the CPW, where the ferromagnet is absent. This control experiment shows, that the NV centers are indeed only sensitive to RF fields oscillating at their ESR frequency, see Appendix Section C.2. Apart from a faint second ESR signal at around 1.4 GHz, which stems from a transition within the excited state (see Figure 2.14), the signals at other frequencies can only be understood if there is a process which up-converts the excitation frequency to the NV center ESR. All other signals visible in Figure 6.2 must involve some form of frequency up-conversion.

Moving towards lower frequencies, the next strong feature that catches the eye appears at 1.9 GHz at a slightly elevated bias field of 3 mT to 5 mT (labeled as NLSW). The frequency equals two thirds of the NV centers' ESR frequency. This signal can be attributed to nonlinear spin waves, which appear in soft magnetic materials at half-integer multiples of the excitation frequency. These were already mentioned in Section 6.1. The signal is observed twice with opposite polarity, again, because of the field modulation scheme employed. This means, the spin waves are actually present in the whole field range from 3 mT to 5 mT. This can be seen from a comparison to microwave AM modulated measurements, shown in Appendix Section C.1. The observed signal is in good agreement with recent SNS-MOKE results by Dreyer *et al.* [77]. This work focuses entirely on these nonlinear spin waves. However, they are observed only in a much narrower range of bias fields. This is due to the reliance of SNS-MOKE on the phase stability of the observed effect. A fluctuating phase of the spin waves leads to a vanishing signal in SNS-MOKE. NV center magnetometry, on the other hand, is not sensitive to the phase of the spin waves, which extends the range in which they can be measured to fields where the phase becomes unstable.

At frequencies below 1.5 GHz, a strong signal is observed at a field following the expected FMR of the NiFe layer. The signal continues down to a few MHz. Likewise, a signal with opposite polarity is visible at almost zero bias field. These signals mark a range in between which various magnetic excitations exist, possibly a number of DE-like spin waves. In this field range, the excitation amplitude is comparable in magnitude to the applied bias field, which possibly leads to chaotic switching processes in the

ferromagnet, giving rise to incoherent excitations, i.e. magnetic noise which may lead to a quenching of the PL.

The most striking feature, and the one which was in focus of this thesis, are the sharp signals which appear at specific frequencies below 1 GHz and at bias fields below 3 mT. Figure 6.3 shows a measurement of the frequency and field range of interest with an increased resolution. From this measurement, it can be seen that the series of sharp lines continues down to at least 20 MHz.

A closer look at the individual lines reveals a splitting with increasing bias field, very much like the ESR signal at 2.87 GHz. The splitting is not equal for all lines, but scales with the frequency at which the lines occur. These frequencies are not irregular, but exactly match integer fractions of the NV centers' ESR frequency. This suggests that, in fact, they resemble replica of the ESR, just with a rescaled frequency axis, i.e. a process up-converts the excitation frequency into the ESR frequency. Because this process is only observed in presence of the ferromagnetic layer, it is reasonable to assume that the dynamics inside the ferromagnet is responsible, i.e. spin waves are generated, which precess with a frequency multiple of the excitation frequency. The NV centers sense the stray fields emitted by the spin waves, which oscillate with the up-converted spin wave frequency. The large number of sharp lines, observed even at a few tens of MHz, indicates that the process actually resembles a frequency comb, where any excitation frequency is up-converted to many higher harmonic frequencies at the same time. Remarkably, this frequency comb spans at least six octaves. When one of the comb lines matches the ESR frequency, the PL signal changes. The wide range of the frequency comb implies that the conversion process is largely independent of the excitation frequency.

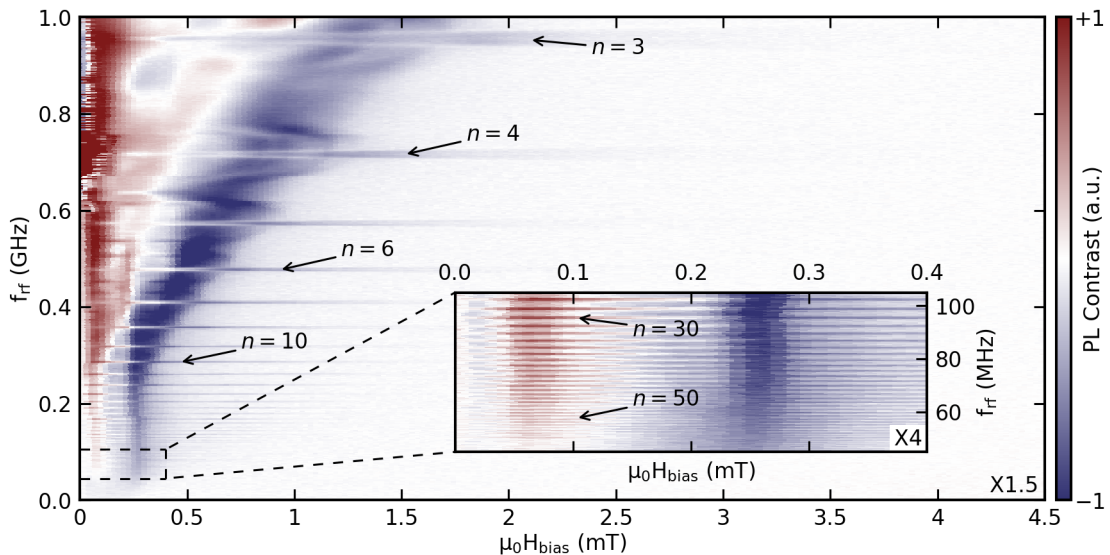


Figure 6.3. | NV center magnetometry measurement with increased field and frequency resolution. The inset with even finer resolution reveals signals down to 20 MHz, surpassing the 50th harmonic. For better visibility, the contrast is amplified by a factor of X1.5 in the main figure and X4 in the inset. Figure adapted from [30].

6.4. Analyzing the Response at the Excitation Frequency

The NV center magnetometry measurements reveal, that upon exciting the NiFe film with a single frequency f_{rf} , not only spin waves precessing at that exact frequency are generated, but also higher harmonics thereof. If additional spin waves are indeed present, the response at the excitation frequency should deviate from the behavior expected from the model of a simple harmonic oscillator, i.e. a Lorentzian resonance line shape of the precession of the magnetization. The line shape is determined by the power transferred from the excitation field to the magnetic system, which can drastically change if, in addition to the FMR, different modes are excited.

To analyze the response at the excitation frequency, SNS-MOKE measurements are performed. The sample is excited at a constant RF frequency, while the bias field is swept. The MOKE signal was demodulated at an alias frequency corresponding to the excitation frequency. The frequency mixing process, which is used in SNS-MOKE, is described in Section 3.2.4. The measurements were repeated at different RF frequencies and power levels. As expected from the LLG, the low power sweeps yield a Lorentzian line shape, from which the resonance field is determined.

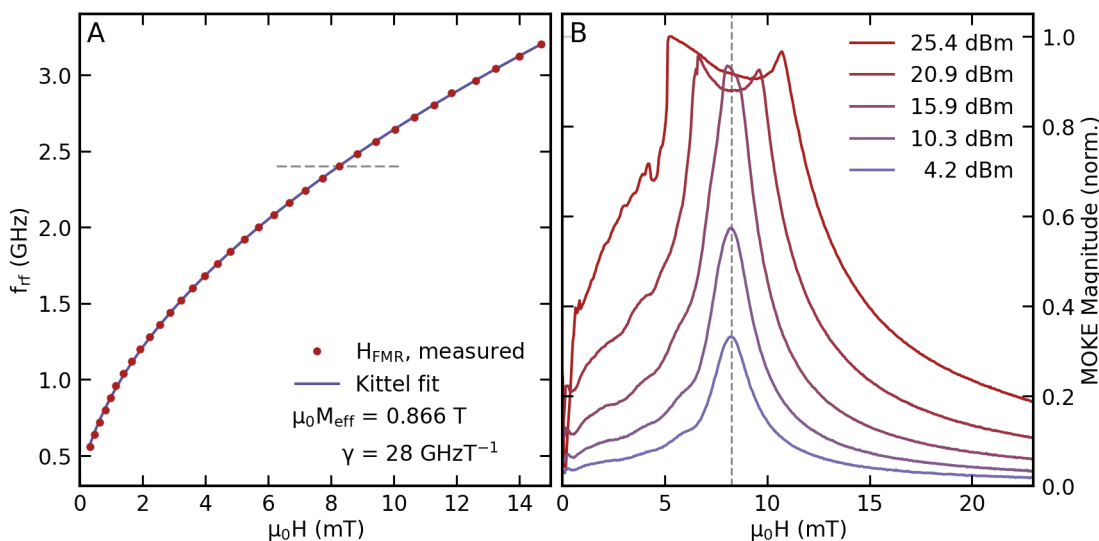


Figure 6.4. | **A:** Resonance field of the uniform mode for excitation frequencies from 500 MHz up to 3.2 GHz. The data were fitted using the Kittel equation. **B:** Power-dependent line shape of the uniform resonance mode (FMR) at a frequency of 2.4 GHz (grey dashed line in panel A). As the power increases, the initially Lorentz-like line shape becomes more and more distorted, especially in the low-field range. Both measurements have been conducted using SNS-MOKE. Figure adapted from [30].

The extracted resonance fields at different excitation frequencies are fitted to the Kittel equation (Equation 2.36), which allows to extract magnetic parameters of the NiFe film. This is depicted in Figure 6.4 A. The effective magnetization obtained amounts to $\mu_0 M_{\text{eff}} = 866 \text{ mT}$ and the gyromagnetic ratio to $\gamma = 28 \text{ GHz/T}$. These parameters are well expected for a NiFe film of 20 nm thickness.

Moving towards higher power levels, the line shape of the resonance changes signif-

icantly and becomes increasingly distorted, especially at the lower-field flank of the resonance. This is indicative of spin wave modes with wave vectors of $k \neq 0$, which are excited due to scattering processes and become more and more dominant at large excitation amplitudes. The deviation from the Lorentzian line shape, especially in the range of 0 mT to 5 mT, coincides with the field range where the higher harmonics of the excitation frequency have been observed with confocal NV center microscopy.

6.5. SNS-MOKE Maps at Low Bias Fields

As a next step, the spin waves which constitute the frequency comb are mapped using SNS-MOKE. The technique allows to detect arbitrarily chosen frequency components of the spin waves which are excited in the sample, independent of the excitation frequency. Magnitude and phase of the spin waves can be obtained simultaneously. As the sample is scanned under the microscope, spatially resolved images are recorded, which show the spatial distribution of the spin waves oscillating at the selected detection frequency.

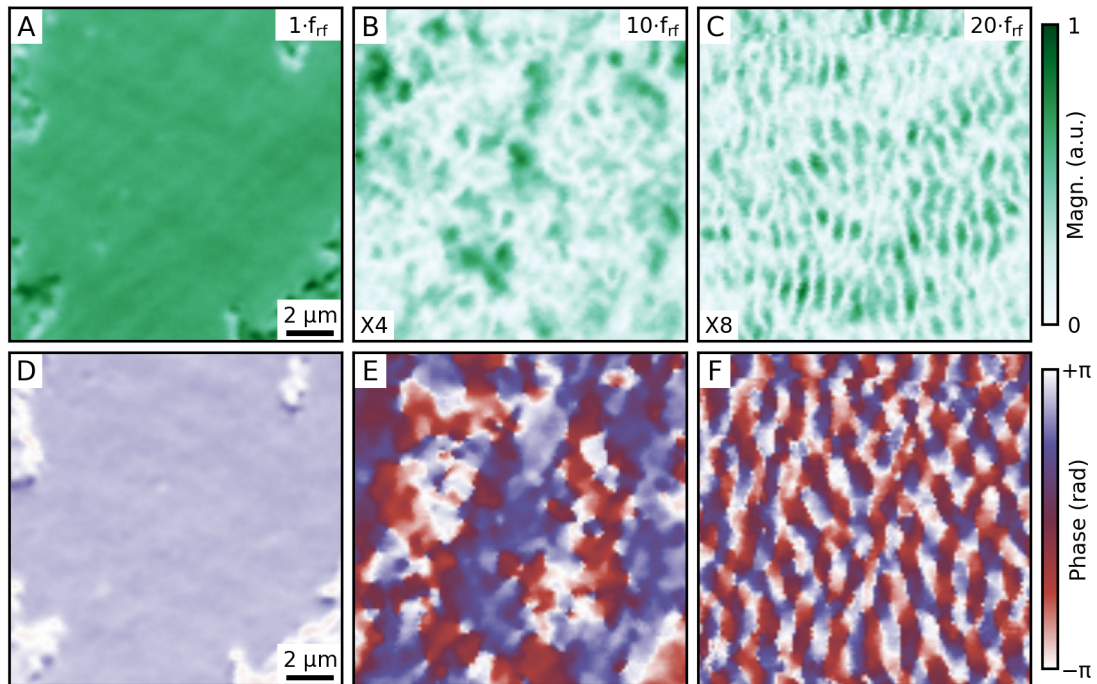


Figure 6.5. | Spatially resolved SNS-MOKE measurements conducted on the extended NiFe film in the center of the signal line of the CPW. The demodulation frequency was set to obtain the signal components directly at the excitation frequency of $f_{\text{rf}} = 191.4$ MHz, at ten times, and at twenty times the excitation frequency. A static bias field of 0.5 mT was applied along the CPW (horizontal direction) during the measurement. **A-C:** Magnitude of the demodulated signal. The signals of the different harmonics are plotted to the same scale, except, to improve visibility, the contrast was amplified by a factor of X4 in panel B and X8 in panel C. **D-F:** Phases of the demodulated signals with respect to the excitation frequency. Figure adapted from [30].

Figure 6.5 shows simultaneously recorded measurements at three different frequency components: one, ten and twenty times the excitation frequency of $f_{rf} = 191.4$ MHz. The signal demodulated directly at the excitation frequency has a largely constant magnitude and a uniform phase across the measurement area. The inhomogeneities visible in the corners of the measurement area are not of magnetic origin, but caused by nano diamonds on the sample. A homogeneous response is expected, since the NiFe layer is excited well below its FMR condition. Here, the magnetization follows the homogeneous excitation field more or less directly, i.e. all magnetic moments are precessing with the same phase and the wave vector is approximately zero.

As expected from the NV center magnetometry measurements, the 10th and 20th harmonic of the excitation frequency indeed show non-vanishing signals. Unsurprisingly, the magnitude of these spin waves is smaller than the response at f_{rf} by a factor of four and eight, respectively. Unlike at the fundamental frequency, the spin wave pattern is not homogeneous, but exhibits a certain position-dependent phase relation with respect to the excitation frequency. For the 10th harmonic this phase appears rather disordered. The 20th harmonic, however, displays a well ordered phase pattern with a much smaller feature size, or a larger wave vector.

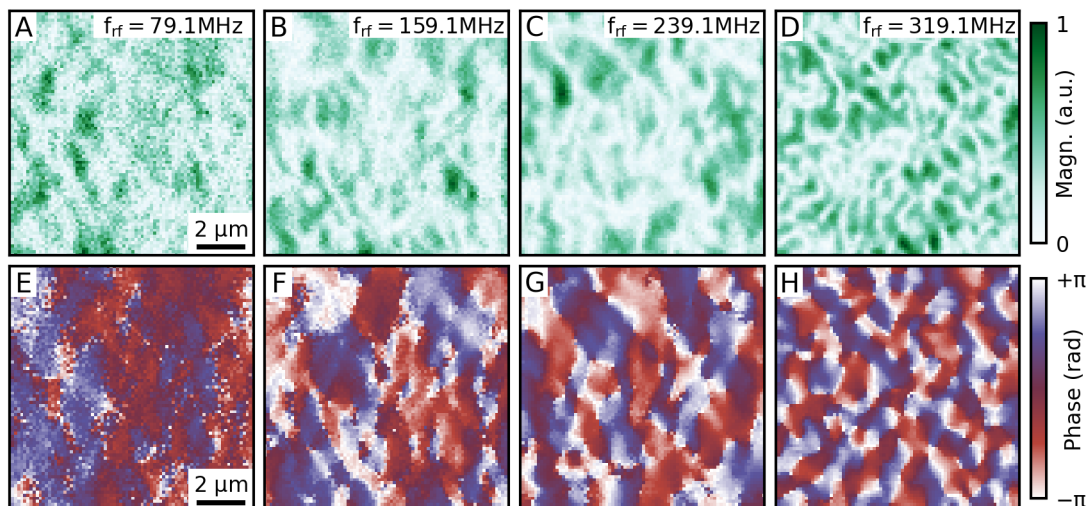


Figure 6.6. | Series of spatially resolved SNS-MOKE measurements conducted on the extended NiFe film in the center of the signal line of the CPW. The excitation frequency was varied and the signals were demodulated at the 10th harmonic of the respective excitation frequency. A static bias field of 0.5 mT was applied along the CPW (horizontal direction). **A-D:** Magnitudes of the demodulated signals, plotted to the same scale. The excitation frequency is shown in the upper right corner. **E-H:** Phases of the demodulated signals with respect to the excitation frequency.

The comb lines observed with NV center magnetometry extend all the way down into the range of a few tens of MHz, suggesting that the comb generation is largely independent of the excitation frequency. This behavior is investigated through a series of SNS-MOKE measurements with excitation frequencies between 79 MHz and 319 MHz. In Figure 6.6, a spatially resolved mapping, exemplary at the 10th harmonic of the

respective excitation frequency, is shown. For any of these frequencies, an inhomogeneous spin wave patterns can be observed, i.e. a frequency comb is generated. This confirms that, independent of the excitation frequency, spin waves precessing at integer multiples of this frequency are generated.

When comparing the spin wave patterns of the individual measurements, an increasing wave vector with increasing excitation frequency is observed. A higher excitation frequency also means a higher frequency of the respective 10th harmonic, which is detected in this measurement. Like in the previously discussed comparison of different harmonics of the same excitation frequency, higher spin wave frequencies appear to show a clearer phase pattern.

Still, it is not clear what exactly is the decisive factor that determines the observed wave vectors. To clarify this, the data from the same measurements are evaluated in a different way. Figure 6.7 shows the spin wave patterns for the different excitation frequencies, but this time evaluated at different harmonics, such that the frequency of detection is almost identical (around 955 MHz). This measurement shows that the spin wave pattern indeed depends on the mode number. The two measurements with a high harmonic number (Figure 6.7E and F with $n = 12$ and $n = 6$, respectively) display similar wave vectors. Lower harmonic numbers show an increasingly uniform response.

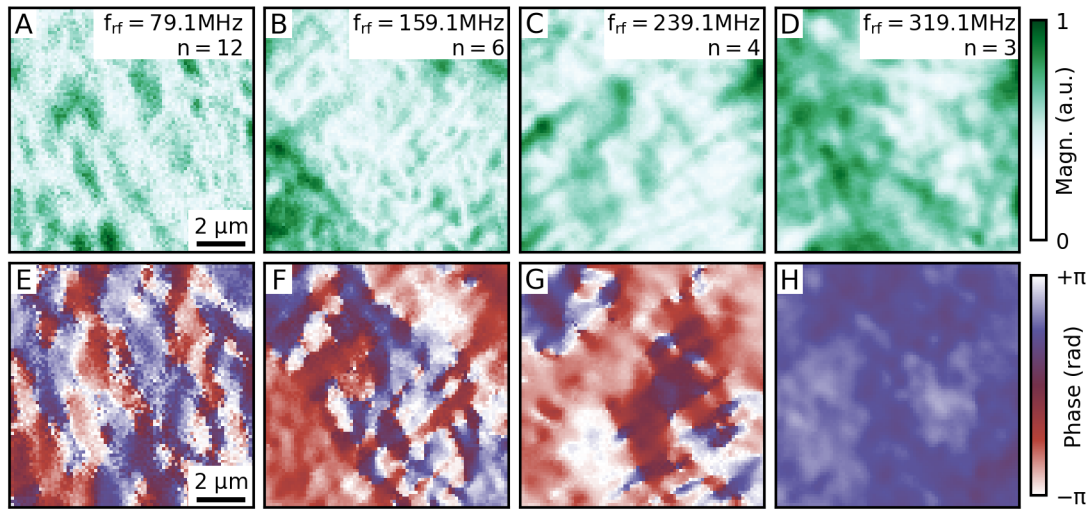


Figure 6.7. | Series of spatially resolved SNS-MOKE measurements conducted on the extended NiFe film in the center of the signal line of the CPW. The excitation frequency was varied and the signals were demodulated at different harmonics, such that the demodulation frequency is similar for all measurements (around 955 MHz). A static bias field of 0.5 mT was applied along the CPW (horizontal direction). **A-D:** Magnitudes of the demodulated signals, plotted to the same scale. The excitation frequency and the harmonic number are shown in the upper right corner. **E-H:** Phases of the demodulated signals with respect to the excitation frequency.

A possible explanation may be as follows: The observed phase pattern is the result of a complex interference process of spin waves. Slight spatial inhomogeneities in the excitation field, or perhaps in the sample itself, may alter the phase of the response. In the case of identical excitation and detection frequency, i.e. at the FMR condition, small

inhomogeneities of the excitation field or the sample itself do not perturb the phase of the uniform precession enough to disturb the picture of a homogeneous response. The higher the harmonic mode number, the larger the discrepancy between the excitation and the detection frequency. Inhomogeneities in the phase of the fundamental mode are amplified for higher frequencies and could lead to an increasing spatial modulation of the generated spin waves. The closer both frequencies are, the fewer harmonics need to be bridged and small inhomogeneities have less influence.

To further investigate the nature of the spin waves which oscillate at the different harmonic frequencies, Figure 6.8 shows a full set of phase maps of all harmonics, from the 1st to the 18th. The sample was excited with a frequency of $f_{\text{rf}} = 239.1$ MHz. Remarkably, besides the direct excitation at the FMR condition, which leads to a uniform precession (i.e. constant phase), also for the second and third harmonic, the phase signal is almost uniform. Starting from the 4th harmonic, a phase pattern is visible, whose feature size decreases with increasing harmonic mode number. This suggests that lower harmonics are fundamentally different in nature than the higher ones. Full sets of phase maps for other excitation frequencies are shown in Appendix D. For all probed frequencies from 79 MHz to 399 MHz, the behavior is very similar.

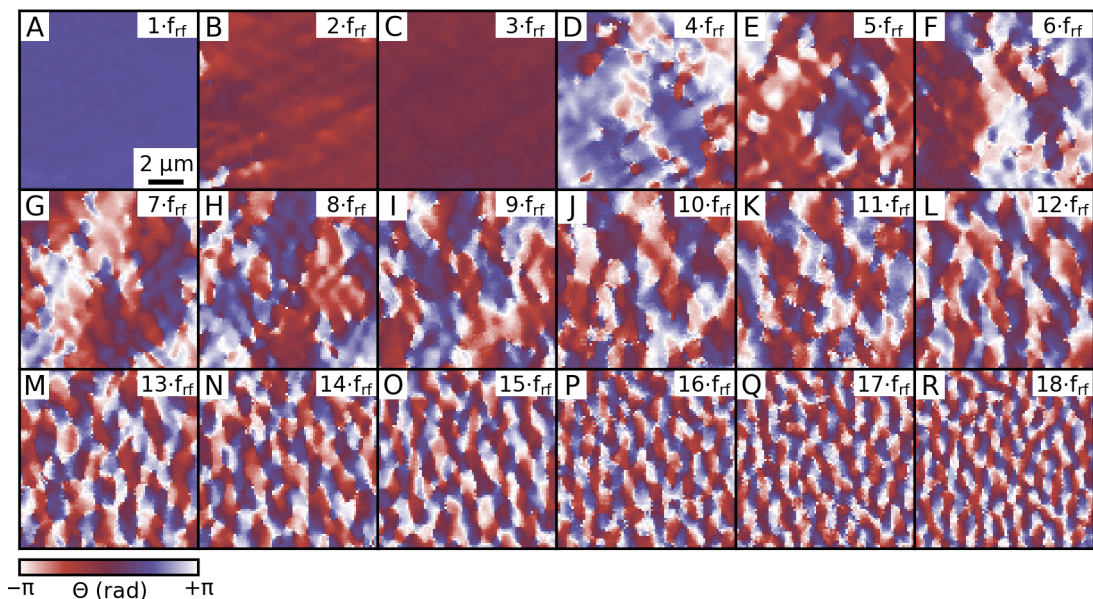


Figure 6.8. | Phase of the spin waves at different harmonics measured by SNS-MOKE from the 1st to the 18th harmonic of the excitation frequency of $f_{\text{rf}} = 239.1$ MHz.

From these phase patterns, the wave vectors of the spin waves can be extracted by performing a two-dimensional Fourier analysis. Exemplary momentum-space plots are shown in Figure 6.9 A-C for the 5th, 10th and the 15th harmonic. In case of a uniform precession, the momentum image shows a single intensity maximum at $k_x, k_y = 0$ (see Figure 6.9 A), while for higher harmonics, the intensity is distributed along two arcs at finite wave vectors, which shift toward larger wave vectors with increasing harmonic frequency. In any case, there is minimal signal along $k_x = 0$. This might be a result of

the excitation geometry, i.e. the RF field applied in y -direction.

The radius of the arc, which represents the total in-plane wave vector, is plotted against the frequency for each individual harmonic in Figure 6.9D. The analysis was repeated for different excitation frequencies. Additionally, the band of spin wave modes which are allowed in a 20 nm thick NiFe film was calculated for different angles between the wave vector of the spin waves and the external field, following Equation 2.45 and Equation 2.44, shown as a grey background. The extreme case, when the wave vector matches the field direction, is the BVSW geometry. A perpendicular alignment marks the DE geometry.

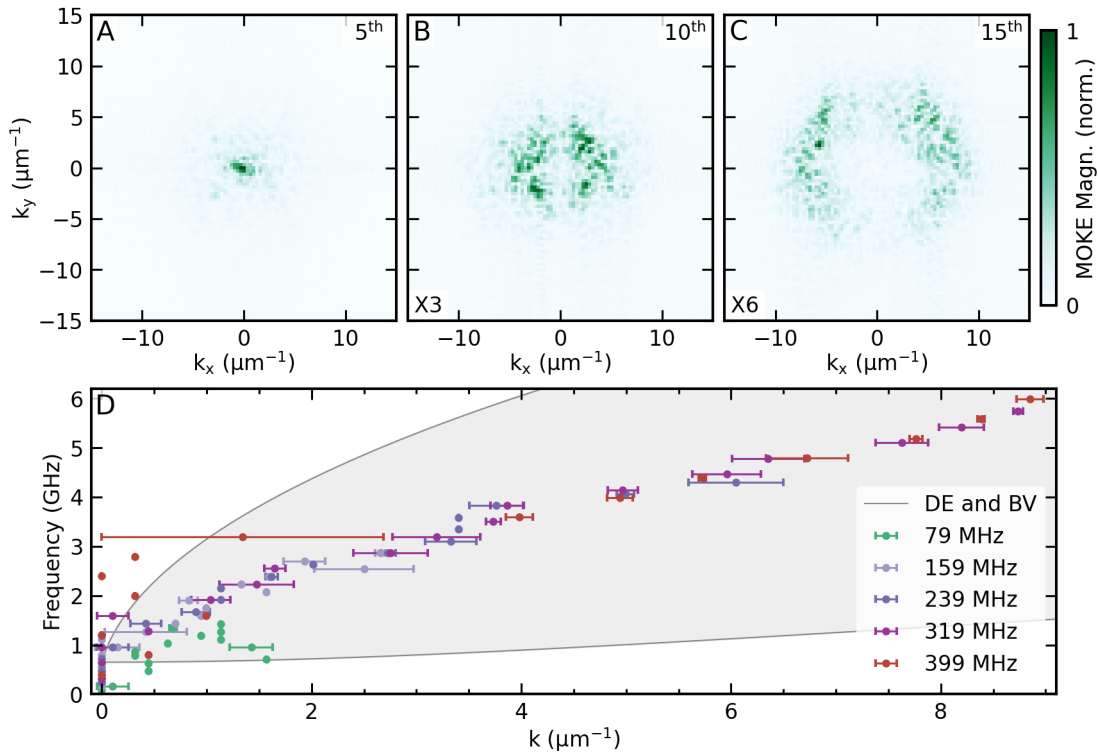


Figure 6.9. | **A-C:** Two-dimensional Fourier transforms of the spin wave phase maps of different harmonics at an excitation frequency of 319 MHz. These represent the distribution of wave vectors in x - and y -direction. The evaluation was repeated for different excitation frequencies. **D:** Total in-plane wave vectors versus the frequency of the harmonic, obtained by determining the radius of maximum intensity of the arcs. The error bars represent the uncertainty in the determination of the maximum. The data are aggregated for different excitation frequencies. The grey shaded area represents the spin wave band spanning from DE to BVSW geometry, calculated for a 20 nm-thick NiFe film. Figure adapted from [30].

The analysis reveals, that the response is homogeneous for the first few harmonics, as long as the frequency is below the spin wave band. This can be understood, as the magnetization is able to directly follow the total external magnetic field, which is the sum of static bias and RF excitation field. As this field has the same phase across the sample, no phase deviations in the response are expected.

When the harmonic frequency starts to lie within the spin wave band, the wave vector increases. Especially for higher harmonic modes, for all excitation frequencies the wave

vectors follow a common linear dependence on the respective frequency, located roughly in the center between DE and BSW geometry. A linear dependence in the spin wave band structure implies, that the phase velocity of the spin waves is the same for all harmonics, which is a hint for the origin of the spin waves.

6.6. Simulation of an Ideal NiFe Film

To learn about the nature of the high harmonic generation of spin waves, micromagnetic simulations are employed, starting with the most simple model, an ideal, infinitely-sized NiFe film. The simulations were performed using *Mumax3*, which has been described in Chapter 5.

6.6.1. Simulation Geometry and Sequence

In all simulations presented in the following, the x -direction represents the direction along the waveguide. This is also the direction in which the static bias field is applied. Perpendicular to that, in y -direction, a sinusoidally oscillating excitation field is applied. If not stated otherwise, the bias field has a magnitude of 0.5 mT and the excitation field has a peak amplitude of $700 \mu\text{T}_p$ and a frequency of 191.4 MHz.

The geometry in all simulations is chosen to be a two-dimensional grid, i.e. a single layer of moments. A two-dimensional simulation drastically reduces computation time compared to a fully three-dimensional model. While the software still properly takes into account dipolar effects scaling with layer thickness, a 2D simulation cannot model inhomogeneities in the magnetization along the z -direction. For example, it is unable to reproduce PSSW modes. These modes are not believed to play a major role in the frequency multiplication process, as the PSSW frequencies in a 20 nm-thick NiFe film are well above the relevant frequency range. It is, thus, well justified to treat the problem as two-dimensional.

The grid spacing in the simulation defines a maximum wave vector which can be represented. The spacing is set to be $d = 20 \text{ nm}$ in all directions. The resulting maximal wave vector is so large ($k = 2\pi/d = 314 \mu\text{m}^{-1}$), that this limit is of no concern for the effects to be simulated. The simulated grid consists of $256 \times 256 \times 1$ cells. In real units, the volume amounts to $5 \mu\text{m} \times 5 \mu\text{m}$ in x - and y -direction and 20 nm in z -direction, matching the thickness of the real film. To approximate an infinitely extended, ideal film, periodic boundary conditions are used. Furthermore, all magnetic moments (all cells) were set to have the same magnetic parameters. These parameters are listed in Appendix H.

To start the simulation, the magnetization is initialized to point along x -direction, but with a slight random variation across the whole volume. This state is equivalent to fully saturating the sample in a high magnetic field. The reason for introducing the small variation of the direction is to break the otherwise perfect symmetry. In order to

reach the ground state, the simulation is run for 10 ns before the bias field is switched on. After another 10 ns of relaxation the RF excitation field is applied.

With applied RF field, initially there is a transient dynamic phase in which the motion of the magnetization is chaotic. The system first needs to settle into a periodic regime, which takes a few tens nanoseconds. This initial phase is not representative of the actual measurement, since the excitation field is continuously present for the duration of the measurement. To only capture the periodic motion and to make sure that the settling phase does not influence the data analysis, the data of the first 200 ns after initiating the excitation field is discarded.

6.6.2. Simulation Results

Without excitation, the magnetization would entirely point along x -direction. The x -component of the magnetization would be unity, while the y - and z -components would be zero. The excitation field leads to a periodic, steady state precession of the magnetization vector around the equilibrium position. During the precession, the y -component of the magnetization oscillates sinusoidally around zero with the excitation frequency, as shown in Figure 6.10 B. The same is true for the z -component, which, however, is barely visible at the linear scale of the figure, which is normalized to the value of M_S .

In bulk material without anisotropy, the magnetization would precesses in a circular orbit around its equilibrium direction (the external field). This means, that m_y and m_z would oscillate with the same amplitude and frequency, and m_x would stay constant. This is not the case for a thin film, where the orbit of precession is elliptical. The large shape anisotropy due to the finite film thickness of only 20 nm strongly reduces the excursion angles in z -direction. As a result, the magnetization vector remains almost in the plane of the film and precesses on an extremely elliptical orbit with a large m_y -component and only a tiny m_z -component, which is about two orders of magnitude weaker. Still, the absolute value of the magnetization vector must remain unchanged. As a consequence, also the m_x -component must change during the precession. More details become visible when examining the response in frequency space. This is done by performing a Fourier transform of the time-domain data, and shown in Figure 6.10 C-E. The most prominent peaks in the m_x -spectrum are a peak at zero frequency, which is due to the predominant orientation of the magnetization in x -direction, and at twice the excitation frequency. The m_y - and m_z -spectra show the largest magnitude at the excitation frequency. The observed behavior is in line with the macrospin model, i.e. a perfect film behaves like a single spin with a certain anisotropy, which is excited by an RF field to oscillate.

The spectra also reveal harmonic frequency components at integer multiples of the main oscillation frequencies of the components. These harmonics are generated due to the intrinsic nonlinearity of the LLG. This comes about because the precession of

the magnetization generates additional stray fields. These oscillating fields add to the effective field that enters the LLG and modulate it. This alters the dynamics and is responsible for the generation of these higher harmonics.

In relation to the excitation frequency, only even harmonics are present for m_x and only odd harmonics appear for m_y and m_z . This is in contrast to the confocal NV center magnetometry measurements, which show all components with similar magnitudes. A cross-talk between the components of the magnetization vector is absent in this simulation, because it relies on inhomogeneous magnetic stray fields which would require breaking the symmetry.

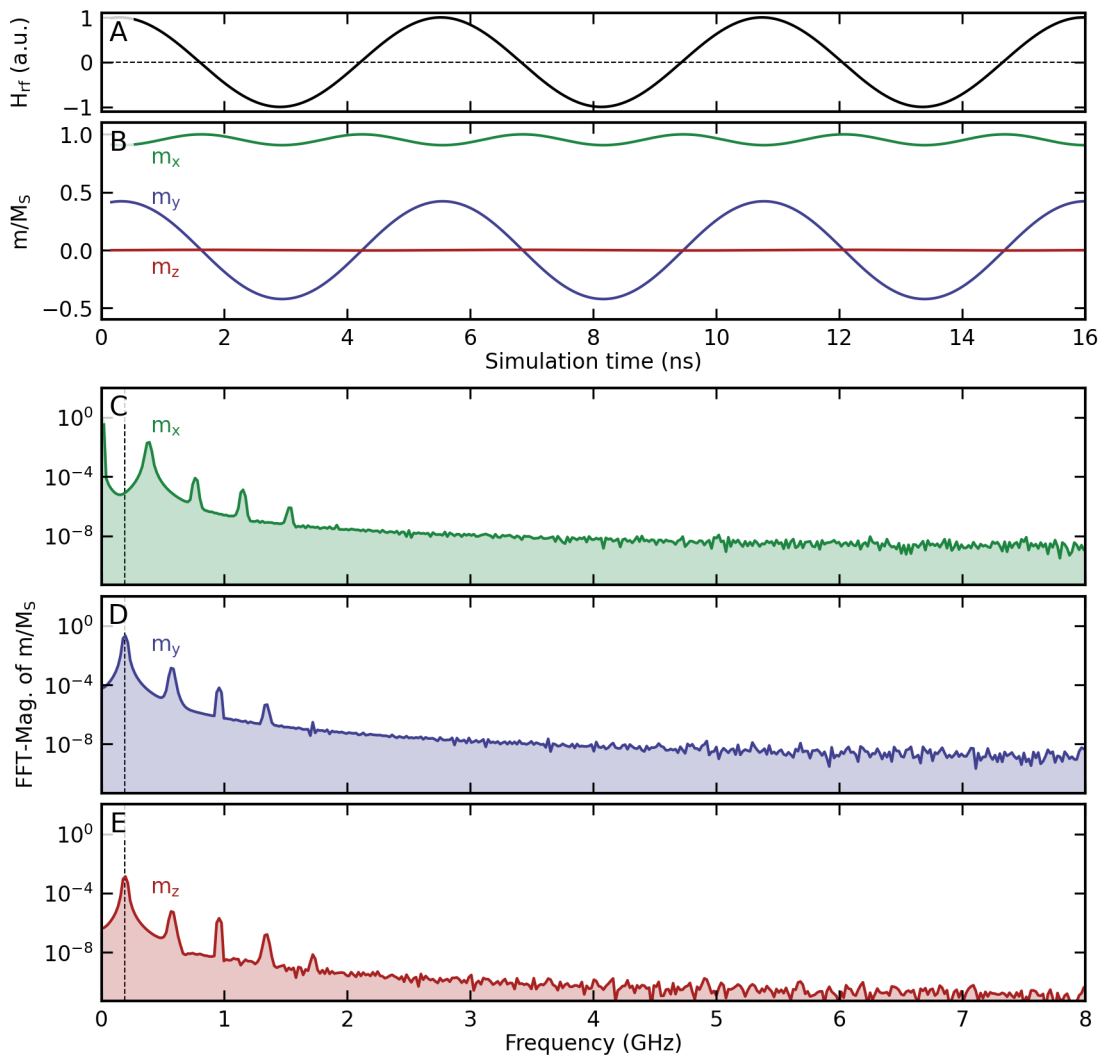


Figure 6.10. | Simulation of an infinitely large, ideal NiFe film. The film is magnetized in x -direction by a static bias field of 0.5 mT. Additionally, RF excitation of $700 \mu\text{T}_P$ is applied in y -direction at a frequency of 191.4 MHz. **A:** Excitation field H_{rf} . **B:** x -, y - and z -components of the magnetization of a single cell of the simulation, which are oscillating as a response to the excitation field. **C-E:** Magnitude of the Fourier transforms of the response of all three components. The excitation frequency is marked by the dashed lines.

The magnitude of the higher harmonics quickly decreases with the harmonic number. There already is a difference of about two orders of magnitude between the first and the second harmonic. Since NV centers are sensitive to a frequency of about 2.87 GHz, which equals the 15th harmonic in this scenario, it is hardly conceivable that these higher harmonics due to the nonlinearity of the LLG are responsible for the detected signals.

Both, the absent mixing of harmonic frequencies between the components of the magnetization, as well as the rapid decay, signify that the most simple model of a perfectly ordered thin film does not reproduce the effect. This leads to the conclusion that some form of magnetic disorder must to be present in the sample, which is responsible for the observed behavior.

6.7. Kerr Microscopy Measurements

To identify the magnetic inhomogeneities in the sample, wide-field Kerr microscopy is employed. It allows to record images of the magnetization state at different bias fields. The measurements were conducted in longitudinal MOKE geometry, i.e. the external magnetic field is applied along the direction of the NiFe stripe. Therefore, the microscope is sensitive to the magnetization component along the stripe. In general, also the out-of-plane component of the magnetization contributes to the signal. This small contribution is suppressed by subtracting Kerr images with opposite incidence angle of the light, yielding a pure longitudinal contrast.

Due to the magnetic softness of NiFe, bias fields as low as 1 mT along the stripe are sufficient to fully saturate the magnetization, as can be seen in Figure 6.11 A and F. Fields in between, and especially around 0 mT, lead to the emergence of a pronounced concertina-like domain pattern with inhomogeneous magnetization vectors (Figure 6.11 B to E). Due to the inhomogeneous magnetization, a hysteresis of the film, displayed in Figure 6.11 G, shows a rounded shape with small steps indicating the switching of small regions of the film.

Non-uniform switching of the film hints toward a spatial variation of magnetic properties. For example, roughness of the film could lead to a spatially dependent modulation of the effective field due to uncompensated microscopic stray fields. It could either be caused by an inhomogeneous thickness of the film itself, by surface roughness of the film, or by roughness of the underlying substrate or material layers. In addition, the polycrystallinity of the NiFe and impurities due to the growth process may locally alter the magnetic properties of the film. All of these causes, or a combination thereof, effectively break the symmetry of the system. This leads to a state known as concertina pattern, which is expected for long stripes of soft magnetic materials [188].

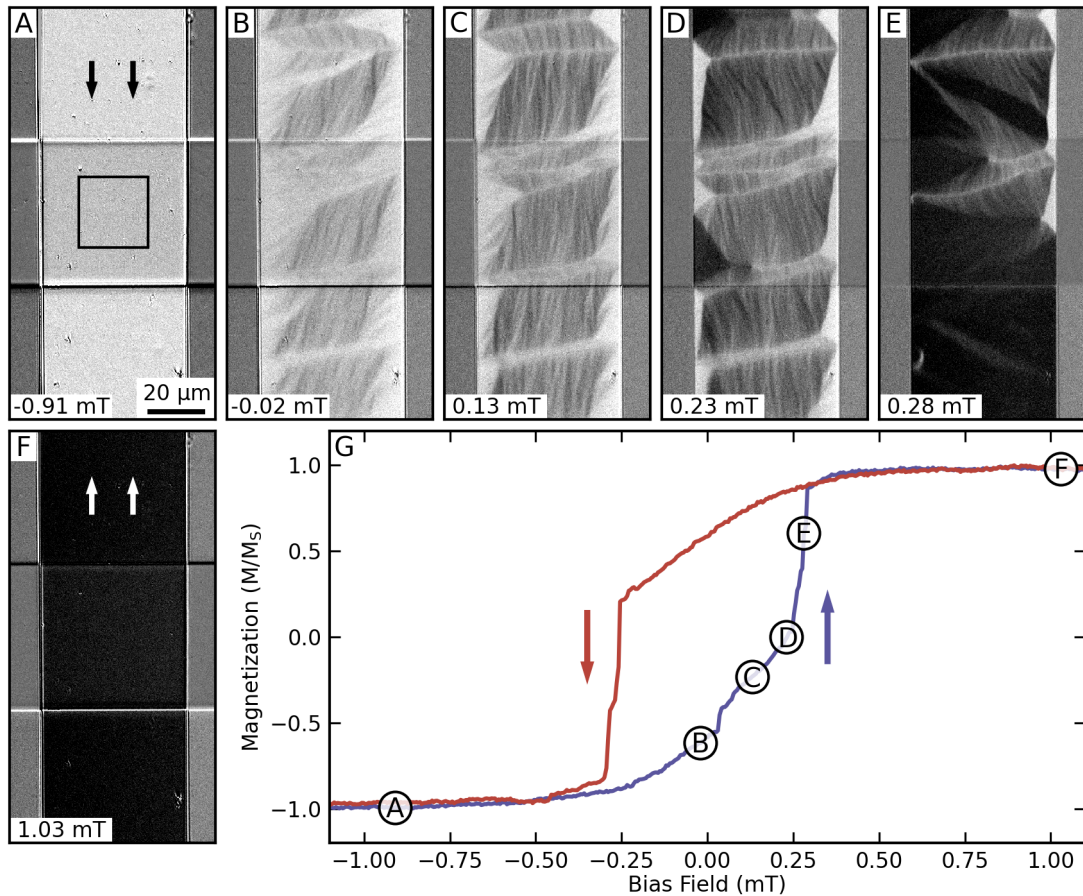


Figure 6.11. | Kerr microscopy images of the sample. The image was taken in longitudinal MOKE geometry under alternating illumination, ensuring a pure image of the longitudinal magnetization component. **A-F:** Images of the magnetization at fields from -1 mT to 1 mT. Black and white arrows indicate the direction of the magnetization in the saturated states. **G:** Magnetic hysteresis of the film obtained by averaging the signal over the area indicated by the black square in panel A while sweeping the field. The coercive field of the film is approximately 0.3 mT.

6.8. Simulation of a Stripe with Inhomogeneous Magnetization

To approach the non-uniform magnetization of the real sample in a simulation, a more complex geometry is introduced. The much more realistic model has the shape of a semi-infinite stripe, which is close to the film on the signal line of the real sample. Furthermore, the properties of the magnetization are not uniform, but the simulated volume is divided into a number of regions with different properties.

6.8.1. Simulation Geometry

From the measurements, it is not expected that spin waves with large wave vectors are involved in the frequency multiplication process. This justifies a larger spacing of the simulation grid of 100 nm. The larger spacing allows to simulate a 25 μm-wide

stripe, half as wide as the stripe on the real sample. Simulating a stripe is done by modifying the boundary conditions compared to the previous simulation: along x -direction, still, periodic boundary conditions are employed, while in y -direction, fixed boundary conditions are used. There still might be a minor difference in stiffness of the simulated and real film due to shape anisotropy, but it is expected to be negligible. The stripe is divided into many, randomly shaped regions, as depicted in Figure 6.12 A. The size of the regions is on the order of $\sim 1 \mu\text{m}$. A small uniaxial anisotropy of $K_U = 500 \text{ J/cm}^3$ is set for all regions, together with a randomly varying anisotropy direction. The saturation magnetization is the same in all regions.

6.8.2. Static Behavior

Figure 6.12 B and C show the m_y -component of the magnetization, relaxed into its ground state at zero field and at a field of 0.5 mT in x -direction, respectively. In this simulation, the magnetization does not just show a uniform state, but regions where it tilts in positive or negative y -direction. This is the concertina pattern, typical for stripes of ferromagnetic material, which also has been observed in the real sample using Kerr microscopy. The domain pattern present in the ground state reduces the demagnetizing energy compared to a fully homogeneous magnetization state. The exact appearance of the domains is guided by local internal fields and the shape anisotropy.

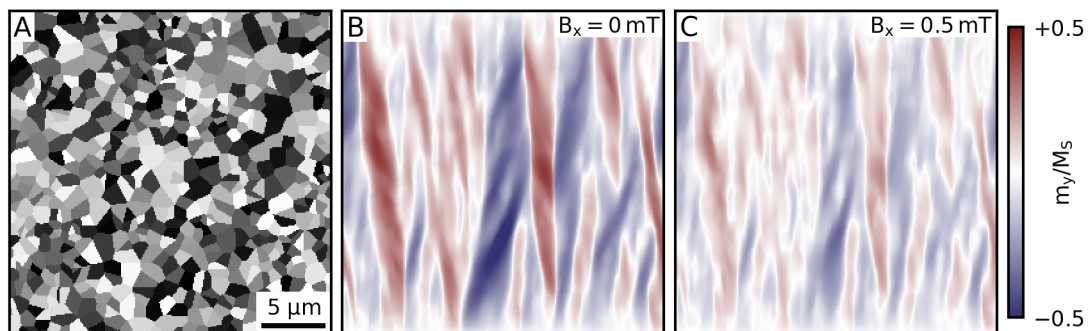


Figure 6.12. | Simulation of a semi-infinite stripe with regions, where the direction of the anisotropy is randomly varied. The stripe has a width of $25 \mu\text{m}$. **A:** Distribution of regions. Every shade of grey represents a different, random anisotropy direction. **B:** Simulated ground state at zero bias field. **C:** Simulated ground state at a static bias field of 0.5 mT in x -direction. Both panels show a buckling of the magnetization into a concertina-like pattern.

The concertina pattern is most pronounced at zero field. Any additional field in x -direction forces the magnetization into a more parallel alignment. On close look, the m_y -component is weaker at the top and bottom end of the figure, which marks the boundaries of the stripe. In these regions, the shape anisotropy of the stripe favors an alignment of the magnetization parallel to the stripes edges, reducing m_y .

6.8.3. Dynamic Response

An RF excitation field leads to a switching of the different magnetic regions, everywhere across the sample. Figure 6.13 shows snapshots of the m_y - and m_z -component of the magnetization during one period of the excitation field. The average magnetization tilts during the excitation cycle significantly and oscillates in $\pm y$ -direction, as a consequence of the sum of the static bias field in x - and the excitation field applied in y -direction. On top of that, the different internal fields at every boundary result in a different timing of the switching with respect to the excitation field, i.e. a different phase relation. Upon switching, spin waves appear everywhere across the stripe.

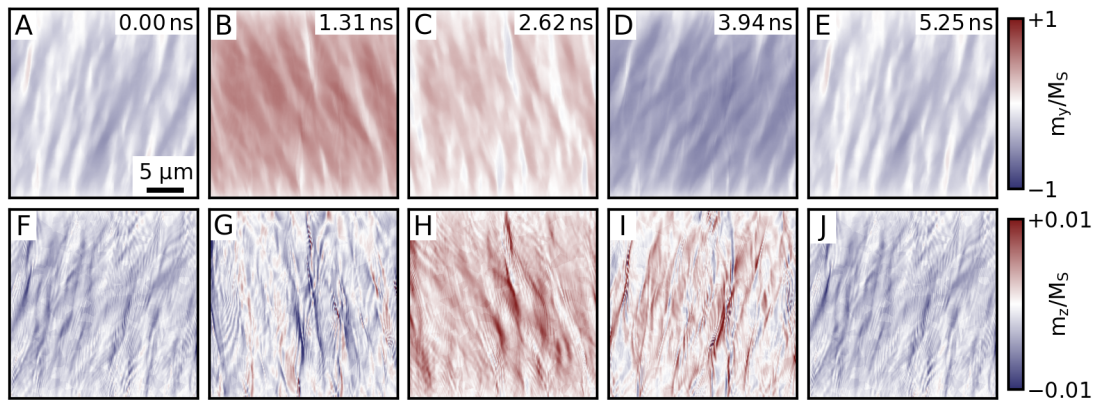


Figure 6.13. | Simulation of a semi-infinite stripe with grains where the direction of the anisotropy is varied randomly. The stripe has a width of $25 \mu\text{m}$. RF excitation of $700 \mu\text{T}_P$ is applied in y -direction at a frequency of 191.4 MHz . **A-E:** Snapshots of the y -component of the magnetization during a full cycle of the excitation. **F-J:** Snapshots of the z -component of the magnetization. Spin waves are emitted throughout the stripe and propagate in different directions.

An evaluation of the dynamics at a certain position is performed in Figure 6.14, which, as the corresponding figure for the previously discussed simulation of the perfect film, shows time traces of the excitation field in panel A, the magnetization components in panel B and the Fourier spectra thereof in panel C. The magnetization time trace is plotted for different cells of the simulation (light shaded graphs in panel B). The exact shape of the curves strongly depends on the position. The response averaged across all cells (dark shaded graphs in panel B) oscillates sinusoidally, much like in the simulation of the perfect film. This indicates, that the spin wave generation process must be very local and averages out across the sample. The Fourier spectra of the magnetization components were calculated for a simulation cell in the center of the volume. They display an emerging frequency comb, that stretches way into the GHz range. The magnitude of the harmonics only slowly decays with frequency, as could be seen from the confocal NV measurements on the real sample. Compared to the highly symmetric situation in the perfect film, the imbalance between even and odd harmonics is lifted because of the much increased mixing of the components, mediated by inhomogeneous internal fields due to the greater disorder in the system.

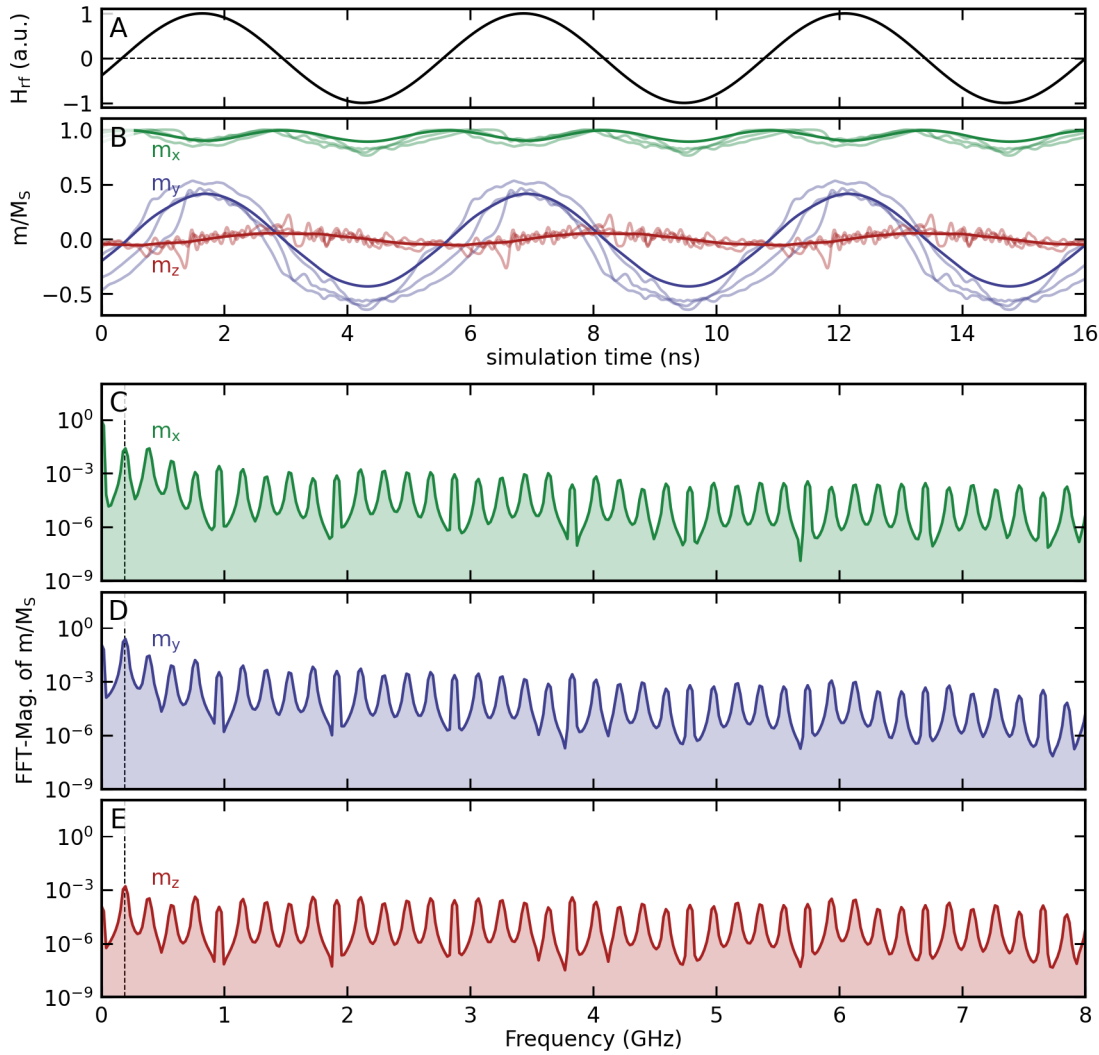


Figure 6.14. | Simulation of a semi-infinite stripe with grains where the direction of the anisotropy is varied randomly. The stripe has a width of $25\ \mu\text{m}$. It is magnetized along x -direction by a static bias field of $0.5\ \text{mT}$. RF excitation of $700\ \mu\text{T}_P$ is applied in y -direction at a frequency of $191\ \text{MHz}$. **A:** Time trace of the excitation field H_{rf} . **B:** x -, y - and z -components of the magnetization. The dark shaded curves are the mean values averaged across the whole sample. The light shades represent single cells in the center of the stripe, and $12.5\ \mu\text{m}$ in x and y direction. For better visibility, the z -component is magnified by a factor of X20. **C:** Fourier transform of the response of all three components, showing a frequency comb with many high harmonics. The evaluated cell is in the center of the stripe.

The spatial variation of the response can be examined in a spatial map of the magnitude and phase of the Fourier components of the time trace, which is presented in Figure 6.15. Panels A-C show the magnitudes and D-F the phases of spin waves precessing at the 1st, 10th and 20th harmonic of the excitation frequency. The first harmonic shows an almost uniform phase, as is expected from the uniform response of the magnetization to the excitation field. However, the 10th and 20th harmonic show regular phase patterns. These are directly comparable to the spin wave patterns measured by SNS-MOKE, which were discussed in Section 6.5. The close match with the experimen-

tal data supports the validity of the simulated model. A magnetic stripe consisting of small regions with slightly different properties well reproduces the observed dynamics.

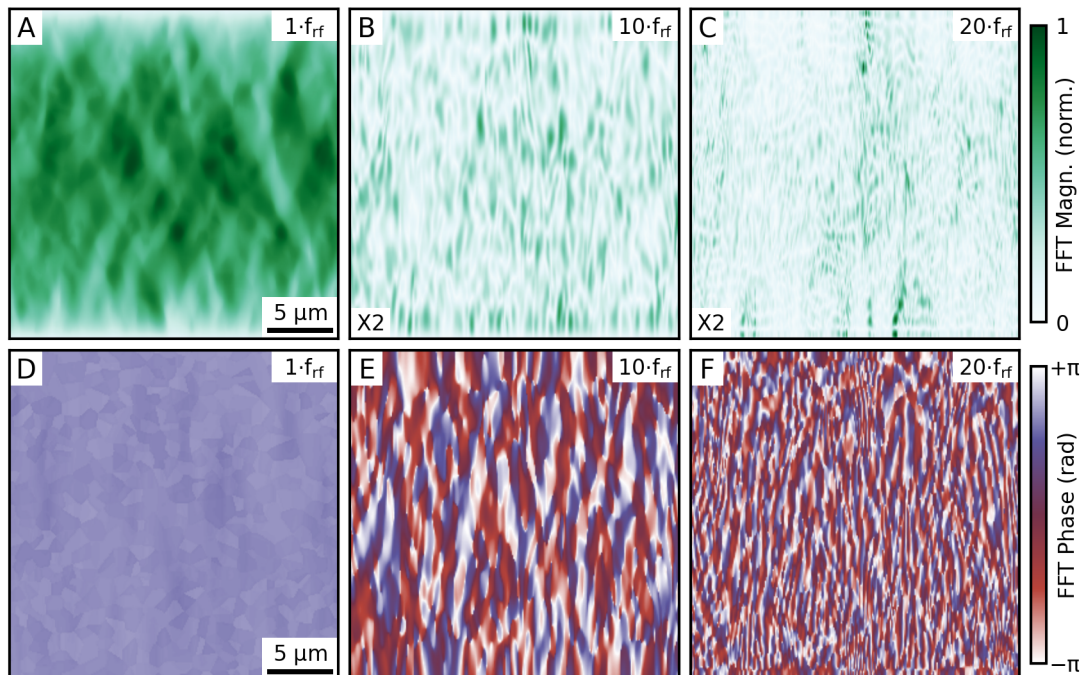


Figure 6.15. | Simulation of a semi-infinite stripe with small regions, where the direction of the anisotropy is randomly varied. The stripe has a width of $25\ \mu\text{m}$. It is magnetized along x -direction by a static bias field of $0.5\ \text{mT}$. RF excitation of $700\ \mu\text{T}_P$ is applied in y -direction at a frequency of $191\ \text{MHz}$. **A-C:** Magnitude of the Fourier components of the z -component of the magnetization. **D-F:** Phase of the Fourier components at the 1st, 10th and 20th harmonic of the excitation frequency.

The spin wave patterns that emerge for the higher harmonics can be understood as a superposition of the spin waves that are emitted at every boundary between two regions, where the magnetization tilts and switches due to the RF excitation. Because of the spatial variation of the internal fields, different regions have different threshold fields to trigger their switching. Hence, the switching occurs at a different points in the excitation cycle, i.e. at a different phase. Furthermore, the spin waves which are emitted when the first regions switch propagate across the sample. Their stray fields add to the effective field that the magnetization experiences in other places. This can ultimately trigger or delay the switching of other regions and, in this way, lead to synchronization. The result of these processes is an overall non-vanishing magnitude and a different phase relation of the spin waves with respect to the excitation field, depending on the exact position on the sample.

6.9. Simulation of an Individual Boundary Between Two Magnetic Regions

In the previous section, the fundamental differences in the simulated dynamic response between an ideal film and a more realistic NiFe film were evaluated and discussed. The reason for introducing regions with different magnetic parameters was to mimic the slight spatial variation of the properties, which inevitably is present in a real sample. These could be caused, for example, by variations of the film thickness, surface roughness, anisotropies due to strain or the orientation of the crystallites, of which real NiFe consists, or a different saturation magnetization due to deviations of the stoichiometry or impurities. Independent of the exact cause, this variation breaks the perfect symmetry of the sample. The aim is to understand the consequences of this symmetry breaking. For this purpose, the simulated problem is simplified. The following simulation examines the behavior that emerges when only two areas with a difference in one of the magnetic properties meet at a boundary. This much simpler problem will help to develop a microscopic model, that leads to the generation of the observed high harmonic spin waves.

6.9.1. Simulation Geometry

For this purpose, a magnetic stripe is simulated with a single boundary between the two areas. The simulation volume is divided into two regions, a left region where the magnetic properties are kept unchanged and a right region where M_S is reduced by 20%. Fixed boundary conditions are used along both, x - and y -direction. Like this, the simulation would resemble a magnetic square consisting of two regions. To make it appear as a stripe, the surface charges at the $\pm x$ edges of the simulation volume are artificially removed. In this way, the simulation mimics an infinitely long stripe with a single step in M_S at its center. In this simplified model, the cell size can be reduced back to 20 nm, to allow for spin waves with high wave vectors, as they cannot be fully excluded from playing a role in the process. Due to limited computational resources, the number of simulated cells is limited to 256×256 . The simulated stripe hence has a width of about 5 μm . This does not influence the magnetic behavior significantly, aside from a small contribution to the shape anisotropy, which tends to increase magnetic stiffness. The setup of the simulation is shown in Figure 6.16 A.

6.9.2. Static Behavior and Switching Model

As in the previous simulations, a static bias field of 0.5 mT is applied along x -direction. This time, due to the presence of the boundary and the difference in M_S between the two regions, the ground state is not a homogeneous magnetization pointing purely in x -direction. At the position of the step, stray fields emerge. The normal component of the magnetic flux density \mathbf{B} must be continuous across the boundary. This implies

that, since $\mathbf{B} = \mu_0 (\mathbf{H} + \mathbf{M})$, if there is a discontinuous decrease in \mathbf{M} , the magnetic field \mathbf{H} must increase, giving rise to an additional demagnetizing field \mathbf{H}_D .

This comes with an additional energy penalty and gives rise to a new ground state, which is reached when the magnetization in the vicinity of the step slightly tilts towards one or the other direction. The tilt of the magnetic moments comes with an energy cost, as well, but at the same time reduces the stray fields at the boundary, as depicted in Figure 6.16 B. The panels D-F show the three components of the magnetization from the simulated ground state. The tilt is best visible in the m_y -component, displayed in Figure 6.16 E. At the same time, there is only a slight decrease in m_x (panel D) in the vicinity of the boundary and almost no change in m_z , again, due to the shape anisotropy (panel F).

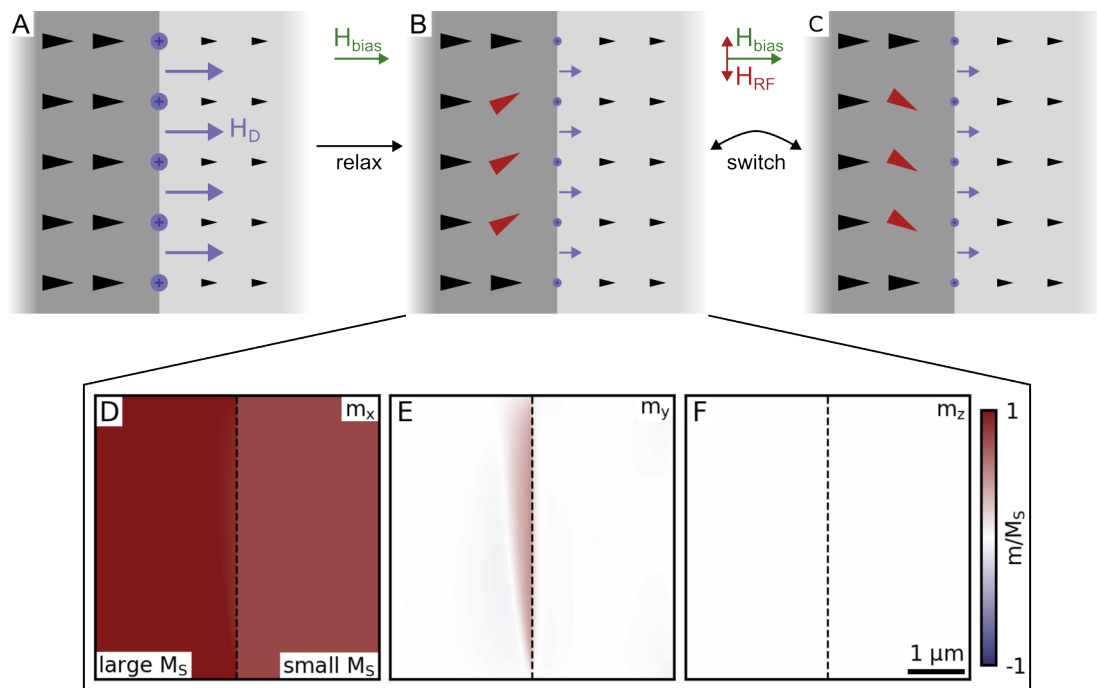


Figure 6.16. | Model of a single step in a semi-infinite stripe. In the right region, the saturation magnetization is 20% smaller than in the left. The stripe has a width of 5 μm . **A:** Hypothetical situation if all moments would point along x -direction. This is not the ground state, as stray fields would emerge from the boundary (blue arrows). **B:** True ground state, where moments at the boundary tilt to reduce stray field energy. **C:** Upon excitation the system can switch into a second possible low-energy state and keeps oscillating between both states. **D-F:** Simulated ground state without excitation field. A static bias field of 0.5 mT is present in x -direction. The dashed line indicates the boundary between the regions. Figure adapted from [30].

6.9.3. Dynamic Response

In this simple model, there are two energetically degenerate ground states (positive or negative m_y -component). When an oscillating excitation field is applied in y -direction, this degeneracy is lifted and at a certain point the magnetization overcomes the energy barrier due to the stray field at the boundary and switches into the other state, depend-

ing on the current phase of the excitation field. This switching is not to be confused with a full switching of the magnetization from m to $-m$, but rather a rapid change in tilt angle by a few or 10s of degrees, depending on the exact setup of the step and the energies involved.

The rapid switching appears first in a single point, which then propagates along the region boundary, similar to a one-dimensional domain wall. Naturally, the switching magnetization generates spin waves which propagate away from the boundary. Figure 6.17 shows snapshots of the y - and z -components of the magnetization across one period of the excitation field. As the excitation frequency in this simulation was 191.4 MHz, one period is about 5.2 ns.

The snapshots show the switching point moving in y -direction at first, until it reaches the boundary, and then moving in $-y$ -direction in the second half of the excitation cycle. While it does so, spin waves are generated which propagate away from the boundary. The velocity of the switching point is about 4 km/s, while the spin wave velocity is only approximately 1 km/s. The effect is thus similar to a supersonic air plane generating a cone of sound waves behind. The angle between the wave fronts and boundary is a result of the different velocities. The spin waves only slowly disperse when moving away from the boundary, which is evident by the almost linear dispersion observed in the experiment. This gives them solitonic character.

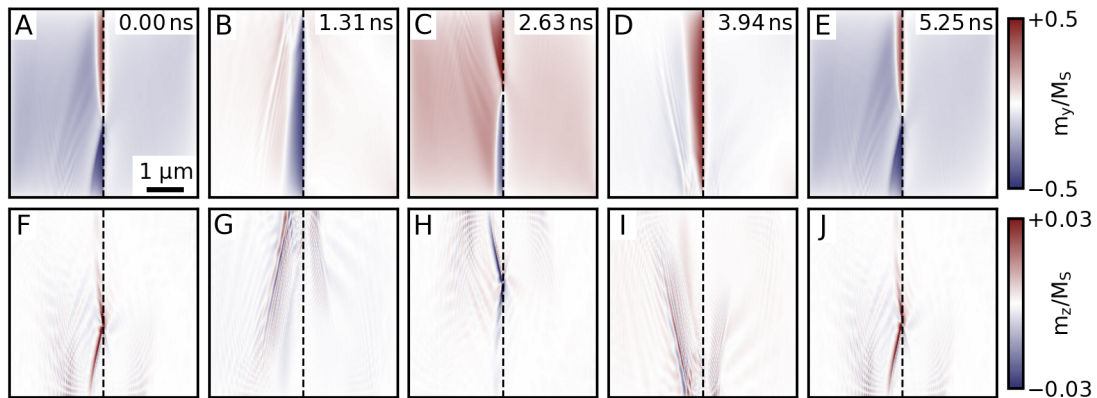


Figure 6.17. | Simulation of a single step in a semi-infinite stripe. RF excitation of $700 \mu\text{T}_P$ is applied in y -direction at a frequency of 191.4 MHz. **A-E:** Snapshots of the y -component of the magnetization during a full cycle of the excitation. **F-J:** Snapshots of the z -component of the magnetization. Upon switching spin waves are emitted from the boundary and propagate away from it. The dashed line indicates the boundary between the regions.

In the snapshots, it is visible that in the left region the spin waves are stronger than in the right region. This is due to the difference in M_S . The tilting initially appears only in the region with large M_S , and this is also what generates the switching effect and ultimately the spin waves. Only then, they can partially transmit through the boundary into the right region with 20% smaller M_S and propagate there.

The time evolution and Fourier transform of the magnetization are evaluated near the boundary, as displayed in Figure 6.18. Panel A shows the sinusoidal excitation field.

The time trace of the magnetization, shown in Figure 6.18 B, differs significantly from previous simulations. While it still exhibits the periodicity of the excitation field, the m_y -component (blue) almost resembles a square waveform, indicative of the switching behavior. During the switching, a rapidly oscillating m_z -component (red) is present. Lighter shades of the traces indicate positions further away (100 nm and 200 nm) from the boundary. The larger the propagation distance, the more rounded the shape of the waveform becomes, because of the gradual dispersion of the frequency components contained in the spin wave cone.

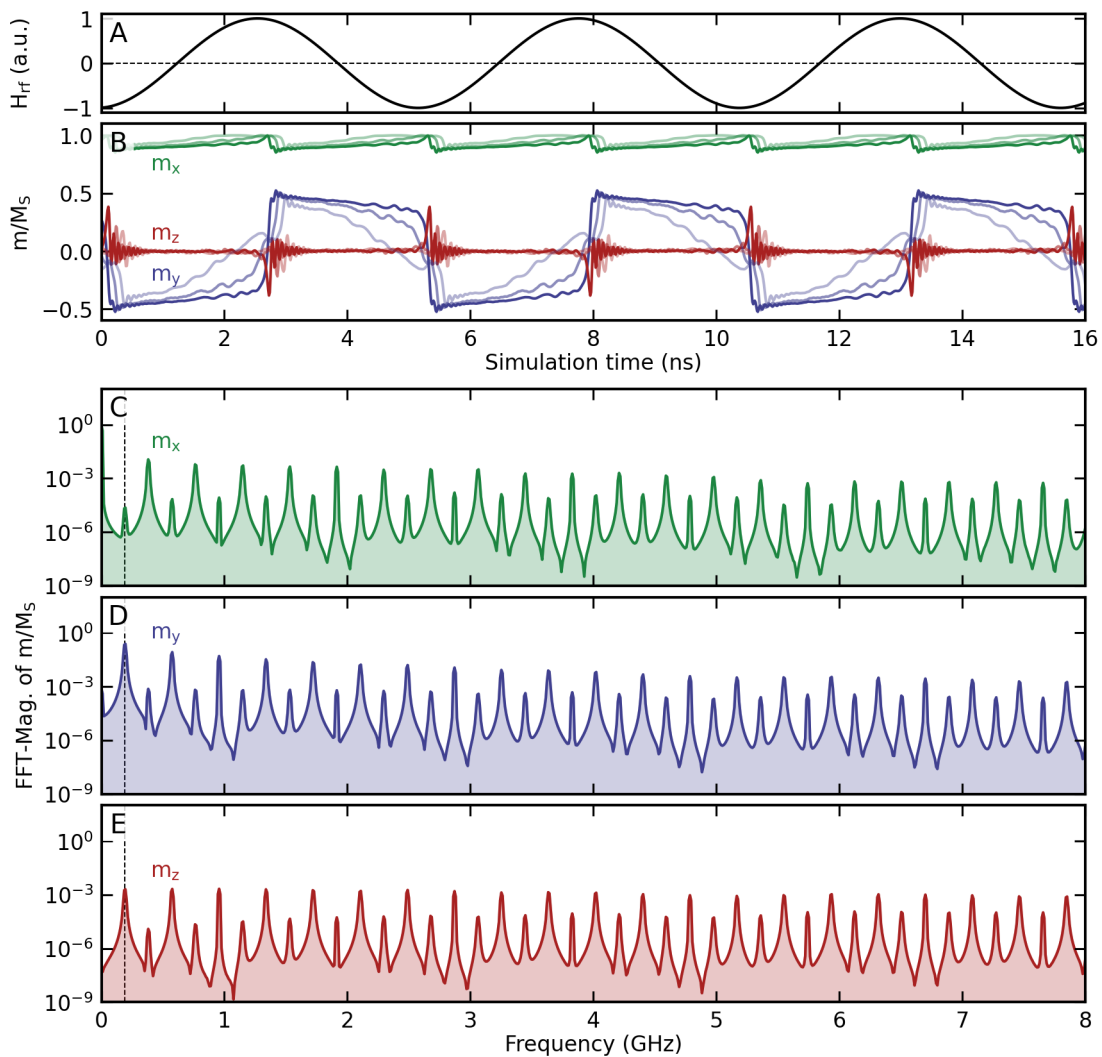


Figure 6.18. | Simulation of a semi-infinite stripe with a single step. The stripe is magnetized along x -direction by a static bias field of 0.5 mT. RF excitation of $700 \mu\text{T}_p$ is applied in y -direction at a frequency of 191.4 MHz. **A:** Time trace of the excitation field H_{rf} . **B:** Time evolution of the x -, y - and z -components of the magnetization, evaluated in a single cell of the simulation in the center of the stripe. The different shades represent cells directly at the boundary (darkest), as well as at 100 nm and 200 nm distance from it (lightest). For better visibility the z -component is magnified by a factor of five. **C:** Fourier transform of the response of all three components, showing a frequency comb with many high harmonics.

Figure 6.18 C shows the FFT of the time traces, evaluated directly at the boundary between the two regions. All components of the magnetization show a frequency comb extending from the base frequency of 191 MHz all the way up to several GHz, with only slowly decaying magnitude. In the ideal film, the difference in magnitude between the first and the second next harmonic already is about two orders of magnitude, while in the step model, the difference is less than one order of magnitude. The decay decreases even further for higher harmonics and reaches a plateau. In the simulation of a perfect film, there was no mixing between the m_x -, m_y - and m_z -components of the magnetization. In the simulation with a simple step, there already is sufficient cross-talk and mixing between the components due to the broken symmetry, that all harmonics appear in the spectra for all components.

The two-area model not only works when the saturation magnetization is different between the two regions. The same role can be fulfilled by thickness or anisotropy (-direction) of the material, as all of those may lead to stray fields and induce a similar tilting and potentially a similar frequency comb generation. The behavior of the magnetization in this simple simulation already fits the observed signals well. It is the basis for the previously discussed more realistic model with many different magnetic regions, where this kind of switching occurs at every boundary, resulting in the emission and interference of the high harmonic spin waves.

6.10. Miniaturizing Active Structures

In the previous sections, the effect of frequency multiplication was studied in a continuous NiFe film. To utilize all magnonic frequency multiplication in future devices, it is crucial to shrink the active structures significantly, at least down into the micrometer regime. The following section contains measurements of the high harmonics obtained within such microstructures. For this, samples with a new layout were fabricated, as is described in the following. These samples were investigated by means of SNS-MOKE microscopy, and in addition, scanning NV center microscopy. This new tool is used with the aim to image the spatial distribution of the magnetization with the highest possible spatial resolution.

6.10.1. Sample Layout

The samples were fabricated in a similar way as the previously investigated samples with extended NiFe layer. A schematic of the sample layout is shown in Figure 6.19. First, a resist mask of the CPW was fabricated by optical lithography on undoped silicon substrate. Subsequently, a thin adhesion layer of titanium was deposited, followed by 100 nm of gold using sputter deposition. In a second EBL step, an additional resist mask was created. This contains the elliptically and rectangularly shaped elements on the signal line and also inside the gap of the CPW, as well as an extended area on the signal line of the CPW. The elements have the sizes $2.5 \mu\text{m} \times 5 \mu\text{m}$, $5 \mu\text{m} \times 10 \mu\text{m}$, $10 \mu\text{m} \times 20 \mu\text{m}$ and $15 \mu\text{m} \times 30 \mu\text{m}$. After development, NiFe with the thicknesses of 5 nm, 10 nm or 20 nm was deposited using sputter deposition, followed by a 5 nm-thick gold capping layer to prevent oxidation. After lift-off, the preparation continues as with the previous samples by mounting them on a sample holder, wire bonding them to RF contacts and dispersing nano-diamonds on the CPW.

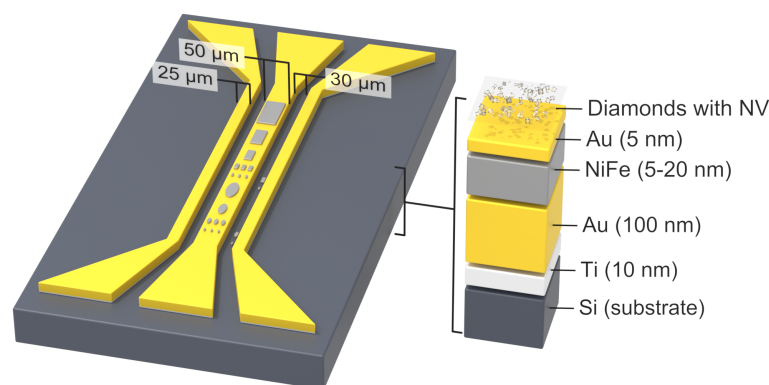


Figure 6.19. | Sample layout, consisting of a CPW with elliptical and rectangular NiFe elements on the signal line and in the gap. The structures are capped by a thin gold layer to prevent oxidation, before the nano-diamonds were applied via drop casting. For clarity in the sample figure, the gold capping and nano-diamonds are hidden.

6.10.2. SNS-MOKE Measurements on NiFe Devices

This section contains a set of SNS-MOKE measurements on a $10\ \mu\text{m} \times 5\ \mu\text{m}$ rectangular microstructure, see Figure 6.20, and an elliptical microstructure, shown in Figure 6.21. The thickness of the devices is 20 nm. The measurements were taken in the same way as before and show the spin wave magnitude as well as phase for the the 1st, 10th and 15th harmonic of the excitation frequency. During the measurements, a small static bias field was applied along the long axis of the elements. The strength of the bias field was chosen such, that the signal of the higher harmonics was maximized. A general trend is, that the optimal bias field increases with decreasing structure size. This is not surprising due to the increased demagnetizing fields in smaller structures, which are compensated by that. The excitation frequency in the measurements was 241.1 MHz.

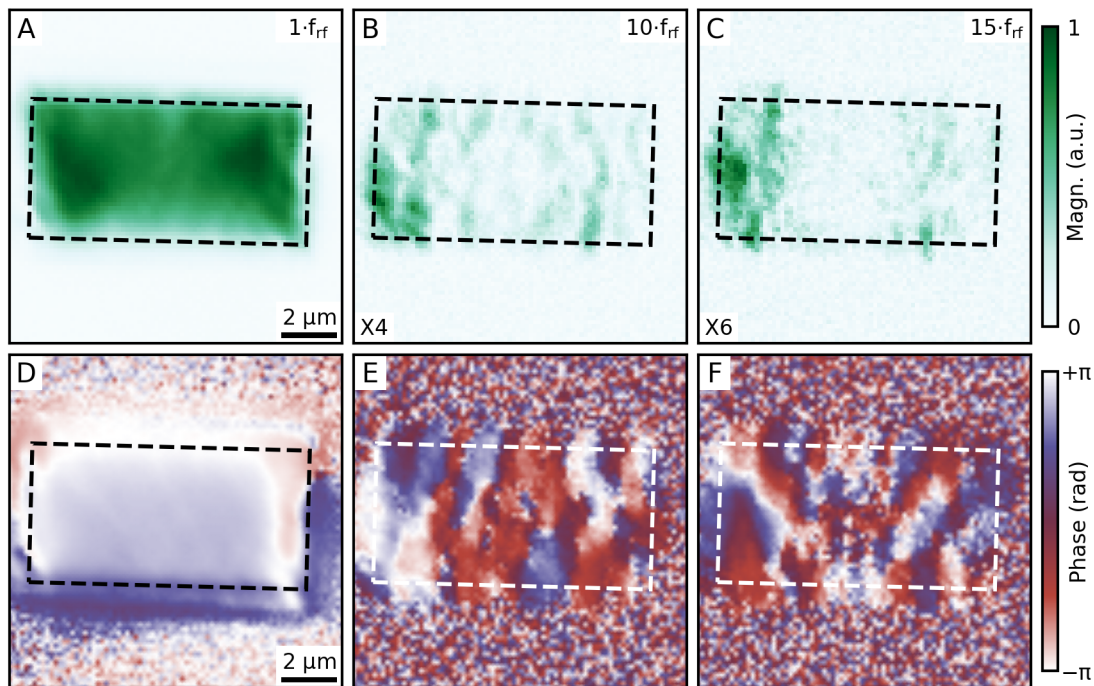


Figure 6.20. | SNS-MOKE measurement of spin waves in $10\ \mu\text{m} \times 5\ \mu\text{m}$ rectangular microstructure, excited at 241.1 MHz. A static bias field of 1.27 mT was applied along the CPW. **A-C:** Spin wave magnitude at the 1st, 10th and 15th harmonic of the excitation frequency. The signal for the harmonics was amplified by the factor denoted in the lower left corner of the sub-figures to improve visibility. **D-F:** phase of the spin waves with respect to the excitation frequency. The dashed lines indicate the outlines of the device.

The measurements show clearly, that the high harmonic spin waves are present in those microstructures, as well. While the phase of the fundamental excitation of the rectangle appears almost homogeneous, the elliptical element displays a clear jump in phase between the top and bottom half of the structure. This is a consequence of a vortex core present inside the ellipse. In general, it is found that the small devices often tend to contain inhomogeneities like vortex cores in the case of elliptical elements or domains in the rectangular elements, which interfere with the frequency multiplica-

tion process. Additional SNS-MOKE measurements on structures of different sizes are shown in Appendix E.

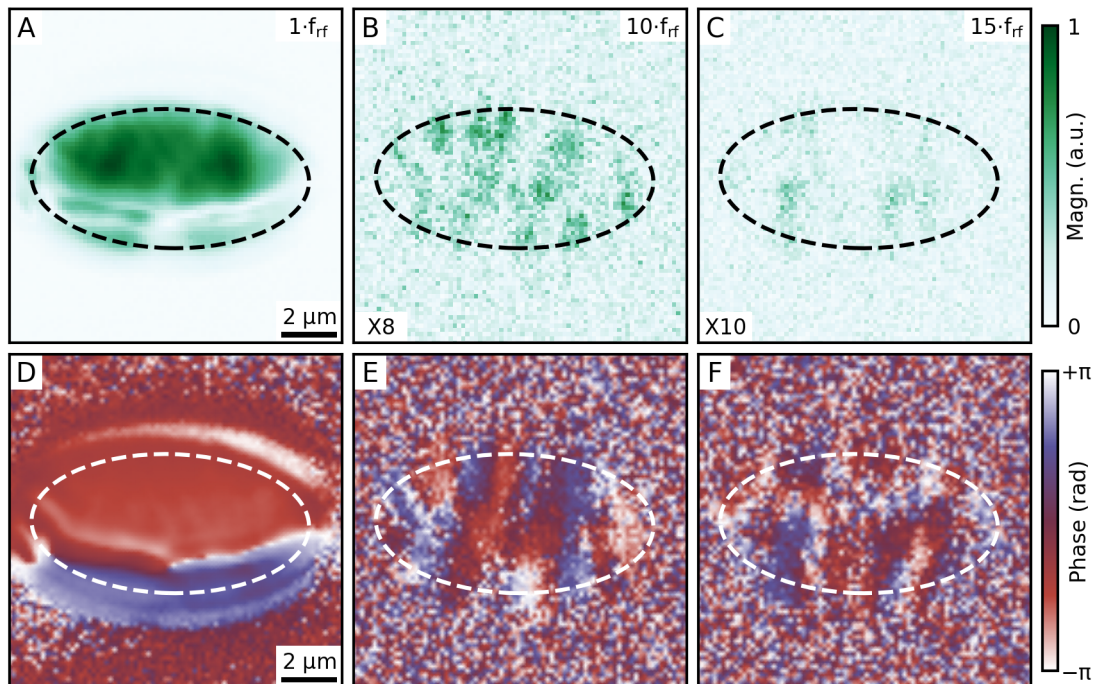


Figure 6.21. | SNS-MOKE measurement of spin waves in $10\ \mu\text{m} \times 5\ \mu\text{m}$ elliptical microstructure, excited at 241.1 MHz. A static bias field of 0.76 mT was applied along the CPW. **A-C:** Spin wave magnitude at the 1st, 10th and 15th harmonic of the excitation frequency. The signal for the harmonics was amplified by the factor denoted in the lower left corner of the sub-figures to improve visibility. **D-F:** phase of the spin waves with respect to the excitation frequency. The dashed lines indicate the outlines of the device.

6.10.3. Scanning NV Center Magnetometry on NiFe Devices

As structure sizes become smaller, in the range of a few micrometers, the limit of spatial resolution becomes increasingly relevant and hinders the detection of magnetic phenomena inside the structures. To improve the spatial resolution beyond that of SNS-MOKE microscopy, scanning NV center microscopy is used. The method has been described in Section 3.3.4. It uses a single NV center located inside a diamond AFM tip to sense the magnetic stray fields emitted by the sample.

In the following, scanning NV center microscopy is used to obtain static maps of the magnetic structure of a sample via the emitted magnetic stray fields. In addition, a new measurement scheme is tested, which is able to sense the dynamics of the magnetization within the structures.

Static Field Maps

Maps of the stray fields which are emitted by a sample can be obtained by scanning diamond tip which contains the NV center across the surface of the sample at a constant

height. An RF frequency is applied via an external antenna close to the tip. At every position, the excitation frequency is swept and the optical fluorescence signal is recorded. The PL spectra reveal dips in intensity due to the ESR of the NV center. From the Zeeman shift of the ESR frequency, the static field can be directly calculated as the shift is directly proportional to the magnetic stray field.

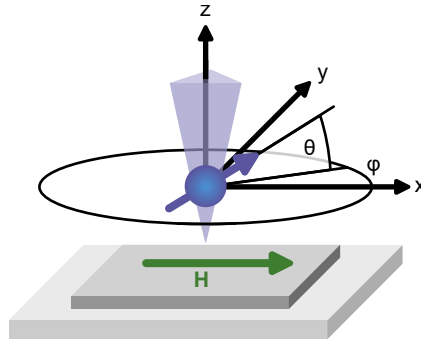


Figure 6.22. | Geometry of the scanning NV center magnetometry measurements. The orientation of the axis of the NV depends on the crystal direction of the diamond with respect to the sample. The depicted coordinate system is used throughout all following measurements. The long axis of the devices is oriented along the x -direction, as is the applied bias field.

As the NV center is sensitive to the projection of the field on its axis, the orientation of the NV center needs to be taken into account. This, on the first glance, complicates the data evaluation, but it also allows to obtain all vector components of the magnetic field when measurements of the same sample taken with different NV orientations are combined. The extracted field values represent the field at the position of the NV center, i.e. in a certain height above the sample. The distance between the NV center and the sample limits the achievable spatial resolution, which in the case of the presented measurements is in the order of 100 nm.

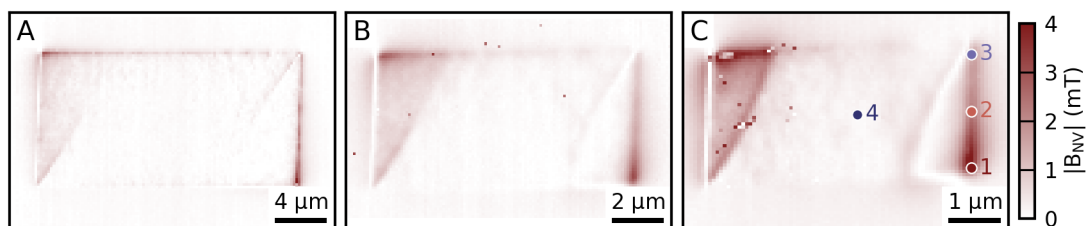


Figure 6.23. | Maps of the stray field above rectangular NiFe microstructures. The thickness of the structures is 10 nm. The dimensions are **A**: $20\ \mu\text{m} \times 10\ \mu\text{m}$, **B**: $10\ \mu\text{m} \times 5\ \mu\text{m}$ and **C**: $5\ \mu\text{m} \times 2.5\ \mu\text{m}$. The color indicates the absolute stray field emitted by the structure, measured at the position of the NV center. The measurements were taken in presence of a magnetic field of 0.3 mT. The marker indicate the positions evaluated in Figure 6.24. The orientation of the NV center in the measurements is $\theta = 29^\circ$ to the surface and almost aligned with the x -direction ($\phi = -5.9^\circ$). It hence senses a combination of the out-of-plane z -and the in-plane x -component of the stray fields.

Figure 6.23 displays maps of the magnetic stray field emitted by rectangular devices of different sizes. The thickness of the ferromagnetic film is 10 nm. All three devices display a similar inhomogeneous magnetization pattern with domain walls close to their left and right edges. In the center they are homogeneously magnetized. In this region no stray fields are emitted, besides small spatial fluctuations which are potentially caused by surface roughness. The smaller the device the further the domain walls extend into the center.

Figure 6.24 shows frequency scans taken at the positions 1–4 marked in Figure 6.23. From such scans at every position on the sample, the field maps are produced.

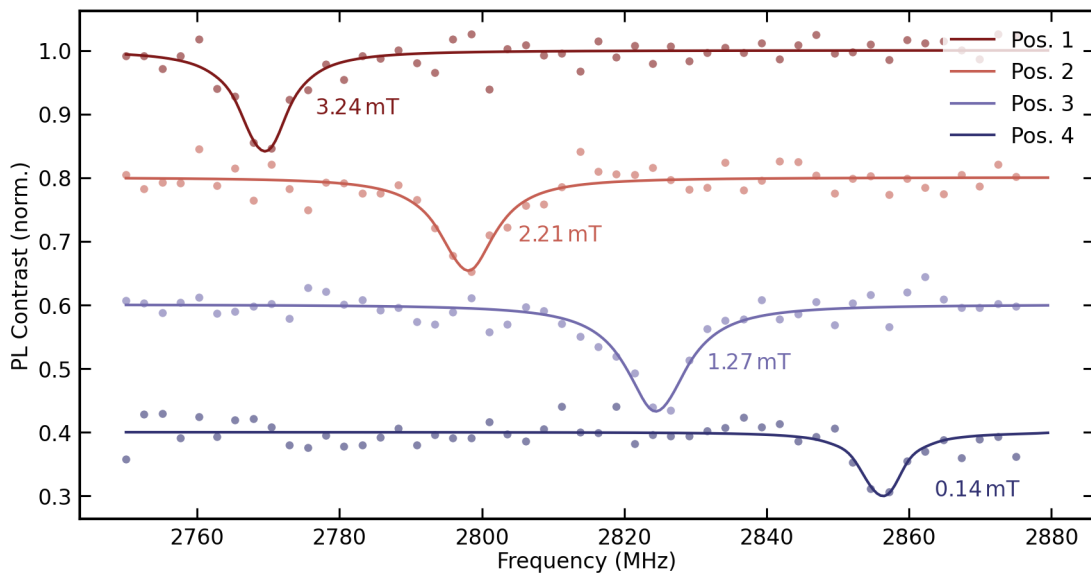


Figure 6.24. | PL spectra captured at exemplary positions on the sample, marked in Figure 6.23 C. Each spectrum shows a 10 % to 15 % quenching of the PL at the Zeeman-shifted ESR frequency. The spectra are shifted in y -direction for clarity. Each spectrum is fit to a Gaussian (solid lines) to determine the Zeeman shift, which is then used to calculate the local magnetic field according to Equation 3.6.

In Figure 6.25, a comparison of two different structures is made, a $10\ \mu\text{m} \times 5\ \mu\text{m}$ rectangle and a $5\ \mu\text{m} \times 2.5\ \mu\text{m}$ ellipse with different thicknesses of 20 nm and 5 nm. The thick rectangular device in Figure 6.25 A displays a characteristic Landau pattern, while the ellipse in Figure 6.25 B is in a vortex state. Both structures with a thickness of only 5 nm show an almost homogeneous magnetization state, except for the left and right edges, where stray fields are emerging. This is well expected since the magnetic anisotropy in thinner films, i.e. the dipolar contribution to the magnetic energy, tends to favor a homogeneous magnetization state.

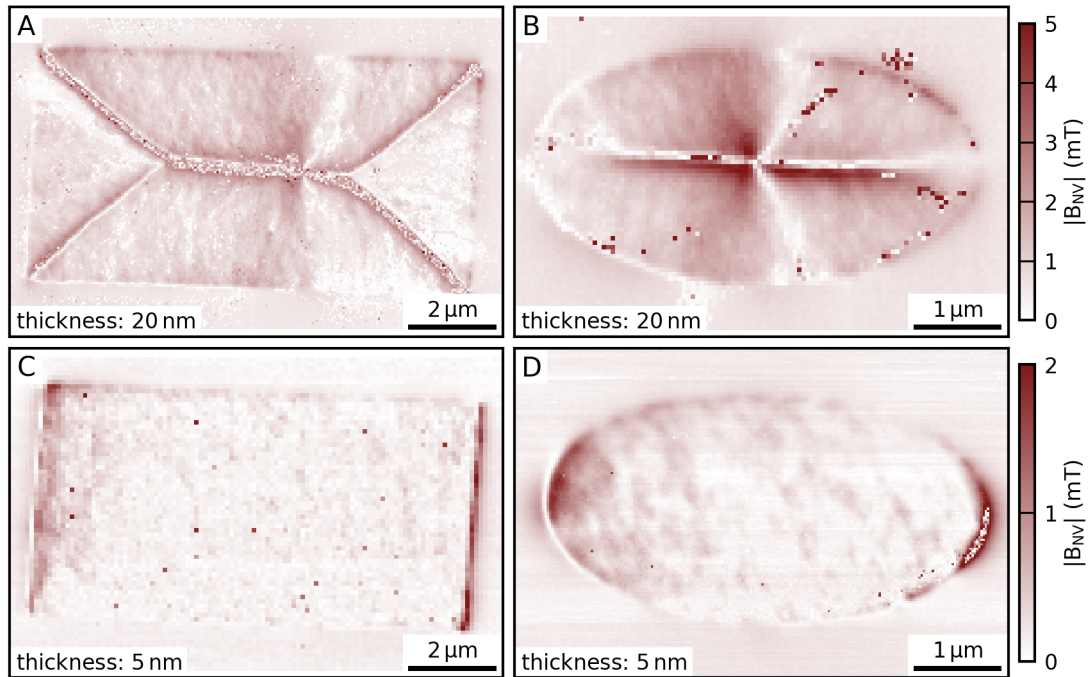


Figure 6.25. | Field maps on $10 \mu\text{m} \times 5 \mu\text{m}$ rectangles and $5 \mu\text{m} \times 2.5 \mu\text{m}$ ellipses, taken in the same way as in the previous map. **A, B:** The thickness of the ferromagnetic film is 20 nm. **C, D:** Thickness of 5 nm. The orientation of the NV center in the measurements is $\theta = 29^\circ$ to the surface and almost aligned with the x -direction ($\phi = -5.9^\circ$).

Dynamic Fluorescence Quenching

Instead of using the ESR frequency to calculate the magnetic stray field, the amount of quenching of the PL, i.e. the integrated area under the fitted Gaussian, can be evaluated. This does not yield the magnetic field strength, but an entirely different kind of contrast. The integrated fluorescence intensity instead directly corresponds to the spin wave magnitude, which can be mapped across the sample.

Moreover, during the course of the investigation of the structures, it was found that the contrast maps determined from the high-frequency ESR ($|0\rangle \rightarrow |+1\rangle$) and low-frequency ESR ($|0\rangle \rightarrow |-1\rangle$) transitions, in fact, are not equal. In the measurement displayed in Figure 6.26, RF excitation is applied to the device via the structured CPW. During the measurement, a static bias field of 0.5 mT was applied along the long axis of the rectangle. Figure 6.26 A and Figure 6.26 B show the quenching maps extracted from the low- and high frequency excitation of the NV center, respectively. Figure 6.26 C shows the difference of both.

The mapped wave pattern can be identified with an MSSW spin wave mode, which is excited in the magnetic film at the applied frequency. The difference map shows the resulting standing spin wave in a phase sensitive fashion. This can be explained by interference of the excitation field with the dynamic stray fields emitted by the precessing magnetization. Because spin waves and their stray fields are chiral, the

superposition with the homogeneous excitation field results in a total field with a certain handedness. The strength of this field depends on the local strength of the spin wave, i.e. the position of knots and anti-knots of the wave. The relative phase of the spin wave in the anti-knots determines the handedness of the total field. This field leads to a preferential excitation of one or the other ESR transition of the NV center, which is due to selection rules for optically excited electronic transitions, i.e. conservation of angular momentum upon absorbing a photon. This results in the visibility of only every second anti-knot in each of the two quenching maps.

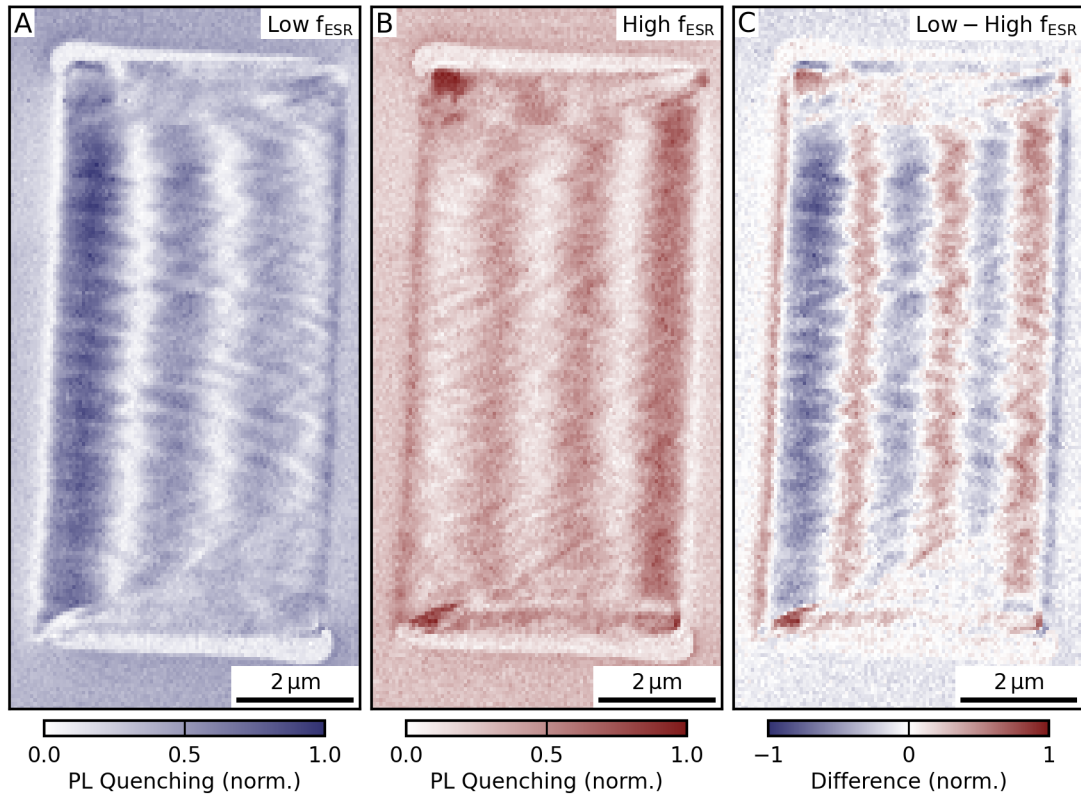


Figure 6.26. | PL quenching map of a rectangular device with a size of $10 \mu\text{m} \times 5 \mu\text{m}$ and a thickness of 10nm . A magnetic bias field of 0.5mT is applied along the long axis of the device. RF excitation is applied via the waveguide structured on the sample at a frequency of 2.87GHz . **A:** Resonance quenching at the low-frequency ESR transition. **B:** Resonance quenching at the high-frequency ESR transition. **C:** Difference of A and B. The orientation of the NV center in the measurements is almost in-plane ($\theta = 0.7^\circ$) and rotated versus the x -direction by $\phi = -27.6^\circ$.

The results are in line with similar findings from Lüthi *et al.*, who used a similar interference of dynamic stray fields of a spin wave propagating inside a YIG waveguide with an external RF field to image the spin wave [189]. The finding brings phase resolution to the otherwise phase-insensitive method of NV microscopy.

Fluorescence Quenching at Higher Harmonics

The same scheme can be applied to image higher harmonics generated within the magnetic device. In Figure 6.27, a frequency of 1.43 GHz is applied via the CPW. This corresponds to half of the ESR frequency of the NV center. This time, there is no direct excitation of the ESR. Nevertheless, inside the device spin waves are generated which precess at the 2nd harmonic of the excitation frequency. This frequency can be detected by the NV center. 2nd harmonic spin waves appear to be present throughout the device. It can be assumed, that the surface roughness and/or the finite size of the device provides sufficient symmetry breaking to enable the previously described frequency multiplication process.

For the higher harmonics, the contrast mechanism is not clear, as the excitation field cannot directly interfere with the stray fields emitted by the spin waves. Still, a phase-resolved imaging seems to be possible. This means, that a stationary field with a certain locally-dependent handedness must be present due to the spin waves. It could be stabilized by a small 2nd harmonic frequency component already present in the excitation frequency due to an imperfect frequency source.

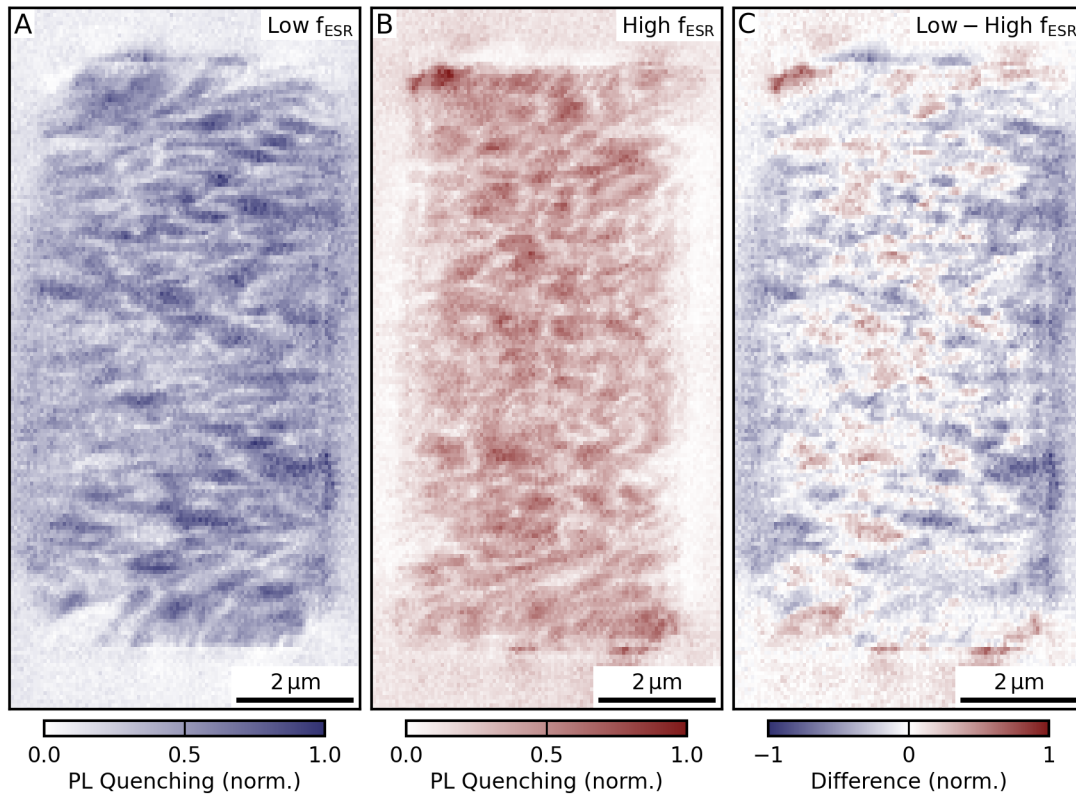


Figure 6.27. | PL quenching map of a rectangular device which is $10\ \mu\text{m} \times 5\ \mu\text{m}$ in size and 10 nm thick. A magnetic bias field of 0.5 mT is applied along the long axis of the device. RF excitation is applied via the waveguide structured on the sample at a frequency of 1.43 GHz. **A:** Resonance quenching at the low-frequency ESR transition. **B:** Resonance quenching at the high-frequency ESR transition. **C:** Difference of A and B. The orientation of the NV center in the measurements is almost in-plane ($\theta = 0.7^\circ$) and rotated versus the x -direction by $\phi = -27.6^\circ$.

Likewise, the measurement can be conducted for the 3rd harmonic, as depicted in Figure 6.28. The excited 3rd harmonic spin waves are more localized at the far ends of the rectangles, up to the positions of the previously observed domain walls (see Figure 6.23). In this regions, the magnetization appears to be less stiff and can thus more readily react to the excitation field, leading to larger excursion angles. In addition, the domain walls can move in a nonlinear way due to the excitation field and can, in this way, act as another source of high harmonic spin waves.

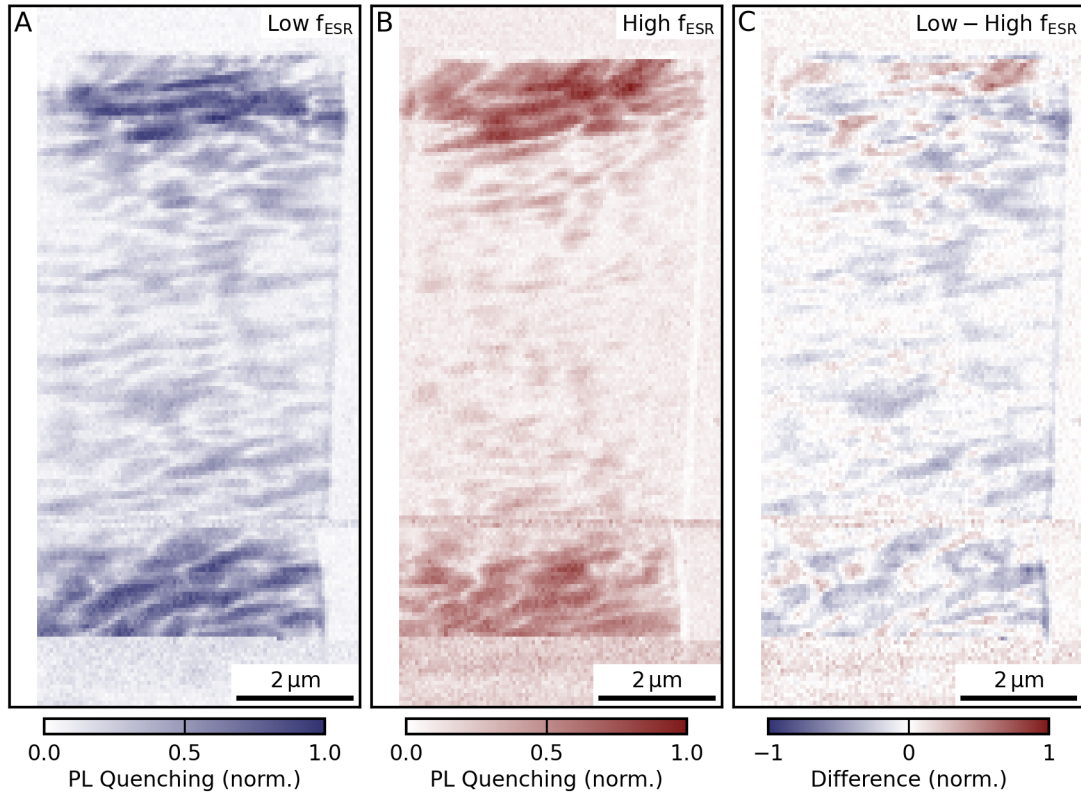


Figure 6.28. | PL quenching map of a rectangular device which is $10\ \mu\text{m} \times 5\ \mu\text{m}$ in size and $10\ \text{nm}$ thick. A magnetic bias field of $0.5\ \text{mT}$ is applied along the long axis of the device. RF excitation is applied via the waveguide structured on the sample at a frequency of $0.91\ \text{GHz}$. **A:** Resonance quenching at the low-frequency ESR transition. **B:** Resonance quenching at the high-frequency ESR transition. **C:** Difference of A and B. The orientation of the NV center in the measurements is almost in-plane ($\theta = 0.7^\circ$) and rotated versus the x -direction by $\phi = -27.6^\circ$.

6.11. Assessment of the Different Optical Methods

Confocal NV center magnetometry can circumvent the optical resolution limit by utilizing an ensemble of atomically small defects in nano-diamonds, which are each able to detect signals far beyond the diffraction limit. However, due to the large ensemble of diamonds, although the sensitivity to large wave vectors is secured, the actual spatial resolution is still poor and determined by the spatial distribution of the diamonds. Furthermore, NV center magnetometry is limited in the frequency range that can be

detected to around 2.8 GHz, depending on the magnetic field. This limitation can be circumvented by mixing a potential spin wave frequency, which lies outside of the detection band, with a second, auxiliary frequency (or even a spin wave with a different frequency), to generate a mixing frequency that again lies within this band, which was recently shown by Carmiggelt *et al.* [171]. A general benefit of NV microscopy is, that the method is not limited to coherent processes, but is able to also detect incoherent signals.

In contrast, SNS-MOKE strongly relies on the coherence of a signal with respect to the excitation source. This allows to detect and map the phase of the spin waves, but also renders it insensitive to incoherent excitations, such as thermal spin waves. Phase-resolved maps of spin waves are highly useful to study their wave vectors and propagation. The spatial resolution is limited by the optical diffraction limit, which is superior to the previously described confocal NV magnetometry. However, the signal sensitivity decreases as the signal of spin waves with large wave vectors increasingly average out, as soon as their wavelength becomes comparable to the size of the focal spot. Confocal NV center magnetometry, despite having a worse spatial resolution, is able to detect more than 50 harmonics of the frequency comb with a sufficient signal-to-noise ratio, while for SNS-MOKE the signal magnitude decays much more rapidly. A strong benefit of SNS-MOKE is, that the detection band can be tuned to almost arbitrary frequencies, which allows for frequency-dependent studies.

Furthermore, it was shown that scanning NV center magnetometry can be used not only to map static domain patterns, but to image the dynamics of the magnetization, for example the spin waves generated at higher harmonics of the excitation frequency. This is facilitated by the interference of the excitation field with the stray fields emitted by the spin waves, which, due to the handedness of the resulting field, yields phase resolution. This measurement scheme lets dynamic scanning NV center microscopy not only compete with confocal NV magnetometry, but also with SNS-MOKE. In combination, the different measurement modes of NV center magnetometry, as well as SNS-MOKE are very useful to map static and dynamic properties of magnetic samples on the micro-to-nanometer scale. Especially the phase-resolved measurement scheme provides a useful tool to further investigate frequency conversion processes with high spatial resolution in small structures. This is necessary to further miniaturize the magnetic devices and to explore the influence of shape, thickness and material parameters on their dynamics.

Construction of a Multi-Purpose Near Field Setup

A central aim of this thesis is to explore optical methods which are sensitive to magnetic excitations and potentially circumvent the optical diffraction limit. In the previous chapter, atomically sized defect centers in nano-diamonds played the role of local sensors, that make it possible to detect signals of spin wave phenomena with wavelengths smaller than the size of the optical focal spot. Furthermore, a single NV center inside of an AFM tip was utilized to obtain spatially resolved measurements of magnetic samples with a resolution three times better than the optical diffraction limit.

A different approach is to confine the focal spot of a probing laser itself to a smaller volume. This can be done with the help of a conducting nanoscopic tip. The tip can be electrically polarized to generate strong localized dipole fields, leading to a nano-focusing of the illuminating light underneath the tip apex. The general principle of the technique has been described in Section 3.3.5. The aim of this chapter is to construct a general-purpose scattering scanning optical near field microscopy (s-SNOM) setup and to combine it with a high-resolution spectrometer to enable Brillouin light scattering (BLS) measurements with nanoscopic resolution. This will allow to analyze minute shifts in photon energy of the scattered light, to detect magnetization dynamics in a sample.

The entire s-SNOM setup, as sketched in Figure 7.1, is constructed in a way to allow for convenient switching between different measurement methods and geometries, which require different light sources, detectors and optics. In the figure, the core parts of the setup are highlighted with a green background. The chapter first presents the operational principle of the apparatus and the optical setup. It is shown how the s-SNOM setup can be used for phase-resolved detection of optical near fields with an optical resolution way beyond the diffraction limit. This technique allows to directly probe the optical properties of a sample.

Furthermore, the near field setup is extended to utilize the inelastic scattering of light, i.e. not only is the intensity of scattered light detected, as in conventional s-SNOM, but the scattered light is also analyzed with a high-resolution spectrometer, to determine shifts in photon energy. Such shifts originate from the interaction of the photons with phononic or magnetic excitations in the sample. The section starts with a detailed examination of the newly developed experimental technique, which is called *nano-focused BLS*. The method is related to commercially available nano-focused Raman spectroscopy, but aims at much smaller shifts in photon energies (i.e. in the GHz range,

instead of several THz). This poses much higher requirements on the experimental setup. First, a stabilized narrow-band laser source was installed and coupled into the s-SNOM. To detect the minute energy shifts of the photon energy of the scattered light, a special high-resolution, high-throughput spectrometer was constructed, tested and integrated with the instrument. Such a combination of s-SNOM and BLS has not been demonstrated before and will allow for nano-scale detection of BLS signals. As the development process of nano-focused BLS is still ongoing, the chapter primarily focuses the details of the construction of the different parts of the setup (sections with red background in Figure 7.1). This is concluded by first test measurements, which demonstrate the working principle and an outlook.

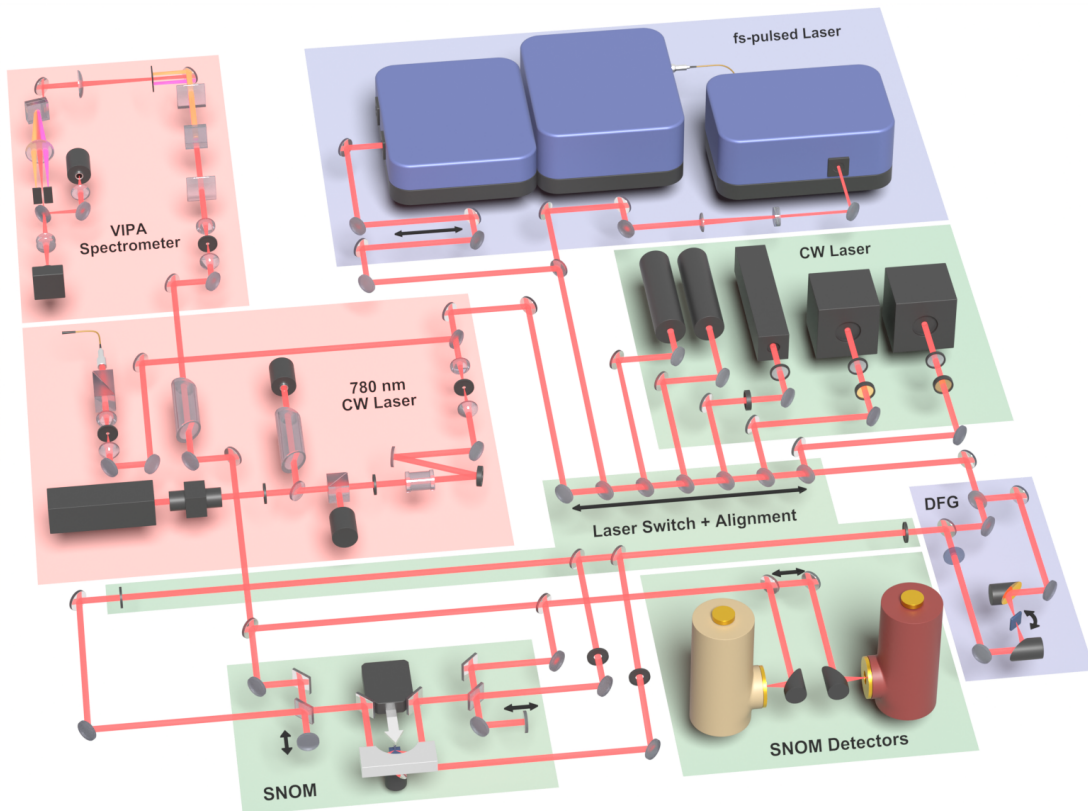


Figure 7.1. | Overview of the near field microscopy setup. The parts highlighted in green are the core parts. This includes the base unit, a range of CW laser sources, an alignment area, and detectors. Parts highlighted in red are used for nano-focused BLS spectroscopy. Parts highlighted in blue are used for generating broad band MIR light for FTIR spectroscopy.

Besides nano-focused BLS, there are two additional measurement techniques which have been realized with the multi-purpose s-SNOM setup. First, the near field setup was used to demonstrate another novel experimental method, *Near Field Assisted Heating*, which is a combination of transport measurements with s-SNOM. Here, a magnetic sample is locally heated using the nano-focused laser spot underneath the s-SNOM tip. The heat gradient generated by the absorbed laser power gives rise to a voltage via to the anomalous Nernst effect (ANE). This voltage can be detected electrically in suitably

patterned structures. This method has proven capable of imaging domain patterns in ferromagnetic devices of in-plane magnetized CoFeB and out-of-plane-magnetized Co-Ni multilayer structures with sub-100 nm resolution. The results have been published by Pandey *et al.* [190]. Furthermore, the method has been used to image the inhomogeneous magnetization state in wire structures, which consist of the chiral antiferromagnet Mn_3Sn [191]. More details of both studies are presented in Appendix A.

Second, a Fourier transform infrared (FTIR) spectroscopy setup is implemented with the purpose to measure absorption spectra of materials with the nanoscopic resolution provided by s-SNOM (blue parts in Figure 7.1). For this, a broad band mid infrared (MIR) light source is built using difference frequency generation (DFG). The application of this method is unrelated to magnetic imaging, but instead aims on nano-scale spectroscopy of different organic molecules and nano-structures. The details of the setup are presented in Appendix B.

7.1. General s-SNOM Setup

The s-SNOM setup built during the course this thesis is based on the commercial *Neascope* system from the company *Neaspec*. The system is set up around a central unit, which, most importantly, contains an AFM system. The AFM consists of a three-axis coarse and fine (piezo-) stage to position the sample under the AFM tip. The tip is mounted on a three-axis movable tip holder which features a piezo actuator to excite mechanical oscillation of the tip. A deflection laser is reflected from the back side of the tip onto a segmented photodetector, to sense the tip oscillation. This allows for an operation in both, tapping and contact mode. To observe the sample during coarse positioning, the base unit contains a wide-field microscope.

What sets an s-SNOM apart from an ordinary AFM are the additional optical components. A main parabolic mirror is used to focus laser light on the tip. At the same time, this mirror collects the light which is scattered back from the near field of tip and sample. Different mirrors and beamsplitters in the sample chamber are used to guide the light from outside of the base unit toward the parabolic mirror and tip, as well as to reflect the collected near-field light from of the base unit toward a detector. The optical setup is symmetrical to both sides of the sample holder. This allows to illuminate the tip and to detect the scattered light from both sides of the device with different experimental configurations. A third option to illuminate the sample is using a parabolic mirror located below the sample holder. The different experimental geometries are further discussed in Section 7.1.3.

The laser light for the s-SNOM is generated by a variety of different light sources set up on the optical table around the base unit. The scattered light is detected with different detectors, depending on measurement mode and laser wavelength. To facilitate fast switching between the measurement modes and geometries, switching between different laser sources and detectors is automated.

Interferometric measurements can be performed by placing two interchangeable interferometer units in the sample chamber on designated locations to both sides of the sample. They can be used for phase-resolved s-SNOM measurements in the different geometries, as well as for FTIR spectroscopy.

7.1.1. Light Sources

The s-SNOM setup is designed such, that the optical components used (mostly mirrors) are largely independent of the laser wavelength. In principle, the instrument can operate with light from the UV all the way into the THz range. In general, the efficiency of the tip-enhancement increases with wavelength. This is due to the increased absorption-induced losses for photon energies close to the plasma frequency of the coating of the tip (Pt-Ir alloy), as well the materials the mirrors are made of (e.g. Al, Ag or Au). Remarkably, due to the tip enhancement effect, the spatial resolution of the instrument is largely independent of wavelength. Depending on the physical phenomenon to be observed, the wavelength of the light source has to be chosen accordingly.

While FTIR spectroscopy requires a broadband light source, other applications, such as the imaging of plasmonic modes in antenna structures, require narrow-band and wavelength-matched light sources. The instrument can be operated with CW lasers as well as with pulsed lasers for time-resolved measurements using pump-probe schemes.

In the setup, different CW laser sources are available, see Figure 7.2. First, there are two HeNe lasers with 543 nm and 633 nm, and a power of a few mW each. HeNe lasers offer a good beam quality. They are easily visible and most useful as alignment lasers. Because of the low available power, they can only be used to a limited extend for near field measurements. Furthermore, there is a near infrared (NIR) solid-state laser with a wavelength of 1050 nm and a power of up to 1 W. Last, two MIR lasers with wavelengths of 5 μm and 8 μm are set up. They offer a power on the order of 50 mW to 80 mW. All IR lasers can be used for standard SNOM measurements, but also in near field ANE measurements, which are described in Appendix A. Their power and polarization state can be controlled by a combination of a half waveplate (HWP) and a polarizer (P).

The selection of the laser source, which is used for a measurement, is automated. This is done by aligning all lasers to follow parallel beam paths. A mirror, mounted on a motorized linear stage, can be moved in perpendicular direction to the laser beams. It is aligned such that any selected laser will follow a common path after reflecting from this mirror. During the switching process all lasers are blocked by automated shutters. Once the mirror has reached its new position, the corresponding shutter is opened and the laser can be used. Seamless switching between different lasers can only be achieved if all lasers enter the SNOM base unit in exactly the same way, i.e. in the same direction (angle) and at the same position. This is achieved by aligning all lasers through an alignment path defined by two irises, which are located behind the

laser selection stage. This makes sure, that no manual alignment is necessary when the illumination laser is switched between any of the available sources.

Switching between the different illumination geometries in the SNOM is realized manually via flip mirrors. In the same way, flip mirrors are used to switch between left- and right-side detection and the detection with a spectrometer, which is explained in Section 7.2.

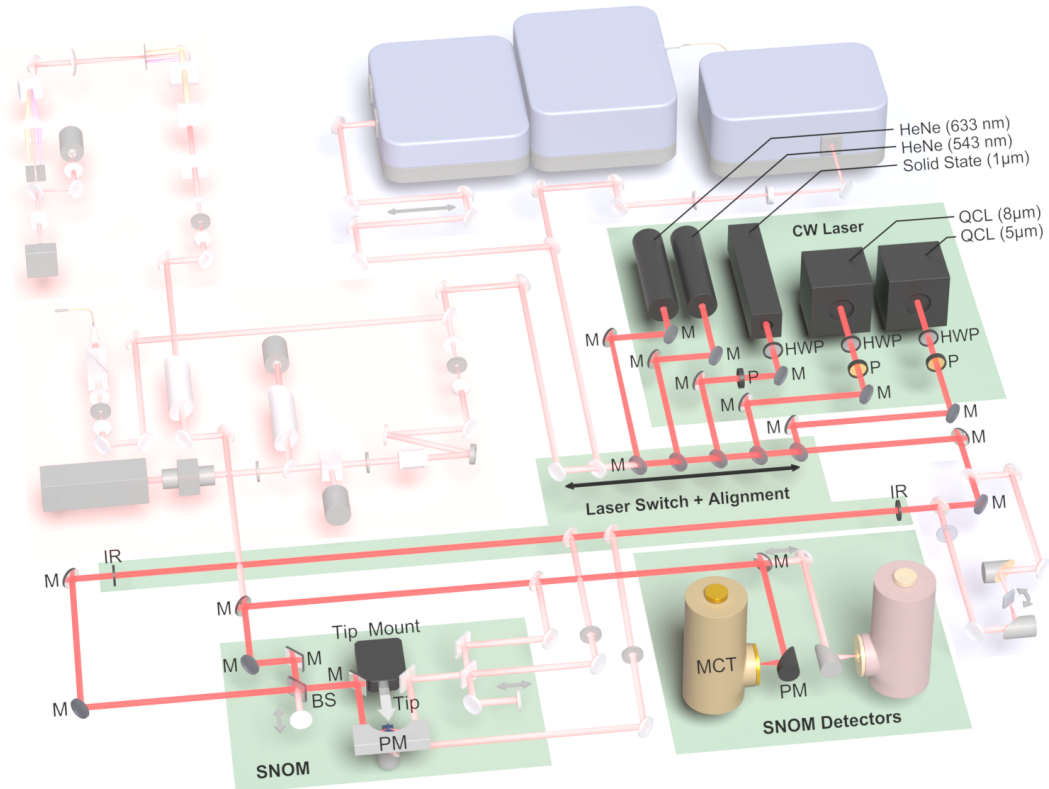


Figure 7.2. | Core parts of the s-SNOM setup. This includes an array of CW laser sources with wavelengths ranging from 543 nm to 8 μm , a laser switching stage for illumination, an alignment path, the base unit with the SNOM tip and focusing optics, and MCT detectors to detect the scattered light.

In addition to the laser described above, there are four other light sources. These have not been mentioned, since they are specifically meant to be used with their corresponding measurement modes. Two CW frequency stabilized narrow band 780 nm lasers are used for nano-focused BLS spectroscopy, see Section 7.2. Furthermore, there are two femtosecond NIR laser sources, one with a central wavelength of 1550 nm and a second one with a broad emission spectrum ranging from 1700 nm to 3000 nm. The lasers can be used either individually, or in combination to generate broad band MIR light through DFG. This tunable broadband MIR light source is used for FTIR spectroscopy, see Appendix B.

7.1.2. Detection of Scattered Light

In s-SNOM measurements, the light from the near field of the sample is scattered by the tip into the far field. It is collected by a parabolic mirror and guided toward a detector. The choice of the detector depends on the measurement mode and on the wavelength of the laser in use. In the basic s-SNOM modes, point detectors are used. The main detector in the setup is a mercury cadmium telluride (MCT) detector, which is used to detect VIS to MIR light. The working principle of MCT detectors was described in Section 3.3.5. For nano FTIR spectroscopy measurements, an additional MCT detector is used, which is sensitive to wavelengths of up to 12 μm . The signal from the detectors is amplified and can be demodulated on either a harmonic of the tapping frequency of the SNOM cantilever, or on sidebands thereof, in case of an interferometric detection; see Section 7.1.4 for details on demodulation options. As the tapping frequency of the tip typically is on the order of 250 kHz, the demodulation requires a detection bandwidth of above 1 MHz, to be able to detect up to the 4th harmonic of the near field signal.

Switching between different detection paths, depending on illumination geometry, is done via flip mirrors. The detection beam paths for all geometries are aligned similarly to the illumination paths, such that at a certain position all beams coincide. This allows to switch detectors, again, by using a motorized mirror without the need for manual realignment.

The nano-focused BLS, which is described in Section 7.2, does not require a single point detector. Instead, the light is detected dispersively in a spectrally resolved manner. The light exiting the SNOM can therefore be diverted by a flip mirror toward the custom-built spectrometer, which is described in Section 7.2.4.

7.1.3. Measurement Geometries

There are three different illumination and detection geometries. First, the light can be focused on the tip and the sample from above. This is called reflection mode. In reflection mode, the incident angle of the laser is $\sim 60^\circ$ with respect to the surface normal. In the instrument there are two directions of incidence possible, with azimuthal angles of $\pm 45^\circ$ to the left and to the right of the sample. In both, the left and the right reflection geometry, the mirror, that focuses the incoming collimated laser beam onto the tip, also collimates the scattered light. Hence, the beam paths of incoming and scattered light overlap. The beams are separated by beamsplitters, located to the left and right of the sample inside the sample chamber. The beam path of the two reflection geometries is depicted in Figure 7.3 A. The third measurement geometry is transmission geometry, shown in Figure 7.3 B. It uses a second parabolic mirror, which is located underneath the sample, to focus the laser on the sample from below. The main parabolic mirror above the sample is again used to collect and collimate the scattered light.

The reflection geometry has the advantage of a simpler alignment, since it involves only a single parabolic mirror. A major drawback of this geometry is the incidence angle of the light on the sample, which deviates from the normal direction due to geometrical constraints. This has the effect, that the phase fronts of the light are tilted with respect to the sample surface. This can be an issue for certain phase-sensitive measurements, where a homogeneous excitation phase across the sample is required, e.g. in plasmonics. In this case, when antenna structures reach sizes comparable to the laser wavelength, the antennas experience a phase retardation of the excitation field depending on their position on the sample. During the the measurement, the sample is scanned laterally. Hence, the excitation phase will also depend on the scanning position, which further distorts the measured phase and makes it difficult to interpret the result. The transmission mode avoids this issue, as here, the laser is focused from the back side onto the sample under normal incidence. Therefore, the angle of the phase fronts of the laser matches with the sample surface, leading to a constant excitation phase across the sample. This solves the issue of clean antenna excitation and decouples it from the scanning position.

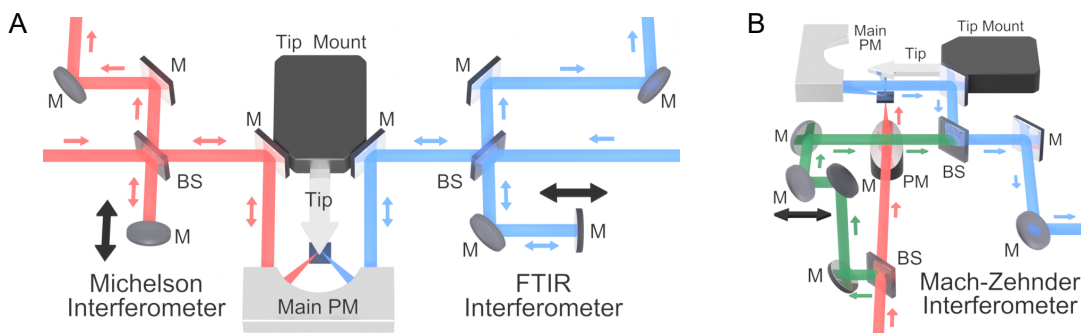


Figure 7.3. | Sketch of the three illumination geometries available in the setup. **A:** There are two reflection geometries, depicted by the red and blue beam paths. In both, the light is focused on tip and sample from above by the same parabolic mirror that also collects the scattered light. In the left reflection geometry (red beam path), the collected light can interfere with a reference beam split from the incident beam in a Michelson interferometer, to enable phase-resolved measurements (see Section 7.1.4). The right reflection geometry (blue beam path) uses a slightly different interferometer design to enable FTIR spectroscopy (see Appendix B). **B:** The light is focused from below the sample through the substrate onto the tip (red beam path), while it is collected by the main parabolic mirror and sent to the detector (blue). This makes a different interferometer design necessary, a Mach-Zehnder interferometer (green beam path), to enable phase-resolved s-SNOM measurements in transmission geometry. The black arrows indicate mirrors whose position is modulated.

Compared to the reflection geometry, the transmission geometry has the additional requirement that the sample substrate needs to be transparent for the laser wavelength and sufficiently backside polished. In this mode, the alignment of the parabolic mirrors is more challenging than in reflection geometry, as it involves two mirrors which need to be aligned with respect to each other and the tip. Also, the index of refraction and the thickness of the substrate need to be taken into account. Illumination under normal

incidence has the advantage that the light polarization and hence the direction of the electric field of the excitation is fully in-plane and can be freely set by using a HWP before the laser is coupled into the instrument. In reflection geometry, the polarization is usually kept along the tip, which maximizes coupling and field strength under the tip and yields the best near field signal. In-plane polarization (cross-polarized to the tip) is also possible at the cost of decreased signal strength.

7.1.4. Interferometric Detection of Near Fields

The detection of the scattering-induced phase shifts of the light is achieved by following the approach described in Section 3.3.5. The s-SNOM tip is operated in tapping mode, which generates frequency components in the optical signal at harmonics of the tapping frequency. A phase-modulated reference beam is needed to interfere with the sample beam on the detector. The reference beam is split from the main incident laser beam by a beamsplitter. It is back-reflected from a mirror, which is attached to a piezo actuator. The piezo actuator oscillates at a certain frequency (in the range of 300 Hz), leading to a modulation of the travel distance of the light and hence a phase modulation of the reference beam. In reflection geometry, the type of the interferometer which fulfills this purpose is a Michelson interferometer, shown as the red beam path in Figure 7.3 A. Upon interference of sample and reference beam, sidebands are generated in the detector signal, which contain the phase information of the scattered light. Performing a lock-in demodulation and comparing the relative amplitudes of even and odd sidebands allows to separate the optical amplitude from the phase due to their respective cosine- and sine-dependencies. This allows to recover the true amplitude and phase of the electrical near field around the sample and enables the detection of resonances in the dielectric function or plasmonic responses of the sample.

7.1.5. Interferometric Detection in Transmission Geometry

The interferometric detection scheme can be adapted to the transmission geometry, too. Here, the Michelson-type interferometer is replaced with a Mach-Zehnder interferometer which allows to have an independent beam in- and output by using two distinct beamsplitters to split the reference beam from the incident laser and to combine it with the sample beam (green beam path in Figure 7.3 B).

To demonstrate the interferometric detection, a measurement was performed on a microstructured gold disk. The disk is illuminated with 8 μm laser light through the substrate from below, using the secondary parabolic mirror in transmission geometry. The topography of the disk is shown in Figure 7.4 A. While scanning the sample under the s-SNOM tip, the scattered light is detected. The signal is simultaneously demodulated at different harmonic orders of the tapping frequency (1st to 4th), respectively. For each harmonic, this yields amplitude (Figure 7.4 B to E) and phase (Figure 7.4 F to I) maps of the scattered near field.

The electric field of the laser resonantly excites the 1st electric dipole mode of the disk. Characteristic for this mode are two maxima of the scattered intensity along the diameter of the disk. These two maxima show different phases in the light emitted by the disk, with a phase shift between the two maxima of 2π . This precisely matches the expectations for an electrical dipole mode.

Comparing the maps demodulated at different orders, the signal which is demodulated directly at the tapping frequency (1st order) differs most from the higher order signals. This indicates, that there is a strong background signal, which stems from light unrelated to the actual near field. This may be light directly scattered from the tip or the tips shaft, without interacting with the sample at all. Due to the tapping motion of the tip, this light is still modulated with the tapping frequency and leads to a contribution to the demodulated signal. The higher orders show only minor differences. The 2nd order still contains a weak background, while for the 3rd and 4th order, no background signal is observed. For these, the amplitude images also show the most symmetric dipole mode of the disc. Similar to the scattered amplitude, the phase maps are less distorted at higher orders.

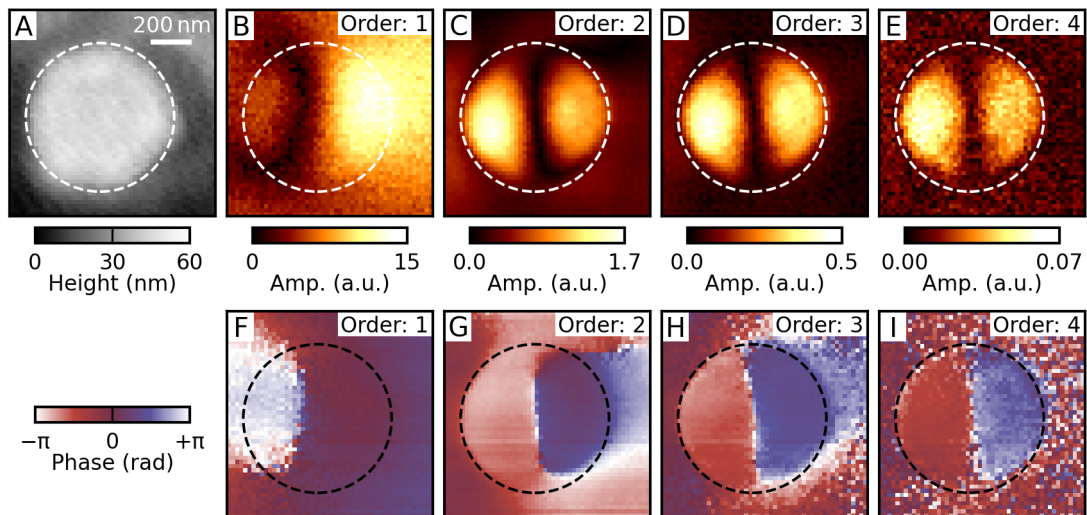


Figure 7.4. | s-SNOM measurement on a gold disk with a diameter of ≈ 700 nm. The measurement was taken in transmission geometry with an $8\ \mu\text{m}$ MIR laser as light source. Interferometric detection was employed to separate the optical amplitude from the phase. **A:** AFM topography measurement, **B-E:** Amplitude and **F-I:** Phase shift of the scattered light, demodulated at the 1st to 4th harmonic order of the tapping frequency.

A drawback of the demodulation at a higher order of the tapping frequency is the reduced signal. It decreases from one order to the next by roughly one order of magnitude. This means, that a trade-off has to be made between a clear, background-free signal and a good SNR. It should be noted that this trade-off depends on the tapping amplitude, the wavelength of the light and the strength of near field scattering by the structure. In general, the background is stronger for shorter wavelengths of the light. In most cases, demodulating at the 3rd harmonic order is a good compromise.

7.2. Inelastic Light Scattering Beyond the Diffraction Limit: Nano-Focused BLS

The near field techniques described in the previous sections rely on elastic scattering of light. The approach presented in the following instead utilizes inelastic near field scattering. An established method, which combines tip enhancement with inelastic light scattering is tip enhanced Raman spectroscopy (TERS). In TERS the light scattered from the SNOM tip is analyzed in a spectrometer, usually equipped with an optical diffraction grating and a charge coupled device (CCD)-camera sensor to detect the spectrum of the scattered light. As described in Section 2.3, the spectral distribution of the light contains information about excitations in the sample, such as phonon or magnon modes. The spectrometers are designed to yield high sensitivity with short integration times to keep the measurement time for two dimensional TERS images manageable. To distinguish between far and near field light, usually two spectra are recorded, one with the SNOM tip approached to the sample and one where the tip is retracted. The difference of the two spectra marks the contribution from the near field. Due to the field enhancement by the s-SNOM tip, the technique profits from an enhanced spatial resolution compared to standard microscopes.

The aim in this thesis is to investigate magnons in magnetic materials. Depending on material, the resulting energy shifts of the scattered photons are potentially much smaller than what Raman spectroscopy covers. Therefore, the method needs to be adapted to the typical energy range of BLS spectroscopy.

In ferromagnets, magnon frequencies often are in the GHz range. For comparison: The light of a visible laser with a wavelength of 780 nm has an absolute frequency of 384.3 THz. The expected shifts are on the order of 20 ppm. To detect these minute energy shifts, strict requirements on the setup need to be fulfilled, concerning the spectral stability and purity of the light source, the spectral resolution of the spectrometer and the suppression of Rayleigh scattered light.

7.2.1. Previous Technical Developments

Previous works regarding the combination of optical near field techniques with inelastic light scattering were mostly focused on TERS. A first work that successfully demonstrated the combination of an AFM with a Raman spectrometer dates back into the year 2000. Anderson probed a sample with an AFM tip, while simultaneously shining a laser from the back side of the sample. He showed, that the presence of the tip leads to an enhancement of the Raman signals, which he detected from different thin films on the sample surface [192]. In a similar study from the same year, Stöckle *et al.* reported a thirty-times increased Raman signal of a molecular layer on the surface of a sample if the tip is brought in contact [193]. In these studies, the main attention went toward the increased signal, less so on an affect of the tip on the spatial resolution achievable

with the technique. Since then, the method has developed from a proof-of-principle into a valuable tool for optically detecting chemical fingerprints of various substances on the surface of a sample.

In 2010 Jersch *et al.* used an aperture-type SNOM system to investigate localized magnetic excitations in elliptical NiFe elements. In this study, a lateral resolution of 55 nm could be achieved, which is limited by the size of the aperture in the SNOM tip [194]. This was a first successful demonstration of a system that combines aperture-SNOM with BLS. That said, this type of SNOM has significant limitations and drawbacks compared to s-SNOM. For once, the tips are complicated to fabricate and very expensive. In addition, they are much more fragile than s-SNOM tips, which cost only a fraction of tips with an aperture. s-SNOM promises much more robust signals and potentially offers a two times better spatial resolution. A more recent example that combines s-SNOM with inelastic light scattering is a study by Kusch *et al.*. Here, an s-SNOM setup was equipped with a grating spectrometer. The setup was used to detect the chemical fingerprint of an organic compound adsorbed to a substrate using TERS [37]. This spectrometer was designed for the detection of Raman scattering and is not suitable for BLS. Nevertheless, these technical advancements indicate, that it should be possible to construct an s-SNOM setup capable of BLS measurements.

7.2.2. Overview of the Nano-Focused BLS Setup

Figure 7.5 shows a complete schematic of the nano-focused BLS setup, which has been constructed. It consists of the light source (located in the lower red area), the s-SNOM base unit (lower green area) and the spectrometer (upper red area). The light from the light source is routed via the common laser switch (upper green area) and coupled into the s-SNOM. The scattered light from the s-SNOM is routed to the spectrometer with a preceding step of spectral filtering (also located in the lower red area). All parts are described in detail in the following sections.

7.2.3. Frequency-Stabilized Single Mode Laser Source

Two major requirements on a light source for BLS spectroscopy are a stable emission frequency and a narrow emission linewidth. For the nano-focused BLS setup, a CW laser with a wavelength of 780 nm is used. This wavelength coincides with an absorption line of Rubidium vapor, the so-called Rb D2 line. This absorption line is frequently used as an absolute frequency standard, as the energy of this electronic transition solely depends on constants of nature and is extremely narrow. In addition, it can be tuned by external magnetic and electric fields (Zeeman and Stark effect). It is independent of external influences, such as pressure and temperature of the gas. Rb spectroscopy is a well established method, that can be used to stabilize a laser to the absorption line, which provides an absolute frequency standard. Natural Rb gas is a mixture of two stable isotopes, ^{85}Rb and ^{87}Rb . In the present setup, isotopically pure ^{87}Rb is used,

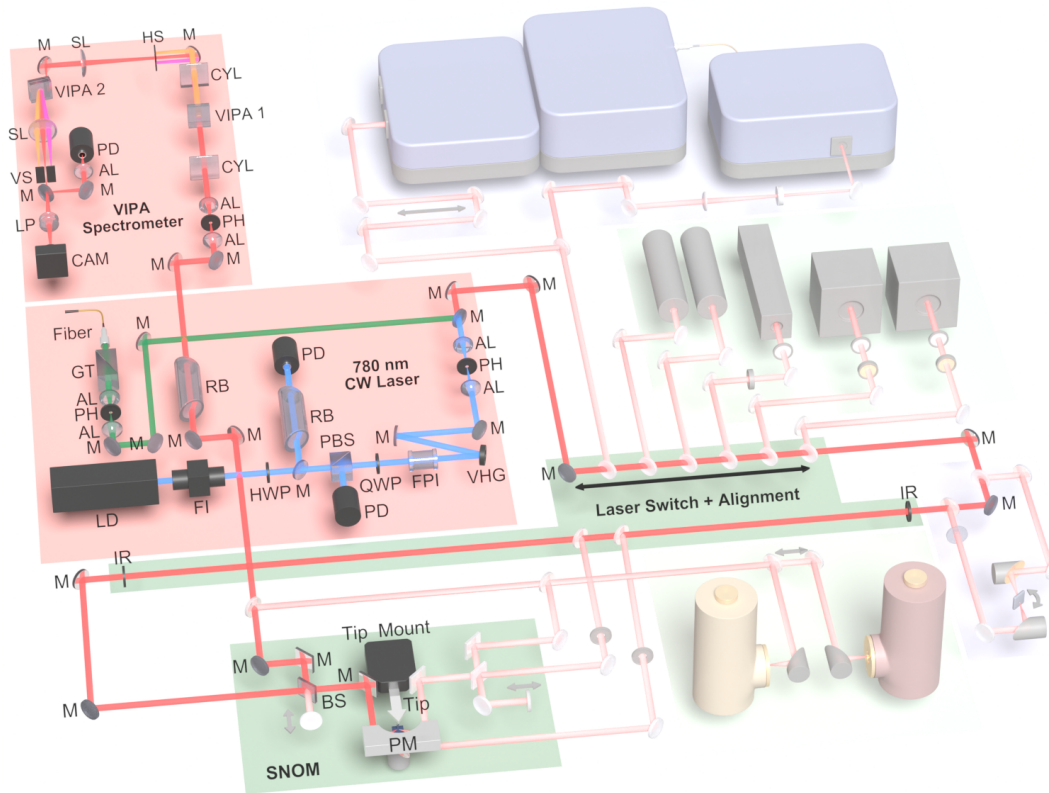


Figure 7.5. | Schematic of the nano-focused BLS setup. It consists of a 780 nm stabilized CW laser source which is coupled into the s-SNOM base unit, and the VIPA spectrometer to detect shifts in photon energy.

as a mixture of isotopes would exhibit twice the number of absorption lines, and, due to dilution of the gas, reduced contrast in absorption. To achieve a stabilization, the laser wavelength is slightly modulated, e.g. by modulating the diode current in case of a diode laser. This leads to a modulation in the laser intensity transmitted through the gas cell filled with Rb vapor due to the wavelength-dependent absorption. Lock-in demodulation of the signal yields a phase-sensitive error signal, which is used to lock the laser wavelength to the absorption with the help of a PID feedback loop.

The spectroscopy of atomic absorption lines is complicated by Doppler broadening. This is due to the isotropic movement of the gas atoms at different velocities. Doppler broadening increases the linewidth of the individual absorption lines from a few MHz to about 1 GHz at room temperature, and thus fully smears out the hyperfine structure. The broadening can be avoided by using saturated absorption spectroscopy (SAS). In SAS, a strong laser beam first saturates all Rb atoms which move at a certain velocity where the Doppler-shifted absorption matches the laser wavelength. A second, much weaker probe beam counter-propagates through the vapor cell. It is used to probe the absorption. If the atoms which are saturated move in the direction of the probe beam the Doppler shift has the opposite sign and a different velocity class of atoms is probed than the one which is saturated. Only when the atoms have a vanishing velocity

component in the direction of the laser beams, the probed atoms are exactly those which have been saturated by the pump beam. In this case, the probe beam experiences less absorption compared to all other cases. This effectively eliminates Doppler broadening and makes it possible to observe the hyperfine splitting of the Rb D2 line [195]. With this method, the photon energy of the laser can be actively stabilized to just a few MHz at an absolute photon energy of 384.3 THz.

Besides stabilization of the laser, the Rb standard is useful in a second way when constructing a nano-focused BLS instrument: It provides an extremely narrow-band notch filter, which can be used to suppress Rayleigh-scattered light without disturbing the Stokes and anti-Stokes scattered BLS photons. This filtering is further described in Section 7.2.5.

The processes to be observed with BLS are in the GHz range. Hence, the bandwidth of the laser should be well below this frequency range, i.e. a few MHz at maximum, in order to not affect the measurements. Energy broadening in the distribution of photon energies emitted by the laser directly translates into a broadening of the peaks observed in the BLS spectrum. Two different light sources which fulfill the requirements for BLS were set up and tested as part of this thesis. The first light source (blue beam path in Figure 7.5) is a CW distributed feedback (DFB) diode laser from the company *Sacher Lasertechnik* (labeled as LD in Figure 7.5). This laser diode directly emits at a central wavelength of 780 nm. A periodic structure within the active medium of the laser diode ensures that only a single lasing mode is active and a sufficiently large mode-hop free tuning range can be achieved. The emission frequency of the lasing mode can be tuned by changing the diode current and the temperature. A laser diode has a limited range of mode-hop free tuning. In the case that mode hops interfere with the diode current modulation, the temperature can be adjusted to change the center frequency of the diode.

Semiconductor diodes are sensitive to light which is scattered back into the diode, which leads to destabilization or even damage. To avoid this, a two-stage Faraday isolator (FI) is used, which acts as an optical diode. It only allows light to pass in one direction while blocking the reverse direction, effectively protecting the laser diode from any back-scattered light. The FI provides a reverse power suppression of 60 dB.

To stabilize the laser frequency, a small fraction of the beam is diverted and sent through a gas cell containing ^{87}Rb vapor (labeled as RB). The intensity transmitted through the vapor cell is detected with a photodetector (PD). The locking on the Doppler-broadened absorption lines works as previously described.

A drawback of semiconductor laser diodes is that the gain of the active medium spreads across a broad range of photon energies. This gives rise to an effect called amplified spontaneous emission (ASE). Due to ASE, in addition to its lasing mode, the diode also emits a background of spontaneously emitted incoherent photons, which are amplified as well and cover a broad range of energies. This reduces the contrast that can be achieved in BLS measurements. To filter this light from the laser beam, a two-

stage filtering system is employed. The filtering follows the scheme used by Schlüßler *et al.* [196].

In the first stage, a piezo-tunable Fabry-Pérot interferometer (FPI) is employed. The transmission spectrum of an FPI exhibits periodic maxima of almost full transmission whenever the distance between the two mirrors of the FPI matches integer multiples of the wavelength of the light. When this condition is met, the light waves are reflected repeatedly between the two mirrors and interfere constructively at the output side. If the mirror distance deviates from this condition, there is destructive interference and the light is instead back-reflected from the FPI. The FPI transmission spectrum consists of a series of sharp peaks separated by wide plateaus of high reflectivity. The spacing of the transmission peaks for a single wavelength defines the free spectral range (FSR), which for the FPI in use amounts to 15 GHz in photon frequency.

To use the FPI as a laser-line filter, the mirror distance needs to be matched to the emission frequency of the laser. Here, the light which is back-reflected from the FPI can be used. To separate it from the incoming light without significant losses, the scheme of a so-called *poor mans isolator* is used. It builds on the fact that the handedness of circularly polarized light switches upon reflection from the FPI. The linearly polarized light from the laser is rotated by 45° after passing the FI. This first is corrected by a HWP, which rotates the polarization into vertical direction. After this, the light passes a polarizing beam splitter (PBS), followed by a quarter wave plate (QWP). The QWP transforms the light into circularly polarized light, whose helicity is flipped upon reflection from the FPI.

The same QWP converts the back-reflected light back into linearly polarized light, which is now rotated in polarization by 90° with respect to the incident light. Subsequently, it is reflected from the PBS and detected by a photo diode. When the laser emission strongly differs from the transmitting frequencies of the FPI, the intensity measured on the photo diode is increased. If they are in close vicinity, the photo diode measures a sinusoidally modulated intensity, which stems from the modulation of the laser frequency used to lock on the Rb absorption line. The modulated signal can be used a second time to tune the mirror distance of the FPI using built-in piezo actuators such, that its transmission window matches the laser frequency. The regulation to lock the FPI on the emission frequency of the laser works in the same way as was described for the laser stabilization.

In this way, the FPI suppresses most of background emission from the laser diode due to the ASE. Because of the periodic transmission maxima of the FPI, ASE photons of certain energies can still pass this first filter stage (see Figure 7.6, blue lines). To also suppress these, a second stage of filtering is necessary. It uses a volume holographic grating (VHG), which is a mm-thick glass substrate with a periodically modulated refractive index, forming planes inside the volume similar to the lattice planes in a crystal. The transmission and reflection of light from such filters is governed by the Bragg condition, which dictates the angle of constructive interference θ for a given

wavelength of the light λ and distance between the planes d :

$$n\lambda = 2d \sin \theta. \quad (7.1)$$

There are different diffraction orders for $n = 0, 1, 2, \dots$. The VHG used here is designed to work in reflection geometry. It reflects light whenever the Bragg condition is matched, i.e. whenever the angle of incidence of the light matches with the phase difference which occurs between individual beams of light reflected from the planes in different depths of the material. By changing the angle of the VHG, its reflection wavelength can be tuned. The angle is set such that the reflected intensity is maximal for the laser in use. Photons with an energy deviating from the central emission line of the laser are transmitted through the VHG and thus removed from the reflected beam (see Figure 7.6, grey shaded areas). Due to its larger bandwidth of ≈ 150 pm (or 300 GHz) than the FPI, the VHG effectively suppresses the remaining lines of ASE beyond 150 GHz. After this two-stage filtering, only the central wavelength of the laser and a few close ASE lines remain. This is not an issue since, due to the design of the spectrometer (matched FSR), these emission lines are imaged on the same pixels of the spectrometer camera where the Rayleigh peaks appear and which are ignored anyways. Following the ASE filtering, the beam is focused through a pinhole to ensure a clean mode profile. After this, the light is suitable to be used in the nano-focused BLS setup.

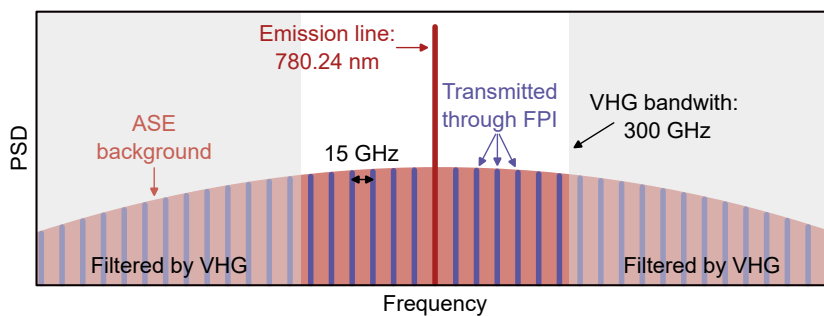


Figure 7.6. | Two-stage filter employed for the single mode diode laser. The diode emits a broad ASE background (red area) besides its emission line (dark red line). The narrow-bandwidth FPI filters the ASE background, but due to its FSR has multiple, 15 GHz-spaced emission windows (blue lines). The VHG has a broader bandwidth and suppresses a large range of the remaining ASE (grey shaded area).

A second laser, which was evaluated and set up for the use in the nano-focused BLS experiment, is a frequency doubled solid-state fiber laser (green beam path in Figure 7.5) from the company *Shanghai Precilaser*. It consists of an external cavity seed laser, that uses an Er-doped fiber as gain medium. It emits at a central wavelength of 1560 nm. Subsequently, the light is amplified and frequency doubled inside a second harmonic generation (SHG) crystal, to achieve an output at twice the frequency (or half the wavelength) of the seed laser, resulting in an output wavelength of 780 nm. The use of nonlinear frequency doubling has the advantage that ASE, which might be emitted by the seed laser, is strongly suppressed, as it will not be converted due to its low power.

The locking of this laser works in a similar way as described for the diode laser, by using Rb absorption spectroscopy. In this case SAS is used to eliminate Doppler broadening and allow to even lock to the hyperfine absorption peaks. The laser output passes a polarizer (GT) to ensure a clean polarization state and is focused through a pinhole to ensure a clean Gaussian mode profile, before it is coupled into the s-SNOM system. Due to the higher output power (600 mW), better stability and superior emission spectrum, this laser proves to be superior over the diode laser source and will be used in the nano-focused BLS setup.

7.2.4. High Throughput VIPA Spectrometer

Besides a stable and narrow-band light source, the nano-focused BLS setup requires a spectrometer which achieves high contrast, high frequency resolution and high throughput. For this purpose, a specialized spectrometer is constructed. Usually, in state-of-the-art BLS spectrometers, piezo-tunable FPIs are scanned and the transmitted light is detected by a sensitive photodetector. A tandem design of two FPIs is used to maximize finesse and FSR. This design was developed by Sandercock and coworkers [145, 197]. The wavelength of the light is encoded in the FPI mirror position. This method yields an exceptionally high contrast and spectral resolution, but as most of the light entering the spectrometer is not used for most of the time, it is also much slower than dispersive spectrometers. Scanning FPI spectrometers are therefore inconvenient to use in combination with a scanning probe method, as the measurement time is strongly limited by sample drifts and needs to be kept as small as possible. Measurements over the course of many hours, which are not exceptional for spatially resolved micro BLS studies, are not feasible.

Therefore, a different approach is necessary which eliminates the need for scanning optics inside the spectrometer to capture a spectrum. In a spatially resolved measurement, this is necessary at every single sample position. In a dispersive spectrometer, the light is dispersed spectrally and imaged on a (usually line-shaped) camera sensor. This allows to simultaneously capture a full spectrum, however, at the cost of reduced contrast. Dispersive spectrometers which rely on gratings or prisms lack the spectral resolution which is necessary for BLS experiments, or would need to be many meters in size. The spectrometer which is constructed for the nano-focused BLS system uses so-called *virtually imaged phased arrays (VIPAs)* [198], which are a different kind of dispersive elements achieving large dispersion at a much smaller total footprint.

Working Principle of a VIPA

A VIPA is an optical element, which is closely related to an FPI. It consists of two plano-parallel reflecting surfaces, usually the polished surfaces of a millimeter-thick glass substrate, which form a cavity. Light can enter the cavity through an anti-reflection-coated entrance slit. The remaining surface on the entrance side is coated

with a highly reflecting coating ($\sim 100\%$); the exit surface is slightly less reflecting ($\sim 90\%$). Light entering the VIPA reflects many times inside, while part of it leaves through the exit facet.

Contrary to an FPI, which usually is designed to work with collimated light, the light is focused on the entrance slit of the VIPA. As a result, the light enters and propagates under different angles (different wavevectors) simultaneously, leading to different conditions for interference of the exiting light. Light with a specific wavelength only interferes constructively for specific exit angles and forms approximately plane waves. Light with a different wavelength exits under a different angles. In this way, a VIPA disperses the light along a specific axis which is its tilt direction [199]. A sketch of the beam path inside a VIPA is shown in Figure 7.7.

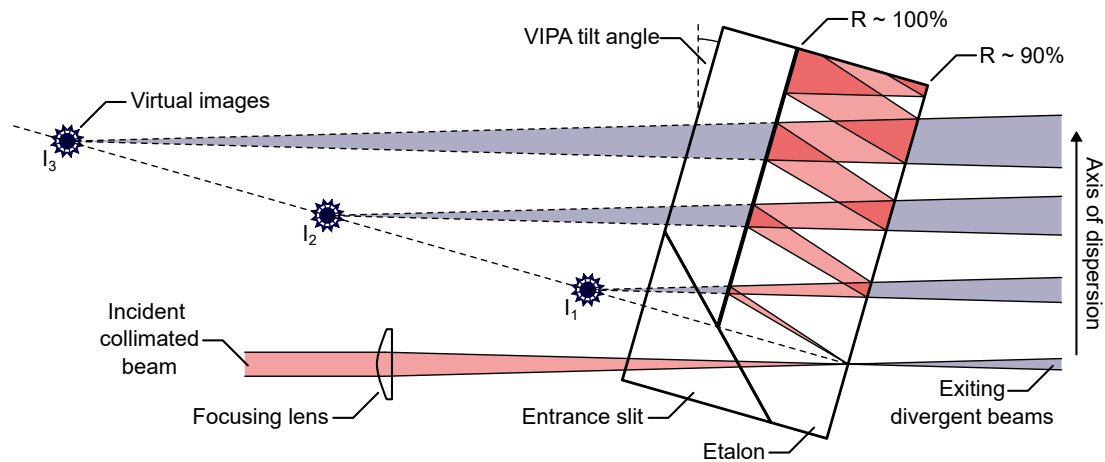


Figure 7.7. | Schematic of a VIPA. The collimated incident beam is focused on an entrance slit. Inside the etalon, the beam reflects back and forth between a highly reflecting surface ($R \sim 100\%$) and the partially reflecting output facet ($R \sim 90\%$). Upon each reflection, a part of the light exits the VIPA. It has traveled an optical path length depending on its entrance angle, and appears to stem from virtual images of the entrance slit. The light from these virtual sources interferes, depending on its wavelength, constructively under different exit angles. The large difference in the optical path length between the virtual sources leads to a dispersion much greater than what can be achieved with diffraction gratings. The dispersion can be controlled by the VIPA's tilt angle.

What sets a VIPA apart from ordinary diffraction gratings or prisms, is the large difference in path length between the individual interfering beams. The two facets of the cavity have a distance of around 5 mm, which results in an optical path difference of 14 mm between two round trips of the light, assuming normal incidence and an index of refraction of 1.4 for the glass of which the VIPA is fabricated. In reality, the light does not reflect under normal incidence, but under an angle, which further increases the path difference. The large path difference between the interfering beams (compared to the wavelength of the light of 780 nm) dramatically increases the dispersion and allows for a frequency resolution in the order of 100 MHz. Because of the low absorption losses inside the medium and the high reflectivity of the interfaces of the VIPA, the light takes

hundreds to thousands of round trips inside, depending on tilt angle. The tilt angle changes the path difference between the light beams and hence the dispersion. The large number of interfering beams with large phase differences sharpens the angular distribution of the dispersed spectrum. As all beams need to interfere constructively, the angular range in which this condition is fulfilled becomes smaller with increasing number of participating beams. This allows for the high spectral resolution.

Similar to an optical grating, a VIPA generates higher orders of diffraction. The VIPAs used in the spectrometer have a FSR of 15 GHz. This means, that light which is frequency shifted by this amount exits the VIPA under the same angle as light from the next diffraction order, which is not frequency-shifted. This, it is imaged on the same position on camera sensor and, thus, can not be distinguished by the spectrometer anymore.

Spectrometer Setup

The spectrometer built in this thesis uses a two stage design with two VIPAs. It follows a design described by Berghaus *et al.* [200]. A sketch of the beam path is shown in Figure 7.8. The light, which is focused through an entrance pinhole of the spectrometer, is collimated and then imaged by a cylindrical lens on the entrance slit of the first VIPA. This VIPA disperses the light in vertical direction. The spectrally dispersed light is imaged by a subsequent cylindrical lens on a horizontal slit-aperture. The aperture is located in the focal plane of the cylindrical lens. Position and width of the aperture represent a first spectral filter for the light. It can be set such, that the Rayleigh light of first and second diffraction order is exactly blocked. Only the frequency shifted light which is imaged in between the two Rayleigh peaks can pass the slit aperture. For increased spectral resolution and background suppression, a second VIPA is employed. A spherical lens images the light which passes the first slit on the entrance slit of the second VIPA, which is rotated by 90° . This VIPA disperses the light in horizontal direction. It is followed by another spherical lens which, again, images the light on a now vertical slit aperture, which is positioned in the focal plane of the lens. It serves the same purpose as the first slit, but in the horizontal direction. In this way, a two stage filtering of the Rayleigh light is achieved. The light which passes the second slit is then imaged on a camera and the spectrum is evaluated using a software, that was developed for this purpose.

Like in any other spectrometer, there is a certain amount of background light. This can be, for example, stray light stemming from imperfect optical elements inside the spectrometer, undesired reflections or scattering, or simply light with entirely different photon energies, which enters the spectrometer from the outside. Background light generally reduces the contrast of the spectrum, since it reaches the detector, as well, and reduces the dynamic range. This problem is partially mitigated by dispersing the spectrum in two dimensions. Due to the two orthogonal VIPAs the spectrum

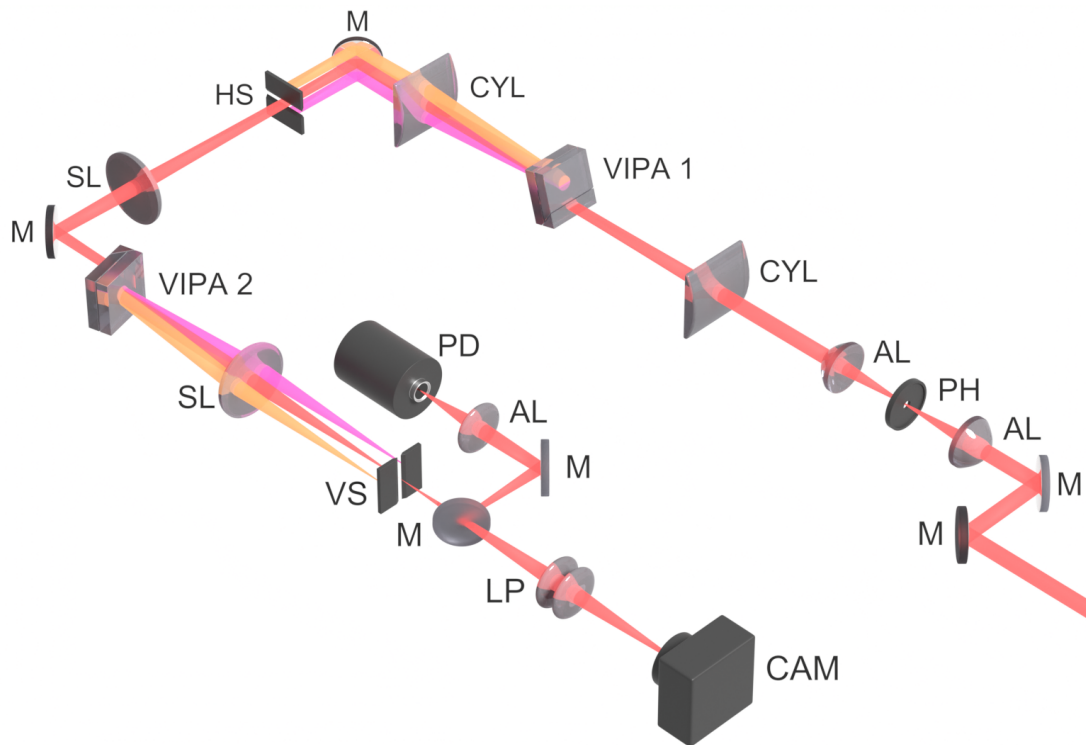


Figure 7.8. | Schematic of the VIPA spectrometer. The light is focused through an entrance pinhole (PH) by an aspherical lens (AL). Subsequently, a cylindrical lens (CYL) focuses the light into the first VIPA, which disperses it in vertically (orange and purple beams), followed by a second cylindrical lens to image it on a first image plane. In a second stage, the light is focused into the second VIPA by a spherical lens (SL), resulting in an additional dispersion in horizontal direction. A second lens images the light in a second image plane, which is then, again, imaged either on a camera (CAM) using a matched lens pair (LP) or on a single photodetector (PD). Horizontal and vertical slit apertures (HS and VS) can be used to restrict the range of photon energies which pass onto the detector.

is dispersed along an arc roughly following the diagonal of the image plane. The background light, on the other hand, reaches all pixels of the sensor with an equal probability. This improves the ratio between signal and background on the relevant pixels as most of the background photons can be readily discarded.

Figure 7.9 shows an image recorded by the camera of the spectrometer in different configurations. For this, the laser was directly coupled into the spectrometer. Without any of the VIPAs inserted, there is no dispersion and the collimated incident beam is visible as a single large spot on the image (Figure 7.9 A). Figure 7.9 B and Figure 7.9 C show the change of the camera image if either one of the two VIPAs is inserted into the beam path. The light is dispersed in the vertical or radial direction, leading to horizontal stripes or rings. The position on the camera now corresponds to a certain photon frequency. There are many orders of diffraction visible. The frequency difference between two orders of diffraction equals 15 GHz, the FSR of both VIPAs. Figure 7.9 D shows the combined effects of both VIPAs. The light of a single order of diffraction follows the dashed, green curve on the image sensor.

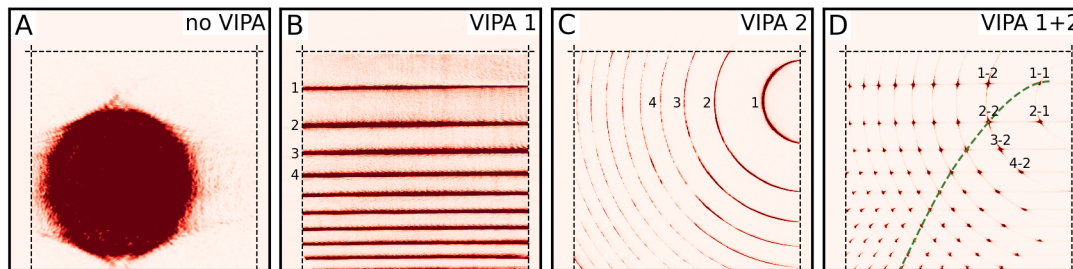


Figure 7.9. | Camera images of the laser spot in the VIPA spectrometer. The dashed lines indicate the positions of the slit apertures. **A:** Image of the collimated laser beam without inserted VIPAs. **B:** Image with only the 1st, horizontally oriented VIPA inserted. The light is dispersed vertically. **C:** Image with only the 2nd, vertically oriented VIPA inserted. The light is dispersed in radial direction. **D:** Image with both VIPAs inserted. The combined dispersion occurs along the diagonal, indicated by the green line. The numbers label the first few diffraction orders.

7.2.5. Spectral Filtering of Rayleigh Scattering

Elastically scattered components of the light are a major issue for BLS and Raman scattering experiments. They are usually much more intense than any inelastic scattering and need to be suppressed, as they otherwise can easily saturate the camera sensor in the spectrometer. There are different ways to achieve Rayleigh suppression.

The most simple way, which is usually employed in Raman spectroscopy, is to use optical edge filters. Such filters exist as low- or high-pass variants and block the high or low wavelength region of the spectrum of the scattered light. The filter is chosen such, that its cut-off wavelength is slightly below/above the Rayleigh wavelength. This simple solution has the drawback that, depending on the filter type, only either the Stokes or the anti-Stokes part of the spectrum can be observed. A better solution in that regard are notch filters, which suppress only a narrow band around the Rayleigh peak. Both filter types are limited in the steepness of the cut-off wavelength, which leads to losing part of the otherwise observable spectrum close to the Rayleigh peak (typically up to 100 cm^{-1} or 3 THz). An improvement for notch filters are the aforementioned VHGs. Due to the holographic character, the block-band is much more narrowly defined. Still, a spectral region of about 1 THz around the Rayleigh peak is blocked. Therefore, they are still not suitable for BLS spectroscopy.

Instead, the atomic absorption of Rb vapor, which was used to stabilize the laser source, can be used again, but this time to filter the Rayleigh peak. For this purpose, the light passes through a second gas cell filled with Rb vapor. Since the laser frequency is already locked on the frequency of the absorption line, the cell is most effective in absorbing the elastically scattered light before it enters the spectrometer. The spectral width of the absorption line is determined by Doppler broadening, resulting in a filter bandwidth in the order of 500 MHz .

In the present setup, isotopically pure ^{87}Rb is used. The relevant atomic transitions are from $5s_{1/2}$ to the $5p_{3/2}$ orbitals of Rb. Due to hyperfine splitting, the $5s_{1/2}$ orbital

is split into two levels spaced by approximately 6.8 GHz. The $5p_{3/2}$ orbital is split into four energy levels with spacings in the order of 70 MHz to 270 MHz. The splitting of the $5p_{3/2}$ orbitals is not relevant, as it is hidden by Doppler broadening. The splitting of the $5s_{1/2}$ orbital, on the other hand, leads to a drawback of the Rb filter, which is a second absorption band within the FSR of the spectrometer. Isotopic purity of the Rb gas is important, as any other isotopic species would give rise to even more absorption bands slightly shifted in energy, which would further disturb the detection of BLS light. A second limitation of the Rb filter is that the absorption of the Rayleigh light strongly depends on the light intensity itself. Too high intensity leads to saturation of the Rb atoms, which reduces the attenuation. Therefore, the intensity of the light that is filtered is limited to the $\sim 100 \mu\text{W}$ range, which is usually the case for s-SNOM.

7.2.6. Evaluation of the Setup and Test Measurements

To validate the function of the VIPA spectrometer, a series of tests has been performed. Different polymer samples were placed in the SNOM microscope while the tip was retracted. The measurements, displayed in Figure 7.10, show additional peaks in between the Rayleigh peaks. Those are caused by photon-phonon scattering inside the materials.

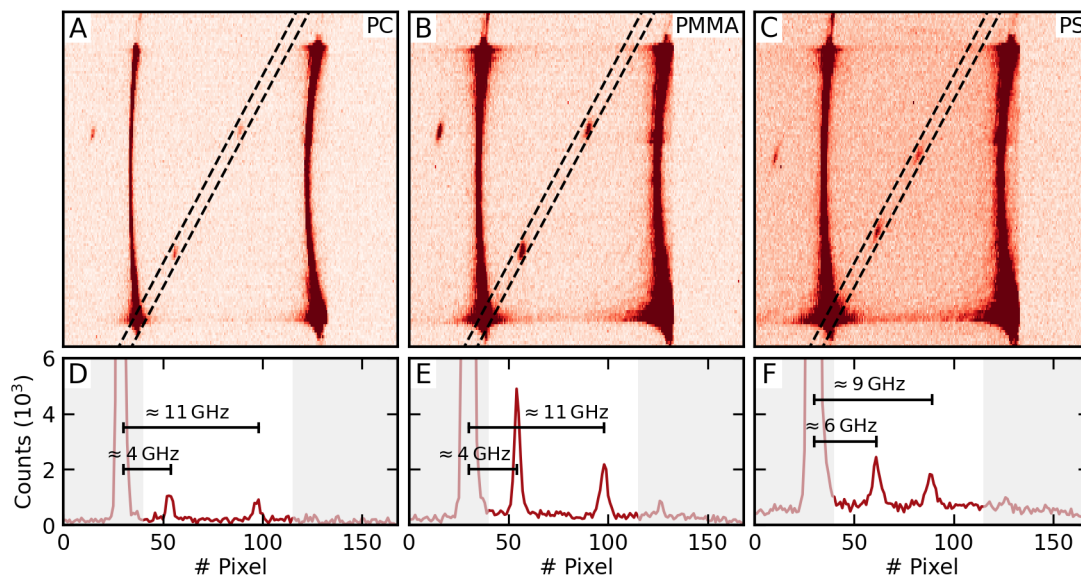


Figure 7.10. | **A-C:** Camera images of the VIPA spectrometer taken on samples of polycarbonate (PC), polymethyl methacrylate (PMMA) and polystyrol (PS). The additional peaks are due to inelastically scattered photons. **D-F:** BLS spectra extracted from the areas marked by the dashed lines in panels A-C. The scales indicate approximate frequency differences with respect to the 1st Rayleigh peak. The Rayleigh peak of the 2nd diffraction order is not visible as it is cut by the slit aperture inside the spectrometer.

The specific phonon modes that can be observed by BLS are determined by the exact scattering geometry, which is a consequence of the conservation of momentum and the excitability of the mode determined by the light polarization [201]. Furthermore, the

frequencies of the phonons depend on Young's modulus of the material, and hence on the exact composition and the temperature, making it hard to compare the peak positions to a reference.

From the camera images, the spectra are extracted (Figure 7.10 D-F). The samples of PC and PMMA show peaks at approximately the same positions, shifted by ~ 4 GHz and ~ 11 GHz with respect to the first Rayleigh peak. The two peaks correspond Stokes and anti-Stokes scattering of the same phonon mode. This means, if the Stokes mode is shifted by $\Delta f = 4$ GHz, the anti-Stokes peak will appear at $f_{\text{FSR}} - \Delta f$. Since the FSR of the system is 15 GHz, this corresponds to 11 GHz. However, there is some ambiguity as it is not clear which of the two peaks actually corresponds to Stokes and anti-Stokes scattering, so the frequency shifts could be swapped. The PS sample shows different shifts of ~ 6 GHz and ~ 9 GHz. This suggests, that the origin of the shifts is a similar phonon mode for the PC and PMMA sample, but a different mode for PC.

7.2.7. Future Application of the Technique in Experiments

The primary purpose of the nano-focused BLS setup will be to measure magnetic excitations with high spatial resolution provided by the s-SNOM tip. To do so, a specialized sample holder was designed and fabricated. This sample holder allows to provide microwave excitation of up to 15 GHz to the sample. It also allows to apply a small magnetic field in the order of 10 mT. A design sketch is shown in Figure 7.11. In addition, DC contacts offer the possibility to apply voltages or currents to a sample.

Driven spin waves in an extended ferromagnetic layer provide an excellent way to calibrate the spectrometer, by subjecting the sample to a number of known RF frequencies and observing the BLS peaks of the uniform response (FMR mode). This will also allow to distinguish between Stokes and anti-Stokes peaks in the spectrum, depending on the direction they shift when changing the excitation frequency. A restriction of BLS spectroscopy is the requirement of conservation of momentum. This, however, is lifted in presence of the s-SNOM tip, as it provides the wide a range of momenta due to its nano-scale size. This will make it possible to detect excitations, such as the uniform magnon mode ($k_{\text{sw}} = 0$), which possess a momentum otherwise unsuitable for being detected in reflection geometry ($k_{\text{sw}} \approx 2k_{\text{Ph},\parallel}$).

The range of studies where nano-focused BLS could be of use is broad. An application of the technique will be in the mapping of localized spin wave modes in magnetic microstructures, similar to the studies conducted by Jersch *et al.* in elliptical NiFe elements [194]. A second example are inhomogeneous spin waves generated due to multi-magnon scattering, as were investigated by Hache *et al.* in magnonic waveguides [202]. In general, the technique will be of use whenever spatially high-resolved mapping of spin wave modes is of interest, which are either localized within magnetic micro structures, or possess large wave vectors.

Finally, the technique will enable further investigation of the frequency multiplication

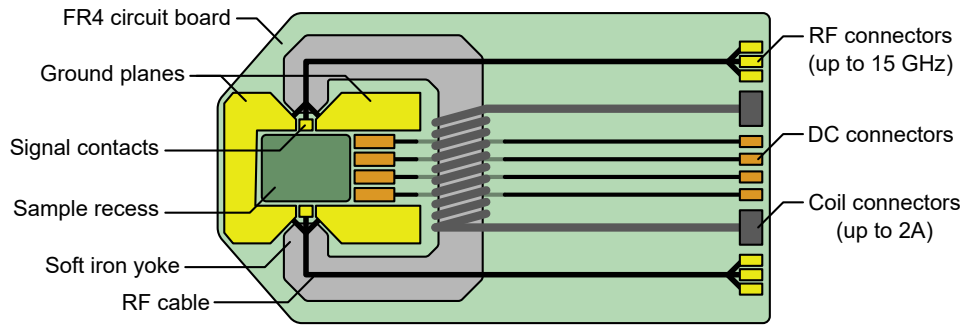


Figure 7.11. | Design of a sample holder for nano-focused BLS measurements on ferromagnetic samples. A miniaturized electromagnet with a yoke is used to apply magnetic fields. RF cables are used to guide microwaves to the sample. DC contacts can be used to apply additional voltages or currents to the sample.

process described in Chapter 6 and [30]. In any of those cases, the potentially superior spatial resolution due to the s-SNOM technique can lead to better understanding of the spin waves under investigation.

7.2.8. Outlook to Further Improvements of the Setup

The previous sections described the state of the nano-focused BLS setup so far. Further improvements are conceivable to improve the performance in multiple aspects. These are discussed in the following.

Increase of FSR and Contrast of the Spectrometer

To increase the FSR, it is possible to exchange one of the VIPAs with another VIPA which possesses a different FSR. The total FSR of the spectrometer corresponds to the least common multiple of the FSRs of both VIPAs. A design with two different VIPAs was described by Berghaus *et al.* [203]. A complication of this design is that the spectrum is not anymore simply distributed along a single line, but split into different segments which appear at different positions in the camera image and need to be stitched together. In addition, more than two VIPAs can be employed in the spectrometer to increase the contrast, as was demonstrated by Scarcelli *et al.* [204].

Rayleigh Suppression

A major task in BLS spectroscopy is to provide a sufficient suppression of the elastically scattered light, the Rayleigh peak. A simple solution is to extend the travel path of the light through the Rb vapor, either by allowing for multiple passes through the Rb cell or by using more and longer Rb cells. A longer travel path through the Rb vapor increases the interaction volume and hence the number of atoms which can contribute to the absorption, improving the attenuation.

Raman Separation

In the tests of the setup which were carried out, under certain conditions a constant background signal was observed across the whole FSR of the spectrometer. This background is potentially due to Raman scattering, which occurs either on the sample or inside a optical element in the beam path. Raman-scattered light has large shifts in photon energy with a much broader spectral linewidth. Therefore, it appears as a continuum in the BLS spectrum. A VHG is the ideal optical element to filter Raman scattered photons before reaching the spectrometer. It reflects light within a narrow frequency band, which would be the Rayleigh and BLS light, while the the Raman-scattered light passes and is discarded. Because a VHG works in reflection geometry, it cannot be readily inserted into the beam path. Instead, the path needs to be altered to match the reflection angles before the light is coupled into the BLS spectrometer. This configuration should lead to a suppression of the continuous spectral background observed. In addition a VHG would allow to feed the separated Raman-scattered light into an additional Raman spectrometer to simultaneously perform TERS measurements.

Suppression of Far Field Scattering

The BLS spectrometer presented functions by spectrally dispersing the light and imaging it on a CMOS camera. While this is convenient to simultaneously detect a full spectrum at once, the sensitivity and speed of the camera are limited. A point detector, on the other hand, can allow for a much more sensitive measurement and, due to its higher bandwidth, for a demodulation of the signal. Such demodulation enables to distinguish the near field signal from the far field background, much better than just subtracting two images with approached and retracted s-SNOM tip. To utilize such a detector, a single spectral component of the light can be separated using the already set up slit apertures, which, due to their positioning in the image planes of the spectrometer, act as spectral filters. The separated component is then imaged on the detector instead of the camera. The detector signal can be demodulated on the tapping frequency of the SNOM tip. Analog to s-SNOM measurements, this will allow to truly separate the components scattered from the near field from the undesired far field reflections. However, due to the low light intensities of the individual BLS components, the requirements on the sensitivity of the detector and its dynamic range are high. In that regard avalanche photodiode (APD) detectors seem to be most suitable. Furthermore, electronic components such as amplifiers and filters need to be chosen carefully to match the needed bandwidth without introducing additional noise.

Conclusion

This work, which had the aim to explore optical techniques to study properties of magnetic materials with a spatial resolution beyond the optical diffraction limit, brought two main results. In the first part, an all-magnonic frequency conversion process was investigated in $\text{Ni}_{80}\text{Fe}_{20}$. Upon MHz RF excitation, spin waves are generated, which form a six-octave spanning frequency comb that reaches well into the GHz range. This process was studied in a comprehensive fashion using complementary optical methods: primarily confocal NV center magnetometry, SNS-MOKE, and scanning NV center magnetometry.

Using all these methods in combination with micromagnetic simulations, the nature of the high harmonic spin waves was studied and their origin could be explained. The mechanism for the frequency comb generation was found to rely on switching events of different regions of the magnetic film, which can only exist in soft magnetic materials at low bias fields. The spin waves emitted interfere and lead to a synchronization of the switching events, resulting in the observed coherent response. This process is affected by the underlying magnetization pattern, the bias field, and the shape and size of the magnetic structures. The combination of the different measurement methods was key to uncover the physics of this initially unexpected process.

By moving toward small structures, SNS-MOKE microscopy measurements have confirmed that frequency comb generation is still present in confined geometries, albeit at a reduced efficiency. Besides this, the results from the previously conducted confocal NV center microscopy measurements were extended to the scanning NV center microscopy approach. Scanning NV center magnetometry provides a new mean to investigate the magnetization dynamics at an even higher spatial resolution, which has proven to be in the range of 100 nm. This is an improvement of more than two to three times compared to conventional, diffraction-limited techniques. It was shown, that scanning NV microscopy can be used to image the dynamics of a sample. This is facilitated by the interference of the excitation field with the stray field emitted by the spin waves, which provides phase resolution.

In the second part of this thesis, a novel nano-focused BLS setup was constructed. This was done with the aim to provide an optical method, which can be used to investigate the dynamics of magnetic materials at the nano-scale. For this, a multi-purpose near field setup was built and tested. Furthermore, a high-throughput, high-resolution VIPA spectrometer was designed, constructed and tested, together with a stabilized narrow-band light source. Initial test measurements on different polymer samples demonstrate the function of the BLS system. Further work and test measurements

are needed to demonstrate the spatial resolution of the setup and to improve the suppression of undesired non-BLS light in the spectrometer. Nano-focused BLS will add a new tool to the experimental toolbox to investigate magnetism and magnetic phenomena beyond the diffraction limit.

Heat-Assisted Detection of Magnetization

Near field assisted heating is a method that builds on s-SNOM. Instead of detecting the scattered light from the enhanced near field, it relies on the fraction of the light absorbed by the sample. The absorption of the light leads to local heating, which influences a sample in different ways. Due to the strong confinement of the incident light under the s-SNOM tip, a highly localized heat source is generated, which subjects the sample to a heat gradient. In magnetic materials, these heat gradients can give rise to magneto-thermal transport effects, such as the anomalous Nernst effect (ANE), which was introduced in Section 3.1.2. When the tip is scanned across an area of the sample where the magnetization changes (e.g. a domain wall), the electrical signal due to the ANE changes accordingly. The nanoscopic heat source enables local transport measurements and allows to map the local magnetic state of the sample with high spatial resolution.

Magneto-thermal methods have recently been used to image magnetic domains in non-collinear antiferromagnets, like CuMnAs, where the tip-induced temperature gradient leads to a signal via the magneto-Seebeck effect [205]. Another example is the mapping of magnetic domains in CoFeB [190, 206] or octupole domains in the non-collinear antiferromagnet Mn₃Sn via the ANE [207].

This also is the relevant effect used in the study presented in the following. In a magnetic sample, the ANE can generate an electric field \mathbf{E}_{ANE} due to a heat gradient, which can be picked up as a voltage V_{ANE} across a suitably structured device, e.g. a thin wire. It depends on the magnetization vector \mathbf{M} and the ANE-constant of the material S_{ANE} :

$$V_{\text{ANE}} \propto \mathbf{E}_{\text{ANE}} = \mu_0 S_{\text{ANE}} \nabla T \times \mathbf{M}. \quad (\text{A.1})$$

The voltage is generated perpendicular to both, the magnetization direction and the heat gradient. This makes it clear, that the geometry needs to be chosen correctly so the correct vector components are picked up.

A.1. Imaging of Ferromagnetic Domains in In-Plane Magnetized CoFeB

In the co-authored work from Pandey *et al.* [190], the s-SNOM setup is used to provide the nano-focused heat gradient to ferromagnetic samples and electrically detect the ANE voltage, while scanning the sample to image the magnetization pattern.

As a first demonstration of the method, scanning ANE microscopy was used to image domain patterns in a 15 nm-thick CoFeB wire. This was done using a conventional microscope equipped with a $NA = 0.7$ objective lens to focus the light. The method is then adapted to be used with the s-SNOM setup. Here, a MIR laser with a wavelength of $8\ \mu\text{m}$ is used to illuminate the tip to generate the temperature gradient on the sample. For background suppression, the signal is demodulated on the 2nd harmonic of the tapping frequency ω , as was described in Section 3.3.5. An example for a measurement is shown in Figure A.1.

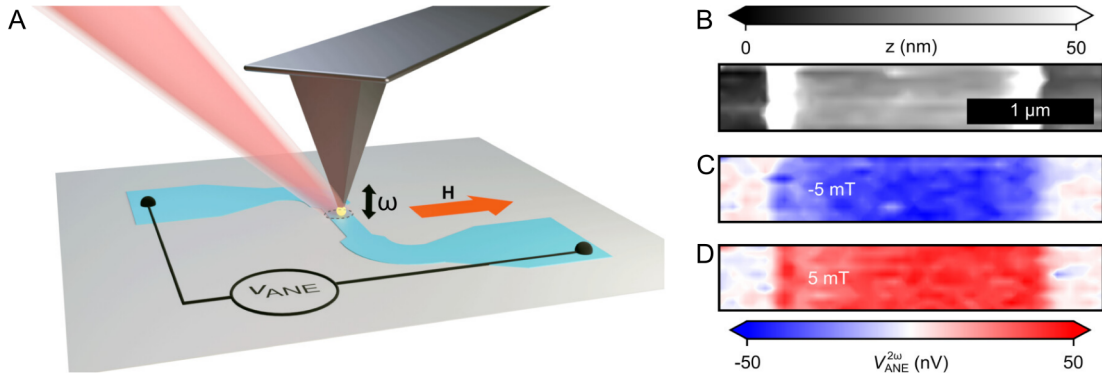


Figure A.1. | **A:** Sketch of the CoFeB device in the s-SNOM setup. The tip generates a field-enhanced nano-scale temperature gradient, which gives rise to the ANE voltage V_{ANE} . **B:** Height map of a section of the wire measured by AFM. **C, D:** Map of the ANE voltage with an applied external field of $\pm 5\ \text{mT}$, which saturates the magnetization perpendicular to the wire. Image adapted from [190].

To determine the spatial resolution, $\text{Co}_{20}\text{Fe}_{60}\text{B}_{20}$ devices were investigated. These square-shaped devices have lateral dimensions of $33\ \mu\text{m}$ and a thickness of $45\ \text{nm}$. The magnetization in these devices lies in the plane of the sample and follows a well-known Landau pattern. A line scan across the domains was conducted, from which the spatial resolution can be extracted. The results were compared to scanning-ANE measurements conducted on similar devices using the conventional microscope. The spatial resolution in the microscope is limited to $\approx 760\ \text{nm}$, mostly due to the spot size of the focused laser beam. The near field ANE setup achieves a spatial resolution of $\approx 74\ \text{nm}$, which is an improvement of roughly one order of magnitude. This comes under the assumption, that the magnetization pattern changes abruptly between the two domains at the top and bottom side of the device. It is influenced by the spread of the heat inside the sample, which is determined by the heat conductivity and influences the temperature gradient.

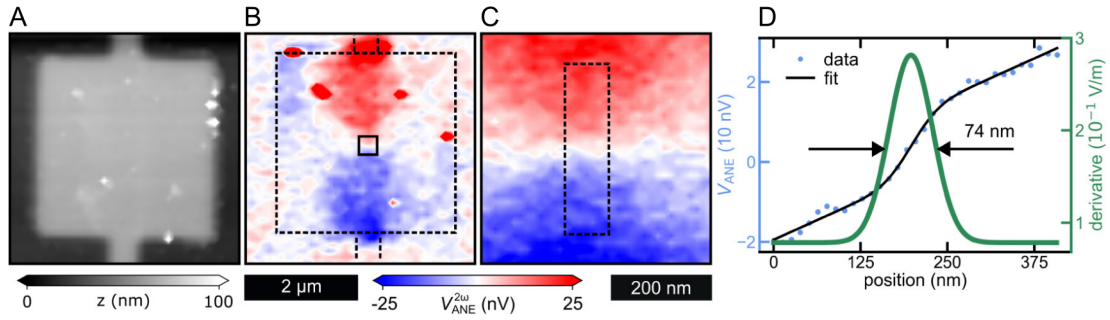


Figure A.2. | **A:** Topography map of the $\text{Co}_{20}\text{Fe}_{60}\text{B}_{20}$ device measured by AFM. **B:** Map of the ANE voltage with no applied magnetic field. The device is in its ground state, which is a Landau pattern. The dashed lines indicate the outline of the device. **C:** Zoom of the black square in the center of B. **D:** Blue data points show the ANE voltage along the vertical direction within the dashed rectangle in C, averaged along the horizontal direction. The data are fitted by an error function (black curve). The green curve shows the derivative of the error function, a Gaussian with an FWHM of 74 nm, which is a measure for the spatial resolution. Image adapted from [190].

A.2. Imaging of Ferromagnetic Domains in Out-of-Plane Magnetized Co-Ni Multilayer Stack

The scanning ANE was used to also examine out-of-plane magnetized materials [190]. Here, Co-Ni multilayer films structured into thin wires with widths of down to 700 nm were scanned. Out-of-plane magnetization does not lead to an ANE voltage if only the out-of-plane temperature gradient is considered. However, it was shown that also in-plane heat gradients can give rise to a sizable ANE voltage [190]. One needs to take into account the counter-acting effects, which arise due to the limited spot size. The in-plane heat gradients on both sides of the spot are of opposite sign, which leads to a cancellation of the electric fields generated due to the ANE and a vanishing ANE voltage, if the magnetization is uniform. The situation is different when the magnetization is non-uniform, e.g. in domain walls, or at the edges of the device. Here, a non-zero voltage can be detected, which allows to deduce the domain pattern. This was done from the scans of the wires and the result is in agreement with Kerr microscopy.

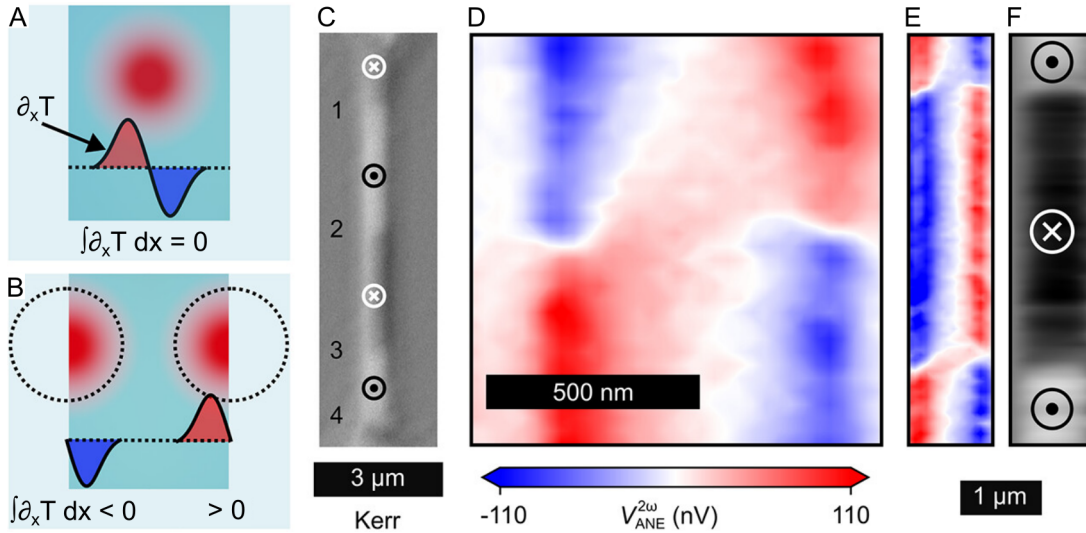


Figure A.3. | **A:** Sketch of the heat gradient $\partial_x T$ in the plane of the sample, as it is generated by the focused laser. If the sample is homogeneous (no magnetic domains and no differences in absorption) the effects average out and no ANE voltage can be detected, since the signs of the in-plane gradient due to the left and the right side of the laser spot are opposite. **B:** Origin of the edge effect. At the edges of the wire the absorption for a part of the laser spot differs strongly due to the change of material, which changes the temperature gradient asymmetrically and gives rise to a non-zero ANE voltage with a sign depending on the side of the device. **C:** Kerr image of the Co-Ni wire, showing four domain walls perpendicular to the wire (numbered). **D:** Map of the ANE voltage around domain wall 3. There is a strong signal at the edges of the wire due to the edge effect. The signal vanishes in the center of the wire, as the out-of-plane magnetization aligns with the out-of-plane temperature gradient, suppressing an ANE signal. Furthermore, the ANE voltages due to the in-plane temperature gradients average out in the wire center. **E:** Larger map of the ANE voltage showing the domain walls 2 and 3. **F:** Domain pattern of the magnetic wire reconstructed by integrating over the measured ANE voltage perpendicular to the wire. Image adapted from [190].

A.3. Imaging of the Magnetization State of the Non-Collinear Antiferromagnet Mn_3Sn

In a second co-authored work, the non-collinear AFM Mn_3Sn was investigated [191]. In this work, thin films were structured into 500 nm-wide wires to enable the measurement of the ANE voltage, which is generated in transverse direction to the magnetic moment and the temperature gradient. It was shown, that the structured thin films exhibit a non-zero net magnetic moment, attributed to a slight canting of the magnetization in the Kagome plane. This moment can be partially switched using in-plane magnetic fields. Nevertheless, there is a non-switchable, field-independent component of the signal. A possible origin of this contribution are magnetic moments that are pinned. A large amount of pinning sites is expected in the sample, as the film is polycrystalline. A second, entirely non-magnetic cause of a field-independent signal is the Seebeck effect, which can give rise to thermal voltages at the boundaries between different grains of the film. The ratio of the switchable contribution to the signal in the examined sample is found to be 19%.

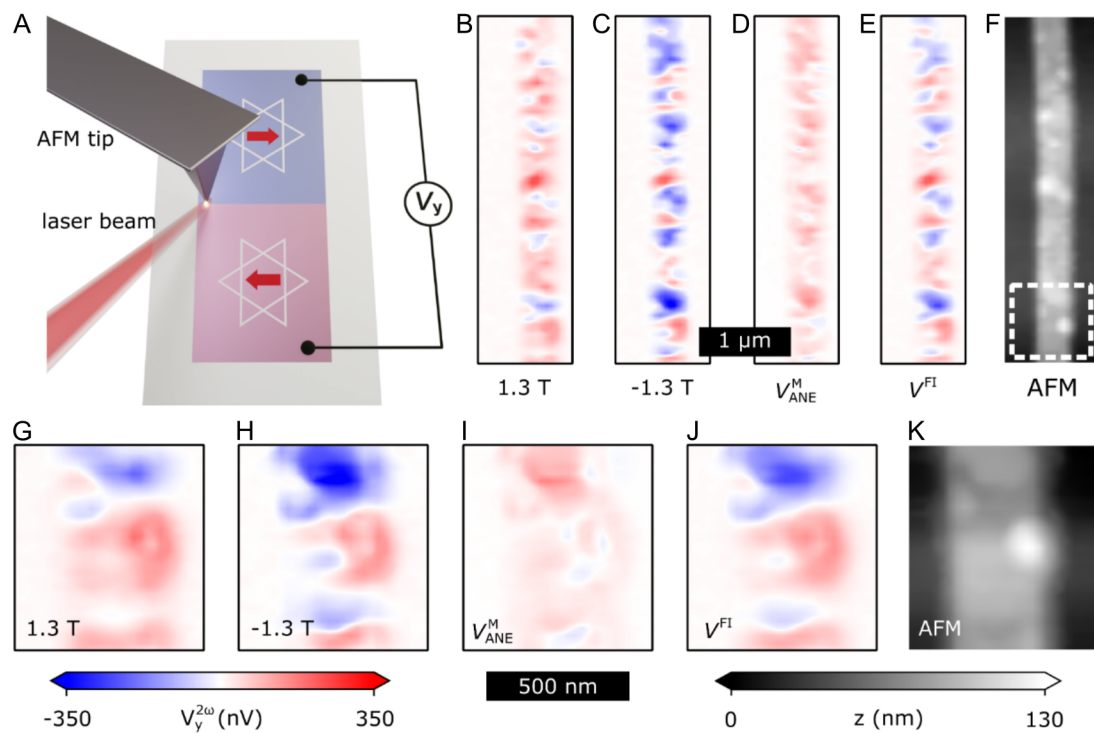


Figure A.4. | Scanning ANE measurements of Mn_3Sn wire. **A:** Schematic showing the s-SNOM tip illuminated by a laser beam, which generates the heat gradient. The sample shows two configurations of the magnetization within the Kagome plane. A voltage is measured along the wire. **B, C:** Maps of the ANE voltage measured after subjecting the sample to a magnetic field of ± 1.3 T. The voltage signal was demodulated at the 2nd harmonic of the tapping frequency of the s-SNOM. **D:** Magnetic contribution to the ANE voltage, obtained as the difference between the two saturated maps. **E:** Field-independent contribution obtained as the sum of the two saturated maps. **F:** Topography measured by AFM. **G-K:** Zoom to a region marked by the white square in F; the signals correspond to B-F. Image adapted from [191].

Nano FTIR Spectroscopy

In Chapter 7, a multi-purpose near field setup has been described. This setup can be used to realize different measurement geometries and methods, such as phase-resolved scattering and nano-focused BLS. It is also possible to combine s-SNOM with absorption spectroscopy. This section briefly covers nano FTIR spectroscopy.

B.1. Working Principle of FTIR Spectroscopy

In FTIR spectroscopy the sample is illuminated by a broad-band light source. The reflected (or transmitted) light, which contains information about the sample, is sent through an interferometer (usually Michelson type). Here, it interferes with a reference beam, before it is detected by a detector. The spectral components, which make up the broad band light, interfere individually, either constructively or destructively, depending on the individual phase difference between the arms. The phase difference, in turn, depends on the wavelength of the component. To enable a wavelength-sensitive detection, the length of one arm of the interferometer is scanned. This effectively modulates the phase of the reference beam, leading to an intensity modulation at the detector. Since the beam is made up of different spectral components with different wavelengths, each component is encoded in a different frequency of this modulation. This has the advantage, that the detector does not need to be wavelength-sensitive to detect the spectral composition of the light reaching it. Instead, a simple FFT of the time trace of the signal throughout the scan of the interferometer arm directly yields the entire spectrum.

B.2. Nano FTIR Spectroscopy Setup

In nano FTIR spectroscopy, the s-SNOM tip is used in the same way as described in Chapter 7 in reflection geometry. The incident light is focused on the tip, where it is enhanced in the near field of the tip. The scattered light is sent to the interferometer. The sample can be scanned underneath the tip to map the response with the enhanced spatial resolution of the near field technique, which is in the order of 20 nm. The schematic of the setup is shown in Figure B.1. The areas with blue background indicate parts of the setup for generating the broad band laser light. Green areas indicate the main parts of the s-SNOM setup, laser alignment and detection. The interferometer is located to the right of the main SNOM unit.

As the name implies, FTIR spectroscopy usually operates in the IR range of the spectrum. In the present setup, the broad band light is generated by means of *difference frequency generation (DFG)* inside a GaSe crystal. The setup is described in the following section. The generated light covers a range from $5.5\ \mu\text{m}$ to $9\ \mu\text{m}$ (or $1100\ \text{cm}^{-1}$ to $1800\ \text{cm}^{-1}$). The scattered light is detected by means of a broad band MCT detector. The described nano FTIR spectroscopy setup allows to measure absorption spectra even of single molecules, due to the near field enhancement and the increased spatial resolution.

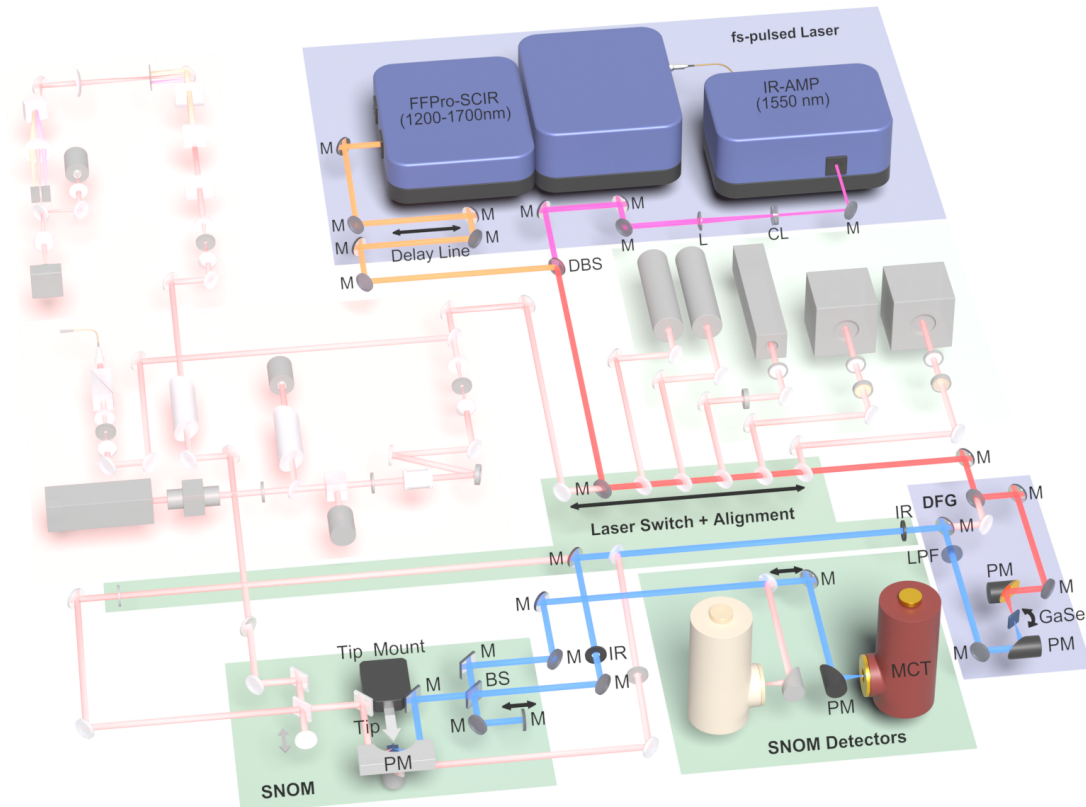


Figure B.1. | Optical path of the nano FTIR spectroscopy setup. Two femtosecond pulsed lasers, a broad band (orange beam) and an amplified oscillator (purple beam) are combined with a dichroic beamsplitter (DBS). The broad band laser beam can be delayed using an optical delay line, to overlap the laser pulses with the amplified oscillator beam in time. The light is focused into a GaSe crystal (red beam) using a parabolic mirror (PM). Inside the crystal, DFG light is generated, which is collimated, filtered using a long pass filter (LPF, cut-on at $3.6\ \mu\text{m}$) and sent to the s-SNOM (blue beam). The FTIR interferometer is located to the right of the base unit. A broad band MCT detector detects the scattered light.

B.2.1. Broad Band MIR Light Source

The broad band light, which is necessary for FTIR spectroscopy, is generated by means of DFG. Therefore, two laser beams are required. The setup is shown in Appendix B. The laser system in use is the *FFPro* system from the company *Toptica Photonics*. The system is based on an Er-doped fiber oscillator, which generates laser pulses with

a central wavelength of 1560 nm at a repetition rate of 80 MHz. The pulses are amplified and sent through a nonlinear fiber, which compresses the pulses. Due to the compression, a super-continuum is generated, resulting in more broad band pulses with a wavelength ranging from 1.6 μm to 3 μm . The pulse length is ≈ 100 fs. The super-continuum beam is sent via a delay line to a beamsplitter, to combine it with the second laser beam necessary for DFG. The second beam is generated by splitting part of the light from the oscillator and sending it through an optical fiber to an external amplifier (IR-AMP). The amplified, narrow-band beam (purple) is matched in diameter with the super-continuum beam (orange) with a Galilei telescope. Both beams are combined using a dichroic beamsplitter and the pulses are overlapped in time using the delay line.

To generate light with the difference frequency of the two beams, two requirements need to be fulfilled. The first requirement is energy conservation, meaning the energy of the resulting light is in the range of the differences in photon energies between the super-continuum and the narrow band beam. The second requirement for a conversion is the conservation of the momentum of the photons. As two initial photons carry non-zero momentum the resulting photon must carry the same. The linear photon dispersion in vacuum forbids a conversion process. However, in matter, the dispersion is modified due to the interaction. This is described by the index of refraction of the material and manifests in Snell's law of refraction. In general, the index of refraction of a material depends on the wavelength. In birefringent materials, it additionally depends on the polarization of the light. This can be used to compensate for the momentum mismatch between photons of different energy, a process called *phase matching*.

To do this, the combined beam (red) is focused into a birefringent GaSe crystal. The index of refraction of this material happens to be such that, given a correct incidence angle and orthogonal polarization of the beams, the difference in momentum between the photons involved is exactly compensated. The angle of incident for phase matching is $\approx 35^\circ$ to the surface normal of the crystal. Tilting the crystal to slightly different angles enables phase matching for a different range of photon energies. Subsequently to the crystal a parabolic mirror collimates the light and a long pass filter (cut-on wavelength 3.6 μm) blocks the remaining pump light. The DFG light passes the filter and is coupled into the s-SNOM.

Confocal NV Center magnetometry

C.1. Comparison of Modulation Techniques

To enable a detection using lock-in techniques, the signal needs to be indirectly modulated. There are different ways to achieve this, e.g. by modulating the excitation amplitude or the bias field. Both methods are compared in Figure C.1. Modulating the RF amplitude, i.e. periodically switching the excitation on and off (RF-AM), yields the change of the signal due to the presence of the RF excitation. This method is preferred for signals with a weak dependence on the bias field, for example the faintly visible ESR signal stemming from the transition within the excited triplet state of the NV center. The signal is visible as a broad background at a frequency of ≈ 1.4 GHz at zero field and splits with increasing field.

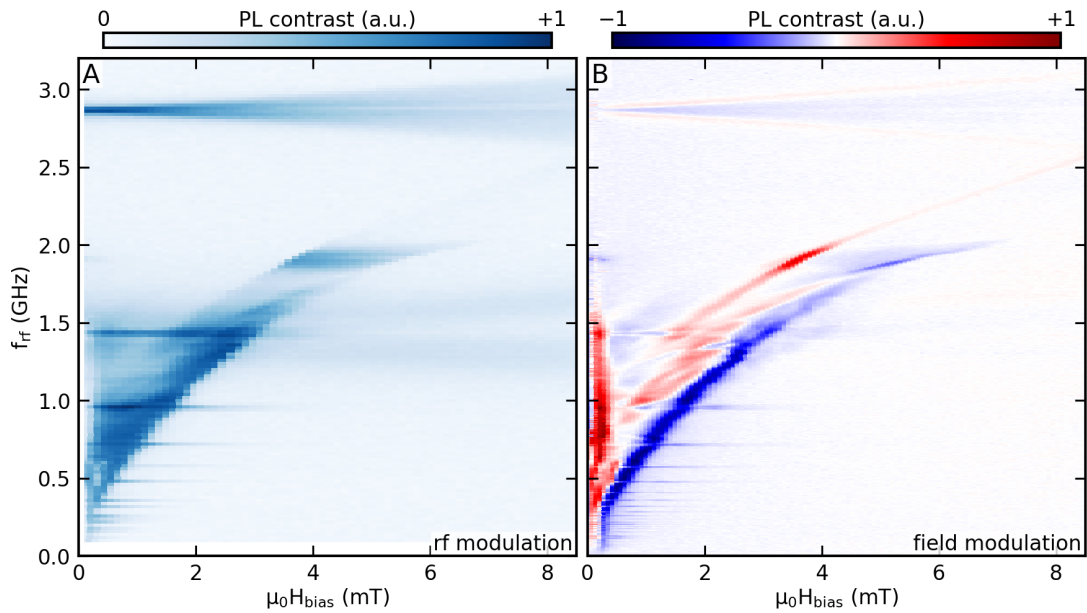


Figure C.1. | Comparison of modulation techniques used in NV magnetometry measurements. **A:** Modulation of the excitation amplitude. **B:** Modulation of the bias field. Figure adapted from [30].

For signals with a strong field dependence, modulating the the field is preferred, as it achieves a better SNR. The measurements obtained with this method represent the derivative of the PL signal with respect to the field direction. The method, hence, is not suitable for detecting features which only weakly depend on the external field. Additionally, the modulation depth must be chosen carefully to avoid artificial broadening of the signals due to the modulated field and to achieve an optimal SNR.

C.2. Comparison of NV Measurements on the Signal Line and in the Gap of the CPW

To make sure that the PL signals measured are not artefacts caused by the measurement apparatus, but truly originate from the ferromagnetic layer, a control measurement is conducted with same parameters on the signal line and in the gap of the CPW. Evidently, both the signal at 1.9 GHz as well as the frequency comb signals are only present when the NiFe layer is in direct vicinity of the NV centers. The small difference in background intensity is most likely due to the different reflectivity of the underlying material, the GaAs substrate in the gap of the CPW and a 20 nm-thick NiFe layer on top of the 100 nm-thick Au on the signal line. In the latter case, the reflectivity is higher than bare GaAs, leading to a higher detected intensity of the fluorescence light, which is emitted isotropically in all directions and partially reflected by the underlying material.

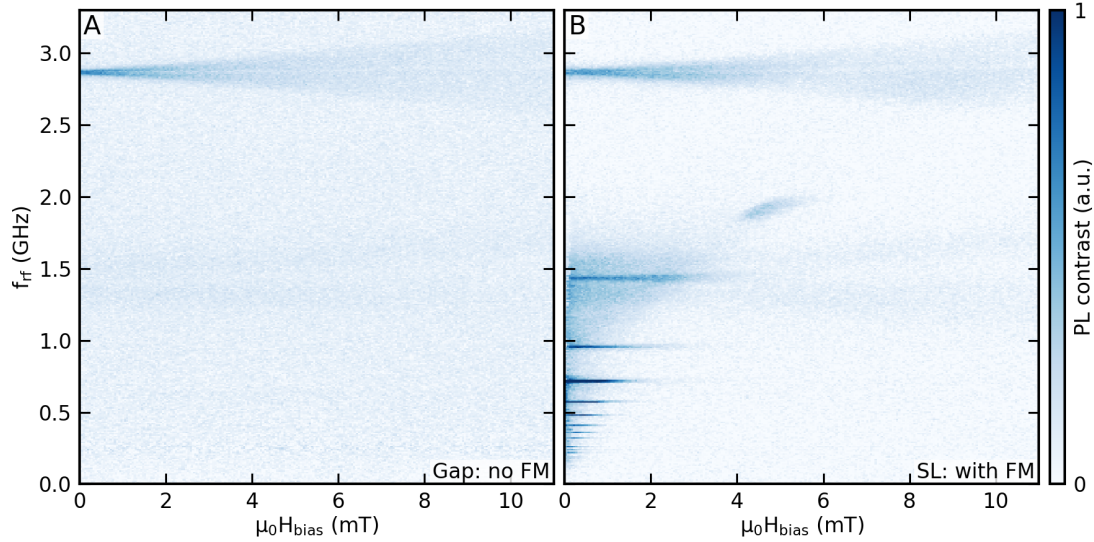


Figure C.2. | **A:** NV magnetometry measurement in the gap of the CPW. No FM material is present in the vicinity of the NV centers. **B:** Measurement with the same parameters on the signal line of the CPW, where an underlying NiFe layer is present. Both measurements were taken with RF-AM. Figure adapted from [30].

C.3. Nonlinear Spin Waves at Half Integer Multiples of the Driving Frequency

In the NV magnetometry measurements, a striking feature is visible at an excitation frequency of 1.9 GHz (see Figure C.3 A). This frequency corresponds to $3/2$ of the ESR frequency of the NV. The feature can be attributed to nonlinear spin waves which precess at half integer multiples of the excitation frequency. The existence of these spin waves was theoretically described by Bauer *et al.* [75] and later comprehensively experimentally investigated by Dreyer *et al.* using SNS-MOKE [77]. According to Bauer *et al.*, the spin waves arise when the magnetization follows a strongly elliptical trajectory upon excitation with large excursion angles. This happens in magnetic thin films at low magnetic bias fields. The consequence of the large excursion angles is, that the magnetic energy potential landscape cannot be considered constant throughout the precession cycle. Instead, the potential is modulated, leading to a modulation of the magnetic resonance frequency. The analytical model of Bauer *et al.* shows, that under these conditions these nonlinear spin waves exhibit strongly increased lifetimes when excited above a certain threshold power. This expected behavior can also be observed in the confocal NV magnetometry measurements, as can be seen in Figure C.3 C, blue curve.

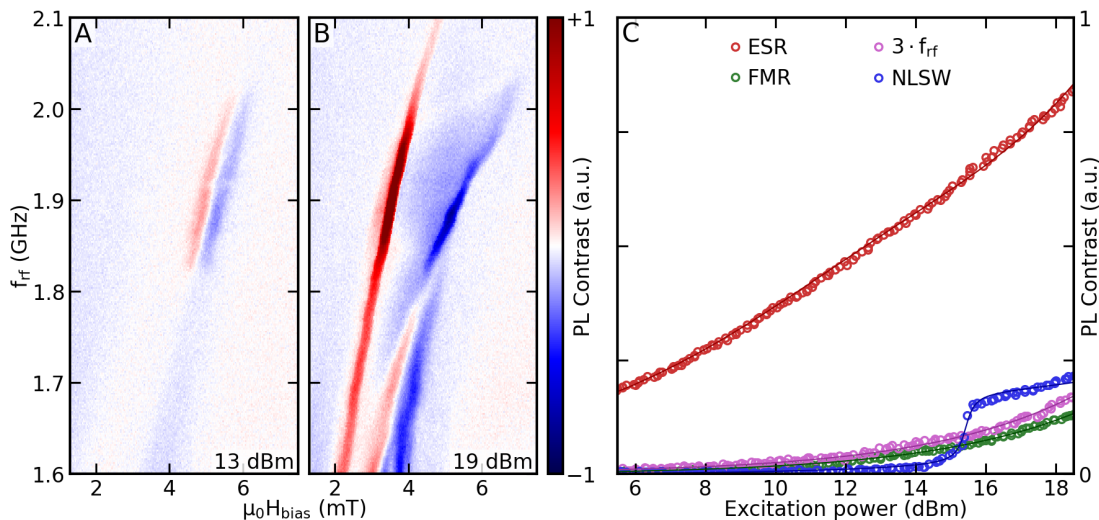


Figure C.3. | **A, B:** NV magnetometry measurement of nonlinear spin waves oscillating at $3/2$ of the excitation frequency in a NiFe film. The measurements were taken at the threshold power, where the feature just becomes visible, and well above. The frequency conversion makes it possible to detect these spin waves, as the precession frequency matches the ESR of the NV centers. **C:** Measurements of the power dependence of the different mechanisms that generate the PL contrast: excitation at the ESR frequency (red), excitation at the FMR frequency of the NiFe film (green), excitation at $1/3$ of the ESR frequency (pink), which is converted due to the frequency comb generation into into the detectable ESR frequency, as well as excitation of nonlinear spin waves precessing at $3/2$ of the ESR frequency (blue). Figure adapted from [30].

C.4. Standing Spin Wave Modes at the Edge of the CPW

It has been elaborated in Chapter 6, that NV center magnetometry has an advantage over other diffraction limited methods in the fact, that it uses an ensemble of nanoscale sensors, which enable it to detect stray fields localized on the nanoscale. However, the actual spatial resolution is limited by the distribution of the nano diamonds on the sample, which can be quite inhomogeneous and is, thus, usually rather poor. However, the spatial resolution is good enough to resolve inhomogeneous magnetization features on the micrometer scale, as is shown in Figure C.4. The NiFe layer on top of the signal line of the waveguide is excited by the RF fields at a frequency of 2.87 GHz in the same geometry as in Chapter 6. The symmetry of the magnetic film is broken at the edge of the waveguide, which enables to observe a standing wave pattern along the edge. These spin waves are identified with a MSSW mode, as their wave vector points perpendicular to the bias field applied along the waveguide in x -direction. As the bias field is increased from 1.6 mT to 6 mT, the wavelength of the observed spin wave pattern also increases from 10 μm to 20 μm . This is caused by the increased magnetic stiffness of the ferromagnetic film, which moves the dispersion towards higher frequencies and reduces the wave vector at a given frequency.

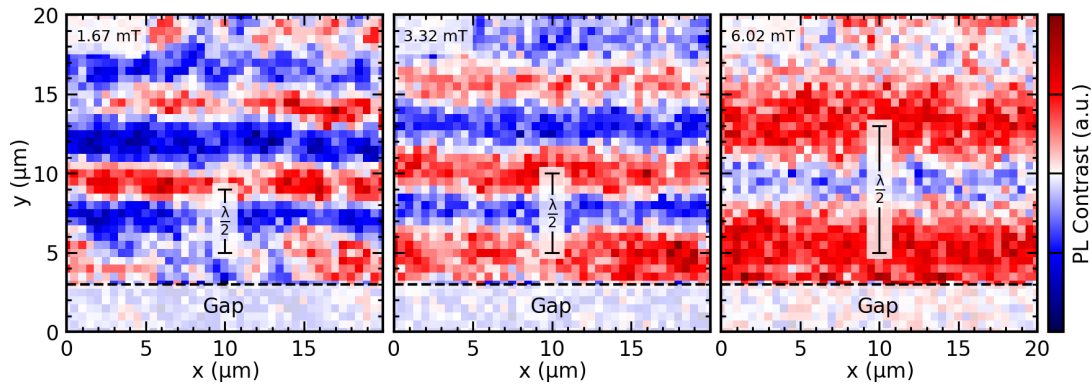


Figure C.4. | Spatially resolved confocal NV center magnetometry measurements of MSSW modes excited in a NiFe thin film on the CPW of the sample investigated in Chapter 6. The measurement area is located on the edge of the signal line of the CPW, which is used for RF excitation at a frequency of 2.87 GHz. Static bias fields were applied along the CPW in x -direction.

A standing wave pattern consists of anti-knots, where the magnetization precesses, and knots, where it effectively stands still. Due to the precession, the anti-knots generate additional stray fields above the sample surface to which the NV centers are exposed. The NV centers sense magnetic stray fields because they shift the ESR frequency, giving rise to a modulation of PL contrast. Hence, a high PL intensity in the figure marks the location of anti-knots, which are spaced by only half the actual wavelength of the spin wave, as the technique is not sensitive to the phase of the precession.

C.5. Measurement on YIG

A confocal NV center magnetometry measurement was conducted on a 200 nm-thick YIG thin film on gadolinium gallium garnet (GGG) substrate. Similar to the previously discussed measurements on NiFe samples, the RF excitation was done via a CPW structured on the sample.

As the most prominent feature, a strong response of the uniform mode can be observed, accompanied by additional spin wave modes at lower bias fields. These correspond to MSSW spin waves. Furthermore, the ESR of the NV centers is visible at 2.87 GHz, splitting with increasing field. At small excitation frequencies, a faint replica of the uniform mode is visible. This likely is an artifact caused by the RF source, which also outputs a signal component at the 2nd harmonic of the set frequency, albeit at a power level reduced by 30 dB. In addition, a range of parametric spin wave modes is observed, precessing at the 2nd harmonic and at 3/2 of the excitation frequency (visible at 1.4 GHz and 1.9 GHz, respectively). The signal in the frequency range from 3 GHz to 3.5 GHz at fields of up to 10 mT can be attributed to the 2nd PSSW mode.

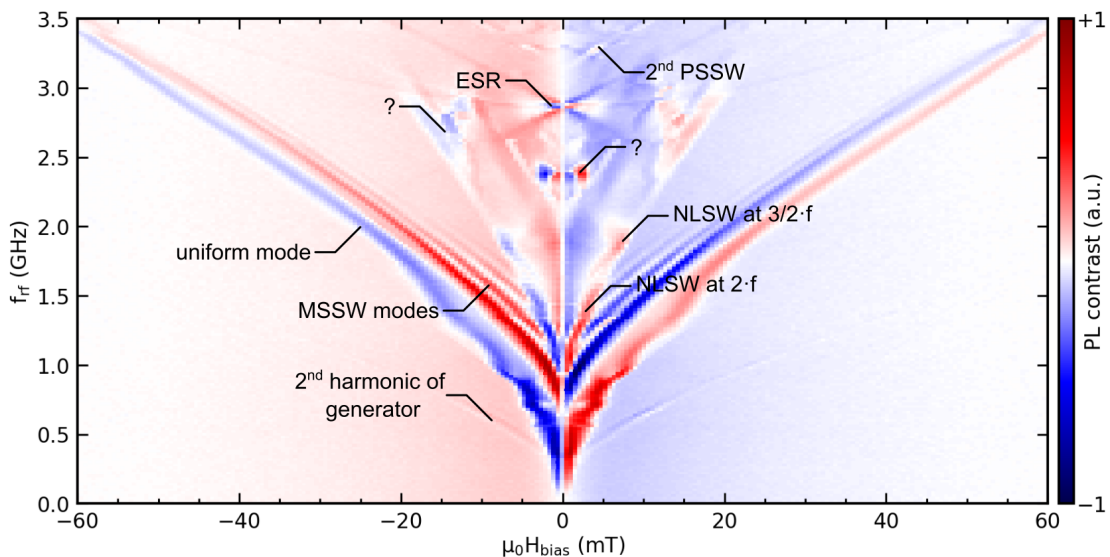


Figure C.5. | NV magnetometry measurement on a 200 nm-thick YIG thin film. The nominal excitation power was ≈ 15 dBm. Figure adapted from [30].

There are still certain features with unknown origin, mainly the intense signal at a frequency of 2.4 GHz close to zero bias field and the enhancement of the signal between 2.5 GHz to 3 GHz at 10 mT to 15 mT. In contrast to the NiFe films investigated before, the magnetization inside the YIG film is more homogeneous. As a consequence, the frequency multiplication process at MHz excitation frequencies cannot be observed. There are no switching processes of the magnetization in different regions of the sample, which is the requirement for the process to occur.

C.6. NV-Center Ground State Hamiltonian

The electronic states of the negatively charged NV^- center can be calculated using the ground state Hamiltonian presented in Equation 2.75. In matrix form, this Hamiltonian reads as

$$\hat{H} = \begin{bmatrix} \gamma B_z + D & \gamma \left(\frac{\sqrt{2}B_x}{2} - \frac{\sqrt{2}iB_y}{2} \right) & E \\ \gamma \left(\frac{\sqrt{2}B_x}{2} + \frac{\sqrt{2}iB_y}{2} \right) & 0 & \gamma \left(\frac{\sqrt{2}B_x}{2} - \frac{\sqrt{2}iB_y}{2} \right) \\ E & \gamma \left(\frac{\sqrt{2}B_x}{2} + \frac{\sqrt{2}iB_y}{2} \right) & -\gamma B_z + D \end{bmatrix}. \quad (\text{C.1})$$

It can be obtained by inserting the spin operators for an $S = 1$ system.

$$\hat{S}_x = \frac{1}{\sqrt{2}} \begin{bmatrix} 0 & 1 & 0 \\ 1 & 0 & 1 \\ 0 & 1 & 0 \end{bmatrix}, \hat{S}_y = \frac{1}{\sqrt{2}i} \begin{bmatrix} 0 & 1 & 0 \\ -1 & 0 & 1 \\ 0 & -1 & 0 \end{bmatrix}, \hat{S}_z = \begin{bmatrix} 1 & 0 & 0 \\ 0 & 0 & 0 \\ 0 & 0 & -1 \end{bmatrix} \quad (\text{C.2})$$

$$\hat{\mathbf{S}} = \begin{pmatrix} \hat{S}_x \\ \hat{S}_y \\ \hat{S}_z \end{pmatrix} \quad (\text{C.3})$$

SNS-MOKE: Phase Maps at Different Excitation Frequencies

This section shows the full set of phase maps measured by SNS-MOKE. The maps display the spatial variation of the phase of the spin waves which are generated at high harmonics of the excitation frequency, as described in Chapter 6. The measurement was repeated on the same sample at different excitation frequencies from 79.1 MHz to 399 MHz.

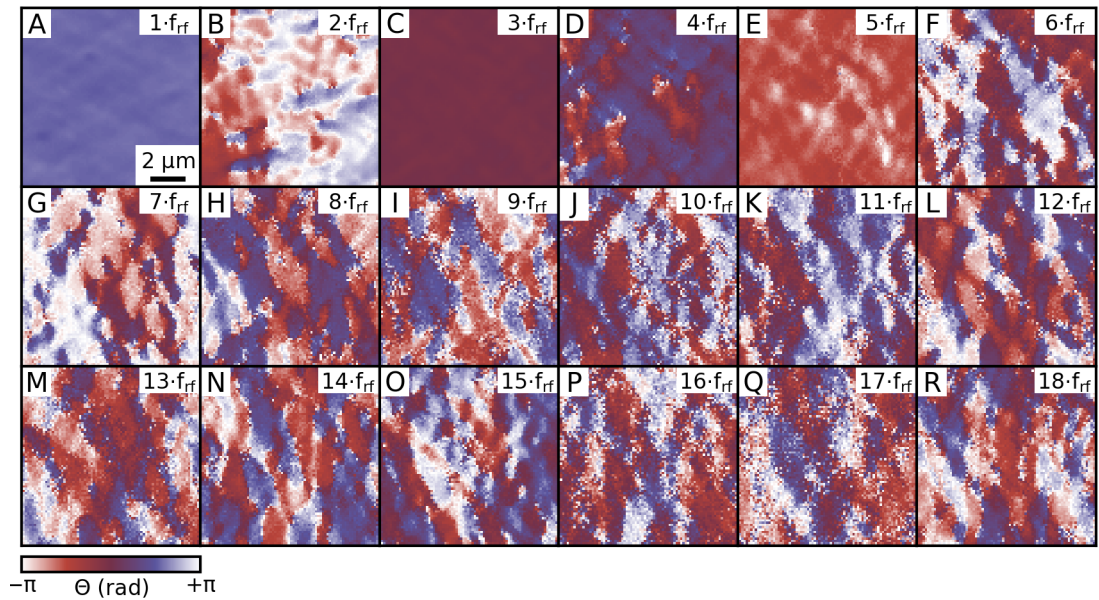


Figure D.1. | Phase of the spin waves at different harmonics measured by SNS-MOKE from the 1st to the 18th harmonic of the excitation frequency $f_{rf} = 79.1$ MHz.

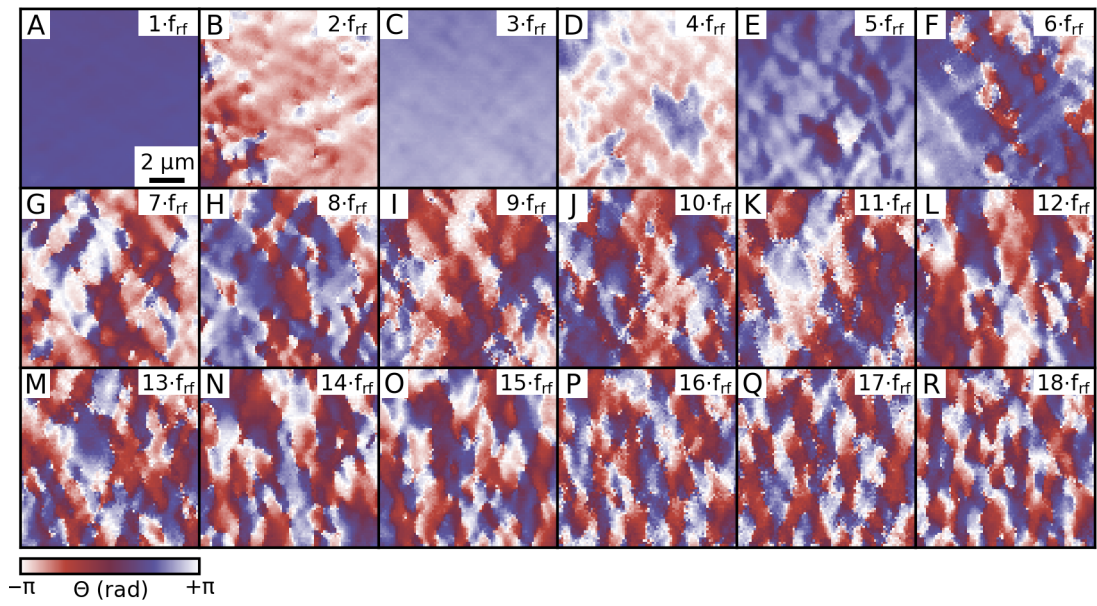


Figure D.2. | Phase of the spin waves at different harmonics measured by SNS-MOKE from the 1st to the 18th harmonic of the excitation frequency $f_{rf} = 159$ MHz.

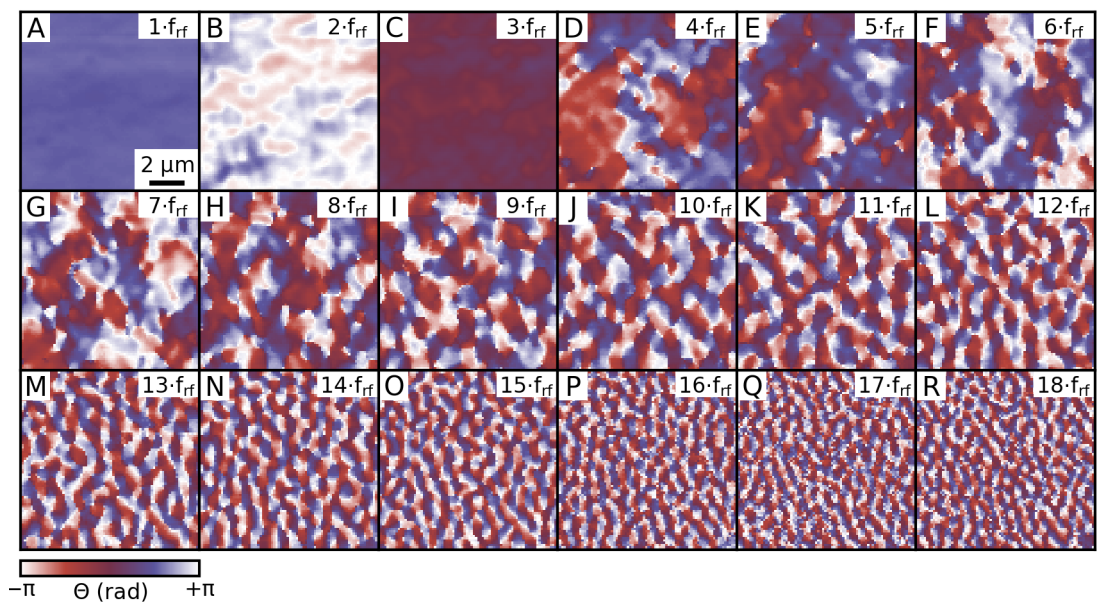


Figure D.3. | Phase of the spin waves at different harmonics measured by SNS-MOKE from the 1st to the 18th harmonic of the excitation frequency $f_{rf} = 319$ MHz.

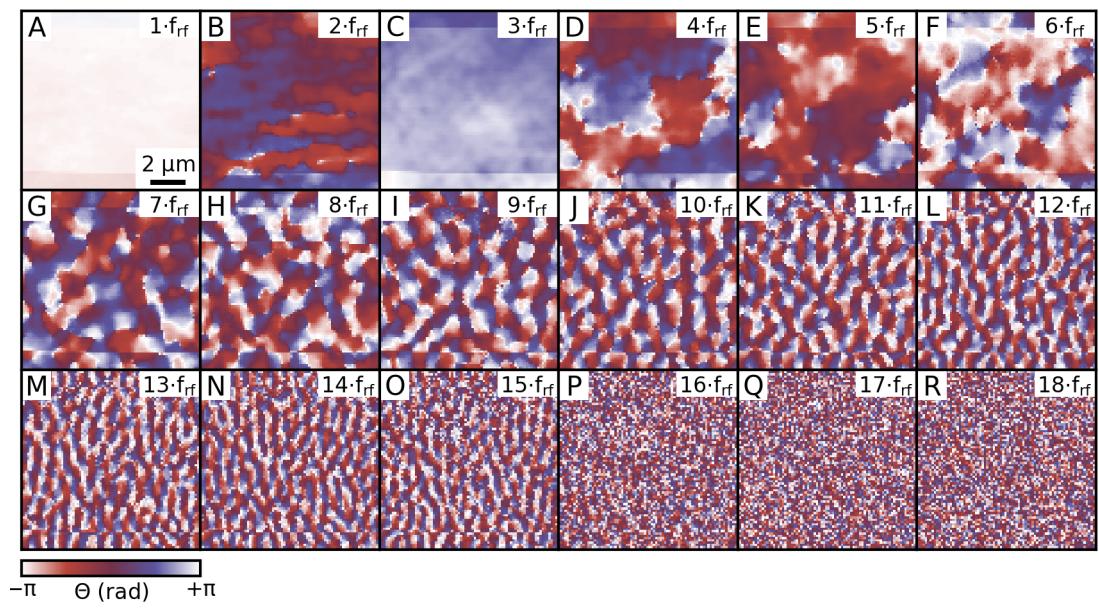


Figure D.4. | Phase of the spin waves at different harmonics measured by SNS-MOKE from the 1st to the 18th harmonic of the excitation frequency $f_{rf} = 399$ MHz.

SNS-MOKE: High Harmonic Spin Waves in Microstructures

The following figures show SNS-MOKE measurements of the high harmonic spin waves conducted on elliptical and rectangular microstructures. The microstructures are arranged on the signal line of a CPW, as depicted in Figure 6.19. Their sizes are $30\ \mu\text{m} \times 15\ \mu\text{m}$, $20\ \mu\text{m} \times 10\ \mu\text{m}$, $10\ \mu\text{m} \times 5\ \mu\text{m}$, as well as $5\ \mu\text{m} \times 2.5\ \mu\text{m}$. The thickness of the NiFe layer is 20 nm. For all measurements, a small bias field was applied along the CPW, which also means along the long axis of the devices. The bias field was chosen to maximize the signal obtained at the harmonics and hence differs between the devices.

The measurements show, as in the extended film, that coherent high harmonics are generated also in microstructures. The trend of larger wave vectors for higher harmonics holds, as well. The magnitude of the higher harmonics decreases in smaller structures. Especially in the smallest devices even the 1st harmonic shows a certain degree of inhomogeneity. This is attributed to an inhomogeneous magnetization pattern in the structures.

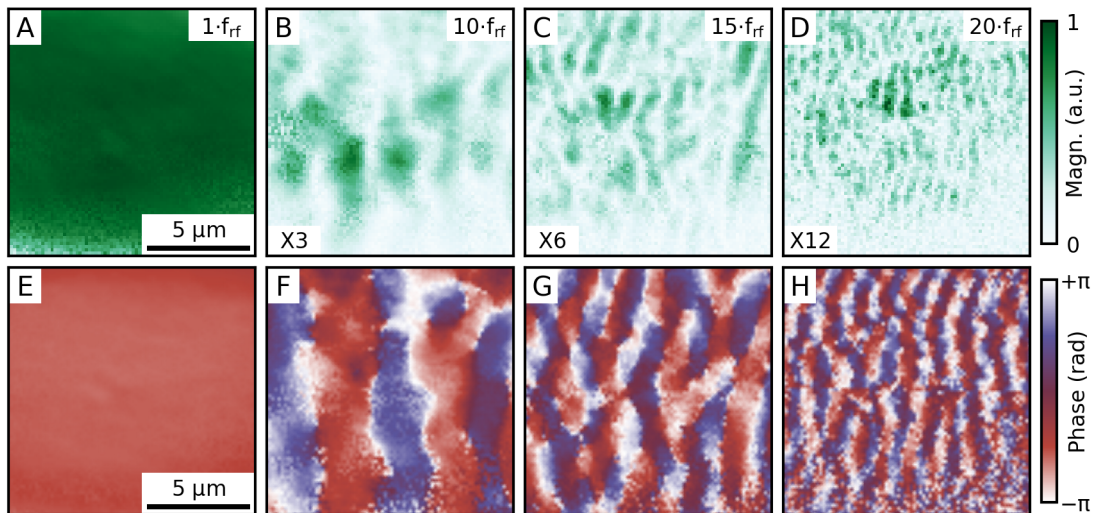


Figure E.1. | SNS-MOKE measurement of spin waves in the center of a $30\ \mu\text{m} \times 15\ \mu\text{m}$ -sized elliptical microstructure, excited at 241.1 MHz. A static bias field of 0.53 mT was applied along the CPW. **A-D:** Spin wave magnitude at the 1st, 10th, 15th and 20th harmonic of the excitation frequency. The signals were amplified by the factor denoted in the lower left corner of the sub-figures to improve visibility. **E-H:** phase of the spin waves with respect to the excitation frequency.

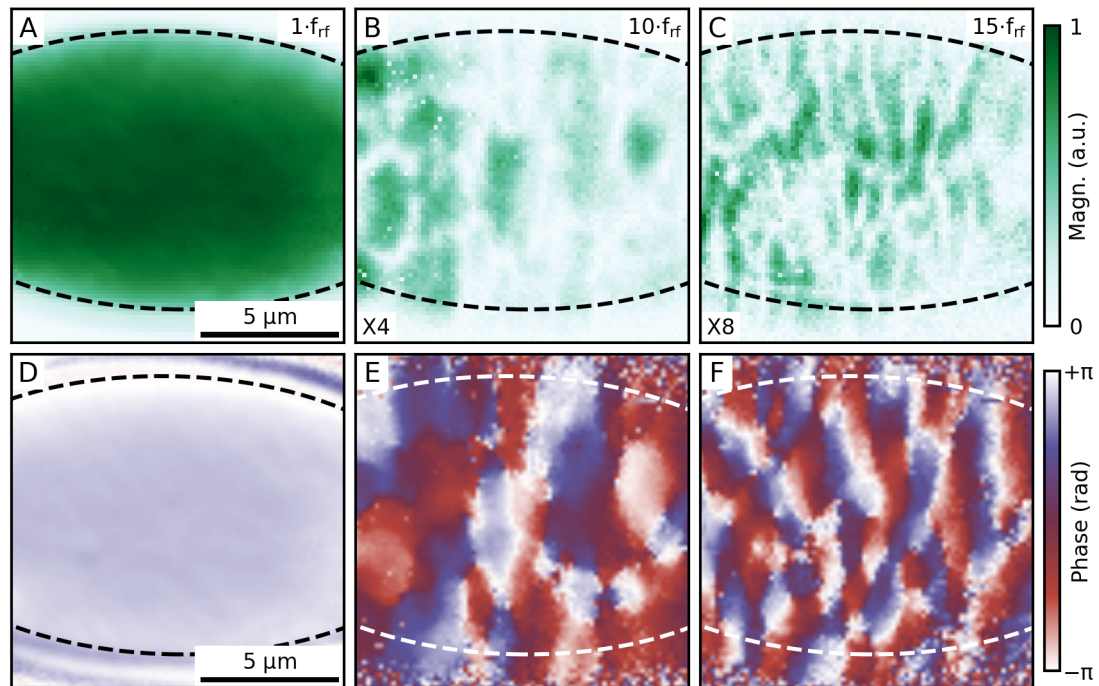


Figure E.2. | SNS-MOKE measurement of spin waves in $20\ \mu\text{m} \times 10\ \mu\text{m}$ -sized elliptical microstructure, excited at 241.1 MHz. A static bias field of 0.8 mT was applied along the CPW. **A-C:** Spin wave magnitude at the 1st, 10th and 15th harmonic of the excitation frequency. The signals were amplified by the factor denoted in the lower left corner of the sub-figures to improve visibility. **D-F:** phase of the spin waves.

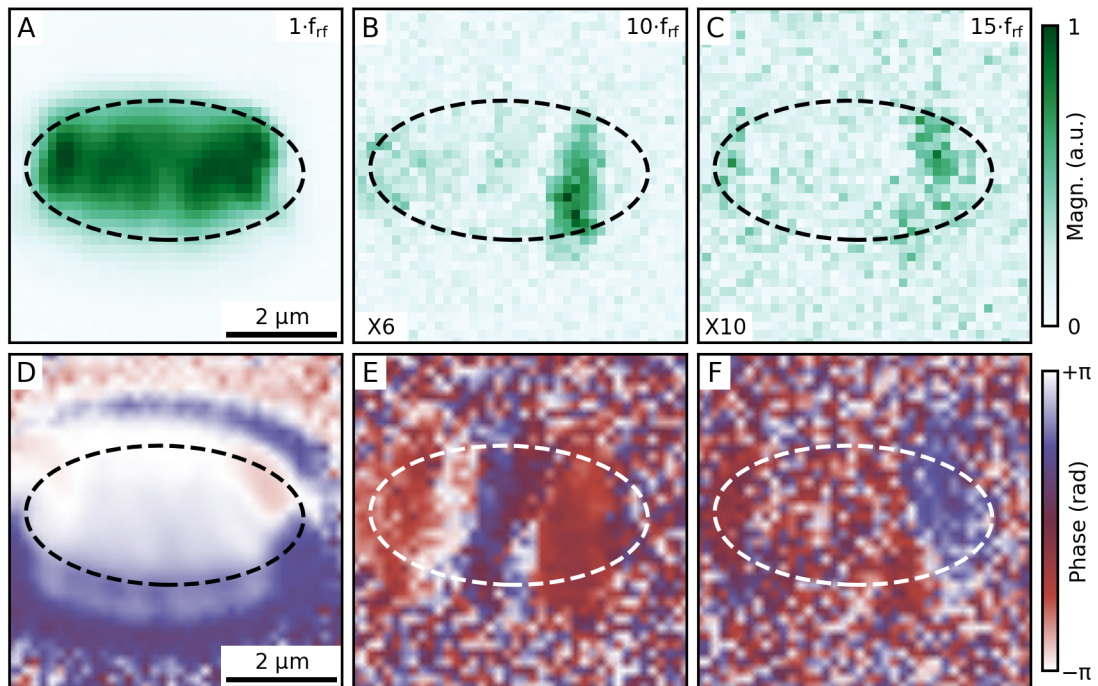


Figure E.3. | SNS-MOKE measurement of spin waves in $5 \mu\text{m} \times 2.5 \mu\text{m}$ -sized elliptical microstructure, excited at 241.1 MHz . A static bias field of 1.88 mT was applied along the CPW. **A-C:** Spin wave magnitude at the 1^{st} , 10^{th} and 15^{th} harmonic of the excitation frequency. The signals were amplified by the factor denoted in the lower left corner of the sub-figures to improve visibility. **D-F:** phase of the spin waves.

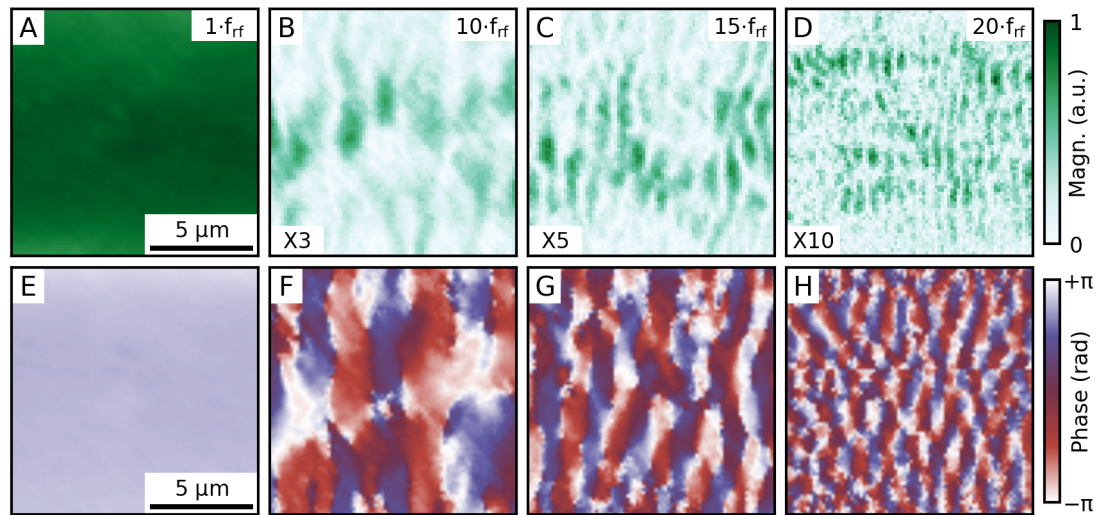


Figure E.4. | SNS-MOKE measurement of spin waves in the center of a $30 \mu\text{m} \times 15 \mu\text{m}$ -sized rectangular microstructure, excited at 241.1 MHz . A static bias field of 0.93 mT was applied along the CPW. **A-D:** Spin wave magnitude at the 1^{st} , 10^{th} , 15^{th} and 20^{th} harmonic of the excitation frequency. The signals were amplified by the factor denoted in the lower left corner of the sub-figures to improve visibility. **E-H:** phase of the spin waves.

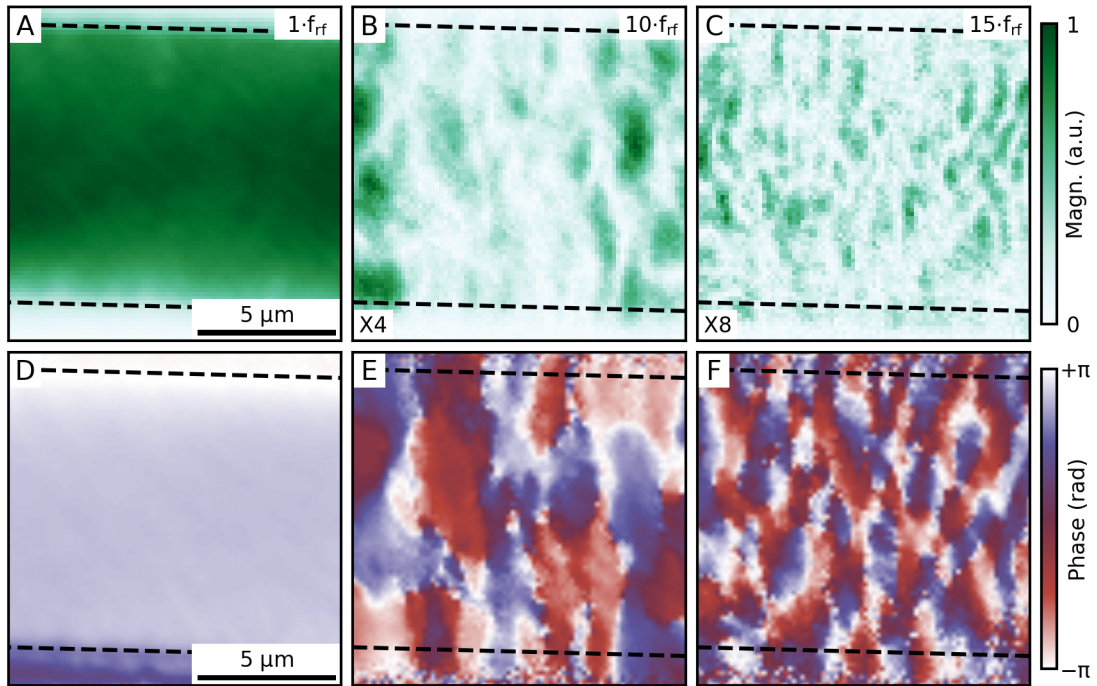


Figure E.5. | SNS-MOKE measurement of spin waves in $20\ \mu\text{m} \times 10\ \mu\text{m}$ -sized rectangular microstructure, excited at 241.1 MHz. A static bias field of 1.07 mT was applied along the CPW. **A-C:** Spin wave magnitude at the 1st, 10th and 15th harmonic of the excitation frequency. The signals were amplified by the factor denoted in the lower left corner of the sub-figures to improve visibility. **D-F:** phase of the spin waves.

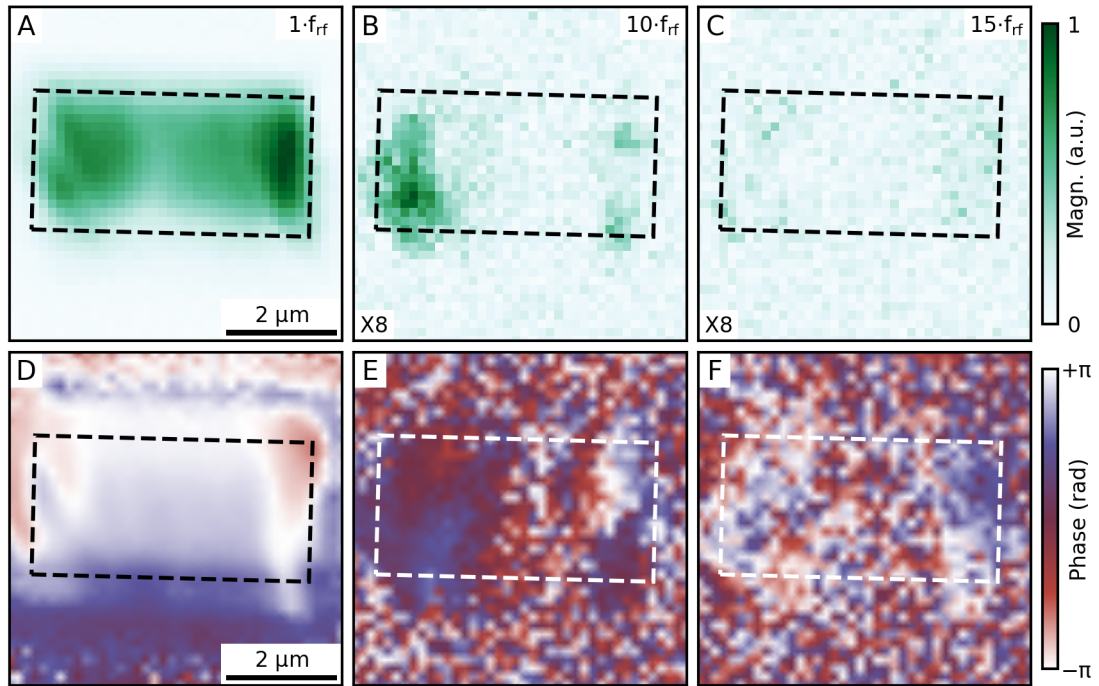


Figure E.6. | SNS-MOKE measurement of spin waves in $5\ \mu\text{m} \times 2.5\ \mu\text{m}$ -sized rectangular microstructure, excited at 241.1 MHz. A static bias field of 1.97 mT was applied along the CPW. **A-C:** Spin wave magnitude at the 1st, 10th and 15th harmonic of the excitation frequency. The signals were amplified by the factor denoted in the lower left corner of the sub-figures to improve visibility. **D-F:** phase of the spin waves.

Comparison of SNS-MOKE with Inductive FMR

In this section, the two methods, SNS-MOKE and inductive FMR are compared. To illustrate the difference in the information that can be obtained with both methods, a micro-structured ferromagnetic sample is chosen. The sample consists of micrometer-sized $\text{Ni}_{80}\text{Fe}_{20}$ elements on top of a CPW, matching the layout of the sample in Figure 6.19, but with a slightly different material stack. It consists of a GaAs(001) substrate, a CPW made from a 3 nm Cr adhesion layer, followed by 100 nm of Au, 20 nm-thick NiFe elements, and finally a 3 nm Al_2O_3 capping layer.

As described in Section 3.1.1, inductive FMR measures the absorbed power of the RF signal applied to the sample. The results are shown in Figure F.1. During the measurement, the excitation frequency f_{ex} was fixed while the external magnetic field was scanned. A small additional modulation field was applied to enable lock-in amplification of the signal. The absorbed RF power is proportional to the imaginary part of the magnetic susceptibility. From the LLG equation, this quantity is expected to follow a Lorentzian line shape around the resonance field H_r with a FWHM denoted by ΔH . Due to the additional field modulation, the signal shape, instead, represents the derivative of a Lorentzian resonance line with respect to the field.

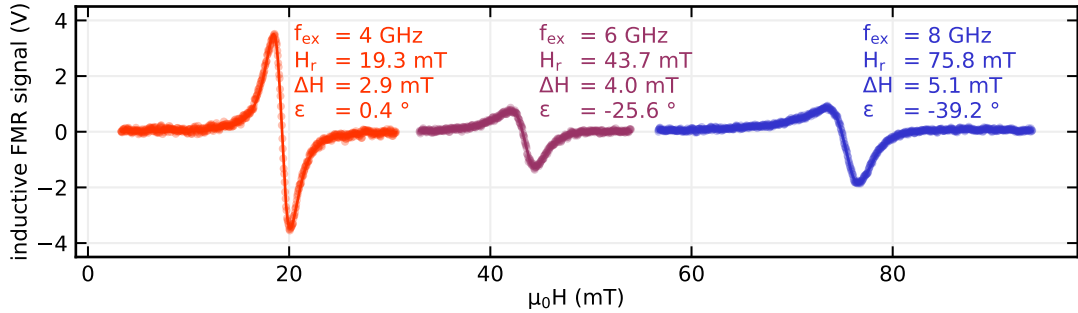


Figure F.1. | Inductive FMR measurement of the sample described above. The solid lines show the fit of the data to Equation 3.2. The results of the fit are displayed next to the curves.

Furthermore, electrical resonances inside the RF components of the setup or the CPW on the sample can add additional phase shifts ϵ of the signal, leading to mixing of the real and imaginary parts of the susceptibility and an asymmetrical line shape. This is accounted for in the fit Equation 3.2. The most important parameters that can be extracted from the fit are the resonance field and the resonance linewidth.

The FMR measurements represent the magnetic response averaged across the whole

sample. It cannot resolve differences that can occur between the micro-fabricated structures. The situation is different for SNS-MOKE. Here the magnetization dynamics is probed locally with diffraction-limited spatial resolution (≈ 250 nm). The method is described in detail in Section 3.2.4. As in the inductive measurements, the excitation frequency is fixed, while the externally applied magnetic field is scanned. SNS-MOKE traces were measured on a comparably large elliptical structure ($30 \mu\text{m} \times 15 \mu\text{m}$) and on the smallest element ($5 \mu\text{m} \times 2.5 \mu\text{m}$). The traces are shown in Figure F.2 A and Figure F.2 B, respectively. The SNS-MOKE magnitude is directly proportional to the imaginary part of the magnetic susceptibility. Hence, the data can be fitted by a Lorentzian. This fit works reasonably well for the large device and the extracted parameters are in agreement with the parameters extracted from the FMR measurement. However, there are small deviations visible at the lower-field side of the main resonance peaks. These indicate the presence of MSSW spin waves. The overlap between these spin waves and the main FMR increases dramatically in the smaller device and makes it hard to even determine the peak that represents the uniform mode. The signal cannot be fitted with a single Lorentzian anymore. The issue can be circumvented by fitting a number of Lorentzian lines. However, this very quickly complicates the data evaluation procedure and makes it prone to misinterpretations.

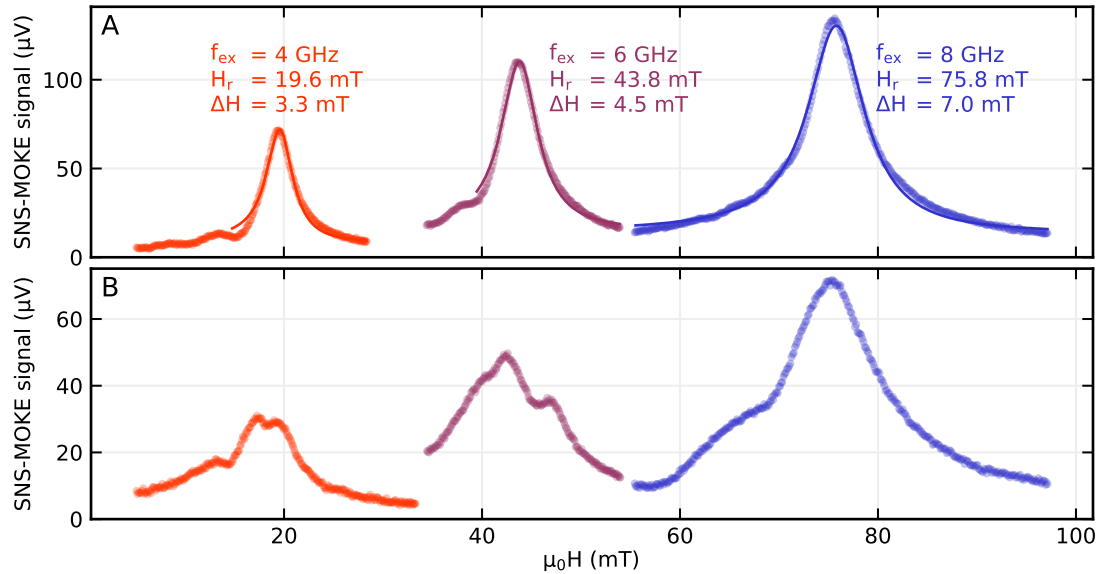


Figure F.2. | SNS-MOKE measurements on two elliptical devices on the same sample as in Figure F.1. **A:** Element of size $30 \mu\text{m} \times 15 \mu\text{m}$. The solid lines show the fit of the data to a Lorentzian. The results of the fit are displayed next to the curves. **B:** Element of size $5 \mu\text{m} \times 2.5 \mu\text{m}$. The line shape is more complicated due to additional excited spin wave modes.

These strong differences between the individual magnetic elements are proof, that inductive FMR misses plenty of features present in the sample, as it can only measure the response averaged across the whole sample. Spatially resolved techniques, like SNS-MOKE, can go much further to resolve and investigate such features.

Sample Fabrication Recipes

G.1. Electron Beam Lithography

E-Beam Resist

type	positive
material	PMMA
concentration	9 %
molecular weight	200k
manufacturer	Allresist
product id	AR-P 641

Spin-Coating

velocity	6000 rpm
duration	45 s

Baking

temperature	200 °C
duration	120 s

E-Beam Exposure

working distance	10 mm
aperture	60 μm
area dose	190 pAcm^{-2}

Development

developer	MIBK:IPA (1:1)
duration	12 s
stopper	IPA

Lift-Off

solvent	acetone
temperature	50 °C
duration	>30 min
ultrasonic bath	if required

G.2. Atomic Layer Deposition of Al_2O_3

precursor gas	TMA
cracking gas	H_2O
chemical reaction	$\text{Al}_2(\text{CH}_3)_6 + 3\text{H}_2\text{O} \rightarrow \text{Al}_2\text{O}_3 + 6\text{CH}_4$
chamber temperature	80 °C
deposition rate	$\approx 1.25 \text{ \AA/cycle}$

Micromagnetic Simulations

H.1. Material Parameters

Saturation magnetization	$M_S = 866 \text{ kA/m}$
Damping parameter	$\alpha = 0.008$
Exchange energy	$13 \times 10^{-12} \text{ J/m}$
Uniaxial anisotropy	$K_U = 500 \text{ J/m}^3$ in x -direction

Bibliography

- [1] E. Deelman et al. “High-performance computing at a crossroads”. In: *Science* 387.6736 (2025), pp. 829–831. DOI: 10.1126/science.adu0801.
- [2] F. Peper. “The End of Moore’s Law: Opportunities for Natural Computing?” In: *New Generation Computing* 35.3 (2017), pp. 253–269. DOI: 10.1007/s00354-017-0020-4.
- [3] J. Von Neumann. “First draft of a report on the EDVAC”. In: *IEEE Annals of the History of Computing* 15.4 (1993), pp. 27–75. DOI: 10.1109/85.238389.
- [4] A. V. Chumak et al. “Magnon spintronics”. In: *Nature Physics* 11.6 (2015), pp. 453–461. DOI: 10.1038/nphys3347.
- [5] B. Flebus et al. “The 2024 magnonics roadmap”. In: *Journal of Physics: Condensed Matter* 36.36 (2024), p. 363501. DOI: 10.1088/1361-648x/ad399c.
- [6] K. Baumgaertl and D. Grundler. “Bistable nanomagnet as programmable phase inverter for spin waves”. In: *Applied Physics Letters* 118.16 (2021). DOI: 10.1063/5.0048825.
- [7] T. Brächer, P. Pirro, and B. Hillebrands. “Parallel pumping for magnon spintronics: Amplification and manipulation of magnon spin currents on the micron-scale”. In: *Physics Reports* 699 (2017), pp. 1–34. DOI: 10.1016/j.physrep.2017.07.003.
- [8] H. Merbouche et al. “True amplification of spin waves in magnonic nanowaveguides”. In: *Nature Communications* 15.1 (2024). DOI: 10.1038/s41467-024-45783-1.
- [9] S.-K. Kim, K.-S. Lee, and D.-S. Han. “A gigahertz-range spin-wave filter composed of width-modulated nanostrip magnonic-crystal waveguides”. In: *Applied Physics Letters* 95.8 (2009). DOI: 10.1063/1.3186782.
- [10] H. Merbouche et al. “Frequency Filtering with a Magnonic Crystal Based on Nanometer-Thick Yttrium Iron Garnet Films”. In: *ACS Applied Nano Materials* 4.1 (2021), pp. 121–128. DOI: 10.1021/acsanm.0c02382.
- [11] M. Grassi et al. “Slow-Wave-Based Nanomagnonic Diode”. In: *Physical Review Applied* 14.2 (2020). DOI: 10.1103/physrevapplied.14.024047.
- [12] Q. Wang et al. “Reconfigurable nanoscale spin-wave directional coupler”. In: *Science Advances* 4.1 (2018). DOI: 10.1126/sciadv.1701517.

-
- [13] Q. Wang et al. “A magnonic directional coupler for integrated magnonic half-adders”. In: *Nature Electronics* 3.12 (2020), pp. 765–774. DOI: 10.1038/s41928-020-00485-6.
- [14] F. Heussner et al. “Experimental Realization of a Passive Gigahertz Frequency-Division Demultiplexer for Magnonic Logic Networks”. In: *physica status solidi (RRL) – Rapid Research Letters* 14.4 (2020). DOI: 10.1002/pssr.201900695.
- [15] A. V. Chumak, A. A. Serga, and B. Hillebrands. “Magnon transistor for all-magnon data processing”. In: *Nature Communications* 5.1 (2014). DOI: 10.1038/ncomms5700.
- [16] K.-S. Lee and S.-K. Kim. “Conceptual design of spin wave logic gates based on a Mach–Zehnder-type spin wave interferometer for universal logic functions”. In: *Journal of Applied Physics* 104.5 (2008). DOI: 10.1063/1.2975235.
- [17] T. Brächer and P. Pirro. “An analog magnon adder for all-magnonic neurons”. In: *Journal of Applied Physics* 124.15 (2018). DOI: 10.1063/1.5042417.
- [18] N. Zenbaa et al. “Realization of inverse-design magnonic logic gates”. In: *Science Advances* 11.21 (2025). DOI: 10.1126/sciadv.adu9032.
- [19] Z. Xiao et al. “Adapting magnetoresistive memory devices for accurate and on-chip-training-free in-memory computing”. In: *Science Advances* 10.38 (2024). DOI: 10.1126/sciadv.adp3710.
- [20] J. Grollier et al. “Neuromorphic spintronics”. In: *Nature Electronics* 3.7 (2020), pp. 360–370. DOI: 10.1038/s41928-019-0360-9.
- [21] Á. Papp, W. Porod, and G. Csaba. “Nanoscale neural network using non-linear spin-wave interference”. In: *Nature Communications* 12.1 (2021). DOI: 10.1038/s41467-021-26711-z.
- [22] L. Körber et al. “Pattern recognition in reciprocal space with a magnon-scattering reservoir”. In: *Nature Communications* 14.1 (2023). DOI: 10.1038/s41467-023-39452-y.
- [23] H. Suhl. “Subsidiary Absorption Peaks in Ferromagnetic Resonance at High Signal Levels”. In: *Physical Review* 101.4 (1956), pp. 1437–1438. DOI: 10.1103/PhysRev.101.1437.
- [24] R. M. White and M. Sparks. “Ferromagnetic Relaxation. III. Theory of Instabilities”. In: *Physical Review* 130.2 (1963), pp. 632–638. DOI: 10.1103/physrev.130.632.
- [25] H. Schultheiss, K. Vogt, and B. Hillebrands. “Direct observation of nonlinear four-magnon scattering in spin-wave microconduits”. In: *Physical Review B* 86.5 (2012). DOI: 10.1103/physrevb.86.054414.

- [26] D. V. Slobodianiuk et al. “Nonlinear Ferromagnetic Resonance in the Presence of Three-Magnon Scattering in Magnetic Nanostructures”. In: *IEEE Magnetics Letters* 10 (2019), pp. 1–5. DOI: 10.1109/lmag.2019.2913132.
- [27] T. Hula et al. “Nonlinear losses in magnon transport due to four-magnon scattering”. In: *Applied Physics Letters* 117.4 (2020). DOI: 10.1063/5.0015269.
- [28] V. E. Demidov et al. “Generation of the second harmonic by spin waves propagating in microscopic stripes”. In: *Physical Review B* 83.5 (2011), p. 054408. DOI: 10.1103/PhysRevB.83.054408.
- [29] S. J. Hermsdoerfer et al. “A spin-wave frequency doubler by domain wall oscillation”. In: *Applied Physics Letters* 94.22 (2009), p. 223510. DOI: 10.1063/1.3143225.
- [30] C. Koerner et al. “Frequency multiplication by collective nanoscale spin-wave dynamics”. In: *Science* 375.6585 (2022), pp. 1165–1169. DOI: 10.1126/science.abm6044.
- [31] T. Sebastian et al. “Micro-focused Brillouin light scattering: imaging spin waves at the nanoscale”. In: *Frontiers in Physics* 3 (2015). DOI: 10.3389/fphy.2015.00035.
- [32] F. Schmidt, W. Rave, and A. Hubert. “Enhancement of magneto-optical domain observation by digital image processing”. In: *IEEE Transactions on Magnetics* 21.5 (1985), pp. 1596–1598. DOI: 10.1109/tmag.1985.1064048.
- [33] I. Soldatov and R. Schäfer. “Selective sensitivity in Kerr microscopy”. In: *Review of Scientific Instruments* 88.7 (2017). DOI: 10.1063/1.4991820.
- [34] J. Lucassen et al. “Optical spin-wave detection beyond the diffraction limit”. In: *Journal of Applied Physics* 133.5 (2023), p. 053902. DOI: 10.1063/5.0131736.
- [35] G. Balasubramanian et al. “Nanoscale imaging magnetometry with diamond spins under ambient conditions”. In: *Nature* 455.7213 (2008), pp. 648–651. DOI: 10.1038/nature07278.
- [36] C. L. Degen. “Scanning magnetic field microscope with a diamond single-spin sensor”. In: *Applied Physics Letters* 92.24 (2008), p. 243111. DOI: 10.1063/1.2943282.
- [37] P. Kusch et al. “Combined Tip-Enhanced Raman Spectroscopy and Scattering-Type Scanning Near-Field Optical Microscopy”. In: *The Journal of Physical Chemistry C* 122.28 (2018), pp. 16274–16280. DOI: 10.1021/acs.jpcc.8b03637.
- [38] P. Grünberg et al. “Brillouin scattering of light by spin waves in thin ferromagnetic films (invited)”. In: *Journal of Applied Physics* 53.3 (1982), pp. 2078–2083. DOI: 10.1063/1.330751.
- [39] N. Bohr, J. R. Nielsen, and L. Rosenfeld. *Early work (1905-1911)*. Amsterdam Oxford: North-Holland, 1986. ISBN: 978-0-7204-1801-9.

- [40] H.-J. Van Leeuwen. “Problèmes de la théorie électronique du magnétisme”. In: *Journal de Physique et le Radium* 2.12 (1921), pp. 361–377. DOI: 10.1051/jphysrad:01921002012036100.
- [41] R. Gross and A. Marx. *Festkörperphysik*. München: Oldenbourg Wissenschaftsverlag Verlag, 2012. ISBN: 978-3-486-71486-9.
- [42] J. H. Van Vleck. *The theory of electric and magnetic susceptibilities*. Oxford, Clarendon Press, 1932.
- [43] W. Heisenberg. “Zur Theorie des Ferromagnetismus”. In: *Zeitschrift für Physik* 49.9 (1928), pp. 619–636. DOI: 10.1007/BF01328601.
- [44] R. Gross and A. Marx. *Festkörperphysik*. 3. Auflage. De Gruyter Studium. Berlin ; Boston: De Gruyter, 2018. 1047 pp. ISBN: 978-3-11-055822-7.
- [45] E. C. Stoner. “Collective electron ferromagnetism”. In: *Proceedings of the Royal Society of London. Series A. Mathematical and Physical Sciences* 165.922 (1938), pp. 372–414. DOI: 10.1098/rspa.1938.0066.
- [46] W. Heisenberg. “Zur Theorie der Magnetostriktion und der Magnetisierungskurve”. In: *Zeitschrift für Physik* 69.5 (1931), pp. 287–297. DOI: 10.1007/BF01391350.
- [47] *Magnetism and magnetic materials*. In collab. with J. M. D. Coey. Cambridge: Cambridge University Press, 2010. ISBN: 978-0-511-84500-0.
- [48] E. C. Stoner and E. P. Wohlfarth. “A mechanism of magnetic hysteresis in heterogeneous alloys”. In: *Philosophical Transactions of the Royal Society of London. Series A, Mathematical and Physical Sciences* 240.826 (1948), pp. 599–642. DOI: 10.1098/rsta.1948.0007.
- [49] A. Hubert and R. Schäfer. “Domain Theory”. In: *Magnetic Domains*. Berlin, Heidelberg: Springer Berlin Heidelberg, 1998, pp. 99–335. ISBN: 978-3-540-64108-7.
- [50] S. S. P. Parkin, M. Hayashi, and L. Thomas. “Magnetic Domain-Wall Racetrack Memory”. In: *Science* 320.5873 (2008), pp. 190–194. DOI: 10.1126/science.1145799.
- [51] T. Holstein and H. Primakoff. “Field Dependence of the Intrinsic Domain Magnetization of a Ferromagnet”. In: *Physical Review* 58.12 (1940), pp. 1098–1113. DOI: 10.1103/PhysRev.58.1098.
- [52] S. Chikazumi. *Physics of ferromagnetism*. 2nd ed. International series of monographs on physics 94. Oxford: Oxford University Press, 1997. ISBN: 978-0-19-851776-4.
- [53] L. H. Thomas. “The Motion of the Spinning Electron”. In: *Nature* 117.2945 (1926), pp. 514–514. DOI: 10.1038/117514a0.

- [54] J. H. E. Griffiths. “Anomalous High-frequency Resistance of Ferromagnetic Metals”. In: *Nature* 158.4019 (1946), pp. 670–671. DOI: 10.1038/158670a0.
- [55] L. D. Landau and E. M. Lifshitz. “Theory of the dispersion of magnetic permeability in ferromagnetic bodies.” In: *Phys. Z. Sowjetunion* 8 (1935), p. 153. (unpublished).
- [56] T. L. Gilbert. “A Lagrangian formulation of gyromagnetic equation of the magnetization field”. In: *Phys. Rev.* 100 (1955), p. 1243.
- [57] T. L. Gilbert. “A Phenomenological Theory of Damping in Ferromagnetic Materials”. In: *IEEE Transactions on Magnetics* 40.6 (2004), pp. 3443–3449. DOI: 10.1109/TMAG.2004.836740.
- [58] J. Slonczewski. “Current-driven excitation of magnetic multilayers”. In: *Journal of Magnetism and Magnetic Materials* 159.1 (1996), pp. L1–L7. DOI: 10.1016/0304-8853(96)00062-5.
- [59] S. Zhang, P. M. Levy, and A. Fert. “Mechanisms of Spin-Polarized Current-Driven Magnetization Switching”. In: *Physical Review Letters* 88.23 (2002), p. 236601. DOI: 10.1103/PhysRevLett.88.236601.
- [60] C. Herring and C. Kittel. “On the Theory of Spin Waves in Ferromagnetic Media”. In: *Physical Review* 81.5 (1951), pp. 869–880. DOI: 10.1103/PhysRev.81.869.
- [61] C. Kittel. “On the Theory of Ferromagnetic Resonance Absorption”. In: *Physical Review* 73.2 (1948), pp. 155–161. DOI: 10.1103/PhysRev.73.155.
- [62] F. Bloch. “Zur Theorie des Ferromagnetismus”. In: *Z. Physik* 61 (1930), pp. 206–219. DOI: 10.1007/BF01339661.
- [63] C. Kittel. *Introduction to solid state physics*. In collab. with P. McEuen. 8th ed. Hoboken, NJ: Wiley, 2018. 692 pp. ISBN: 978-1-119-45416-8.
- [64] B. A. Kalinikos and A. N. Slavin. “Theory of dipole-exchange spin wave spectrum for ferromagnetic films with mixed exchange boundary conditions”. In: *Journal of Physics C: Solid State Physics* 19.35 (1986), pp. 7013–7033. DOI: 10.1088/0022-3719/19/35/014.
- [65] R. W. Damon and J. R. Eshbach. “Magnetostatic Modes of a Ferromagnetic Slab”. In: *Journal of Applied Physics* 31.5 (1960), S104–S105. DOI: 10.1063/1.1984622.
- [66] C. Bayer et al. “Spin-wave excitations in finite rectangular elements of Ni 80 Fe 20”. In: *Physical Review B* 72.6 (2005), p. 064427. DOI: 10.1103/PhysRevB.72.064427.
- [67] D. D. Stancil. *Theory of Magnetostatic Waves*. New York, NY: Springer New York, 1993. ISBN: 978-1-4613-9340-5.

- [68] H. Suhl. “The theory of ferromagnetic resonance at high signal powers”. In: *Journal of Physics and Chemistry of Solids* 1.4 (1957), pp. 209–227. DOI: 10.1016/0022-3697(57)90010-0.
- [69] V. S. L’vov. *Wave Turbulence Under Parametric Excitation: Applications to Magnets*. Red. by F. Calogero et al. Springer Series in Nonlinear Dynamics. Berlin, Heidelberg: Springer Berlin Heidelberg, 1994. ISBN: 978-3-642-75297-1.
- [70] V. E. Zakharov, V. S. L’vov, and S. S. Starobinets. “Spin-wave turbulence beyond the parametric excitation threshold”. In: *Soviet Physics Uspekhi* 17.6 (1975), pp. 896–919. DOI: 10.1070/PU1975v017n06ABEH004404.
- [71] P. Krivosik and C. E. Patton. “Hamiltonian formulation of nonlinear spin-wave dynamics: Theory and applications”. In: *Physical Review B* 82.18 (2010), p. 184428. DOI: 10.1103/PhysRevB.82.184428.
- [72] V. L. Safonov, M. E. McConney, and M. R. Page. “Parallel pumping of spin waves in a ferromagnet revisited”. In: *Journal of Magnetism and Magnetic Materials* 490 (2019), p. 165486. DOI: 10.1016/j.jmmm.2019.165486.
- [73] A. Venugopal, T. Qu, and R. H. Victora. “Nonlinear Parallel-Pumped FMR: Three and Four Magnon Processes”. In: *IEEE Transactions on Microwave Theory and Techniques* 68.2 (2020), pp. 602–610. DOI: 10.1109/TMTT.2019.2952128.
- [74] H. G. Bauer. “Linear and nonlinear magnetization dynamics in thin ferromagnetic films and nanostructures”. PhD thesis. Regensburg: Universität Regensburg, 2014.
- [75] H. G. Bauer et al. “Nonlinear spin-wave excitations at low magnetic bias fields”. In: *Nature Communications* 6.1 (2015). DOI: 10.1038/ncomms9274.
- [76] R. Dreyer. “Magneto-optical super-Nyquist Sampling of linear and non-linear Spin-Wave Phenomena”. PhD thesis. Halle (Saale): Martin-Luther-Universität Halle-Wittenberg, 2021.
- [77] R. Dreyer et al. “Imaging and phase-locking of non-linear spin waves”. In: *Nature Communications* 13.1 (2022), p. 4939. DOI: 10.1038/s41467-022-32224-0.
- [78] M. Faraday and P. Day. *The philosopher’s tree: a selection of Michael Faraday’s writings*. Bristol: Institute of Physics, 1999. 211 pp. ISBN: 978-0-7503-0570-9.
- [79] J. Kerr. “XLIII. On rotation of the plane of polarization by reflection from the pole of a magnet”. In: *The London, Edinburgh, and Dublin Philosophical Magazine and Journal of Science* 3.19 (1877), pp. 321–343. DOI: 10.1080/14786447708639245.

- [80] J. Stöhr. “Exploring the microscopic origin of magnetic anisotropies with X-ray magnetic circular dichroism (XMCD) spectroscopy”. In: *Journal of Magnetism and Magnetic Materials* 200.1 (1999), pp. 470–497. DOI: 10.1016/S0304-8853(99)00407-2.
- [81] C. M. Hurd. *The Hall Effect in Metals and Alloys*. Boston, MA: Springer US, 1972. ISBN: 978-1-4757-0467-9.
- [82] N. W. Ashcroft and N. D. Mermin. *Solid state physics*. Australia Brazil Canada Mexico Singapore United Kingdom United States Boston, MA: Cengage, 2021. 826 pp. ISBN: 978-0-357-67081-1.
- [83] N. Nagaosa et al. “Anomalous Hall effect”. In: *Reviews of Modern Physics* 82.2 (2010), pp. 1539–1592. DOI: 10.1103/RevModPhys.82.1539.
- [84] M. Weiler et al. “Local Charge and Spin Currents in Magnetothermal Landscapes”. In: *Physical Review Letters* 108.10 (2012), p. 106602. DOI: 10.1103/PhysRevLett.108.106602.
- [85] J. E. Hirsch. “Spin Hall Effect”. In: *Physical Review Letters* 83.9 (1999), pp. 1834–1837. DOI: 10.1103/PhysRevLett.83.1834.
- [86] T. Kimura et al. “Room-Temperature Reversible Spin Hall Effect”. In: *Physical Review Letters* 98.15 (2007), p. 156601. DOI: 10.1103/PhysRevLett.98.156601.
- [87] M. Dyakonov and V. Perel. “Current-induced spin orientation of electrons in semiconductors”. In: *Physics Letters A* 35.6 (1971), pp. 459–460. DOI: 10.1016/0375-9601(71)90196-4.
- [88] Y. K. Kato et al. “Observation of the Spin Hall Effect in Semiconductors”. In: *Science* 306.5703 (2004), pp. 1910–1913. DOI: 10.1126/science.1105514.
- [89] K. Uchida et al. “Observation of the spin Seebeck effect”. In: *Nature* 455.7214 (2008), pp. 778–781. DOI: 10.1038/nature07321.
- [90] T. C. Chuang et al. “Enhancement of the anomalous Nernst effect in ferromagnetic thin films”. In: *Physical Review B* 96.17 (2017), p. 174406. DOI: 10.1103/PhysRevB.96.174406.
- [91] P. Sheng et al. “The spin Nernst effect in tungsten”. In: *Science Advances* 3.11 (2017), e1701503. DOI: 10.1126/sciadv.1701503.
- [92] A. Hirohata et al. “Review on spintronics: Principles and device applications”. In: *Journal of Magnetism and Magnetic Materials* 509 (2020), p. 166711. DOI: 10.1016/j.jmmm.2020.166711.
- [93] G. Schmidt et al. “Ultra Thin Films of Yttrium Iron Garnet with Very Low Damping: A Review”. In: *physica status solidi (b)* 257.7 (2020), p. 1900644. DOI: 10.1002/pssb.201900644.

- [94] C. Hauser et al. “Yttrium Iron Garnet Thin Films with Very Low Damping Obtained by Recrystallization of Amorphous Material”. In: *Scientific Reports* 6.1 (2016), p. 20827. DOI: 10.1038/srep20827.
- [95] H. Qin et al. “Nanoscale magnonic Fabry-Pérot resonator for low-loss spin-wave manipulation”. In: *Nature Communications* 12.1 (2021), p. 2293. DOI: 10.1038/s41467-021-22520-6.
- [96] V. Baltz et al. “Antiferromagnetic spintronics”. In: *Reviews of Modern Physics* 90.1 (2018), p. 015005. DOI: 10.1103/RevModPhys.90.015005.
- [97] H. Reichlova et al. “Imaging and writing magnetic domains in the non-collinear antiferromagnet Mn₃Sn”. In: *Nature Communications* 10.1 (2019), p. 5459. DOI: 10.1038/s41467-019-13391-z.
- [98] I. Dzyaloshinsky. “A thermodynamic theory of “weak” ferromagnetism of antiferromagnetics”. In: *Journal of Physics and Chemistry of Solids* 4.4 (1958), pp. 241–255. DOI: 10.1016/0022-3697(58)90076-3.
- [99] T. Moriya. “Anisotropic Superexchange Interaction and Weak Ferromagnetism”. In: *Physical Review* 120.1 (1960), pp. 91–98. DOI: 10.1103/PhysRev.120.91.
- [100] D.-F. Shao and E. Y. Tsybal. “Antiferromagnetic tunnel junctions for spintronics”. In: *npj Spintronics* 2.1 (2024), p. 13. DOI: 10.1038/s44306-024-00014-7.
- [101] L. Šmejkal, J. Sinova, and T. Jungwirth. “Beyond Conventional Ferromagnetism and Antiferromagnetism: A Phase with Nonrelativistic Spin and Crystal Rotation Symmetry”. In: *Physical Review X* 12.3 (2022), p. 031042. DOI: 10.1103/PhysRevX.12.031042.
- [102] L. Šmejkal, J. Sinova, and T. Jungwirth. “Emerging Research Landscape of Altermagnetism”. In: *Physical Review X* 12.4 (2022), p. 040501. DOI: 10.1103/PhysRevX.12.040501.
- [103] L. Šmejkal et al. “Crystal time-reversal symmetry breaking and spontaneous Hall effect in collinear antiferromagnets”. In: *Science Advances* 6.23 (2020), eaaz8809. DOI: 10.1126/sciadv.aaz8809.
- [104] J. F. W. Herschel. *Treatises on physical astronomy, light and sound contributed to the Encyclopaedia metropolitana*. London, R. Griffin, 1828.
- [105] G. B. Airy. “On the Diffraction of an Object-glass with Circular Aperture”. In: *Transactions of the Cambridge Philosophical Society* 5 (1835), p. 283.
- [106] Rayleigh. “XXXI. *Investigations in optics, with special reference to the spectroscopy*”. In: *The London, Edinburgh, and Dublin Philosophical Magazine and Journal of Science* 8.49 (1879), pp. 261–274. DOI: 10.1080/14786447908639684.
- [107] E. Abbe. “Beiträge zur Theorie des Mikroskops und der mikroskopischen Wahrnehmung”. In: *Archiv für Mikroskopische Anatomie* 9.1 (1873), pp. 413–468. DOI: 10.1007/BF02956173.

- [108] F. Keilmann and R. Hillenbrand. “Near-field microscopy by elastic light scattering from a tip”. In: *Philosophical Transactions of the Royal Society of London. Series A: Mathematical, Physical and Engineering Sciences* 362.1817 (2004). Ed. by D. Richards and A. Zayats, pp. 787–805. DOI: 10.1098/rsta.2003.1347.
- [109] P. Aravind and H. Metiu. “The effects of the interaction between resonances in the electromagnetic response of a sphere-plane structure; applications to surface enhanced spectroscopy”. In: *Surface Science* 124.2 (1983), pp. 506–528. DOI: 10.1016/0039-6028(83)90806-3.
- [110] T. Taubner, R. Hillenbrand, and F. Keilmann. “Performance of visible and mid-infrared scattering-type near-field optical microscopes”. In: *Journal of Microscopy* 210.3 (2003), pp. 311–314. DOI: 10.1046/j.1365-2818.2003.01164.x.
- [111] B. Knoll and F. Keilmann. “Enhanced dielectric contrast in scattering-type scanning near-field optical microscopy”. In: *Optics Communications* 182.4 (2000), pp. 321–328. DOI: 10.1016/S0030-4018(00)00826-9.
- [112] R. Loudon. “Theory of the first-order Raman effect in crystals”. In: *Proceedings of the Royal Society of London. Series A. Mathematical and Physical Sciences* 275.1361 (1963), pp. 218–232. DOI: 10.1098/rspa.1963.0166.
- [113] R. J. Elliott. “Raman Transitions in Crystals”. In: *Physics Letters* 3.4 (1963).
- [114] P. A. Fleury and R. Loudon. “Scattering of Light by One- and Two-Magnon Excitations”. In: *Physical Review* 166.2 (1968), pp. 514–530. DOI: 10.1103/PhysRev.166.514.
- [115] N. B. Manson, J. P. Harrison, and M. J. Sellars. “Nitrogen-vacancy center in diamond: Model of the electronic structure and associated dynamics”. In: *Physical Review B* 74.10 (2006), p. 104303. DOI: 10.1103/PhysRevB.74.104303.
- [116] J. R. Maze et al. “Properties of nitrogen-vacancy centers in diamond: the group theoretic approach”. In: *New Journal of Physics* 13.2 (2011), p. 025025. DOI: 10.1088/1367-2630/13/2/025025.
- [117] G. D. Fuchs et al. “Excited-State Spectroscopy Using Single Spin Manipulation in Diamond”. In: *Physical Review Letters* 101.11 (2008). DOI: 10.1103/PhysRevLett.101.117601.
- [118] M. W. Doherty et al. “The nitrogen-vacancy colour centre in diamond”. In: *Physics Reports* 528.1 (2013), pp. 1–45. DOI: 10.1016/j.physrep.2013.02.001.
- [119] D. Aude Craik et al. “Microwave-Assisted Spectroscopy Technique for Studying Charge State in Nitrogen-Vacancy Ensembles in Diamond”. In: *Physical Review Applied* 14.1 (2020), p. 014009. DOI: 10.1103/PhysRevApplied.14.014009.
- [120] L. J. Rogers et al. “Infrared emission of the NV centre in diamond: Zeeman and uniaxial stress studies”. In: *New Journal of Physics* 10.10 (2008), p. 103024. DOI: 10.1088/1367-2630/10/10/103024.

- [121] E. V. Oort, N. B. Manson, and M. Glasbeek. “Optically detected spin coherence of the diamond N-V centre in its triplet ground state”. In: *Journal of Physics C: Solid State Physics* 21.23 (1988), pp. 4385–4391. DOI: 10.1088/0022-3719/21/23/020.
- [122] J. H. N. Loubser and J. A. V. Wyk. “Electron spin resonance in the study of diamond”. In: *Reports on Progress in Physics* 41.8 (1978), pp. 1201–1248. DOI: 10.1088/0034-4885/41/8/002.
- [123] G. D. Fuchs et al. “Gigahertz Dynamics of a Strongly Driven Single Quantum Spin”. In: *Science* 326.5959 (2009), pp. 1520–1522. DOI: 10.1126/science.1181193.
- [124] G. Balasubramanian et al. “Ultralong spin coherence time in isotopically engineered diamond”. In: *Nature Materials* 8.5 (2009), pp. 383–387. DOI: 10.1038/nmat2420.
- [125] E. D. Herbschleb et al. “Ultra-long coherence times amongst room-temperature solid-state spins”. In: *Nature Communications* 10.1 (2019), p. 3766. DOI: 10.1038/s41467-019-11776-8.
- [126] A. P. Nizovtsev. “A Quantum Computer Based on NV Centers in Diamond: Optically Detected Nutations of Single Electron and Nuclear Spins”. In: *Optics and Spectroscopy* 99.2 (2005), p. 233. DOI: 10.1134/1.2034610.
- [127] S. Takahashi et al. “Quenching Spin Decoherence in Diamond through Spin Bath Polarization”. In: *Physical Review Letters* 101.4 (2008), p. 047601. DOI: 10.1103/PhysRevLett.101.047601.
- [128] P. Andrich et al. “Long-range spin wave mediated control of defect qubits in nanodiamonds”. In: *npj Quantum Information* 3.1 (2017), p. 28. DOI: 10.1038/s41534-017-0029-z.
- [129] L. De Broglie. “Waves and Quanta”. In: *Nature* 112.2815 (1923), pp. 540–540. DOI: 10.1038/112540a0.
- [130] J.-C. Jeon et al. “Multicore memristor from electrically readable nanoscopic racetracks”. In: *Science* 386.6719 (2024), pp. 315–322. DOI: 10.1126/science.adh3419.
- [131] M. Farle, T. Silva, and G. Woltersdorf. “Spin Dynamics in the Time and Frequency Domain”. In: *Magnetic Nanostructures*. Ed. by H. Zabel and M. Farle. Vol. 246. Berlin, Heidelberg: Springer Berlin Heidelberg, 2013, pp. 37–83. ISBN: 978-3-642-32041-5.
- [132] I. Razdolski et al. “Analysis of the time-resolved magneto-optical Kerr effect for ultrafast magnetization dynamics in ferromagnetic thin films”. In: *Journal of Physics: Condensed Matter* 29.17 (2017), p. 174002. DOI: 10.1088/1361-648X/aa63c6.

- [133] E. Beaurepaire et al. “Ultrafast Spin Dynamics in Ferromagnetic Nickel”. In: *Physical Review Letters* 76.22 (1996), pp. 4250–4253. DOI: 10.1103/PhysRevLett.76.4250.
- [134] I. Radu et al. “Transient ferromagnetic-like state mediating ultrafast reversal of antiferromagnetically coupled spins”. In: *Nature* 472.7342 (2011), pp. 205–208. DOI: 10.1038/nature09901.
- [135] Y. Hashimoto et al. “Ultrafast time-resolved magneto-optical imaging of all-optical switching in GdFeCo with femtosecond time-resolution and a micrometer spatial-resolution”. In: *Review of Scientific Instruments* 85.6 (2014), p. 063702. DOI: 10.1063/1.4880015.
- [136] K. Perzlmaier, G. Woltersdorf, and C. H. Back. “Observation of the propagation and interference of spin waves in ferromagnetic thin films”. In: *Physical Review B* 77.5 (2008), p. 054425. DOI: 10.1103/PhysRevB.77.054425.
- [137] A. R. Khorsand et al. “Element-Specific Probing of Ultrafast Spin Dynamics in Multisublattice Magnets with Visible Light”. In: *Physical Review Letters* 110.10 (2013), p. 107205. DOI: 10.1103/PhysRevLett.110.107205.
- [138] C. Von Korff Schmising et al. “Element-Specific Magnetization Dynamics of Complex Magnetic Systems Probed by Ultrafast Magneto-Optical Spectroscopy”. In: *Applied Sciences* 10.21 (2020), p. 7580. DOI: 10.3390/app10217580.
- [139] R. Dreyer et al. “Spin-wave localization and guiding by magnon band structure engineering in yttrium iron garnet”. In: *Physical Review Materials* 5.6 (2021), p. 064411. DOI: 10.1103/PhysRevMaterials.5.064411.
- [140] W. D. Wilber et al. “Light-scattering observation of anomalous parametric spin-wave character in subsidiary absorption”. In: *Journal of Applied Physics* 64.10 (1988), pp. 5477–5479. DOI: 10.1063/1.342524.
- [141] P. Kabos, G. Wiese, and C. E. Patton. “Measurement of spin wave instability magnon distributions for subsidiary absorption in yttrium iron garnet films by Brillouin light scattering”. In: *Physical Review Letters* 72.13 (1994), pp. 2093–2096. DOI: 10.1103/PhysRevLett.72.2093.
- [142] S. Demokritov. “Brillouin light scattering studies of confined spin waves: linear and nonlinear confinement”. In: *Physics Reports* 348.6 (2001), pp. 441–489. DOI: 10.1016/S0370-1573(00)00116-2.
- [143] J. R. Sandercock and W. Wettling. “Light scattering from thermal acoustic magnons in yttrium iron garnet”. In: 13.10 (1973). DOI: 10.1016/0038-1098(73)90276-7.
- [144] P. Grünberg and F. Metawe. “Light Scattering from Bulk and Surface Spin Waves in EuO”. In: *Physical Review Letters* 39.24 (1977), pp. 1561–1565. DOI: 10.1103/PhysRevLett.39.1561.

- [145] J. R. Sandercock. “Brillouin scattering study of SbSI using a double-passed, stabilised scanning interferometer”. In: *Optics Communications* 2.2 (1970), pp. 73–76. DOI: 10.1016/0030-4018(70)90047-7.
- [146] R. Mock, B. Hillebrands, and R. Sandercock. “Construction and performance of a Brillouin scattering set-up using a triple-pass tandem Fabry-Perot interferometer”. In: *Journal of Physics E: Scientific Instruments* 20.6 (1987), pp. 656–659. DOI: 10.1088/0022-3735/20/6/017.
- [147] B. Hillebrands. “Progress in multipass tandem Fabry-Perot interferometry: I. A fully automated, easy to use, self-aligning spectrometer with increased stability and flexibility”. In: *Review of Scientific Instruments* 70.3 (1999), pp. 1589–1598. DOI: 10.1063/1.1149637.
- [148] F. Casola, T. Van Der Sar, and A. Yacoby. “Probing condensed matter physics with magnetometry based on nitrogen-vacancy centres in diamond”. In: *Nature Reviews Materials* 3.1 (2018), p. 17088. DOI: 10.1038/natrevmats.2017.88.
- [149] T. Van Der Sar et al. “Nanometre-scale probing of spin waves using single electron spins”. In: *Nature Communications* 6.1 (2015), p. 7886. DOI: 10.1038/ncomms8886.
- [150] C. S. Wolfe et al. “Off-resonant manipulation of spins in diamond via precessing magnetization of a proximal ferromagnet”. In: *Physical Review B* 89.18 (2014). DOI: 10.1103/PhysRevB.89.180406.
- [151] C. S. Wolfe et al. “Spatially resolved detection of complex ferromagnetic dynamics using optically detected nitrogen-vacancy spins”. In: *Applied Physics Letters* 108.23 (2016), p. 232409. DOI: 10.1063/1.4953108.
- [152] P. Maletinsky et al. “A robust scanning diamond sensor for nanoscale imaging with single nitrogen-vacancy centres”. In: *Nature Nanotechnology* 7.5 (2012), pp. 320–324. DOI: 10.1038/nnano.2012.50.
- [153] J. P. Tetienne et al. “Nanoscale imaging and control of domain-wall hopping with a nitrogen-vacancy center microscope”. In: *Science* 344.6190 (2014), pp. 1366–1369. DOI: 10.1126/science.1250113.
- [154] Y. Dovzhenko et al. “Magnetostatic twists in room-temperature skyrmions explored by nitrogen-vacancy center spin texture reconstruction”. In: *Nature Communications* 9.1 (2018), p. 2712. DOI: 10.1038/s41467-018-05158-9.
- [155] I. Gross et al. “Real-space imaging of non-collinear antiferromagnetic order with a single-spin magnetometer”. In: *Nature* 549.7671 (2017), pp. 252–256. DOI: 10.1038/nature23656.
- [156] A. Finco et al. “Imaging non-collinear antiferromagnetic textures via single spin relaxometry”. In: *Nature Communications* 12.1 (2021), p. 767. DOI: 10.1038/s41467-021-20995-x.

- [157] A. Finco et al. “Thermal Spin Wave Noise as a Probe for the Dzyaloshinskii-Moriya Interaction”. In: *Physical Review Letters* 135.13 (2025), p. 136703. DOI: 10.1103/dvbq-9z5f.
- [158] M. Pelliccione et al. “Scanned probe imaging of nanoscale magnetism at cryogenic temperatures with a single-spin quantum sensor”. In: *Nature Nanotechnology* 11.8 (2016), pp. 700–705. DOI: 10.1038/nnano.2016.68.
- [159] S. C. Scholten et al. “Widefield quantum microscopy with nitrogen-vacancy centers in diamond: Strengths, limitations, and prospects”. In: *Journal of Applied Physics* 130.15 (2021), p. 150902. DOI: 10.1063/5.0066733.
- [160] J. R. Maze et al. “Nanoscale magnetic sensing with an individual electronic spin in diamond”. In: *Nature* 455.7213 (2008), pp. 644–647. DOI: 10.1038/nature07279.
- [161] A. Dréau et al. “Avoiding power broadening in optically detected magnetic resonance of single NV defects for enhanced dc magnetic field sensitivity”. In: *Physical Review B* 84.19 (2011), p. 195204. DOI: 10.1103/PhysRevB.84.195204.
- [162] H. Zheng et al. “Zero-Field Magnetometry Based on Nitrogen-Vacancy Ensembles in Diamond”. In: *Physical Review Applied* 11.6 (2019), p. 064068. DOI: 10.1103/PhysRevApplied.11.064068.
- [163] J. M. Taylor et al. “High-sensitivity diamond magnetometer with nanoscale resolution”. In: *Nature Physics* 4.10 (2008), pp. 810–816. DOI: 10.1038/nphys1075.
- [164] F. Münzhuber et al. “Polarization-Assisted Vector Magnetometry with No Bias Field Using an Ensemble of Nitrogen-Vacancy Centers in Diamond”. In: *Physical Review Applied* 14.1 (2020), p. 014055. DOI: 10.1103/PhysRevApplied.14.014055.
- [165] C. Du et al. “Control and local measurement of the spin chemical potential in a magnetic insulator”. In: *Science* 357.6347 (2017), pp. 195–198. DOI: 10.1126/science.aak9611.
- [166] M. R. Page et al. “Optically detected ferromagnetic resonance in diverse ferromagnets via nitrogen vacancy centers in diamond”. In: *Journal of Applied Physics* 126.12 (2019), p. 124902. DOI: 10.1063/1.5083991.
- [167] C. M. Purser et al. “Spinwave detection by nitrogen-vacancy centers in diamond as a function of probe–sample separation”. In: *Applied Physics Letters* 116.20 (2020), p. 202401. DOI: 10.1063/1.5141921.
- [168] B. A. McCullian et al. “Broadband multi-magnon relaxometry using a quantum spin sensor for high frequency ferromagnetic dynamics sensing”. In: *Nature Communications* 11.1 (2020), p. 5229. DOI: 10.1038/s41467-020-19121-0.

- [169] E. Lee-Wong et al. “Nanoscale Detection of Magnon Excitations with Variable Wavevectors Through a Quantum Spin Sensor”. In: *Nano Letters* 20.5 (2020), pp. 3284–3290. DOI: 10.1021/acs.nanolett.0c00085.
- [170] A. Solyom et al. “Probing a Spin Transfer Controlled Magnetic Nanowire with a Single Nitrogen-Vacancy Spin in Bulk Diamond”. In: *Nano Letters* 18.10 (2018), pp. 6494–6499. DOI: 10.1021/acs.nanolett.8b03012.
- [171] J. J. Carmiggelt et al. “Broadband microwave detection using electron spins in a hybrid diamond-magnet sensor chip”. In: *Nature Communications* 14.1 (2023), p. 490. DOI: 10.1038/s41467-023-36146-3.
- [172] R. Schirhagl et al. “Nitrogen-Vacancy Centers in Diamond: Nanoscale Sensors for Physics and Biology”. In: *Annual Review of Physical Chemistry* 65.1 (2014), pp. 83–105. DOI: 10.1146/annurev-physchem-040513-103659.
- [173] F. Dolde et al. “Electric-field sensing using single diamond spins”. In: *Nature Physics* 7.6 (2011), pp. 459–463. DOI: 10.1038/nphys1969.
- [174] D. M. Toyli et al. “Fluorescence thermometry enhanced by the quantum coherence of single spins in diamond”. In: *Proceedings of the National Academy of Sciences* 110.21 (2013), pp. 8417–8421. DOI: 10.1073/pnas.1306825110.
- [175] M. W. Doherty et al. “Temperature shifts of the resonances of the NV - center in diamond”. In: *Physical Review B* 90.4 (2014), p. 041201. DOI: 10.1103/PhysRevB.90.041201.
- [176] T. Plakhotnik et al. “All-Optical Thermometry and Thermal Properties of the Optically Detected Spin Resonances of the NV - Center in Nanodiamond”. In: *Nano Letters* 14.9 (2014), pp. 4989–4996. DOI: 10.1021/nl501841d.
- [177] B. M. Chernobrod and G. P. Berman. “Spin microscope based on optically detected magnetic resonance”. In: *Journal of Applied Physics* 97.1 (2005), p. 014903. DOI: 10.1063/1.1829373.
- [178] M. Vaez-Iravani and R. Toledo-Crow. “Phase contrast and amplitude pseudoheterodyne interference near field scanning optical microscopy”. In: *Applied Physics Letters* 62.10 (1993), pp. 1044–1046. DOI: 10.1063/1.108789.
- [179] N. Ocelic, A. Huber, and R. Hillenbrand. “Pseudoheterodyne detection for background-free near-field spectroscopy”. In: *Applied Physics Letters* 89.10 (2006), p. 101124. DOI: 10.1063/1.2348781.
- [180] A. Vansteenkiste et al. “The design and verification of MuMax3”. In: *AIP Advances* 4.10 (2014), p. 107133. DOI: 10.1063/1.4899186.
- [181] J. J. Joos et al. “Tutorial: Simulating modern magnetic material systems in mumax3”. In: *Journal of Applied Physics* 134.17 (2023), p. 171101. DOI: 10.1063/5.0160988.

- [182] H. D. Arnold and G. W. Elmen. “Permalloy, A New Magnetic Material of Very High Permeability”. In: *Bell System Technical Journal* 2.3 (1923), pp. 101–111. DOI: 10.1002/j.1538-7305.1923.tb03595.x.
- [183] D. Rodrigues et al. “Nonlinear Dynamics of Topological Ferromagnetic Textures for Frequency Multiplication”. In: *Physical Review Applied* 16.1 (2021), p. 014020. DOI: 10.1103/PhysRevApplied.16.014020.
- [184] V. E. Demidov et al. “Resonant frequency multiplication in microscopic magnetic dots”. In: *Applied Physics Letters* 99.1 (2011), p. 012505. DOI: 10.1063/1.3609011.
- [185] H. Ulrichs et al. “Parametric excitation of eigenmodes in microscopic magnetic dots”. In: *Physical Review B* 84.9 (2011), p. 094401. DOI: 10.1103/PhysRevB.84.094401.
- [186] T. Hula et al. “Spin-wave frequency combs”. In: *Applied Physics Letters* 121.11 (2022), p. 112404. DOI: 10.1063/5.0090033.
- [187] F. Groß et al. “Imaging magnonic frequency multiplication in nanostructured antidot lattices”. In: *Physical Review B* 106.1 (2022), p. 014426. DOI: 10.1103/PhysRevB.106.014426.
- [188] J. Steiner et al. “Formation and coarsening of the concertina magnetization pattern in elongated thin-film elements”. In: *Physical Review B* 85.10 (2012), p. 104407. DOI: 10.1103/PhysRevB.85.104407.
- [189] C. Lüthi et al. “Long-range spin wave imaging with nitrogen vacancy centers and time resolved magneto-optical measurements”. In: *Review of Scientific Instruments* 96.3 (2025). DOI: 10.1063/5.0243762.
- [190] A. Pandey et al. “Anomalous Nernst Effect-Based Near-Field Imaging of Magnetic Nanostructures”. In: *ACS Nano* 18.46 (2024), acsnano.4c09749. DOI: 10.1021/acsnano.4c09749.
- [191] A. Pandey et al. *Switching of magnetic domains in a noncollinear antiferromagnet at the nanoscale*. 2024. DOI: 10.48550/ARXIV.2409.15533.
- [192] M. S. Anderson. “Locally enhanced Raman spectroscopy with an atomic force microscope”. In: *Applied Physics Letters* 76.21 (2000), pp. 3130–3132. DOI: 10.1063/1.126546.
- [193] R. M. Stöckle et al. “Nanoscale chemical analysis by tip-enhanced Raman spectroscopy”. In: *Chemical Physics Letters* 318.1 (2000), pp. 131–136. DOI: 10.1016/S0009-2614(99)01451-7.
- [194] J. Jersch et al. “Mapping of localized spin-wave excitations by near-field Brillouin light scattering”. In: *Applied Physics Letters* 97.15 (2010), p. 152502. DOI: 10.1063/1.3502599.

- [195] D. W. Preston. “Doppler-free saturated absorption: Laser spectroscopy”. In: *American Journal of Physics* 64.11 (1996), pp. 1432–1436. DOI: 10.1119/1.18457.
- [196] R. Schlüßler et al. “Mechanical mapping of spinal cord development and repair in living zebrafish larvae using Brillouin microscopy”. In: *bioRxiv* (2018). DOI: 10.1101/181560.
- [197] S. M. Lindsay, M. W. Anderson, and J. R. Sandercock. “Construction and alignment of a high performance multipass vernier tandem Fabry–Perot interferometer”. In: *Review of Scientific Instruments* 52.10 (1981), pp. 1478–1486. DOI: 10.1063/1.1136479.
- [198] M. Shirasaki. “Large angular dispersion by a virtually imaged phased array and its application to a wavelength demultiplexer”. In: *Optics Letters* 21.5 (1996), p. 366. DOI: 10.1364/OL.21.000366.
- [199] A. Mokhtari and A. A. Shishegar. “Rigorous 3d Vectorial Gaussian Beam Modelling of Demultiplexing Performance of Virtually-Imaged_Phased- Assays”. In: *Progress In Electromagnetics Research M* 13 (2010), pp. 1–16. DOI: 10.2528/PIERM10041604.
- [200] K. V. Berghaus, S. H. Yun, and G. Scarcelli. “High Speed Sub-GHz Spectrometer for Brillouin Scattering Analysis”. In: *Journal of Visualized Experiments* 106 (2015). DOI: 10.3791/53468.
- [201] M. Kim et al. “Shear Brillouin light scattering microscope”. In: *Optics Express* 24.1 (2016), p. 319. DOI: 10.1364/OE.24.000319.
- [202] T. Hache et al. “Control of Four-Magnon Scattering by Pure Spin Current in a Magnonic Waveguide”. In: *Physical Review Applied* 20.1 (2023), p. 014062. DOI: 10.1103/PhysRevApplied.20.014062.
- [203] K. Berghaus et al. “High-finesse sub-GHz-resolution spectrometer employing VIPA etalons of different dispersion”. In: *Optics Letters* 40.19 (2015), p. 4436. DOI: 10.1364/OL.40.004436.
- [204] G. Scarcelli and S. H. Yun. “Multistage VIPA etalons for high-extinction parallel Brillouin spectroscopy”. In: *Optics Express* 19.11 (2011), p. 10913. DOI: 10.1364/OE.19.010913.
- [205] T. Janda et al. “Magneto-Seebeck microscopy of domain switching in collinear antiferromagnet CuMnAs”. In: *Physical Review Materials* 4.9 (2020), p. 094413. DOI: 10.1103/PhysRevMaterials.4.094413.
- [206] C. Zhang et al. “Nanoscale Magnetization and Current Imaging Using Time-Resolved Scanning-Probe Magnetothermal Microscopy”. In: *Nano Letters* 21.12 (2021), pp. 4966–4972. DOI: 10.1021/acs.nanolett.1c00704.

- [207] H. Isshiki et al. “Observation of Cluster Magnetic Octupole Domains in the Antiferromagnetic Weyl Semimetal Mn₃Sn Nanowire”. In: *Physical Review Letters* 132.21 (2024), p. 216702. DOI: 10.1103/PhysRevLett.132.216702.

List of Publications

- C. Körner, R. Dreyer, M. Wagoner, N. Liebing, H. G. Bauer, G. Woltersdorf. “**Frequency Multiplication by Collective Nanoscale Spin-Wave Dynamics**”. In: *Science* (2022), 375 (6585), pp. 1165–1169, DOI: 10.1126/science.abm6044
- A. Pandey, R. Dreyer, P. Seyidov, C. Körner, S. Tirpanci, B. K. Hazra, S. S. P. Parkin, G. Woltersdorf “**Origin of Helicity-Dependent Photoconductivity in Magnetic and Nonmagnetic Wires**”. In: *Phys. Rev. B* (2022), 106 (17), p. 174420, DOI: 10.1103/PhysRevB.106.174420
- N. Becker, C. Ulrich, C. Körner, B. Schlecht. “**A novel method for measurements of surface topography in previously inaccessible areas**”. In: *Materials Testing* (2023), vol. 65, no. 12, pp. 1758-1766, DOI: 10.1515/mt-2023-0269
- J.-K. Kim, K.-R. Jeon, P. K. Sivakumar, J. Jeon, C. Körner, G. Woltersdorf, S. S. P. Parkin. “**Intrinsic supercurrent non-reciprocity coupled to the crystal structure of a van der Waals Josephson barrier**”. In: *Nature Communications* (2024) 15, p. 1120, DOI: 10.1038/s41467-024-45298-9
- H. Han, A. Sharma, J. Yoon, Z. Wang, C. Körner, H. Deniz, A. K. Sharma, F. Li, C. Sturm, G. Woltersdorf, S. S. P. Parkin. “**All-Oxide Metasurfaces Formed by Synchronized Local Ionic Gating**”. In: *Advanced Materials* (2024), p. 2401064, DOI: 10.1002/adma.202401064
- A. Pandey, J. Deka, J. Yoon, A. Mathew, C. Körner, R. Dreyer, J. M. Taylor, S. S. P. Parkin, G. Woltersdorf. “**Anomalous Nernst Effect-Based Near-Field Imaging of Magnetic Nanostructures**”. In: *ACS Nano* (2024), 18 (46), pp. 31949-31956, DOI: 10.1021/acsnano.4c09749
- M. Date, F. Petocchi, Y. Yen, J. A. Krieger, B. Pal, V. Hasse, E. C. McFarlane, C. Körner, J. Yoon, M. D. Watson, V. N. Strocov, I. Kostanovski, M. N. Ali, S. Ju, N. C. Plumb, M. A. Sentef, G. Woltersdorf, M. Schüler, P. Werner, C. Felser, S. S. P. Parkin, N. B. M. Schröter. “**Momentum-Resolved Fingerprint of Mottness in Layer-Dimerized Nb₃Br₈**”. In: *Nature Communications* (2025), 16, p. 4037, DOI: 10.1038/s41467-025-58885-1
- A. Pandey, P. Rigvedi, E. Lesne, J. Deka, J. Yoon, W. Hoppe, C. Körner, B. Pal, J. M. Taylor, S. S. P. Parkin, G. Woltersdorf. “**Switching of magnetic domains in a noncollinear antiferromagnet at the nanoscale**”, *under review* (2025), DOI: 10.48550/ARXIV.2409.15533

Curriculum Vitae

Personal Information

Name: Chris Marcel Körner
Nationality: German

Education

- since 2019 Member of the International Max Planck Research School on Science and Technology of Nano Systems (IMPRS-STNS) of the Max Planck Institute of Microstructure Physics in Halle (Saale)
Member of the executive board of the IMPRS-STNS (2023-2025)
- since 2019 **Ph.D. studies** at Martin Luther University Halle-Wittenberg
Supervisor: Prof. Dr. Georg Woltersdorf
Co-Supervisor: Prof Dr. Stuart S. P. Parkin
Thesis: “Optical Microscopy of Magnetic Phenomena Beyond the Diffraction Limit”
Subject Area of Thesis: nonlinear magnetism, NV center magnetometry, SNOM, BLS
- 2016-2019 **Master studies** (M.Sc. in Physics)
at Martin Luther University Halle-Wittenberg
Thesis: “Untersuchung optischer Nah- und Fernfeldeigenschaften metallischer Metastrukturen”
Subject Area of Thesis: scanning optical near field microscopy, optical metastructures
Supervisor: Prof. Dr. Georg Woltersdorf
- 2013-2016 **Bachelor studies** (B.Sc. in Physics)
at Martin Luther University Halle-Wittenberg
Thesis: “Aufbau eines Terahertz Raman-Kopplers zur Messung niederfrequenter Anregungsmoden”
Subject Area of Thesis: Raman spectroscopy
Supervisor: Prof. Dr. Georg Woltersdorf
- 2005-2013 **Abitur** at Burgenland Gymnasium Laucha

Professional Experience

since 2019 **Research Assistant**

at Martin Luther University Halle-Wittenberg, Institute of Physics
Regular Teaching in Basic Physics Lab Courses

2015-2018 **Student Worker**

at Martin Luther University Halle-Wittenberg, Institute of Physics

Conference Contributions and External Workshops

- 2017 **Spring Meeting of the German Physical Society** – Dresden, Germany
Poster: “Optical detection of ferromagnetic resonance via photoluminescence in diamond NV-centers”
- 2018 **Spring Meeting of the German Physical Society** – Berlin, Germany
Poster: “Optical detection of magnetic excitations in ferromagnets via photoluminescence in nearby diamond NV centers”
- 2019 **Spring Meeting of the German Physical Society** – Regensburg, Germany
Talk: “Detection of spin waves in NiFe thin films by luminescence of diamond defect centers”
- 2020 **Joint European Magnetism Symposia** – Online Conference
Talk: “Frequency multiplication effects in thin FM layers detected by diamond NV-center microscopy”
- 2022 **Spring Meeting of the German Physical Society** – Regensburg, Germany
Talk: “Frequency multiplication by collective nanoscale spin wave dynamics”
- 2022 **757. WE-Heraeus-Seminar on Non-Linear Magnetism** – Bad Honnef, Germany
Poster: “Frequency multiplication by collective nanoscale spin wave dynamics”
- 2023 **Spring Meeting of the German Physical Society** – Dresden, Germany
Poster: “Frequency Multiplication by Collective Nanoscale Spin Wave Dynamics”
- 2023 **Near-Field Optical Nanoscopy Summer School** – San Sebastian, Spain
Poster: “Tip-Enhanced Near Field Brillouin Light Scattering”
- 2023 **Magnonics 2023 Conference** – Le Touquet, France
Talk: “Frequency multiplication by collective nanoscale spin wave dynamics”
- 2023 **Joint European Magnetism Symposia** – Madrid, Spain
Poster: “Frequency Multiplication by Collective Nanoscale Spin Wave Dynamics” *Poster Prize Finalist*
- 2024 **International Conference on Magnetism** – Bologna, Italy
Poster: “Frequency Multiplication by Collective Nanoscale Spin Wave Dynamics”
- 2024 **Spin Mechanics Conference** – Greifswald, Germany
Poster: “Frequency multiplication by collective nanoscale spin-wave dynamics”
- 2025 **Spring Meeting of the German Physical Society** – Regensburg, Germany
Poster: “Efficient all-magnonic frequency multiplication in nanoscale devices”

Retreats Attended During the Ph.D. Program

- 2019 Retreat of the NISE Department of MPI Halle – Ringberg, Germany
- 2019 Winter School of the CRC/TRR 227 – Usedom, Germany
- 2022 IMPRS Retreat – Ringberg, Germany
- 2022 IMPRS Retreat – Schkopau, Germany
- 2024 IMPRS Retreat – Bad Schandau, Germany
- 2025 Joint International Retreat of IMPRS and FZU on “NanoSpinTech – Quantum Systems, Probes and Beyond” – Turnov, Czech Republic
- 2025 Joint Winter School of CRC/TRR 227 and IMPRS on “Ultrafast Spin Systems and Correlated Matter” – Halle (Saale), Germany

Complementary Skills Courses Attended During the Ph.D. Program

- 2021 Good Scientific Practice (hosted by InGrA at MLU)
- 2022 Academic writing: How to create good texts (hosted by IMPRS)
- 2022 The Seyence Method for Effective Communication of Science (hosted by IMPRS)
- 2023 Development and Design of Academic Posters (hosted by IMPRS)
- 2024 Introduction to 3D Visualization with Blender for Scientists (hosted by IMPRS)

Eidesstattliche Erklärung

Hiermit erkläre ich, Chris Körner, die vorliegende Arbeit selbständig und ohne fremde Hilfe verfasst zu haben. Es wurden keine anderen als die von mir angegebenen Quellen und Hilfsmittel benutzt. Die den benutzten Werken wörtlich oder inhaltlich entnommenen Stellen sind als solche kenntlich gemacht worden. Ich erkläre, die Angaben wahrheitsgemäß gemacht, keine vergeblichen Promotionsversuche unternommen und keine Dissertation an einer anderen wissenschaftlichen Einrichtung zur Erlangung eines akademischen Grades eingereicht zu haben. Ich bin weder vorbestraft noch sind gegen mich Ermittlungsverfahren anhängig.

Halle (Saale), den 17.10.2025

Chris Körner

Acknowledgments

First, I want to sincerely thank my supervisor, Prof. Georg Woltersdorf for giving me the opportunity to work in his group on many interesting projects. I benefited greatly from his knowledge when dealing with the many different challenges and questions every day. From electron beam lithography to plumbing, from aligning optical setups to maintaining vacuum systems. Having someone with such a comprehensive knowledge and technical understanding in so many different areas of engineering and physics really isn't a matter of course. That gave me the opportunity to learn so much in very different areas. Thank you for always having good advice to solve any problem that came up in the lab and also for the discussions which really helped my understanding, especially in optics and magnetism.

My thanks goes to all my colleagues from the Optics Group, whether former or current, for all of your help throughout the years, the discussions of crazy and less crazy ideas during the coffee breaks, the conference visits with little sleep and lots of coffee to compensate, the BBQ evenings and other group events.

I thank everyone who has been involved in this work, in one way or the other: Niklas Liebing and Simon Wisotzki for teaching me how to prepare samples using lithography. Later on, Wolfgang Hoppe and Alexandra Schrader helped with sample fabrication, as well. Many colleagues performed different measurements: SNS-MOKE measurements were performed by Rouven Dreyer and Paul Rondt. Cora Retzela and Alexandra Schrader worked on the confocal NV magnetometry setup. Richard Hoppe helped setting up the SNOM and performed measurements (and destroyed a few tips in the process). Furthermore, I thank my collaborators from Montpellier University, Aurore Finco, Roméo Beignon and Vincent Jacques for carrying out the scanning NV magnetometry measurements.

I thank the IMPRS of the Max Planck Institute in Halle for the support and the various opportunities to meet new people, the courses and the retreats. I thank the head of institute, Prof. Stuart Parkin, for giving me the opportunity to be part of this research school. A special thanks goes to Ann-Kristin Flieger, who always tries hard to improve IMPRS and to keep it running.

I thank all the people who supported me in the writing of this thesis. Especially to Rouven, Georg, Wolfgang, Seth and Janine for proofreading. Thank you for your valuable feedback which definitely improved this thesis significantly.

Finally, I thank my family, without whom all of this wouldn't have been possible, my parents Tanja and Thomas, my sister Janine and also the rest of my family. During the last years I could always count on your support! Finally, I thank Sinha for enduring the most stressful time with me, the time of writing this thesis.